FERMILAB-THESIS-2020-35

Electroweak interactions in Nucleons and Nuclei

THESIS

SUBMITTED FOR THE AWARD OF THE DEGREE OF

DOCTOR OF PHILOSOPHY
IN
PHYSICS

BY
ZUBAIR AHMAD DAR

UNDER THE SUPERVISION OF
PROF. MOHAMMAD SAJJAD ATHAR

DEPARTMENT OF PHYSICS
ALIGARH MUSLIM UNIVERSITY
ALIGARH – 202002, INDIA
2020

CONTENTS

ACKNOWLEDGMENTS

In the name of Allah, the most gracious the most merciful "Allah supports His victory whom He wills".

All praises are to Almighty Allah Who guides humans through good and bad times. Allah always chooses the best for his creation, it's just the limitation of the human perception of observing the things which force them to decide about the good and bad times. Allah has always guided me with His utmost blessings and I would like to thank Almighty Allah for keeping me strong physically, mentally as well as emotionally to culminate this journey of Ph.D.

The journey of Ph.D. comes with many hardships, occasional frustration, encouragement, trust, and when you are about to taste the experience of completion you realize this journey would not have been possible without the support of many nears and dears who supported unconditionally and helped to accomplish this task, though the cover page will highlight only one name.

First of all, I would like to extend my sincere gratitude towards my mentor and advisor Professor Mohammad Sajjad Athar for his overwhelming support both morally and academically, guidance, motivation, and immense knowledge which *enabled this journey to become less cumbersome. Whenever I found myself in some trouble or directionless, Prof Athar used to be always standing by my side. I have been watching him since last 9 years and his dedication towards profession, regularity and honesty encouraged me to choose him as research guide. I remember one of his lines that "if at the end of the day you realize that you didn't feel you have been honest with time, everything you earn is meaningless". He always showed faith in me and his motivation tips helped me to sustain myself in this journey. I am grateful to him for providing me the opportunity to be a part of the high energy physics community at Fermi National Accelerator Laboratory which is one of the world's finest neutrino facilities. He has also taught me the importance of being organized and having a professional attitude at work. I will always fall short of words to express special thanks to you Sir. I would also like to express my gratitude towards my co-supervisor Dr. Md. Naimuddin. I consider myself blessed and privileged for his significant guidance and encouragement which helped me to remain focused. He has always been available and guided me with the best of his knowledge. Special thanks to Professor Deborah Harris with whom I have worked at Fermi National Accelerator Laboratory. She is a gem of a person. I am really a lucky person to have worked with her. Her kindness and consistent help with sympathetic attitude always helped me to remain on track and not get diverged because of the complicacy of the subject. The discussions with her have always been fruitful as her great insight about the subject is remarkable and profound. I will never forget the long Skype discussion with you Debbie where you entertained my most silly and stupid questions with beautiful explanations. I never hesitated to talk to you whenever I was in some kind of problem. I would like to extend special thanks and gratitude to Prof. S. K. Singh for all his help and guidance during the period I worked at Aligarh Muslim University. He is an inspiration to me because we always used to look at him the way he has been consistent since the last 50 years. I have heard that age is just a number and Prof. S. K. Singh is a living example of this proverb. Thanks to Dr. Sanjeev Kumar from Delhi University as well for helping during my initial years of Ph.D. Special thanks to Ms. Fouzia*

Ahmed for being an inspiration. Her support and encouragement was as important as my advisor's and we always looked at her to take inspiration of how to organize things in a perfect way. She has always supported emotionally and treated me like a family member. Thank you ma'am for listening and appreciating things which I was always hesitant to talk to Prof. Athar.

My sincere thanks to the Chairman, Department of Physics, Prof. B. P. Singh for providing me all the required facilities for the completion of my research work.

Research environment always plays a greater role in conducting research in a peaceful manner. I thank my colleagues Dr. Huma Haider, Dr. Rafi Alam, Dr. Farhana Zaidi, Ms. Faiza Akbar, Ms. Vaniya Ansari, Mr. Prameet Kumar Gaur and Mr. Sayeed Akhter for providing such an environment and being ready to help whenever needed. Also, I would like to thank Dr. Daljeet Kaur for her support and guidance and fruitful discussion.

I owe a sincere thanks to Dr. Atika Fatima whom I have worked closely since the beginning of my Ph.D tenure. She has been a motivation always whenever I felt off the road. She is an amazing friend and colleague. Thanks for all the help, encouragement, guidance and support. This journey would have been quite boring without your support and help.

I want to thank also the non teaching staff of my department, especially to Mr. Naseem Ahmad Khan, Mr. Ashish Jacob, Mr. Musharraf Ali and Mr. Zeeshan Fazal, who relentlessly have been supportive and kind and always attentive to any kind of help I asked for. Thanks are due to seminar staff of the department, specially to Mr. Shakeel Kirmani for his support.

I am highly thankful to my friends Mr. Aadil Rashid, Dr. Shakeel Ahmad Naikoo, Mr. Kaiser Manzoor, Dr. Subzar Ahmad Beigh, Dr. Saleq Omar for their selfless help, motivation and friendly support. Also, special thanks to Ms. Priyanka Kumari and Dr. Sandeep Kaur for help, motivation and encouragement.

Close friends make the good times better and the hard times easier but with some friends it's always opposite. My heartiest appreciation to Dr. Shahid Ahmad Wani for his continuous encouragement, untiring help and strong criticism which helped in confidence building and forced me to stay focused on my goal.

I revere the patronage and moral support extended with love by my family, especially my parents Mr. Nazir Ahmad Dar and Ms. Jawahira Akhtar whose encouragement, support and patience has made it possible for me to complete this journey. It is because of their selfless sacrifices, prayers, encouragement and unconditional love which has led me here. Apart from my interest in physics, it is my mother who has always pushed me to do academics instead of diving into some professional courses. I am proud to say to her now that I attained the highest degree in academics. I also thank my siblings Ifrat Nazir, Asmat Nazir and Ubaid Nazir for their love and support. Also, special thanks to my paternal uncle Gh. Rasool Lone who has been a mentor guiding me with the light of the Holy Quran whenever I get distracted. I dedicate this thesis to my grandma who no one can replace in my life.

I would like to pay my deepest tribute to Aligarh Muslim University which has been my home since last 11 years. The work environment provided by the AMU is phenomenal. I will always pray to Almighty Allah to keep my institution safe and in the best condition. Also, a special tribute to the MINERvA collaboration whom I have been associated with since the last two years. It is a privilege to work with the great scientists involved in many physics analyses. Thanks to Jeff Nelson, Laura Fields, Kevin McFarland, Jorge Morfin, Dan Ruterboris and all the active members of the collaboration for the help and support.

I also would want to thank DST (Govt.of India) for providing me the necessary financial support to carry out this research work.

Zubair Ahmad Dar

LIST OF FIGURES

LIST OF TABLES

LIST OF PUBLICATIONS

International: Direct

1. Daljeet Kaur, **Zubair Ahmad Dar**, Sanjeev Kumar, Md. Naimuddin,
   "Search for the differences in atmospheric neutrinos and antineutrinos oscillation parameters at the INO-ICAL experiment",
   Phys. Rev. D **95**, 093005 (2017).

2. **Zubair Ahmad Dar**, Daljeet Kaur, Sanjeev Kumar, Md. Naimuddin,
   "Independent measurement of muon neutrino and antineutrino oscillations at the INO–ICAL experiment",
   J. Phys. G **46**, 065001 (2019).

3. A. Fatima, **Z. Ahmad Dar**, M. Sajjad Athar and S. K. Singh,
   "Photon induced $K\Lambda$ production on the proton in the low energy region,"
   Int. J. Mod. Phys. E **29**, no.07, 2050051 (2020).

International: Collaboration

1. T. Cai et al. (The MINERνA Collaboration),
   "Nucleon binding energy and transverse momentum imbalance in neutrino-nucleus",
   Phys. Rev. D **101**, 092001 (2020).

2. M. F. Carneiro et al. (The MINERνA Collaboration),
   "High-Statistics Measurement of Neutrino Quasielasticlike Scattering at 6 GeV on a Hydrocarbon Target",
   Phys. Rev. Lett. **124**, 121801 (2020).

3. D. Coplowe et al. (The MINERνA Collaboration),
   "Probing Nuclear Effects with Neutrino-induced Charged-Current Neutral Pion Production",
   Phys. Rev. D **102**, 072007 (2020).

4. A. Filkins et al. (The MINERνA Collaboration),
   "Double-Differential Inclusive Charged-Current ν_μ Cross Sections on Hydrocarbon in MINERvA at $<E_\nu>$ 3.5 GeV",
   Phys. Rev. D **101**, 112007 (2020).

National

1. Daljeet Kaur, **Zubair Ahmad Dar**, Sanjeev Kumar, Md. Naimuddin,
   "The INO-ICAL Sensitivity for the Separate Measurement of Neutrinos/Anti-neutrinos Parameters",
   Springer Proc. Phys. **203**, 423 (2018).

2. Daljeet Kaur, **Zubair Ahmad Dar**, Sanjeev Kumar, Md. Naimuddin,
   "Measurement of Atmospheric Neutrino Mass-Squared Splittings at INO-

ICAL Experiment",
DAE HEP 2018.

3. **Zubair Ahmad Dar**, Daljeet Kaur, Sanjeev Kumar, Md. Naimuddin,
"The measurement of the difference between ν and $\bar{\nu}$ mass-squared splittings in Atmospheric and Long Baseline Neutrino Experiments",
Springer Proc. Phys. **234**, 353 (2019).

4. **Zubair Ahmad Dar**, Daljeet Kaur, Sanjeev Kumar, Md. Naimuddin,
"Independent measurement of neutrino and antineutrino mass-square splittings at the INO-ICAL experiment",
DAE Symp. Nucl. Phys. **62**, 984 (2017).

5. Daljeet Kaur, **Zubair Ahmad Dar**, Sanjeev Kumar, Md. Naimuddin,
"Neutrino/Anti-neutrino oscillation analysis using non-identical atmospheric oscillation parameters",
DAE Symp. Nucl. Phys. **62**, 974 (2017).

6. A. Fatima, **Zubair Ahmad Dar**,
"Photon induced associated production near threshold,
DAE Symp. Nucl. Phys. **64**, 667 (2020).

Part I

Introduction

CHAPTER 1

INTRODUCTION

One of the most important goals of physicists is to find out the ultimate structure of the matter and to understand their interactions. Presently, the theory that describes the fundamental particles and their interactions is the standard model of particle physics. It considers that there are four basic interactions in nature *viz.*, strong, weak, electromagnetic, and gravitational, and corresponding to each interaction, there are mediating particles known as the quanta of interactions. For example, the mediating quanta for the strong interactions are gluons which are of eight different types, for the electromagnetic interactions it is a photon, for the weak interactions there are $W^{\pm}$ and Z bosons and for the gravitational interactions it is the graviton. Since gravitational interaction is much smaller in strength than the other three interactions, therefore, it is not discussed in the presence of any of the other three. The standard model of particle physics has a zoo of 61 fundamental particles comprising of charged leptons ($l^{\pm}; l = e, \mu, \tau$), neutral leptons ($\nu_l, \bar{\nu}_l$), quarks (which come in six flavors *viz.* up, down, charm, strange, top and bottom, and each flavor appears in three different colors *viz.*, red, blue and green) and antiquarks (corresponding to each quark) as well as the mediating quanta discussed above. Now, the quest is to develop a theory that unifies all these fundamental interactions into one. It was Einstein who first attempted to develop a single theoretical framework that can account for all the fundamental interactions of nature resulting in a unified field theory. Particularly, in the early 20th century, attempts were made to unify gravitational and electromagnetic interactions, however, these attempts failed.

The motivation behind the unification of fundamental interactions is also driven by the fact that the standard model of cosmology assumes that the universe started with a big bang from pure energy and after a time $t \sim 10^{-43}$ seconds (Planck's time), the temperature ($> 10^{32}$ K) and density ($> 10^{90}$ kg/m^3) were very high, and during this time, all the four fundamental interactions were one and gradually with expansion, these interactions got decoupled in a time interval of 10^{-35} to 10^{-6} seconds. First, the gravitational interaction got decoupled and then the strong nuclear force got decoupled from the electroweak interactions. Then the electromagnetic force got separated from the weak force and the universe was left with a soup of leptons, quarks, photons, and other particles. Therefore, to describe such a scenario, there must be a theory that treats all the interactions on the same footing. Since then, the efforts are on to unify the fundamental interactions.

The real breakthrough came in 1961 when Glashow [1] constructed a model based on the gauge group SU(2)$\times$U(1) for the weak and electromagnetic interactions of leptons assuming that along with photons, there also exist charged W and neutral Z intermediate bosons. The masses of W and Z bosons were put by hand and therefore the theory was non-renormalizable. In 1967-68, Salam [3] and Weinberg [4] independently constructed SU(2)$\times$U(1) model of electroweak interactions of leptons by introducing spontaneous symmetry breaking of the gauge symmetries. 't Hooft and Veltman [5] and Lee and Zinn-Justin [6] showed that this model is renormalizable. Later, Glashow, Iliopoulos and Maiani [7] extended the model to include the quark sector. The success of this model is startling and various predictions of the model were experimentally observed to a very high accuracy. The last and the most important particle, known by the name Higgs boson, which is the carrier particle of the Higgs field, a field that permeates space and endows all elementary subatomic particles with mass through its interactions with them, was discovered in 2012 by ATLAS and CMS experiments at CERN [2]. The story of electroweak interactions is not complete without due recognition of the neutrino, especially because it has played a pivotal role in the understanding of weak interactions as it is the particle that participates only in the weak interactions. Moreover, trillions of neutrinos pass through our body in each second from several sources, both natural and man-made, and without them stars can not shine, no elements heavier than helium, and so on, regarding which we shall discuss later in this chapter. Now, we shall present in very brief the historical development of neutrinos, their sources, etc.

The hypothesis of the neutrino started with a letter written by Pauli in 1930 [8] to the participants of a nuclear physics conference held in Germany, to solve the two outstanding problems of nuclear physics at that time *viz.*, the puzzle of the energy conservation in the β-decays of nuclei and the anomalies in understanding the spin-statistics relation in the case of ^{14}N and ^{6}Li nuclei. In the letter, Pauli proposed the existence of a new neutral particle inside the nucleus along with the proton, which he called as "neutron" (now known as neutrino) with the following properties:

- Neutron is a spin $\frac{1}{2}$ particle and is a constituent of nuclei.
- Neutrons do not travel at the speed of light.
- Their mass is similar to the electron mass but not larger than 0.01 times the proton mass.
- It has a magnetic moment which is of the order of 10^{-13} cm and is bound in the nucleus by the magnetic forces.
- The neutral spin $\frac{1}{2}$ particle shares the available energy with the electron leading to the continuous energy spectrum of β-electrons.

In 1931, in a conference, where Fermi was also present, Pauli talked about the proposed particle neutron. Fermi was quite impressed with Pauli's idea of the neutron. With the discovery of present-day neutron in 1932 by Chadwick, Fermi in 1933 [9] rechristened Pauli's "neutron" as "neutrino" (meaning the little neutral one) and proposed the theory of β-decays, which was developed by taking the idea of Dirac's particle creation and annihilation, Heisenberg's idea that the neutrons and protons were related to each other and the basic principles of Quantum Electrodynamics (QED), the gauge theory of electromagnetic interactions. In the Fermi theory, there is no change of angular momentum and parity between the initial and the final nuclei and the interaction occurs at a single point as shown in Figure 1.1. The Hamiltonian for the β-decay process viz. $n \to p + e^- + \nu$, is written in terms of the four spinors representing the initial and the final particles and the Dirac γ matrix as:

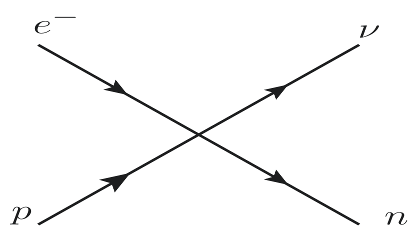

Figure 1.1: Four point Fermi interaction. Weak force turns a neutron into a proton and simultaneously creates an electron and an antineutrino.

$$\mathcal{H} = G\bar{\psi}_p\gamma_\mu\psi_n \ \bar{\psi}_e\gamma^\mu\psi_\nu + h.c., \tag{1.1}$$

where G is the strength of the interaction and the nature of the interaction is taken to be vector in analogy with the electromagnetic interaction. This was a remarkable theory by Fermi as it accounts for all the observed properties of β decay. Moreover, it also predicts the correct shape of the energy spectrum of the emitted electrons. Later, Gamow and Teller [10] extended the theory of β-decays to those nuclei in which a change of angular momentum by one unit and no change in parity was observed. In order to take into account the Gamow-Teller transitions, the Hamiltonian given in Eq. (1.1) has to be redefined, by including all the bilinear covariants *viz.* scalar (1), vector (γ^μ), axial vector ($\gamma^\mu\gamma_5$), tensor ($\sigma^{\mu\nu}$) and pseudoscalar (γ_5) such that

$$\mathcal{H} = \sum_{i=S,V,A,T,P} G\bar{\psi}_p O^i \psi_n \ \bar{\psi}_e O_i \psi_\nu + h.c.. \tag{1.2}$$

Since the beta decays involve very low energies, therefore, in the non-relativistic limit, the pseudoscalar term vanishes. Moreover, the scalar and vector interaction terms appearing in the above Hamiltonian reduce to Fermi interaction, while the tensor and axial vector terms reduce to the Gamow-Teller interaction. Most of the experimental results, at that time, were supporting the Hamiltonian to be of scalar and tensor interaction type while only a few were favoring vector and axial vector combination. However, it was Sudarshan and Marshak [11] who first argued that the weak interaction Hamiltonian should be of $V-A$ type, which very soon got support from Feynman and Gell Mann [12] and Sakurai [13].

Since then many efforts have been made to develop the theory of weak interactions and the major breakthrough came in 1956 when it was proposed that parity may not be conserved in weak interactions in order to understand the $\tau-\theta$ puzzle [14]. Two particles τ and θ with the same mass, charge, and lifetime, were observed experimentally at that time but they decay into different pionic states viz. τ decays to two pions and θ decays to three pions. Since it was confirmed that pions have odd parity, therefore, it was concluded that τ has even parity and θ has odd parity. After analyzing various processes including strong, electromagnetic, and weak, Lee and Yang [15] concluded that there is no experimental evidence for parity conservation in weak interactions and proposed specific experiments to test parity nonconservation in weak interactions. Wu et al. in 1957 [16], performed the celebrated experiment of ^{60}Co nuclei undergoing β-decay into ^{60}Ni nuclei and concluded that parity is violated in weak interactions. The establishment of parity violation in weak interactions, the theoretical development of the two component theory of neutrinos and the measurement of definite helicity states of neutrinos and antineutrinos to be left- and right-handed, respectively, led to the confirmation of the $V - A$ theory of weak interactions.

In the $V - A$ theory, the Hamiltonian for the β-decay process $n \to p + e^- + \nu$ is given as

$$\mathcal{H} = \frac{G_F}{\sqrt{2}} l_\mu J^{\mu\dagger} + h.c. \tag{1.3}$$

where G_F is the Fermi coupling constant, which is related to the factor G appearing in Eq. (1.1) by a factor of $\frac{1}{\sqrt{2}}$, l^μ is the leptonic current, and J^μ is the hadronic current given by the following expressions:

$$l_\mu = \bar{\psi}_e \gamma_\mu (1 - \gamma_5) \psi_\nu, \tag{1.4}$$

$$J^\mu = \bar{\psi}_p \gamma^\mu (1 - g_A \gamma_5) \psi_n, \tag{1.5}$$

with g_A being the axial vector coupling strength. At higher energies, the cross section evaluated in the $V - A$ theory diverges. To avoid such divergences, in analogy with QED, it was conjectured that the weak interactions are mediated by massive spin 1 intermediate vector bosons. It was thought that these massive bosons would solve the divergence problem, but that didn't happen. The presence of massive bosons makes the $V - A$ theory non-renormalizable, however, they played an important role in the development of the standard model of particle physics.

In the standard model of particle physics [17], there exists three flavors of neutrinos viz. ν_e, ν_μ and ν_τ corresponding to the three charged leptons e^-, μ^- and τ^-. These leptons are classified into doublets on the basis of their weak isospin (I_W) quantum number, as

$$\begin{pmatrix} \nu_e \\ e^- \end{pmatrix}, \quad \begin{pmatrix} \nu_\mu \\ \mu^- \end{pmatrix}, \quad \begin{pmatrix} \nu_\tau \\ \tau^- \end{pmatrix}.$$

Similarly, the highest charge state should sit at the top, therefore, the charged antileptons (e^+, μ^+ and τ^+) and the neutral ones ($\bar{\nu}_e$, $\bar{\nu}_\mu$ and $\bar{\nu}_\tau$) are classified under I_W, as

$$\begin{pmatrix} e^+ \\ \bar{\nu}_e \end{pmatrix}, \quad \begin{pmatrix} \mu^+ \\ \bar{\nu}_\mu \end{pmatrix}, \quad \begin{pmatrix} \tau^+ \\ \bar{\nu}_\tau \end{pmatrix}.$$

Although Fermi's theory of β decay gave a very solid foundation for the existence of neutrinos, however, for many years it was considered to be an undetectable particle, as was proposed by Pauli in his original proposal. For example, Bethe and Peierls shortly after the Fermi theory, gave the prediction for the cross section for neutrinos of few MeV energies (like that from a reactor antineutrino) to have cross section $\sim 5 \times 10^{-44}\text{cm}^2$ for $\bar{\nu}_e + p \rightarrow e^+ + n$ scattering, and for such a low cross section (as compared to the strong interaction cross section $\sim 10^{-26}\text{cm}^2$ and electromagnetic interaction induced cross section $\sim 10^{-32}\text{cm}^2$), initially it looked impossible to find a few interaction events. In 1946, it was Pontecorvo who challenged this opinion and proposed the radiochemical method of the neutrino detection. Several experimental efforts were made to detect this elusive particle, however, the real breakthrough came when Reines and Cowan in 1956 [18] at the Savannah river nuclear reactor reported the observation of neutrinos (rather they were antineutrinos as we know today that from the reactors, only antineutrinos are produced) in the reaction

$$\bar{\nu}_e + p \longrightarrow e^+ + n. \tag{1.6}$$

using a 4200 L scintillator detector. e^+ immediately gets annihilated with an e^- in the detector giving rise to two instant photons in the process $e^+ + e^- \rightarrow \gamma + \gamma$, and a delayed photon released from the neutron capture process through $n +^{108}\text{Cd} \rightarrow^{109}\text{Cd} + \gamma$, almost 15 microseconds later. The observation of two instant photons and one delayed photon confirmed the indirect detection of antineutrino from the nuclear reactors. Later, the neutrinos associated with heavy flavors of lepton viz. muon and tauon were observed and were named ν_μ and ν_τ, respectively, in 1963 by Danby et al. [19], and in 2000 by DONUT [20] and later by OPERA [21] collaborations. It was also shown in the experiments that ν_e and ν_μ are different from one another as well as it was independently shown in the experiments that ν_e and $\bar{\nu}_e$ are the two different particles. Since the observation by Reines and Cowan, neutrino physics is in the forefront of, not only, the field of particle physics but also it has helped in the understanding of weak interaction induced phenomenon in nuclear physics as well as getting information about the structure of the hadrons, and in many astrophysical and cosmological phenomenon. The importance of neutrinos and the study of their interaction with the matter may be realized by the fact that several Nobel Prizes have been awarded for physics discoveries in topics either directly in the field of neutrino physics or in the topics in which the role of neutrino physics has been very crucial.

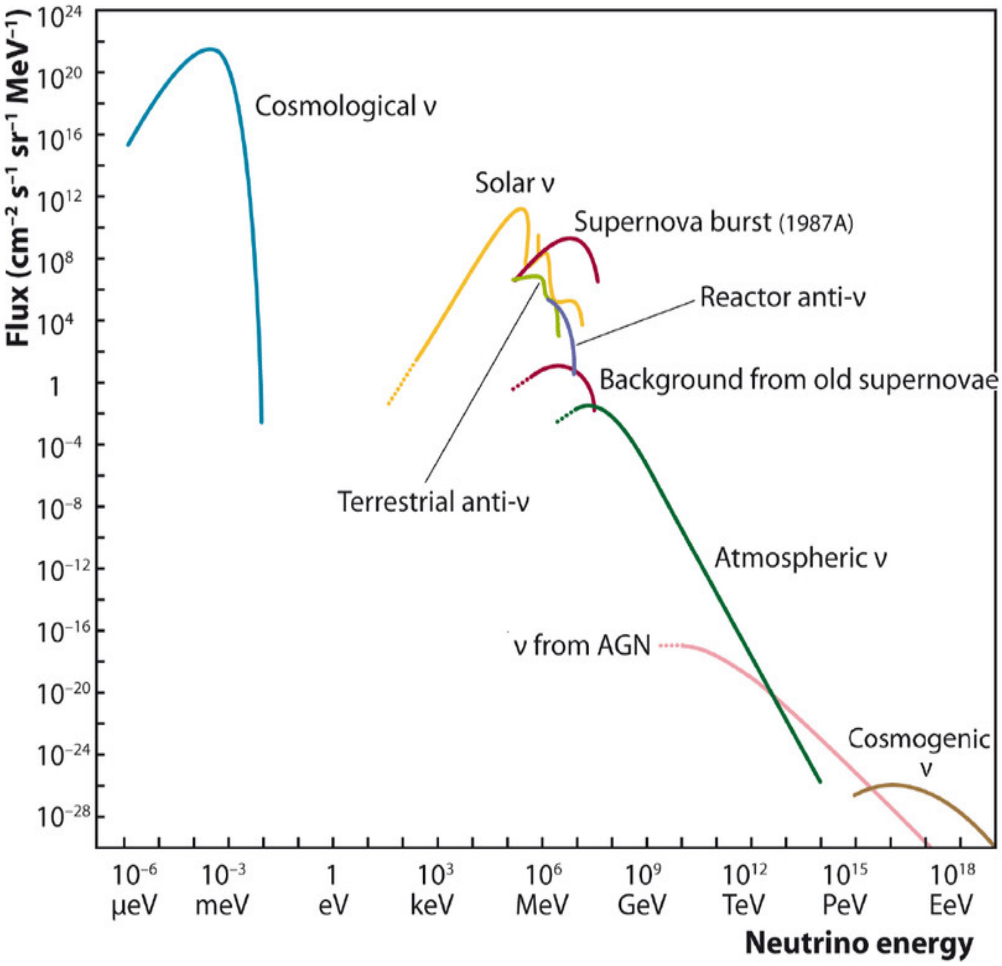

Figure 1.2: Flux of different neutrino sources. Figure has been taken from Ref. [22].

The neutrinos are being produced by various sources including the neutrinos produced in the early universe after the big bang, in the core of the sun and other stars, in the Earth's core, in the atmosphere of the Earth during the decay of secondary cosmic ray particles, in the nuclear reactors, particle accelerators, etc. The neutrinos emitted from the various sources are not of the same energies as well as their distributions are different. This energy range starts from a few μeV for the cosmological neutrinos to more than EeV for cosmogenic neutrinos, which can be observed from the spectrum shown in Figure 1.2. Broadly, one can classify the neutrino production to be of two types, viz., the natural and the man-made sources as:

- **Natural sources:** Relic neutrinos/cosmic neutrino background, solar neutrinos, atmospheric neutrinos, supernova neutrinos, geoneutrinos, ultra-high energy cosmic neutrinos or the neutrinos from the extra-galactic sources, etc.
- **Man-made sources:** Reactor antineutrinos, accelerator neutrinos, neutrinos from the decay of particles at rest, neutrinos from muon storage rings, etc.

Now, we discuss the production mechanism for neutrinos coming from the different sources in brief.

The universe started with a big bang which happened around 13.8 billion years ago and since then, the universe is expanding and cooling. However, during expansion, the universe has passed through different phases, which in the literature are known as the eras or the epoch of the universe and in the different eras, the different particles were created and the fundamental forces were separated from the unified force. When the universe was about 10^{-32} seconds old, it consisted only of radiations and the gravitational force separated out from the other unified forces. During 10^{-32} to 10^{-12} seconds, the first ever particles in the universe were created, which are the W and Z bosons as well as the Higgs bosons. Since the temperature of the universe was very high at that time (of the order of 10^{20}K), these particles were getting created and annihilated in the absence of thermal equilibrium. With further expansion (from 10^{-12} to 10^{-6} seconds), the quark-antiquark pairs were created, which were present in the form of a hot, opaque soup of quark-gluon plasma. During 10^{-6} to 1 second, the temperature was about

10^{16}K, and the quarks which were present in the quark-gluon plasma combined to form the hardons. Under such high temperature, the electrons that collide with protons fuse to form neutrons and neutrinos. Similarly, neutrinos and neutrons also fuse to form electrons and protons *i.e.*, $\nu_e + n \rightarrow e^- + p$. When the universe was quite young $\sim$ 1 sec old, the neutrinos decoupled from the cosmic soup of hadrons and leptons and constitute the "cosmic neutrino background" (which are also called the 'relics of the big bang'). Just like the cosmic microwave background radiation (CMBR), these cosmic neutrinos are present around us with a density of $\sim$ 340 ν/cm^3 of all flavors of neutrinos, but these neutrinos have very low energy of the order of 10^{-4} eV, therefore, it is not possible to observe the relic neutrinos experimentally in the near future. The photons decoupled to form CMBR when the universe was about 380M years old, thus, they give information of that time, however, from the cosmic neutrino background the information about the first few seconds of the big bang could be revealed.

The majority of the neutrinos that come to us are from the Sun and are called solar neutrinos. The Sun as well as all the other stars in the universe shine because of the nuclear fusion process taking place inside the core of the star. In the nuclear fusion process, four protons are fused to form a helium nucleus along with two positrons and two neutrinos and releases $\sim$ 25 MeV of energy,

$$4p \longrightarrow^4 He + 2e^+ + 2\nu_e + 25MeV. \tag{1.7}$$

In the above reaction, $\sim$ 97-98% of the energy is carried away by the photons, and the neutrinos carry only 2-3% of the total energy. Due to the electromagnetic interactions of the photon, it takes a longer time for the photons say almost 10^4 years to come out of the star's core. However, because of the weakly interacting nature of the neutrinos, they take $\sim$ 8 mins to reach earth. Thus, direct information about the core of the sun has been obtained from these neutrinos. Solar neutrinos were first detected by Davis et al. [23] through the reaction

$$\nu_e +^{37} Cl \longrightarrow^{37} Ar + e^-, \tag{1.8}$$

which is sensitive to the electron type neutrinos being produced inside the sun. The experiment observed only 1/3 of the number of neutrinos predicted by the standard solar model formulated by Bahcall [24], and lead to the 'solar neutrino anomaly'. After Davis' experiment, various other experiments like SAGE, Kamiokande, etc., also observed this anomaly in the number neutrinos. This anomaly was later solved by the phenomena known as 'neutrino oscillation', which was first introduced by Pontecorvo [25] in 1957-58 after getting inspired by the formulation of $K^0 - \bar{K}^0$ oscillation mechanism by Gell-Mann and Pais [26]. Pontecorvo argued that "If the theory of two-component neutrino was not valid (which is hardly probable at present) and if the conservation law for neutrino charge took no place, neutrino $\rightarrow$ antineutrino transitions in vacuum would be in principle possible......". We shall discuss the phenomenon of neutrino oscillation later in this chapter.

The atmospheric neutrinos are produced when the high energy primary cosmic rays hit the Earth's atmosphere at a distance of $\sim$ 15 km from the surface of the Earth. The primary cosmic rays consist of $\sim$ 90% protons, 9% α particles, and $<$ 1% heavier nuclei. When these cosmic rays hit the Earth's atmosphere, they interact with the air molecules to produce pions and kaons (which are also called as secondary cosmic rays). These pions and kaons, then, decay to produce $\mu^\pm$ and $\nu_\mu(\bar{\nu}_\mu)$. The $\mu^-(\mu^+)$ is also an unstable particle that then decays to a electron (positron), an electron antineutrino (neutrino), and a muon neutrino (antineutrino). The reactions may be summarized as

$$
\begin{aligned}
p + A_{air} &\longrightarrow n + \pi^+(K^+) + X, \\
n + A_{air} &\longrightarrow p + \pi^-(K^-) + X, \\
\pi^\pm(K^\pm) &\longrightarrow \mu^\pm + \nu_\mu(\bar{\nu}_\mu), \\
\mu^\pm &\longrightarrow e^\pm + \nu_e(\bar{\nu}_e) + \bar{\nu}_\mu(\nu_\mu).
\end{aligned}
$$

The atmospheric neutrino spectrum has a very wide energy range and the main source of neutrinos up to an energy of 100 GeV is the pion decay while the neutrinos of higher energies are obtained from the kaon decay. This is mainly due to the fact that the mean free path at higher energies becomes sufficiently large for the pions and they are able to reach the earth. Since in the cosmic rays, there are more protons than neutrons, the number of π^+, K^+ is more than the number of π^-, K^-, which leads to a larger number of μ^+ than μ^-.

From the above reactions, it may be observed that for a single pion (or kaon) decay, the expected flux ratio of the neutrinos for $\phi(\nu_\mu+\bar{\nu}_\mu)$ to $\phi(\nu_e+\bar{\nu}_e)$ is 2:1. The efforts to search for the atmospheric neutrinos experimentally started in the 1960s, however, with the development of the heavier nuclear targets, in the 1980s in the Kamiokande and IMB collaborations, the atmospheric neutrinos were observed. Moreover, it was found that the observed number of muons had a significant deficit as compared with the Monte Carlo prediction, while the electron events were in agreement to the Monte Carlo predictions. This is known as the atmospheric neutrino anomaly and is resolved by considering the fact that the neutrinos oscillate from one flavor to another, which was confirmed in many atmospheric neutrino experiments. In fact, the 2015 Nobel prize in Physics were awarded to Prof. Takaaki Kajita(Super-Kamiokande Lab, Japan) and Prof. Arthur B. McDonald(SNO Lab, Canada) for their sustained experimental efforts which confirmed the phenomenon of neutrino oscillation in atmospheric and solar neutrinos, respectively.

Supernova neutrinos and antineutrinos of all flavors having energies 10-30 MeV are produced during the death phase of a massive star ($M_{star} \geq 8M_\odot$, where $M_\odot$ is the mass of the Sun that occurs with a supernova explosion. The massive stars use various lighter elements as the fuel for the nuclear fusion process until the formation of iron and with the exhaustion of most of the nuclear fuel, the inner core consists mainly of iron. When the mass of the core exceeds the Chandrasekhar limit ($M_{core} \geq 1.4M_\odot$), the pressure of the degenerate electron gas becomes unable to balance the force of gravity. Due to this, the core contracts more rapidly, which in turn increases the temperature of the core, releasing very high energy gamma rays. As the temperature of the core reaches about 8×10^9K and the density becomes $\sim 10^9$gm/cm^3, the photodisintegration of iron takes place as the high energy photons break iron nuclei into helium and neutron via the reaction

$$\gamma +^{56} Fe \longrightarrow 13^4He + 4n - 124.4\text{MeV}. \tag{1.9}$$

This loss of energy enhances the collapse, which almost becomes a free fall of the matter from the outer layers of the core to the inner core, thus increasing the temperature of the core. With further increase in temperature, the photons become so energetic that the disintegration of helium into proton and neutron takes place, that absorbs about 6 MeV per nucleon energy

$$\gamma +^4 He \longrightarrow 2p + 2n - energy. \tag{1.10}$$

Due to the collapse, the density of the core becomes so high that the electron capture $e^- + p \to \nu_e + n$ takes place. Initially, these neutrinos come out of the core but as the density of the core rises, the neutrinos produced by these processes are trapped in the core that becomes opaque to neutrinos. These neutrinos then interact with the matter present in the core through various processes *viz.*,

$$\begin{aligned} \nu_e + \bar{\nu}_e &\rightleftarrows \nu_l + \bar{\nu}_l \qquad\qquad l = e, \mu, \tau, \\ \nu_l + N &\rightleftarrows \nu_l + N \\ \nu_l + e^- &\rightleftarrows \nu_l + e^-. \end{aligned}$$

When the collapsing core reaches a density of 10^{14} gm/cm^3, which is approximately the same as density of the atomic nuclei, the strong nuclear force comes into play. The core becomes stiff and the neutrons degenerate. The collapse of the inner core is halted because of the neutron degeneracy, but the outer envelope of the core continues with the collapse and the matter from the outer core rebounds with the stiff inner core and shock waves are produced. When the shock waves become energetic enough, the outer envelope of the star explodes at a speed of about 30,000 km/s. With this explosion, around 10^{57} neutrinos of all flavors are released in a very short period of time $\sim$ 10 seconds, which were initially trapped due to the high density of the core. These neutrinos act as the energy carriers and carry about 10^{60} MeV of energy deposited in the core of the star. This explosion is known as the supernova explosion and the core left behind is called the neutron star. In 1987, from the supernova SN1987A explosion, a total of 25 neutrino events were detected at Kamiokande, IMB, and Baksan detectors. However, it is expected that if a supernova explosion takes place in our own galaxy, then about 5,000 to

8,000 neutrino events may be observed in a single detector in a few seconds of time.

In the case of our Earth, it is well known that the information about the core of the earth is very limited. However, with the experimental observation of geoneutrinos, it is now confirmed that in the core of the Earth there exist radioactive elements like isotopes of potassium, thorium and uranium. The geoneutrinos, which are of electron type (ν_e and $\bar{\nu}_e$), are released during the β decay of these radioactive elements. Therefore, the geoneutrinos provide information about the composition of the elements in the core of the earth. The KamLAND as well as the Borexino experiments have observed geoneutrinos through the inverse β decay process.

Since the observation of antineutrinos by Reines and Cowan, the reactor antineutrinos have played a significant role in the understanding of neutrinos as well as in the determination of the neutrino oscillation parameters. The nuclear power plants use neutron-rich elements like ^{235}U, ^{238}U, ^{239}Pu and ^{241}Pu, which undergo fission reaction and produce antineutrinos as the by-product. The flux of these antineutrinos is proportional to the thermal power of the nuclear reactor. For example, in the nuclear fission of ^{235}U, about 200 MeV of energy gets released, and typically in a nuclear fission process, 6 antineutrinos are produced, implying that for a Giga-Watt reactor, in each second about 2×10^{20} antineutrinos are produced. Several experiments using nuclear reactors are presently ongoing, and many more are planned. With the development of neutrino physics and the realization that the natural sources like solar and atmospheric neutrinos have limitations of beam intensity, energy, etc., it was very soon realized that one should go for accelerator neutrinos. In 1960, Schwartz published the first realistic scheme of a neutrino beam for the study of the weak interactions using accelerator sources. The very first neutrino beams were obtained in 1962 using 15GeV AGS accelerator proton beam at Brookhaven striking a beryllium target, and mainly producing pions and a small fraction of kaons. Since then neutrino beams have been extensively used

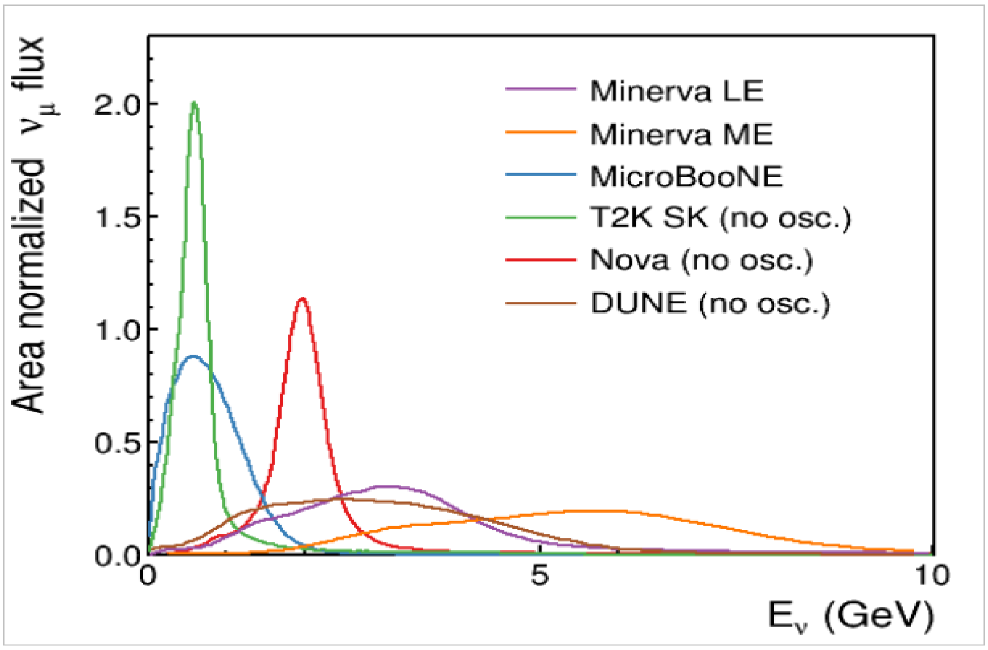

Figure 1.3: Area normalized ν_μ flux as a function of neutrino energy for MINERvA low and medium energy run, MicroBooNE, T2K, NOvA and DUNE experiment. Figure taken from Ref. [27].

in particle physics at CERN in Europe, ANL, BNL, Fermilab in the USA, Tokai and KEK in Japan, etc. In order to obtain the neutrino beam at the accelerators, particle accelerators are used to accelerate the protons to very high energies. Then these highly energetic protons are smashed into a target say graphite or it can be any material that withstands very high temperatures. When the protons traveling near the speed of light hits a target, it slows down and the proton's energy is used to produce a jet of hadrons, which consists mainly of pions and kaons. The charged pions/kaons are unstable and decay predominantly into muons and neutrinos. A charged pion/kaon can be collimated using magnetic horns to produce either neutrinos or antineutrinos by changing the direction of the magnetic field. Thus, to get a neutrino beam in a certain direction, one points the pion/kaon in the direction of the detector. In Figure 1.3, we have shown a typical flux spectrum for the accelerator neutrinos (ν_μ) presently being used or planned to be used like the MINERvA low and medium energy run, MicroBooNE, T2K, NOvA, and DUNE experiments. Generally from the accelerators, neutrino energy beams in

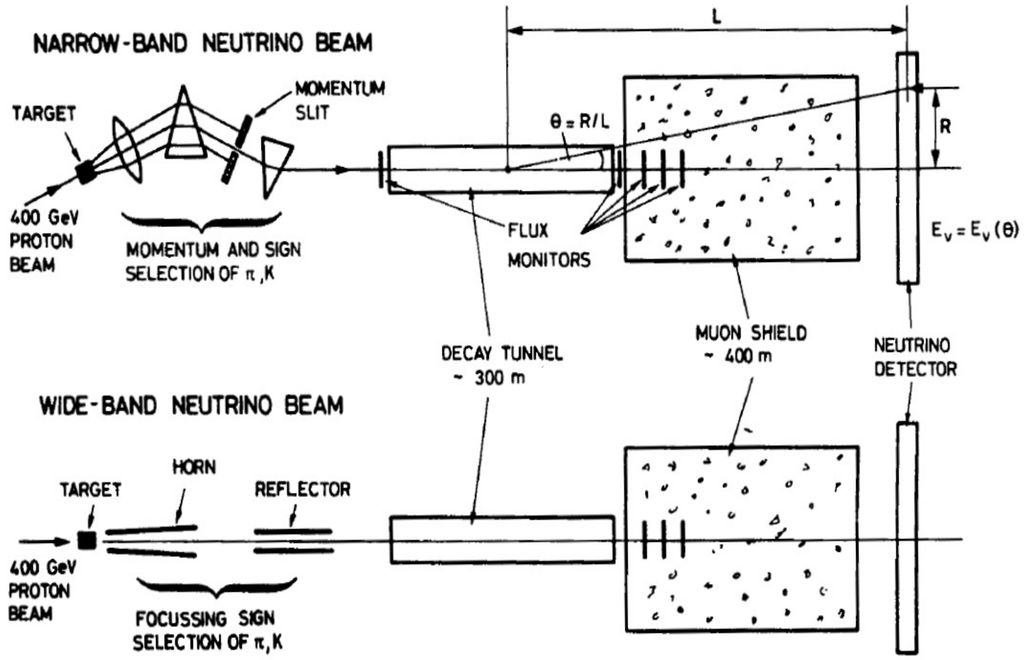

Figure 1.4: Narrow (top) and wide (bottom) band neutrino beam setup.

the range from MeV's to several GeV's are obtained. However, if one uses off-axis facility then a narrow energy band beam at the cost of reduced neutrino flux is obtained. In the case of wide band beam, a cylindrical target struck by the protons is aligned with the decay tunnel and magnetic horns are placed to focus the mesons (Figure 1.4). Mesons decay in the decay pipe to give neutrinos and the neutrino beam so obtained is known as the wide band beam. The drawback with a wide band beam is that it is very difficult to precisely estimate the energy spectrum and relative amounts of the different neutrino species in the beam. The name narrow band neutrino beam refers to the selection of parent mesons in a narrow energy interval. In this case, the cylindrical target struck by the protons is not aligned with the decay tunnel and additional dipole magnets and momentum slits select the mesons of desired energy (Figure 1.4).

Now, let us discuss the neutrino oscillation phenomena in brief. The neutrino oscillation is purely a quantum mechanical phenomena where the neutrinos oscillate from one flavor, say ν_α, to another flavor, say ν_β, where $\alpha, \beta = e, \mu, \tau$; and $\alpha \neq \beta$, while traversing distance. The neutrino oscillation phenomena implies that neutrinos have non-zero mass and the flavor eigenstates of neutrinos are different from their mass eigenstates. As we have discussed earlier, various neutrino experiments have already confirmed the phenomena of neutrino oscillation in solar, atmospheric, reactor and accelerator neutrinos. Here, for completeness, we are discussing the two flavor neutrino oscillation in vacuum, which can be generalized to three flavor oscillation.

In order to study neutrino oscillations, we have to take into account the non-zero mass of neutrino and thus, the flavor and mass eigenstates of neutrinos are different from one another. Assume that the flavor states ν_e and ν_μ participating in the weak interactions are an admixture of the mass eigenstates ν_1 and ν_2 and this mixing between flavor and mass eigenstates is described by a unitary mixing matrix U, which is represented in the two-dimensional space as

$$U = \begin{pmatrix} \cos\theta & \sin\theta \\ -\sin\theta & \cos\theta \end{pmatrix} \tag{1.11}$$

such that

$$\nu_{l=e,\mu} = \sum_{i=1,2} U_{li}\nu_i. \tag{1.12}$$

The unitarity of the U matrix requires that in 2-dimensional space it is described by one parameter which is generally chosen to be θ (mixing angle) such that

$$|\nu_e> \;=\; \cos\theta|\nu_1> + \sin\theta|\nu_2>, \tag{1.13}$$

$$|\nu_\mu> \;=\; -\sin\theta|\nu_1> + \cos\theta|\nu_2> . \tag{1.14}$$

As pure beam of ν_e at $t = 0$ propagates, the mass eigenstates would evolve according to

$$|\nu_1> \;=\; \nu_1(0)e^{-iE_1t} \tag{1.15}$$

$$|\nu_2> \;=\; \nu_2(0)e^{-iE_2t} \tag{1.16}$$

where same momentum states for E_1 and E_2 are considered, $E_1 = \sqrt{p^2 + m_1^2} = p + \frac{m_1^2}{2p}$ and $E_2 = \sqrt{p^2 + m_2^2} = p + \frac{m_2^2}{2p}$, $p \approx E$ in the highly relativistic limit, being the common momentum of neutrinos with energy E_1 and E_2 and m_1 and m_2 are the mass of $|\nu_1>$ and $|\nu_2>$ states, respectively. After a time t, the $|\nu_e(t)>$ will be a different admixture of $|\nu_1>$ and $|\nu_2>$.

The probability of finding ν_μ in the beam of ν_e at a later time t is given by

$$P(\nu_e \to \nu_\mu) = \sin^2 2\theta \sin^2\left(\frac{\Delta m^2}{2E}L\right). \tag{1.17}$$

Thus, we see that for $P(\nu_e \to \nu_\mu) \neq 0$ we need $\Delta m^2 \neq 0$ and $\theta \neq 0$ i.e. we need the mass difference between the neutrinos mass eigenstates to be non-zero implying that at least one of them is massive and the mixing angle θ to be non-zero.

The three flavor neutrinos, viz. ν_e, ν_μ, ν_τ, while propagating in space, travel as some admixture of three neutrino mass eigenstates viz. ν_i $(i = 1, 2, 3)$ with masses m_i, which are related by a 3×3 unitary matrix

$$|\nu_\alpha\rangle = \sum_{i=1}^{3} U_{\alpha i}|\nu_i\rangle \quad (\alpha = e, \mu, \tau)\,. \tag{1.18}$$

$$\begin{pmatrix} \nu_e \\ \nu_\mu \\ \nu_\tau \end{pmatrix} = \begin{pmatrix} U_{e1} & U_{e2} & U_{e3} \\ U_{\mu 1} & U_{\mu 2} & U_{\mu 3} \\ U_{\tau 1} & U_{\tau 2} & U_{\tau 3} \end{pmatrix} \begin{pmatrix} \nu_1 \\ \nu_2 \\ \nu_3 \end{pmatrix}. \tag{1.19}$$

The lepton mixing matrix $U_{\alpha\beta}$, in the above expression, is given by Pontecorvo-Maki-Nakagawa-Sakata [25, 28] (PMNS) mixing matrix as:

$$U = \begin{pmatrix} 1 & 0 & 0 \\ 0 & c_{23} & s_{23} \\ 0 & -s_{23} & c_{23} \end{pmatrix} \begin{pmatrix} c_{13} & 0 & s_{13}e^{-i\delta} \\ 0 & 1 & 0 \\ -s_{13}e^{i\delta} & 0 & c_{13} \end{pmatrix} \begin{pmatrix} c_{21} & s_{12} & 0 \\ -s_{12} & c_{12} & 0 \\ 0 & 0 & 1 \end{pmatrix} \tag{1.20}$$

$$= \begin{pmatrix} c_{12}c_{13} & s_{12}c_{13} & s_{13}e^{-i\delta} \\ -s_{12}c_{23} - c_{12}s_{13}s_{23}e^{i\delta} & c_{12}c_{23} - s_{12}s_{13}s_{23}e^{i\delta} & c_{13}s_{23} \\ s_{12}s_{23} - c_{12}s_{13}c_{23}e^{i\delta} & -c_{12}s_{23} - s_{12}s_{13}c_{23}e^{i\delta} & c_{13}c_{23} \end{pmatrix}, \tag{1.21}$$

where $s_{ij} = \sin\theta_{ij}$ and $c_{ij} = \cos\theta_{ij}(i,j = 1,2,3)$. In this parameterization of the mixing matrix, the mixing parameters can take values in the ranges $0 \le \theta_{ij} \le \frac{\pi}{2}$ $(i,j = 1,3; i \neq j)$ and a $\delta \neq 0, \pi$ would lead to CP violation. The parameters of the matrix are determined in the neutrino oscillation experiments.

In general, the transition probability of oscillation from ν_α to ν_β is given by

$$\begin{aligned} P(\nu_\alpha \to \nu_\beta) &= \delta_{\alpha\beta} - 4\sum_{i>j} Re\left(U^*_{\alpha i}U_{\beta i}U_{\alpha j}U^*_{\beta j}\right)\sin^2\left(\frac{\Delta m^2_{ij}L}{4E}\right) \\ &+ 2\sum_{i>j} Im\left(U^*_{\alpha i}U_{\beta i}U_{\alpha j}U^*_{\beta j}\right)\sin\left(\frac{\Delta m^2_{ij}L}{2E}\right), \end{aligned} \tag{1.22}$$

where $\Delta m^2_{ij} = m^2_i - m^2_j$, with $m_{i,j}; (i,j = 1,2,3)$ being the mass of the neutrino mass eigenstates. Using the above expression in two dimensions would lead to the oscillation probability obtained in Eq. (1.17).

The neutrino oscillation experiments are being performed using detectors having moderate to heavy nuclear targets like ^{12}C, ^{16}O, ^{40}Ar, ^{56}Fe, ^{208}Pb, etc. to get a reasonably large number of events. Many present-day neutrino experiments are taking data in the few GeV ($1 \le E_\nu \le 10$ GeV) energy region of neutrinos and antineutrinos to which some of the neutrino oscillation parameters are sensitive and which is also required to understand CP violation in the lepton sector. This is the energy region which is most intriguing(see Figure 1.5) as it receives the contribution from the Quasielastic Scattering (QE), Inelastic Scattering(IE), Shallow Inelastic Scattering (SIS), and the Deep Inelastic Scattering (DIS) processes.

In these nuclear targets, the interaction takes place with a bound nucleon, where

(i) a hadron has got structure and theoretically these structures are understood in terms of the form factors. Since neutrino interactions have contributions from both the vector and axial vector part, therefore, the form factors are vector (the information is obtained from electromagnetic interactions assuming conserved vector current hypothesis) as well as axial vector form factor

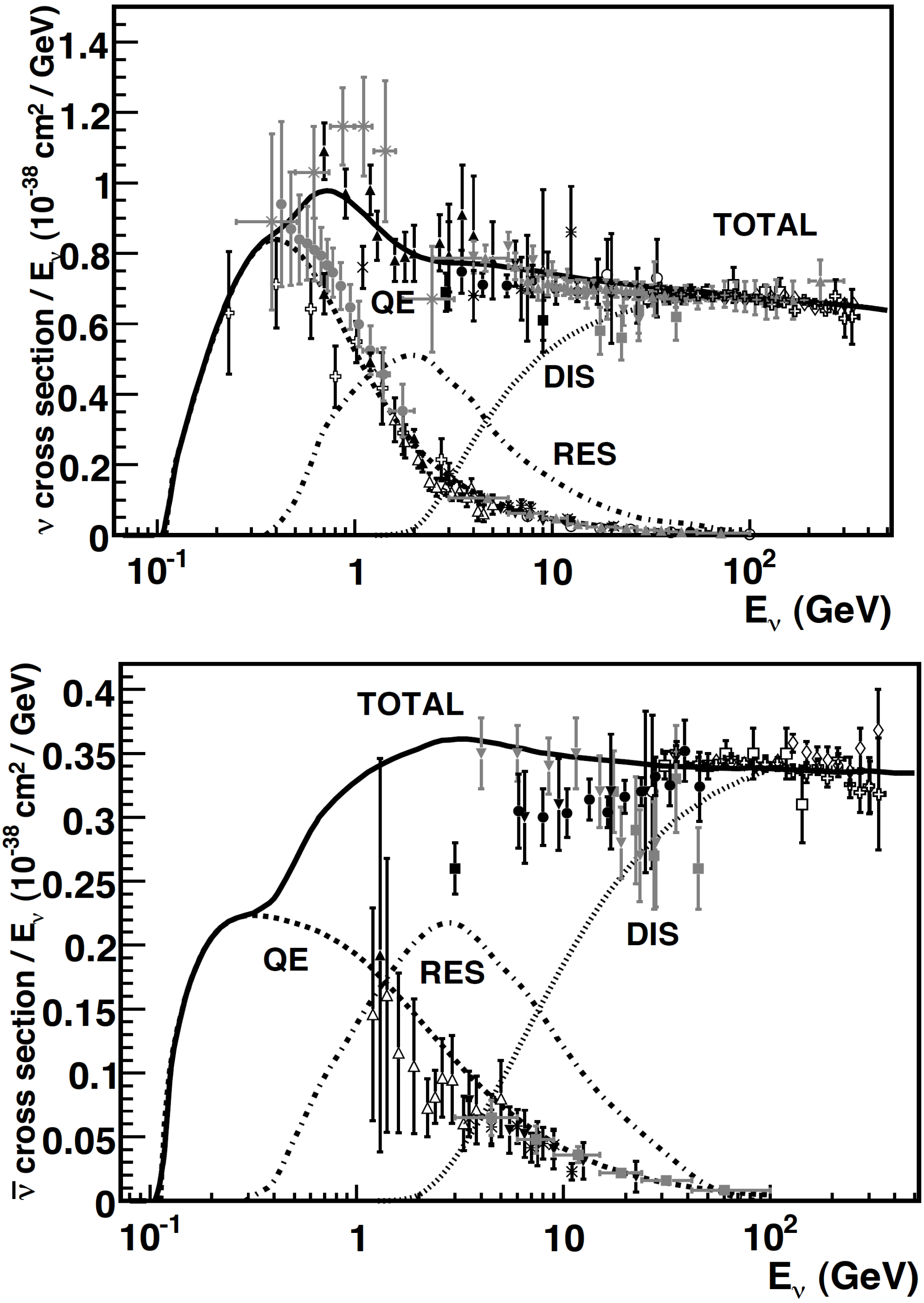

Figure 1.5: Total scattering contribution from the neutrino (upper panel) and antineutrino (lower panel) induced reactions. Figure has been taken from Ref. [29].

which has considerable uncertainty even at the nucleon level as the older experiments performed at ANL and BNL using deuterium targets have large statistical and systematic uncertainties, which are used in the analysis to determine axial vector form factors.

(ii) In the few GeV energy region, when the energy transfer to the target nucleon becomes $\geq$ 300MeV, nucleon and delta resonances, like N^* and Δ^* become significant. The resonances with half-integer spin and isospin ($I = \frac{1}{2}$) are known as the nucleon resonances while the resonances with $I = \frac{3}{2}$ and half integer spin are the delta resonances. More discussion about the nucleon and Δ resonances will be presented in Chapter 6. We have limited information on these $N - N^*$ and $N - \Delta^*$ transition form factors.

(iii) When the nucleons are bound inside the nucleus, nuclear medium effects become important. For example Fermi motion, Pauli blocking, nucleon correlations, initial and final state interaction, etc.

It has been estimated that 25-30% of the uncertainty in the systematics in the cross-section measurement arises due to the lack of the understanding of the these reasons. In the following, we briefly describe Quasielastic Scattering (QE), Inelastic Scattering (IE), Shallow Inelastic Scattering (SIS) and the Deep Inelastic Scattering (DIS) processes. The Feynman diagrams corresponding to the processes discussed above are shown in Figure 1.6.

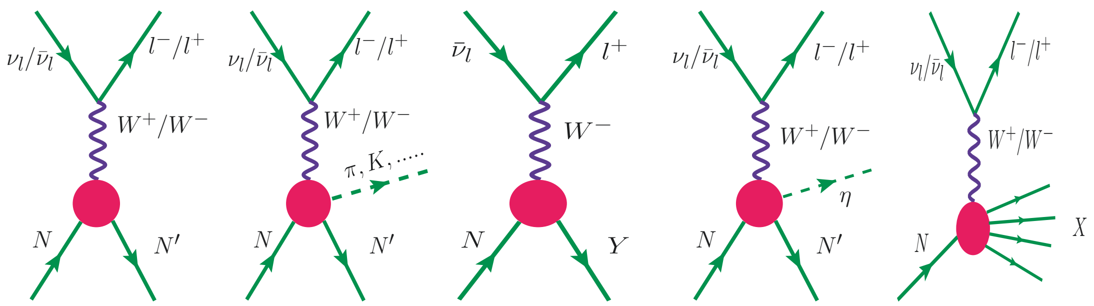

Figure 1.6: Feynman diagram representing (Left to Right) quasielastic scattering process, one pion production, one kaon production, single hyperon production, eta production, and deep inelastic scattering process. The quantities in the parentheses represent the four momenta of the corresponding particles.

- Strangeness conserving ($\Delta S = 0$) quasielastic scattering process

  In the low energy region of neutrinos and antineutrinos (from 0.1 GeV to $\sim$ 1 GeV), the major contribution to the total scattering cross section comes from the quasielastic scattering (see Fig 1.5) where an incoming neutrino or antineutrino interacts with a nucleon and in the final state, a charged lepton, and a nucleon are produced:

$$\nu_l + n \to l^- + p \qquad \text{and} \qquad \bar{\nu}_l + p \to l^+ + n \tag{1.23}$$

  where $N, N' = n$ or p.

- Strangeness changing ($|\Delta S| = 1$) quasielastic scattering process

  The antineutrino induced quasielastic scattering also receives a contribution from the $|\Delta S| = 1$ processes where in the final state a hyperon (Λ, Σ^0 or Σ^-) and an antilepton are produced:

$$\bar{\nu}_l + p \to l^+ + \Lambda \qquad \bar{\nu}_l + p \to l^+ + \Sigma^0 \qquad \bar{\nu}_l + n \to l^+ + \Sigma^-. \tag{1.24}$$

  The $\Delta S = 1$ processes are forbidden in the case of the neutrino induced channel due to the $\Delta S \neq \Delta Q$ rule.

- Inelastic and Shallow Inelastic processes

  With the increase in the energy of the incoming neutrino and antineutrino, the four momentum transferred to the initial nucleon increases, which to inelastic scattering resulting not only the production of the single pion (πN) but also to multiple pions $m\pi N$, $m = 2, 3, ..$, and many other processes like γN, ηN, ρN, KN, $\bar{K}N$ KY, ... in the final states. At low energy transfer i.e. close to the threshold, elementary amplitudes are constrained by the approximate chiral symmetry of QCD, however, as we move away from the threshold region, most of these reactions are dominated by the nucleon and delta resonances, although a significant contribution also comes from non-resonant amplitudes and their interference with the resonant counterpart. For example, in the case of single pion production, $P_{33}(1232)$ more commonly known as the Δ resonance has the dominant contribution, however, in the literature, $P_{11}(1440)$, $D_{13}(1520)$, $S_{11}(1535)$, $S_{11}(1650)$, and $P_{13}(1720)$ resonances are also considered [30]. For ηN production, the nucleon resonances which contribute significantly are $S_{11}(1535)$, $S_{11}(1650)$ [31]. For ΛK production, $S_{11}(1650)$, $P_{11}(1710)$, $P_{13}(1720)$, $P_{11}(1880)$, $S_{11}(1895)$, and $P_{13}(1900)$ resonances are dominant [32].

The Shallow Inelastic Scattering refers to the processes, dominated by non-resonant contributions, in the kinematic region where Q^2 is small and the invariant mass of the hadronic system, W, is above pion production threshold. As W increases above the baryon-resonance dominated region, non-resonant meson production begins to play a significant role. Moreover, with the increase in Q^2, one approaches the onset of the DIS region. This SIS region is poorly understood, both theoretically and experimentally, as this intriguing region encompasses the transition from interactions described in terms of hadronic degrees of freedom to interactions with quarks and gluons described by perturbative QCD. A significant number of events in the MINERvA, NOvA, and the planned DUNE experiment are expected to get contribution from this region. For an excellent review please see Ref.[33].

We describe below, in brief, some of the inelastic processes:

i. One pion production

At neutrino energies of ~ 1 GeV, the single pion production channel makes a significant contribution to the cross section for charged current lepton production and are important processes to be considered in the analysis of oscillation experiments in the few-GeV energy region, which select charged current inclusive events as signal.

The various possible reactions that may contribute to the single pion production either through charged current or neutral current (anti)neutrino induced reaction on a nucleon target are the following:

Charged current(CC) induced processes:

$$\begin{aligned} &\nu_l p \rightarrow l^- p\pi^+ && \bar{\nu}_l n \rightarrow l^+ n\pi^- \\ &\nu_l n \rightarrow l^- n\pi^+ && \bar{\nu}_l p \rightarrow l^+ p\pi^- \\ &\nu_l n \rightarrow l^- p\pi^0 && \bar{\nu}_l p \rightarrow l^+ n\pi^0 \qquad ;\ l = e, \mu \end{aligned} \tag{1.25}$$

and neutral current(NC) induced processes:

$$\begin{aligned} &\nu_l p \rightarrow \nu_l n\pi^+ && \bar{\nu}_l p \rightarrow \bar{\nu}_l p\pi^0 \\ &\nu_l p \rightarrow \nu_l p\pi^0 && \bar{\nu}_l p \rightarrow \bar{\nu}_l n\pi^+ \\ &\nu_l n \rightarrow \nu_l n\pi^0 && \bar{\nu}_l n \rightarrow \bar{\nu}_l n\pi^0 \\ &\nu_l n \rightarrow \nu_l p\pi^- && \bar{\nu}_l n \rightarrow \bar{\nu}_l p\pi^-. \end{aligned} \tag{1.26}$$

Moreover, in experiments that select the quasielastic production of charged leptons as signal for the analysis of oscillation experiments, single pion production channel gives rise to background contribution. For example, neutral current induced neutral pion production is a background to ν_e-appearance oscillation experiments while charged current events producing charged pions contribute to the background in $\nu_\mu-$disappearance experiments. When these processes take place in a nuclear target, the pion production get reduced considerably due to the nuclear medium effects (due to pion absorption in the nuclear medium), or change its identity through a rescattering processes like $\pi^- p \rightarrow \pi^o n$, etc. Due to the pion absorption in the nuclear medium, the events mimic quasielastic reactions, thus, known as quasielastic-like events. Then the multinucleon correlation effects give rise to two particle-two hole contributions(2p-2h), which has been discussed in the literature recently. For a general reading one may see the discussion in Refs. [34, 35].

ii. Multiple pion production

Instead of a single pion, multiple pions may also be produced in the (anti)neutrino induced processes, for example

$$\nu_l(\bar{\nu}_l) + N \rightarrow l^-(l^+) + N' + m\pi, \quad \text{where} \quad m = 2, 3, .. \tag{1.27}$$

iii. Kaon production

The basic reaction for the (anti)neutrino induced charged current kaon production is

$$\begin{aligned} \nu_l + p &\rightarrow l^- + K^+ + p & \bar{\nu}_l + p &\rightarrow l^+ + K^- + p \\ \nu_l + n &\rightarrow l^- + K^0 + p & \bar{\nu}_l + p &\rightarrow l^+ + \bar{K}^0 + n \\ \nu_l + n &\rightarrow l^- + K^+ + n & \bar{\nu}_l + n &\rightarrow l^+ + K^- + n\ . \end{aligned} \tag{1.28}$$

iv. Eta production

The basic reaction for the (anti)neutrino induced charged current eta production is

$$\nu_l + n \rightarrow l^- + \eta + p \qquad \bar{\nu}_l + p \rightarrow l^+ + \eta + n \tag{1.29}$$

v. Associated particle production

The basic reaction for the (anti)neutrino induced associated particle production is

$$\begin{aligned} \nu_l + n &\rightarrow l^- + K^+ + \Lambda & \bar{\nu}_l + p &\rightarrow l^+ + K^0 + \Lambda \\ \nu_l + p &\rightarrow l^- + K^+ + \Sigma^+ & \bar{\nu}_l + p &\rightarrow l^+ + K^0 + \Sigma^0 \\ \nu_l + n &\rightarrow l^- + K^+ + \Sigma^0 & \bar{\nu}_l + p &\rightarrow l^+ + K^+ + \Sigma^- \\ \nu_l + n &\rightarrow l^- + K^0 + \Sigma^+ & \bar{\nu}_l + n &\rightarrow l^+ + K^0 + \Sigma^-, \end{aligned} \tag{1.30}$$

where a strange meson and a strange baryon are produced with opposite strangeness.

↬ Deep inelastic scattering process

In a DIS process, the energy and Q^2 transferred to the target are large, such that the nucleon loses its identity and jet of hadrons are produced. In DIS, a neutrino interacts with a quark of a bound nucleon producing a charged lepton and multiple hadrons X instead of a nucleon in the final state. Thus, the interaction is described in terms of quarks and gluons using perturbative QCD.

The basic reaction for the (anti)neutrino induced charged current deep inelastic scattering process on a free nucleon target is given by

$$\nu_l(k)/\bar{\nu}_l(k) + N(p) \rightarrow l^-(k')/l^+(k') + X(p') \quad l = e, \mu \tag{1.31}$$

where k and k' are the four momenta of incoming and outgoing lepton, p and p' are the four momenta of the target nucleon and the jet of hadrons produced in the final state, respectively.

Presently, I am performing analysis for the DIS events in MINERvA at Fermilab, therefore, for the completeness we are giving the expression of the cross section and discuss the kinematical variables used in the analysis in brief and some of the details will be presented in Appendix A. MINERvA is a dedicated neutrino and antineutrino cross section measurement experiment and uses (anti)neutrino beams in the two energy runs *viz.* the low energy run (the peak of which lies $\sim$ 3 GeV) and the medium energy run (the peak lies at $\sim$ 6 GeV). The MINERvA experiment is using several nuclear targets like ^{4}He, ^{12}C, ^{16}O, ^{56}Fe and ^{208}Pb and the aim is to perform EMC (European Muon Collaboration experiment using charged lepton beams on several nuclear targets) types of measurements to understand the nuclear medium effects in both the neutrino as well as antineutrino modes in the wide region of Bjorken scaling variable x, and the four momentum transfer squared Q^2, covering the quasielastic, inelastic, and the deep inelastic scattering regions. In the medium energy region, it is expected that more than 30% of the events would arise due to DIS processes.

The DIS process is mediated by the W-boson ($W^{\pm}$) and the invariant matrix element corresponding to the reaction given in Eq. (1.31) is written as

$$-i\mathcal{M} = \frac{iG_F}{\sqrt{2}}\, l_\mu \left(\frac{M_W^2}{q^2 - M_W^2}\right) \langle X|J^\mu|N\rangle \,, \tag{1.32}$$

where G_F is the Fermi coupling constant, M_W is the mass of W boson, and $q^2 = (k-k')^2$ is the four momentum transfer square. l_μ is the leptonic current and $\langle X|J^\mu|N\rangle$ is the hadronic current for the neutrino induced reaction (shown in rightmost part of Figure 1.6).

The four momentum transfer square $Q^2 = -q^2 \geq 0$ is expressed in terms of the energy of the incoming neutrino (E_ν), the energy of the outgoing muon (E_μ), and the angle of the outgoing muon (θ_μ) as:

$$Q^2 = 4E_\nu E_\mu sin^2\frac{\theta}{2}, \quad q^2 = -Q^2.$$

Also, the invariant mass of the hadronic system can be written in terms of the four momentum of the particles involved as:

$$W^2 = p_X^2 = (k + p - k')^2$$

which in the lab frame is written as

$$W^2 = 2M_N E_{had} + M_N^2 - Q^2.$$

The different neutrino scattering channels correspond to the different regions of invariant mass W. Also, the number of hadrons in the final state of the DIS process increases with W. The quantities W and Q^2 characterize a DIS event and there is no explicit cut on those values for an event to be DIS type. However, in the literature the accepted quantities, in order to define a pure DIS event, are $Q^2 \geq 1$ GeV^2 and W $\geq$ 2 GeV. The regions of high Q^2 and W are for the neutrino interactions with a free nucleon but in a bound nucleon, these values might get smeared due to nuclear medium effects (such as Fermi motion), and therefore the DIS event sample measured may contain events that are truly not DIS events. Hence, for the DIS measurement, in most of the experiments, there must be a background estimation and subtraction in order to obtain a pure DIS sample.

The cross section is generally expressed in terms of Bjorken variable $x = \frac{Q^2}{2M\nu}$ and $y = \frac{E_\nu - E_l}{E_\nu}$ and the general expression of the double differential scattering cross section (DCX) corresponding to the reaction given in Eq. 1.31 (depicted in Figure 1.6) in the laboratory frame is expressed as:

$$\frac{d^2\sigma}{dxdy} = \frac{yM_N}{\pi}\,\frac{E}{E'}\,\frac{|\vec{k}'|}{|\vec{k}|}\,\bar{\sum}\sum|\mathcal{M}|^2\,, \tag{1.33}$$

The other details are given in the Appendix A.

My thesis is divided into three parts:

- First, I will present the work that I am performing at MINERvA for the last two years. I am stationed at the Fermi National Accelerator Laboratory (FNAL) working in the MINERvA experiment to obtain the double differential deep inelastic scattering cross section in the neutrino mode. The goal is to obtain the ratio of the cross section and the structure functions for different nuclei (^{4}He, ^{12}C, ^{16}O, ^{56}Fe and ^{208}Pb). The results are available for the electromagnetic case but the plan is to obtain the ratio of the weak structure functions for different nuclear targets to understand the nuclear medium effects and this study will also be helpful to understand axial vector contribution. Most of the steps required to obtain the experimental cross section are already completed and the results are included in the thesis. The analysis is getting close to an advanced stage and in the coming weeks, I will be able to obtain the double differential DIS cross section for different nuclear targets used in the MINERvA experiment.
- Second, the work that I did in the INO analysis. This work is dedicated to the study of atmospheric neutrino and antineutrino oscillation parameters at the INO experiment. We present the ICAL sensitivity to confirm a non-zero value of the difference in atmospheric mass squared of neutrinos and anti-neutrinos i.e. ($|\Delta m^2_{32}|$-$|\Delta\overline{m^2}_{32}|$).
- Third, the theoretical work that I have performed at the Aligarh Muslim University. This work has been performed keeping in mind the theoretical development of a model that will describe the associated particle production induced by photons, electrons, neutrinos, and antineutrinos. We have studied the associated particle production induced by photons, which receives the contributions from the non-resonant terms as well as from the nucleon, hyperon, and kaon resonances.

The plan for this thesis is discussed below:

In Chapter-2, we introduce Fermilab's NuMI (Neutrinos at the Main Injector) beam, which is a source of neutrinos and antineutrinos to the MINERvA, MINOS, and NOvA detectors for the cross section and oscillation measurements. We discuss and explain the functioning of the different components of the NuMI like beam design, NuMI target, magnetic horns (required to select the polarity of the particles passing through them) and, hadron absorbers, etc. NuMI beam is predominantly composed of muon neutrinos in the neutrino mode with a small muon antineutrino contribution (5%) and electron neutrino/antineutrino components (total $< 1\%$). Further, we discuss the MINERvA detector design and explain in detail the different components of the detector. The detector starts with the veto walls which helps to identify the muons entering from the front face of the detector, which generally comes from muon-neutrino interactions in the rock surrounding the detector. Then, we have the nuclear target region followed by the active tracker region. The core of the detector is surrounded by large electromagnetic and hadronic calorimeters. Downstream of the MINERvA detector is the MINOS near detector, which acts as the muon spectrometer for the muons entering from the MINERvA detector. Upstream of the veto walls is liquid Helium vessel which also serves as one of the nuclear targets. The details and the working of each region of the detector are explained in this chapter.

In Chapter 3, the processes of reconstruction and simulation is discussed. The reconstruction process is to convert the depositions in the detector into some measurements associated with the particles created in the neutrino interaction. These measurements are then used to obtain the physics results. This chapter describes various steps involved in the reconstruction process including time slices, cluster formation, track reconstruction, MINOS matching of the reconstructed tracks. In order to analyze the experimental data in a better way, simulations are used to understand the behavior of different types of particles and their energy depositions in the detector. So, a description of the simulation used by the MINERvA experiment is discussed as well.

Chapter-4 explains the details of the analysis procedure required to obtain the cross section in the MINERvA experiment. Also, the chapter has a discussion of the different systematics included in the cross section measurement. The different steps which are required to obtain the cross section are event selection, background estimation and subtraction, efficiency correction, unfolding for correcting detector resolution effects, and normalization. In the event selection, the data sample is selected by applying different cuts at the event-by-event level. The optimization of the event selection requirements is done based on several criteria including the signal selection efficiency, purity, to minimize systematic uncertainties. Events are put into the kinematic bins and events are represented then as a histogram. The next step is the background subtraction, which removes the events that pass selection cuts but are not in fact signal. The background events are estimated by Monte Carlo simulation after applying the selection cuts and then referring to the true properties to look at whether an event is a signal or background. A complete procedure of estimation and subtraction of the background events is discussed in the thesis. The shortcomings in detection and event reconstruction in the data result in the smearing of the measurement which is handled with a procedure called unfolding. Here, an unfolding matrix is constructed from the simulation's discrepancies between reconstructed and true quantities. This is basically a mapping of events between the reconstructed and true space. The matrix is then applied to the background-subtracted data distribution, transforming it from a reconstructed into a "true" variable. The background-subtracted and unfolded sample is then repopulated with the signal events that were missed due to inefficiency of the selection cuts and to the detector acceptance or kinematic thresholds through a process called efficiency (and acceptance) correction. The efficiency and the acceptance are simulated together as the number of selected signal events, divided by the total number of signal events, all in bins of the variables of interest. The final step is to normalize the efficiency-corrected distributions and introduces cross section units of measure. We normalize the sample with the muon neutrino flux exposure of the dataset and the number of target protons and neutrons in the allowed neutrino interaction regions of the detector. We also do a bin width normalization to obtain a differential cross section measurement and giving the distribution a final unit of measure [cm^2 /target nucleon/[variable unit]].

In Chapter-5, we have presented a study of the sensitivities to measure the differences between the atmospheric neutrino and antineutrino oscillations in the Iron-Calorimeter detector at the India-based Neutrino Observatory experiment. Charged Current ν_μ and $\overline{\nu}_\mu$ interactions with the detector under the influence of the Earth's matter effect have been simulated for ten years of exposure. The observed ν_μ and $\overline{\nu}_\mu$ events spectrum are separately binned into direction and energy bins, and a χ^2 is minimized with respect to each bin to extract the oscillation parameters for ν_μ and $\overline{\nu}_\mu$ separately. We then present the ICAL sensitivity to confirm a non-zero value of the difference in atmospheric mass squared of neutrino and antineutrino i.e. $|\Delta m^2_{32}| - |\Delta \overline{m^2}_{32}|$.

The magnetized Iron Calorimeter detector at the INO has an excellent feature to identify the neutrinos and antineutrinos on an event by event basis. This feature can be harnessed to detect the differences between the oscillation parameters of neutrinos and antineutrinos independently. In Chapter-6, we presented an analysis of the charged current ν_μ and $\overline{\nu}_\mu$ events under the influence of the earth matter effect using the three neutrino flavor oscillation framework. If the atmospheric mass-squared differences and mixing parameters for neutrinos are different from antineutrinos, we present the prospects for the experimental observation of these differences in atmospheric ν and $\overline{\nu}_\mu$ oscillations at INO. We estimate the detector sensitivity to confirm a non-zero difference in the mass-squared splittings ($|\Delta m^2_{32}| - |\Delta \overline{m^2}_{32}|$) for neutrinos and antineutrinos.

In Chapter-7, we have studied the associated photoproduction of $K\Lambda$ from the proton in the energy region of $E_\gamma < 3$ GeV using an isobar model in which the non-resonant contributions corresponding to the s, t, u channel diagrams are obtained from a non-linear sigma model with chiral SU(3) symmetry. The model also predicts a contact term and its coupling strength in a natural way to preserve the gauge symmetry. The important parameters used in this model are the pion decay constant f_π and the vector and the axial vector current couplings of the baryon octet in terms of the symmetric and antisymmetric couplings D and F, determined from the electroweak phenomenology of nucleons and hyperons. In the non-resonant sector, the model is almost parameter-free except a common cut-off parameter Λ_B, which is used to describe the hadronic form factors at the strong kaon-nucleon-hyperon ($KN\Lambda$) vertices. In the resonance sector, the contribution from the various nucleon resonances (R) in the s channel, the hyperon resonances (Y^*) in the u channel, and the kaon resonances (K^* and K_1) in the t channel, which are present in the PDG having spin $\leq \frac{3}{2}$ and mass < 2 GeV with significant branching ratio in $K\Lambda$ decay mode have been considered. In the case of the nucleon resonances (R), the couplings γNR at the electromagnetic vertices are determined in terms of the helicity amplitudes and the $RK\Lambda$ couplings at the strong vertices are determined by the partial decay width of the resonances (R) decaying to $K\Lambda$. The strong and the electromagnetic couplings of u and t channel resonances are fitted to reproduce the experimental data of CLAS and SAPHIR. The numerical results are presented for the total and differential scattering cross sections and are compared with the available experimental data from CLAS and SAPHIR as well as with some of the recent theoretical models.

In Chapter-8, we summarize the results of this work and conclude our findings. Also, we briefly present the future plans.

Part II

The MINERvA experiment

CHAPTER 2

NUMI BEAMLINE AND THE MINERVA DETECTOR

2.1 NUMI beamline

Neutrinos are produced from various natural and man-made processes. They are the second most abundant particles after photons in the universe. The natural resources include the fusion processes in the Sun, supernova explosions, radioactive decays, cosmic rays, and even relics of the Big Bang. They can be produced in laboratories like nuclear power plants and accelerators. The Fermilab's Main Injector is a particle accelerator providing protons for the NuMI beamline which through subsequent processes is responsible for providing the neutrino as well as antineutrino beams to various detectors including MINERvA, MINOS, NOvA, MicroBooNE, etc. Using this human-controlled source of the neutrinos and antineutrinos, a beam of suitable configuration, high intensity, and broad-spectrum can be achieved. The beam of neutrinos/antineutrinos in NuMI is produced from the collision of the 120 GeV proton beam with the Carbon target resulting in the production of mesons like pions and kaons and their subsequent decay to neutrinos/antineutrinos and muons. The proton beam is incident on a meter long graphite target at an angle of 58 mRad downward from the Fermilab's accelerator producing mesons through the interaction with the nucleons and hence the neutrino/antineutrino beams.

The proton beam is so intense that it is capable of delivering around 60 billion muon neutrinos to the MINERvA detector per second with the widespread of neutrino energies between 0 to 20 GeV. Right after the target, a toroidal magnetic field is applied through magnetic horns in order to filter the pions based on their electric charge. For the (anti)neutrino beam, the horns are run with the positive (negative) polarity, and the pions of specific charge are selected, and then enter into a decay pipe where they decay to produce muons and (anti)neutrinos. Almost a pure beam of neutrinos/antineutrinos is then obtained by removing the leftover hadrons through a hadron absorber, made of steel, aluminum, and concrete, after the decay pipe. To make the pure neutrino beam, we use both the hadron absorber and the next 200m of rock, which absorb the muons that are produced in the pion and kaon decays. A schematic of the beam components is shown in the Figure 2.1.

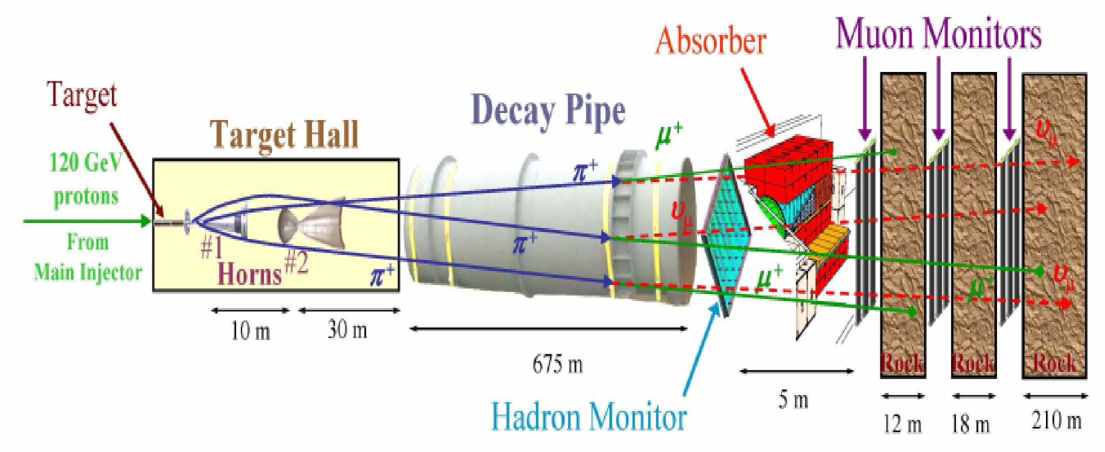

Figure 2.1: The schematic of the NuMI beam components. Figure reprinted from Ref. [36].

The MINERvA detector took data in two energy modes viz. low energy (LE) mode and the medium energy (ME) mode. In the LE configuration of the NuMI beam, the MINERvA took data from 2009-2013 and achieved a neutrino energy peak around 3.5 GeV while in the ME configuration of the NuMI, the MINERvA experiment took data from 2013-2019 and achieved a neutrino energy peak of around 6 GeV. The predicted fluxes in both LE and ME configuration of the detector are shown in the Figure 2.2.

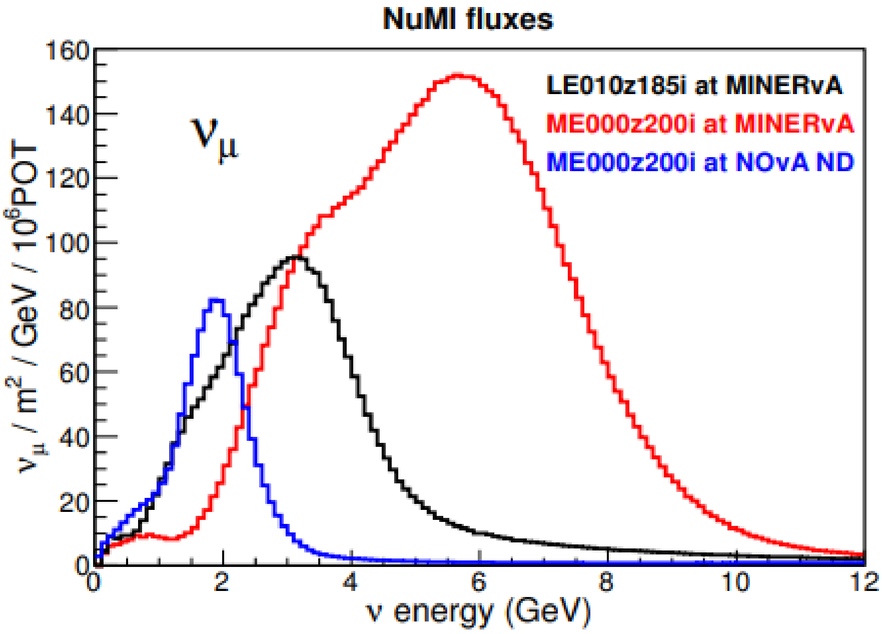

Figure 2.2: The LE and ME configuration fluxes in the MINERvA and NOvA detectors. Figure taken from Ref. [37].

The present analysis described in the later sections is based on the neutrinos taken by the MINERvA detector in the ME configuration. The neutrino data sets used in this analysis correspond to the 12×10^{21} number of protons on target (POT). The ME exposure for the data taking of the MINERvA detector is shown pictorially in Figure 2.3.

2.1.1 The NuMI Beam Design

The creation of the proton beam starts with accelerating a H^- ion source from 35 keV to 750 keV and injecting into the linear accelerator. The Fermilab's linac

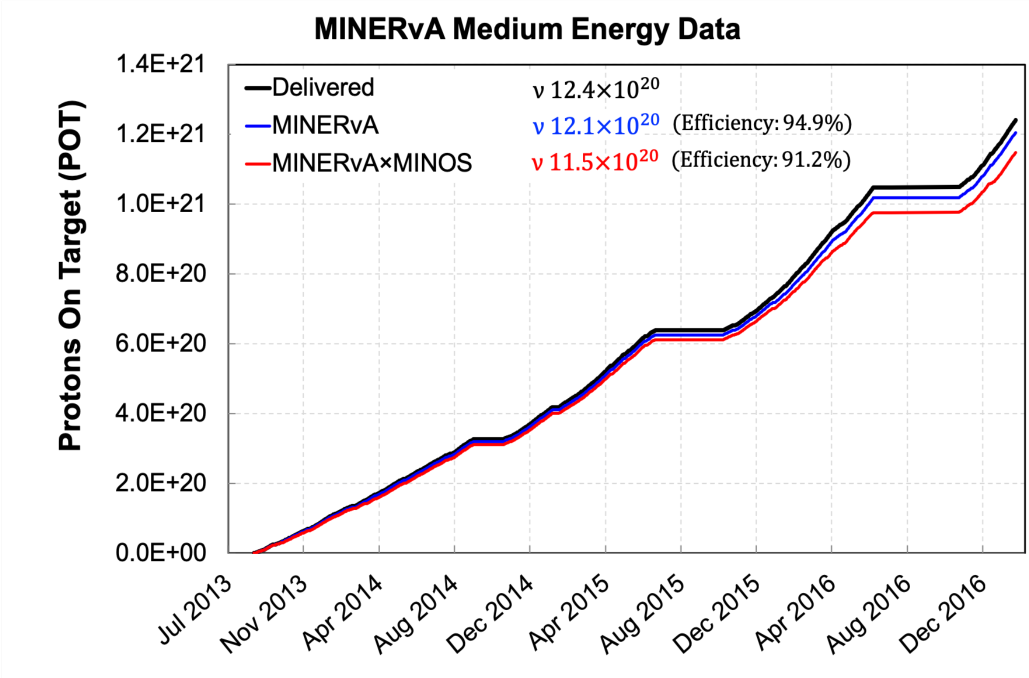

Figure 2.3: The ME configuration data taking period of the MINERvA detector. Figure taken from Ref. [38].

accelerator then accelerates those ions to around 400 MeV which are then supplied to a Booster where the electrons get filtered out by a carbon foil. The 75 m radius Booster accelerates the positively charged protons to around 8 GeV in less than 67 ms over the course of around 40,000 laps. The Booster creates 84 proton bunches with each bunch containing 3×10^{10} protons and is 19 ns apart. The one revolution around the Booster corresponds to the proton bunch grouped into 1.6 μs. The booster delivers these proton bunches to the Recycler where they are stacked resulting in the doubling of the proton bunch intensity.

The protons are next extracted to the Main Injector, located just underneath the Recycler, which accelerates them to 120 GeV. The circumferences of both the Recycler and the Main Injector are seven times larger than that of Booster, hence it allows the injection of seven proton batches into both. In actual, only six proton bunches are injected and one batch space is left for the proton injection process. Each beam spill, containing six batches, passes through a toroid which measures

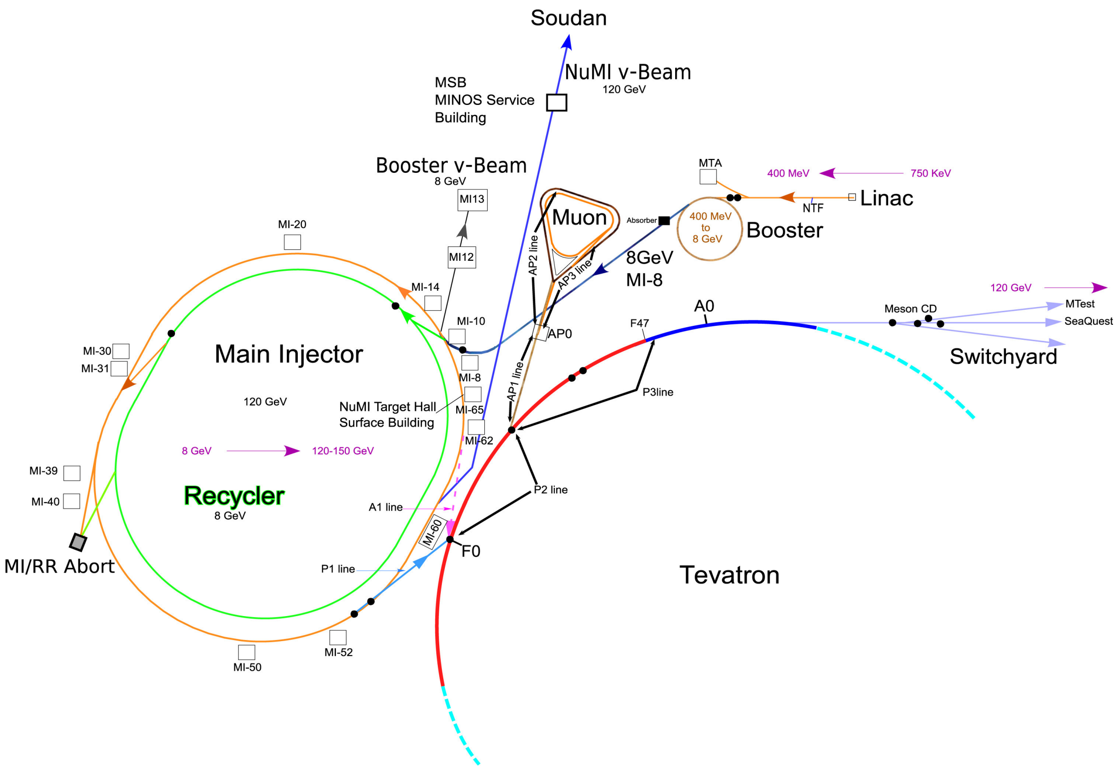

Figure 2.4: A schematic of the Fermilab Accelerator Complex, taken from Ref. [39].

the proton number and the beam is directed to the beam spot size of the target. A method called "slip stacking" was introduced which merges the two proton batches into one resulting nearly double the proton intensity. This job was done earlier by the Main Injector but after the 2013 shutdown, the Recycler was converted into a proton stacker allowing the Main Injector to deliver protons at a maximum rate. The overview of the Fermilab's accelerator complex is shown in Figure 2.4.

2.1.2 NuMI Target

The NuMI proton beam is incident on the NUMI target with a nearly circular cross sectional spot of 1.4 mm (RMS) diameter. The beam from the Main Injector travels around 350 m and is directed at 3.3° downwards to the underground Target Hall. The target must have a capacity to deal with high-power proton beams, heating, any radiation damage, and corrosion of materials. During the ME run of the detector, the target was a 1.2 m long rod consisting of 48 rectangular graphite segments each 24 mm long and with 7.4 $\times$ 63 mm^2 cross section. The length of the rod, in total, corresponds to 2.5 nuclear interaction lengths. The two focusing horns are kept stationary and the target with respect to the first horn was positioned to maximize the off-axis neutrino flux at the NOvA far detector. The different energy spectrum of the neutrinos can be seen in Figure 2.5.

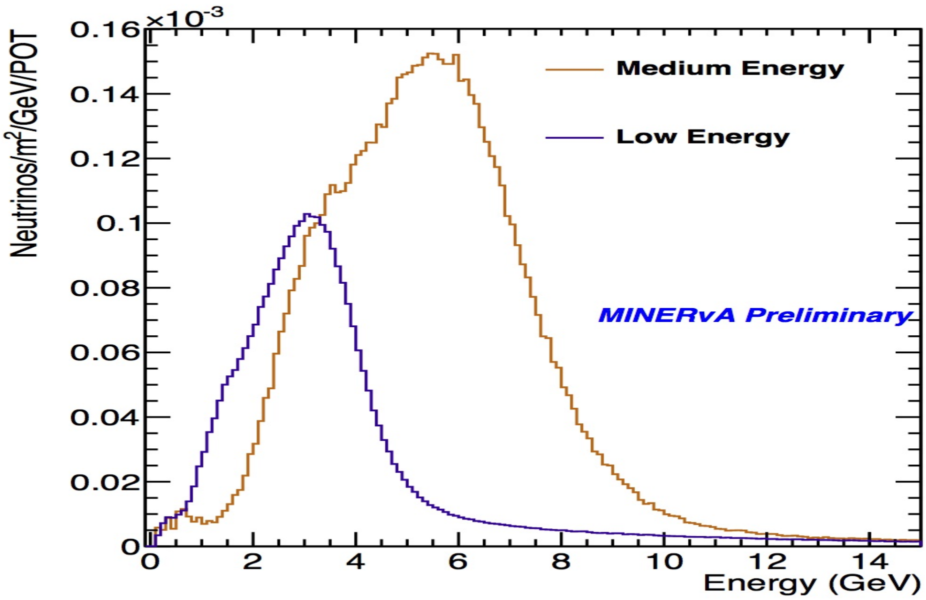

Figure 2.5: The true energy neutrino energy distribution in the MINERvA detector from the simulation: LE and ME. Figure is from Ref. [40].

The length of the target could be increased that would result in more protons interacting in the target, which will produce more neutrinos, but at the same time longer target also absorbs some of the pions produced in the upstream part of the target, so the total neutrino yield is not a simple function of the length of the target. The wider the target is, the more the pions will scatter and then be harder to focus, but the more narrow the target is, the more likely protons escape out the side of the target without producing pions. So, the neutrino yield is also a complicated function of the width of the target. The water cooling pipes are surrounding the target and the whole arrangement is kept in an aluminum container filled with helium gas.

There could be serious damage to the beam components even with a small mis-steering of the beam because of the high power of the proton beam that is incident on the NuMI beamline. The most vulnerable components to the offset parallel beam trajectories are the target cooling, focussing horns, target fins, and the support components. A 150 cm long and 5.7 cm diameter baffle of graphite is introduced upstream of the target to protect these components.

2.1.3 Magnetic Focusing Horns

The beam of mesons produced through the interaction of the protons on the target is then passed through the two magnetic horns Horn 1 and Horn 2 placed downstream of the target region. These magnetic horns direct the mesons with a proper charge towards the downstream neutrino detector and act as hadron lenses by focusing mesons produced from the NuMI target. These horns are each 3 m long in parabolic shape made of aluminum.

These magnetic horns generate a toroidal magnetic field in the volume between the inner and outer conductors when a 200 kA current is pulsed on the surface of the horns. The field is parallel to the beam direction and deflects the hadrons produced by the target. Water is sprayed on the inner conductor in between the proton spills and we assume that there is a 1.5 mm layer of water on the horns at the time that the pions are passing through the horns. Figure 2.6 shows the inner and the outer conductors of the magnetic horns of the NuMI beam. The inner conductors have a parabolic shape and the outer conductor of each horn is just a cylinder. The red arrows show the direction of the current.

The magnetic horns work in two configurations, the forward horn current configuration (FHC) and the reverse horn current configuration (RHC). In the FHC configuration, the horns defocus the negatively charged mesons and focus the

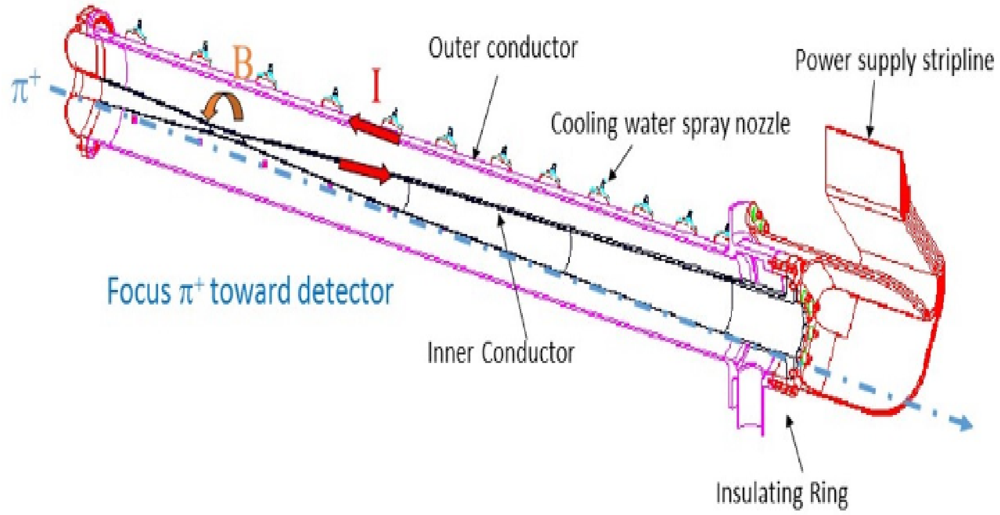

Figure 2.6: The magnetic horn of the NuMI beam. The Figure is from Ref. [41].

positively charged mesons π^+ and K^+ which upon subsequent decay produce a neutrino beam while reducing the antineutrino contributions considerably. The polarity of the applied current can be reversed and an almost pure beam of antineutrinos can be achieved. The present analysis data sets were taken in the FHC configuration of the beam.

The neutrino flux can be adjusted by varying certain parameters of the focusing system like target-horn and horn-horn separation distances. Also, the neutrino peak energy and the event rate can be adjusted by varying the magnitude of the horn current. The horn is like a focusing lens but the focal length is a function of the distance of the target from the horn and the momentum of the pions. So, for a particular distance, a particular momentum of pion will be focused at the best. The hadrons which pass parallel to the beam axis remain unaffected in the magnetic horns. Also, those hadrons remain unaffected in the horn 2 which are well focused in the first horn 1. The over-focused and under focused hadrons from the horn 1 are refocused by horn 2 improving the overall efficiency of the focusing system by around 50%.

Figure 2.7 shows the paths of the hadrons passing through the focusing system.

The under focused and over focused neutrinos dominate the flux peak in the ME run of the detector. The high energy neutrinos/antineutrinos come from the unfocused mesons, and focussed kaons and dominate the higher end of the flux spectrum.

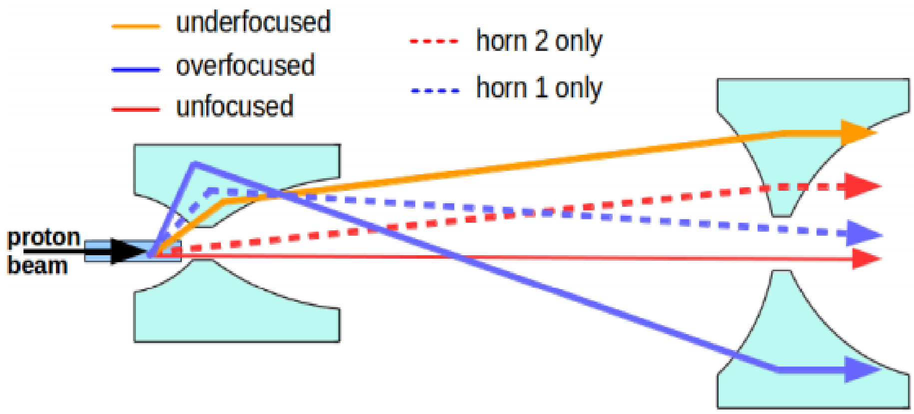

Figure 2.7: The magnetic horn focussing system. Figure is from Ref. [37].

2.1.4 Hadron absorber and Decay pipe

After the focusing horns, at a distance of 46 m, the beam passes through a 675 m long, 2 m diameter helium-filled decay pipe. The mesons (pions/kaons) then decay to the muons and corresponding neutrinos, thus producing a straight beam of neutrinos for the MINERvA detector. The decay pipe length can accommodate the average decay distance of 700 m, which corresponds to that of a 10 GeV pion. The 2 m diameter of the pipe is chosen in order to take into account more meson trajectories resulting in more number of neutrinos. The upstream end of the decay pipe is closed with a thin two-component steel-aluminum window to reduce meson interactions.

There is a series of beam monitors and the absorbers after the decay pipe. The massive aluminum, steel, and concrete NuMI hadron absorber stops any hadrons and electrons that were left in the decay pipe. The 240 m of rock between the last muon monitor and the NuMI Near Detector hall serves as a filter to remove the muons remaining in the beam from the secondary meson decays.

2.2 MINERvA detector

Started in the early 2000s, the MINERvA experiment is the finest high statistics experiment dedicated to studying the neutrino cross sections with a variety of nuclei. The experiment has a goal to set the foundation for future neutrino oscillation experiments by improving the interaction models critical to those measurements. The experiment is going to measure both inclusive and exclusive cross section measurements and to study the nuclear medium effects by taking the measurements on various nuclei. MINERvA completed data taking in Feb 2019 and the analysis of that data is going on. The experiment took data in two different NuMI energies i.e. $< E_\nu >\approx 3.5$ GeV (LE mode) and $< E_\nu >\approx 6$ GeV (ME mode). In the overall run of the experiment ($\approx$ 10 years), a total of 16.1×10^{20} neutrino-mode protons on target (POT) and 14.1×10^{20} antineutrino mode protons on target (POT) were collected.

The MINERvA detector uses a fine-grained extruded polystyrene scintillator for the purpose of tracking and calorimetry measurements. The detector consists of 120 hexagonal modules stacked along the beam direction, which is 5 m long with inner and outer regions. There are four subdetector regions in the inner detector (ID): the nuclear targets region, the active tracking region, the downstream electromagnetic calorimeter (ECAL), and the downstream hadronic calorimeter (HCAL). The outer detector (OD) consists of the hadronic calorimeter which borders and physically supports the ID. The downstream of the detector is the MINOS near detector, which serves as a toroidal muon spectrometer.

The next few sections of the chapter are dedicated to the different components of the MINERvA experiment. The schematic of the detector is shown in the

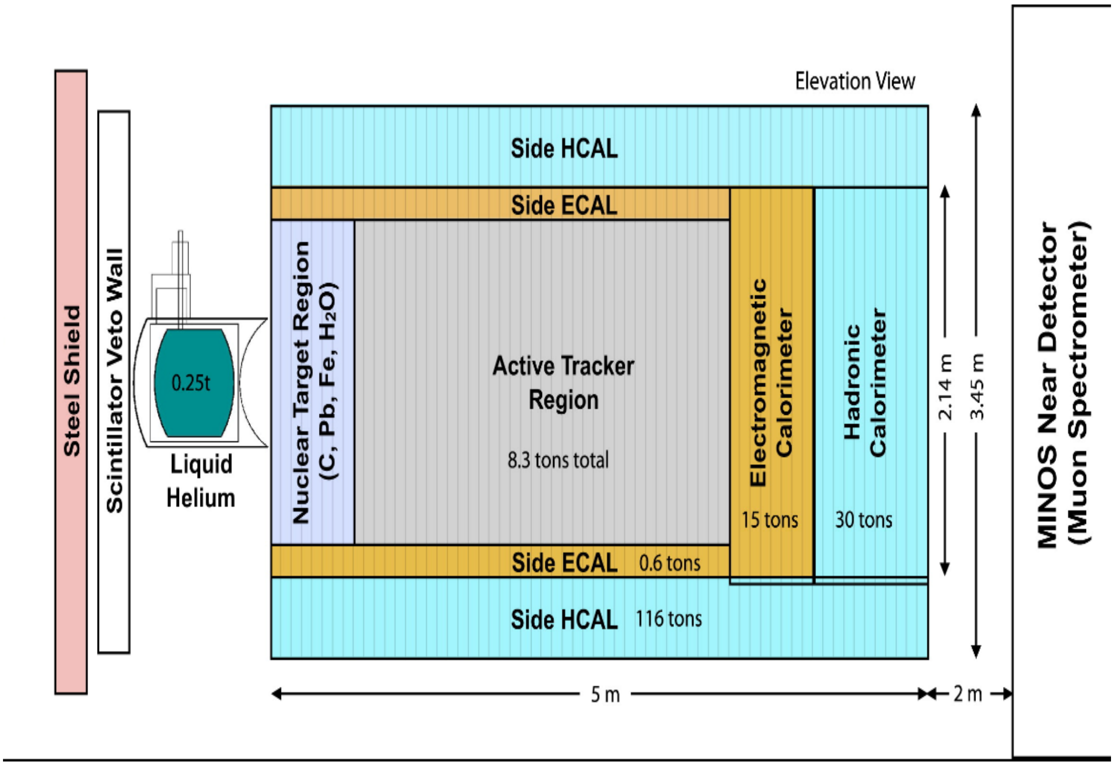

Figure 2.8: The schematic of the MINERvA detector. Figure is from Ref. [42].

Figure 2.9 along the beam direction.

2.2.1 Detector Design

The MINERvA detector is a 5 m long, 1.7 m-apothem regular hexagonal prism aligned along the X-axis. The coordinate system of the detector is as follows: the origin is at the center of the detector, the Z-axis is also the horizontal axis in the detector hall, the X-axis points vertically upwards and the X-axis is orthogonal to both the axes. The NuMI beam directed towards the MINOS far detector points 3.3° downward relative to the z-axis of the detector. The detector has a fully active tracking central core, which is 2.5 m-long, 85 cm apothem. In order to provide support, containment, and even some tracking, the region is surrounded by the active layers of scintillator interspersed with lead and steel plates. There are partially active electronic and hadronic containment calorimeters

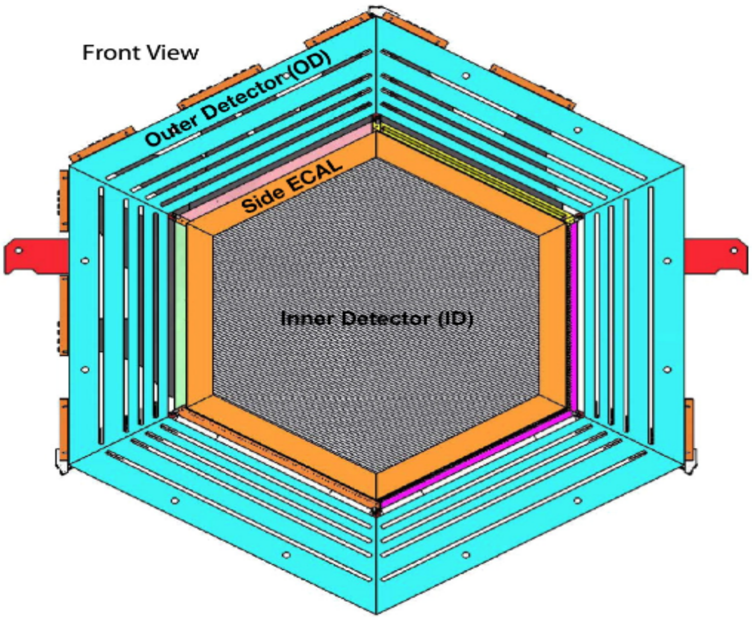

Figure 2.9: The schematic of the MINERvA detector. Figure is from Ref. [42].

at the downstream end of the central tracking region. The active nuclear target region is upstream of the tracking region, and is composed of various materials used to study the atomic mass scaling of neutrino interactions.

2.2.2 Veto Walls

At the extreme upstream of the MINERvA detector is located a veto wall consisting of layered steel-scintillator planes. The veto wall helps to identify the muons entering from the front face of the detector that generally comes from muon-neutrino interactions in the rock surrounding the detector. There is a 2,300-liter liquid helium tank right after the veto wall, so, it is extremely important for any helium target data analysis, located between the veto wall and the main detector, to do the proper identification of the rock muons. The analysis presented in the thesis does not include the data from veto walls because we are looking at neutrino interactions in the solid nuclear targets.

2.2.3 Nuclear Target Region

The Nuclear target region is located upstream of the active tracker region. The region consists of the five passive planes of materials like solid Carbon, Iron, and Lead separated by either two or four tracking modules. Different slabs of pure carbon (C), iron (Fe), and lead (Pb) are used to build the passive target planes. The nuclear target plane 4 is pure lead. The arrangement of the different slabs of iron and lead in the nuclear target plane 1, 2, and 5 is done carefully to minimize systematic uncertainty variations in angular acceptance. The target plane 3 has a composition of all the nuclear materials carbon, lead, iron and in order to have the sufficient neutrino interaction rate, it is designed to be the largest gap as the carbon is the lightest nuclei. The target 3 is nearly half carbon slab, one-third iron slab and, the remaining lead slab and the thickness is approximately twice the thickness of targets 1 and 2. Apart from the five solid targets between targets 3 and 4, there is a water target. The present analysis doesn't include the water target events. The nuclear target region is shown in Figure 2.10. The elemental composition of the nuclear targets is given in Table 2.1.

Material	Density (g/cm^3)	C	Si	Mn	Fe	Cu	Pb
Iron	7.83 ± 0.03	0.13%	0.2%	1.0%	98.7%	-	-
Lead	11.29 ± 0.03	-	-	-	-	0.05%	99.95%
Carbon	1.74 ± 0.01	>99.5%	-	-	-	-	-

Table 2.1: Composition of the nuclear targets as mass percentage. Table reprinted from [42].

In the passive targets, the fiducial volume is defined by a cut requiring the vertex to be within an 85 cm apothem hexagon with a 2.5 cm cut on each side of the division between materials. The information about nuclear targets is given in

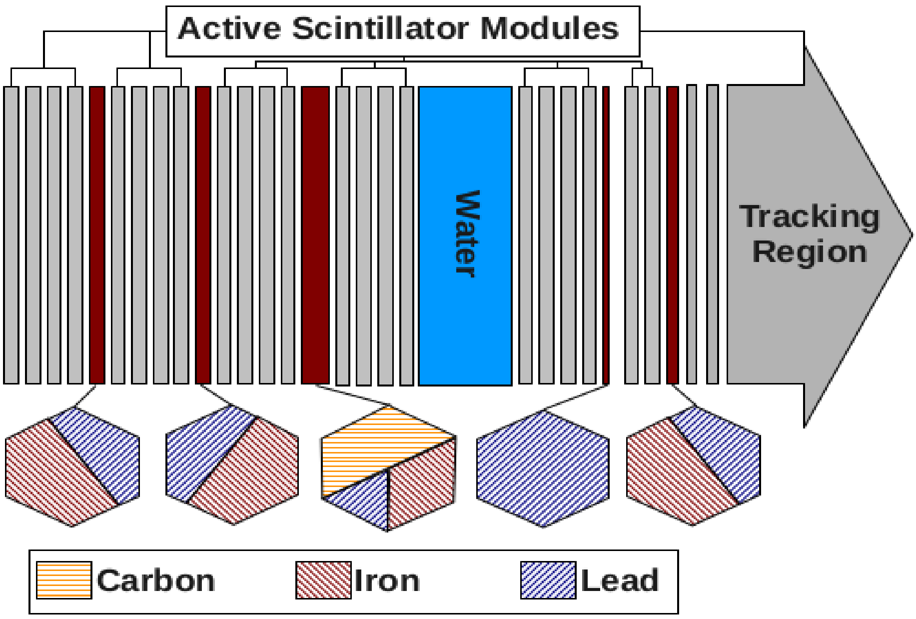

Figure 2.10: The Nuclear target region of the MINERvA detector. Figure taken from Ref. [42].

Table 2.2. There is a less than 2% estimated uncertainty on the fiducial masses due to density and thickness variations.

2.2.4 Active Tracker Region

The tracker region lies downstream of the nuclear target region. The mass percentage of various materials used in the scintillator planes in terms of density and elemental composition are listed in Table 2.3. This is the core of the MINERvA detector where the planes are 2.2 m wide hexagonal-shaped composed of 127 triangular shaped bars of the extruded scintillator (CH) with 33 ± 0.5 mm base and 17 ± 0.5 mm height.

The active tracker region is used to reconstruct tracks of charged particles that travel through the detector. Each tracking module consists of two scintillator planes kept in a hexagonal steel frame. There are 60 tracking modules in the

Target	z-location (cm)	Thickness (cm)	Fiducial Area (cm^2)	Fiducial Mass (kg)	Total Mass (kg)
1-Fe	452.5	2.567± 0.006	15999	322	492
1-Pb	452.5	2.578± 0.012	9029	263	437
2-Fe	470.2	2.563± 0.006	15999	321	492
2-Pb	470.2	2.581± 0.016	9029	263	437
3-C	492.3	2.573± 0.004	7858	158	238
3-Fe	492.3	2.563± 0.004	3694	107	170
3-Pb	492.3	7.620± 0.005	12027	160	258
Water	528.4	17-24± 0.005	25028	452	627
4-Pb	564.5	0.795± 0.005	25028	225	340
5-Fe	577.8	1.289± 0.006	15999	162	227
5-Pb	577.8	1.317± 0.007	9029	134	204

Table 2.2: Nuclear target locations, thickness and fiducial mass. The total mass refers to the entire plane of the target material. Table reprinted from [42].

Material	Density (g/cm^3)	H	C	N	O	Al	Si	Cl	Ti
Scintillator	1.043 ± 0.002	7.6%	92.2%	0.06%	0.07%	-	-	-	-
Coating	1.52	6.5%	78.5%	-	6.0%	-	-	-	9.0%
Lexan	1.2	6.7%	66.7%	-	26.7%	-	-	-	-
PVC tape	1.2	4.8%	38.7%	-	-	-	-	56.5%	-
DP190 transl.	1.32	10.0%	69.0%	2.6%	17.0%	-	-	0.5%	-
DP190 gray	1.70	5.0%	47.0%	1.7%	27.0%	6.0%	6.0%	0.05%	-

Table 2.3: The densities and composition of the various components used in the detector. Table reprinted from [42].

inner tracking region. Table 2.4 lists the composition of scintillator strips and constructed planes. Due to the low density of the scintillator planes, it is not possible for the tracker region to contain all neutrino interactions. Therefore, a 1 mm thick lead collar surrounds the ID which extends to the outer edge and to the sides of the detector called OD. This region acts as a component of EM to slow down or stop the particles leaving the neutrino vertex in the fiducial region. The frame, 56 cm wide, contains four bars of scintillators. The thickness of the OD frames is around 3.49 cm in the tracker region. In order to improve the hermicity, the OD bars are thicker in the hadron calorimetry region. There are over 32,000 channels in MINERvA and, in total, 110 modules in the tracking region.

Component	H	C	O	Al	Si	Cl	Ti
Strip	7.59%	91.9%	0.51%	-	-	-	0.77%
Plane	7.42%	87.6%	3.18%	0.26%	0.27%	0.55%	0.69%

Table 2.4: The mass percentage and the composition of the constructed planes and scintillator strips. Table reprinted from [42].

2.2.5 Calorimetry: Electromagnetic and Hadronic

To the downstream of the active tracker region is the electromagnetic calorimeter (ECAL). Each scintillator plane in the ECAL has a 0.2 cm thick sheet of lead attached. The ECAL region has 10 modules. There exist a transition module between the last and the first tracker module in the ECAL which contains a 0.2 cm thick lead sheet and serves as a particle absorber. The fine granularity of the ECAL region allows a precise measurement of the photon and electron energy. Immediately in the downstream of the ECAL region is the hadronic calorimeter (HCAL) which has 20 modules and the modules are composed of a 2.54 cm thick steel absorber plane where the hadrons will shower and deposit most or all of their energy before leaving MINERvA.

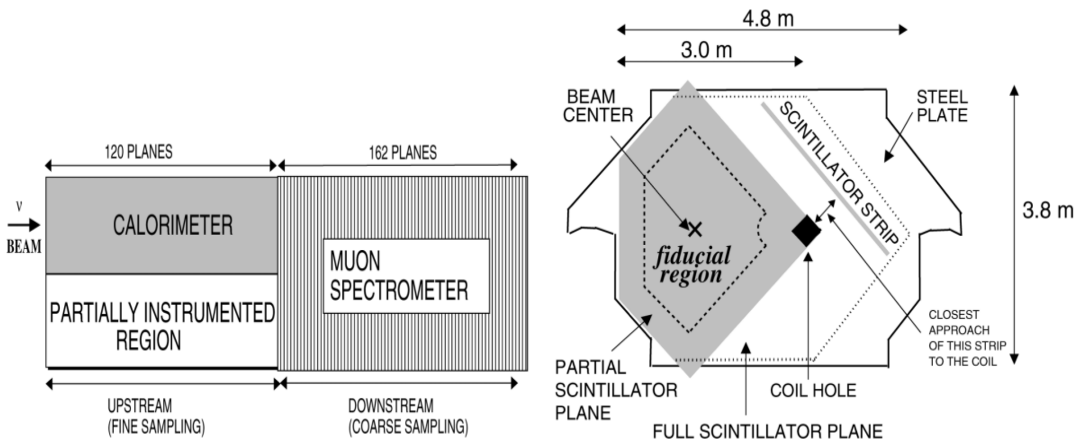

Figure 2.11: Left: the calorimeter and muon spectrometer regions of the MINOS detector. Right: the transverse view of the MINOS detector plane. Figure taken from Ref. [44].

2.2.6 The MINOS near detector

The Main Injector Neutrino Oscillation Search (MINOS) detector [43], shown in Figure 2.11 is located around 2 meters downstream of the MINERvA detector. The MINOS near detector measures the charge and the momentum of the muons exiting the MINERvA detector and serves as the muon spectrometer. MINOS iron calorimeter is a kiloton magnetized iron scintillator with a toroidal magnetic field of 1.3 T. The direction of the magnetic field helps in the determination of the charge of the track entering from the MINERvA detector. This helps to identify whether a given interaction in the MINERvA detector was due to a neutrino or antineutrino. The detector is 16.6 m long having 282 steel planes in total with each steel plane thickness of around 2.54 cm. The calorimeter region, which is the 120 planes just next to the MINERvA experiment, gives a clear picture of the neutrino interactions while the spectrometer region is used to track the through-going muons generated by interactions upstream and to determine their momentum. The region, which is the rest of the 162 planes, is used to track and measure the momentum of the through-going muons.

CHAPTER 3

RECONSTRUCTION AND SIMULATION

3.1 Reconstruction

The energy depositions in the MINERvA detector have to be converted into something meaningful which can be used to extract the physics results from the data. The process of this conversion, where the depositions in the detector are converted into some measurements associated with the particles created in the neutrino interaction, is called reconstruction. The reconstruction algorithm is run over all MINERvA's data to measure and identify the particle tracks in the detector. This is a multistep process where the output of one process serves as an input for the next process. The goal is to produce a collection of measurements related to the particles that are then used to do physics analysis. The different steps involved in the reconstruction process are: time slices, cluster formation, track reconstruction, MINOS matching of the reconstructed tracks. The description of these steps is given in the following sections and more details can be found in Ref. [42].

3.1.1 Time slices

The time profiles of the neutrino interactions in the MINERvA detector are much narrower than 16 μs which makes multiple neutrino interactions happen simultaneously in a pile-up event. The pile-up is then mitigated by forming time slices that are then used for the rest of the reconstruction process. The calibrated time is used to sort the hits within a gate. When the hits firing the discriminator go beyond the charge threshold of 10 photoelectrons within a time window of 25 nanoseconds, time slices are initiated. All the hits which do not fire the discriminator are added to a hit already in the time slice. The single-time slice contains the activity from a single neutrino interaction.

3.1.2 Cluster Formation

The charged particles in the MINERvA detector transverse through the plane generally pass through two strips in a plane and deposit energy and form a group of neighboring hits within the same time slice called a cluster. The strips which are isolated and do not have any neighboring hits are also termed as a cluster. The energy deposition in the strips determines the location of the cluster and is weighted by the energy from all the hits in the cluster. The hit with the highest energy determines the cluster time. The clusters are classified as low activity, trackable, heavy ionizing, superclusters, or cross-talk based on the energy sum and the size of distribution of hits in the cluster. Figure 3.1 shows the different classification of clusters.

The low activity clusters are the ones that have the hit energy sum less than 1 MeV. If the energy deposited in each hit is around 1-8 MeV and the sum of the energy of the hits does not exceed a maximum of 12 MeV, the clusters are termed as trackable clusters. If 1-3 hits in a cluster have energy greater than 0.5 MeV and the sum of the hit energy is greater than 10 MeV, the cluster is called a heavy

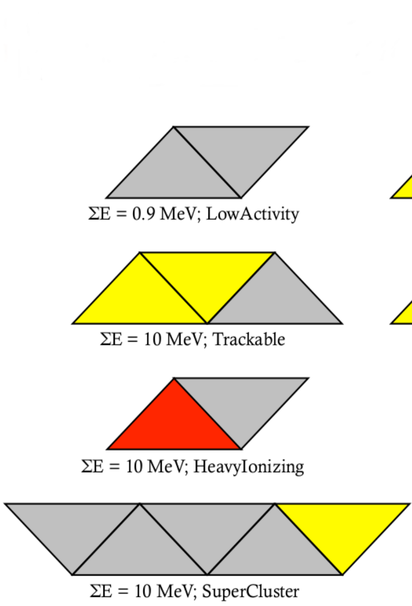

Figure 3.1: The cluster classification based on the hits in the MINERvA detector. Figure taken from Ref. [45]

ionizing cluster. The high angle tracks often create heavy ionizing clusters. The single hits with high energy must be adjacent to each other. The next category is the superclusters, where the distribution of the hits is broad or double-peaked. This type of cluster generally contains more than 5 hits. The cross-talk clusters are the ones where the low energy hits within a cluster are induced by the optical cross talk in PMT.

3.1.3 Track reconstruction

The process of using the clusters to estimate the position parameters of the charged particles is called the track reconstruction. Only one track is needed to obtain the particle trajectory unless particles have a large scattering angle. The reconstructed track then contains the information about the direction, origin, and momentum of the charged particles. Tracks are formed by first combining three clusters that fall in consecutive planes of the same X, U, or V view termed as track seeds. Then, merging of the track seeds of the same view with slope and intercept consistent with a two-dimensional track is done. Only one cluster per plane is required for a track candidate which results in many track candidates from a single detector view composed of clusters. A 3D track then is obtained by merging the 2D tracks in separate views with the condition that they are of the same longitudinal distance and consistent with a 3D line. In order to find the re-scattered tracks, a Kalman filter fit technique is used to do the fitting of the track that takes into account multiple scattering as the track propagates through the detector [46, 47]. In order to search for a muon track, the mass of the muon is considered to calculate the multiple scattering. To extend the track with any cluster object, the track is projected upstream and downstream using the fit obtained. Also, extrapolation of the track is done to the planes where there is no cluster and if a cluster is found that is then added to the track. Not only the trackable and heavily ionizing clusters, but the low activity and superclusters are also included. In a similar way, tracks in MINOS near detector are reconstructed and matched by slope, intercept, and timing of the front-entering MINOS tracks and rear-exiting MINERvA tracks. The MINOS matched tracks, assumed to be muons, are promoted to the primary track whose upstream end defines the primary vertex.

3.1.4 MINOS matching of tracks

MINOS near detector acts as a muon spectrometer for MINERvA. Most of the muons pass into the MINOS near detector after getting produced by the neutrino interactions in the MINERvA detector. The complete reconstruction of the muon energy and trajectory is obtained by taking reconstruction information from the MINERvA as well as MINOS detector. The tracks found in the detectors must be matched with each other and should be within 200 ns of each other in time. The vertex inside the MINOS detector must be located within one of the first four planes of the detector while the tracks must stop within the last five modules of the MINERvA detector.

Two separate methods are implemented to do the track-matching between MINOS near detector and MINERvA viz. the closest method and a track projection method. In the track projection method, the vertex of the MINOS track is extrapolated to the scintillator plane where the MINERvA track ends and the distance between the end points, called match residual, of the MINERvA track and extrapolation MINOS track is calculated. Also, in a similar way, the MINERvA track is extrapolated to the vertex of the MINOS track and again distance is calculated. If both the match residuals are smaller than 40 cm, the track is said to be MINOS-matched. In the case of multiple matches, the smallest individual residual is taken to be the MINOS-matched track.

The closest approach method comes into effect if there is no match distance smaller than 40 cm. This method implements the Euclidean distance minimization in order to find the closest approach of the two tracks by extrapolating the MINOS track towards MINERvA and vice-versa. A track is rejected and not considered MINOS matched if the minimization value does not converge even after 1000 steps. All the MINERvA tracks which are MINOS-matched are exclusively muons (0.2% pions).

3.1.5 Muon Reconstruction

As discussed in the previous section, the MINOS near detector is used by the MINERvA to reconstruct the energy of muons leaving MINERvA. There are two sections of MINOS near detector: the calorimeter region and the spectrometer region. The calorimeter region measures the muon momenta and hadron shower very accurately, while due to the coarser granularity of the spectrometer region, the tracks of the high energy muons are identified. The muons matched to the MINOS are taken as the signature of the CC event.

In MINOS near detector, the muon momentum is measured by the muon track distance and the amount of the curvature, while the muon charge can be identified with the direction of the curvature, hence, identifying the neutrino or antineutrino nature of the interaction in the MINERvA detector. The details of the procedure of measuring the charge and momentum of the muon in the MINOS detector can be found in Ref. [48]. The magnetic field is aligned to bend the muons passing through MINOS either towards or opposite to the magnetic coil, depending on the field direction in the MINOS magnet, providing the maximum track range to measure the muon momentum. The momentum of the muons, from the track range, can be reconstructed to within 2%. When the muons have enough energy (10 GeV) to exit from the back or from the side of the detector, momentum can be reconstructed from range (to within 2.6%) according to:

$$\frac{1}{R} = \frac{0.3 \times B \times q}{p} \tag{3.1}$$

where B is the magnetic field in the MINOS detector, R is the radius of curvature, q is the charge of the muons (eV), and p is the momentum of the muon [49]. A Kalman filter method, similar to that applied in MINERvA, is used for track reconstruction and takes into account a magnetic field map, which is stable with time.

In order to obtain the momentum at the primary vertex, the muon energy calculated in MINOS must be propagated upstream. The Bethe-Bloch equation is used to calculate this energy but the parameters of this equation bring some uncertainty in the measurement.

3.1.6 Hadronic Energy Reconstruction

Hadronic energy or the recoil energy is the energy of the neutrino interaction other than the energy carried by the muon. It is also called E_{had} or E_{recoil} and is reconstructed by summing the corrected energy depositions calorimetrically in the detector. It is expressed in terms of neutrino energy and muon energy as:

$$E_\nu = E_\mu + E_{had}. \tag{3.2}$$

The measurement of the recoil energy is not simple as there are charged particles that can be below the detection threshold and also neutral particles in the final state which usually do not produce scintillations. Thus, the recoil energy is the total energy other than muon energy modified by the calorimetric corrections using simulation. Dependency on the simulation, thus, introduces model dependence in the measurement, which we try to correct using systematic errors. The sum of the energy deposited in the different regions of the MINERvA detector like ECAL, HCAL, and OD is weighted to take into account the additional passive absorber. The weights, or calorimetric constants, are evaluated by $\frac{dE}{dx}$ of a minimum ionizing particle. The reconstructed recoil energy is fit to the true recoil energy to obtain a calorimetric scale. The difference between the neutrino energy and the muon energy is taken as the true recoil energy.

The calorimetric correction due to energy deposited in passive materials is given by:

$$C^i = c^i + \frac{1}{f} \tag{3.3}$$

where, C^i is the correction factor for subdetector i (for example to the tracker, ECAL, and HCAL), c^i is a constant for each subdetector measuring the fraction of seen to unseen energy due to a passive plane, and f = 0.8347 is the fraction of active material in a tracking plane and, for example, for the tracker $c^i = 0$.

The reconstructed recoil is calculated as:

$$E_{had} = \alpha \sum_i C^i E^i \tag{3.4}$$

where, α is the overall scale, with i = tracker, ECAL, HCAL, OD, c^i is the calorimetric constant for sub-detector i, and E^i is the total energy in sub-detector i.

The fractional energy resolution on the reconstructed recoil energy is shown in Figure 3.2.

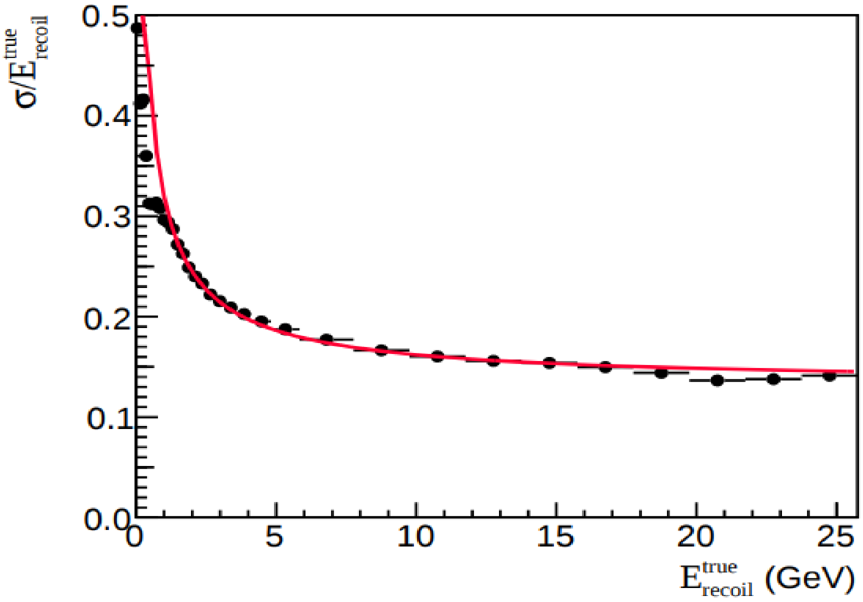

Figure 3.2: Fractional resolution on recoil energy for the CC Inclusive events. The width of a Gaussian fit to the difference between the measured and true recoil energy divided by the true recoil energy is shown by points, binned by true recoil energy. The line represents a functional fit, $\frac{\sigma}{E} = 0.134 \circledast \frac{0.290}{\sqrt{E}}$. Figure taken from Ref. [50].

3.2 Simulation

In order to analyze and interpret the experimental data in an accurate way, the simulations of the particle interactions with matter and modeling of detector geometries are essential. The simulation helps to understand the behavior of different types of particles and their energy depositions in the detector. The software used to generate the simulations produce events ideally resembling those coming from the actual experiment. MINERvA experiment uses the GENIE (Generates Events for Neutrino Interaction Experiments) [51] version 2.8.4 to generate the simulations for different physics processes like quasielastic scattering, resonance production, coherent pion production, neutrino-electron elastic scattering, inverse muon decay, and deep inelastic scattering for CC as well as NC events. This generator models the neutrino flavor interactions over a wide range of energies from MeV to several hundred GeV's.

The initial state is modeled as a relativistic global Fermi gas (RFG) [52]. The CC quasielastic processes with an axial dipole mass of 0.99 GeV (see Ref. [53]) are described by following Ref. [54]. The resonance production is modeled with Rein-Sehgal model [55], while the non-resonant pion production and multi-pion contributions are modeled using a GENIE specific model described in Ref. [56]. Bodek-Yang model [57] is used to incorporate deep inelastic scattering processes into GENIE and the cross section is obtained for scattering off individual partons. Hadronization is implemented through models based on Koba-Nielsen-Olesen scaling [58, 59] and is described by Pythia6 [60]. The 2p2h contributions are incorporated based on the Valencia model described in Refs. [61, 62, 63, 64]. RPA [65] is used to include the long-range correlations in QE interactions. In order to simulate the final state interactions (FSI), GENIE adapts an effective model based on Ref. [66]. Geant4 9.4.2 [67] is used to propagate the final state particles within the detector. The Geant4 simulations of the protons and charged pions [50] are constrained using hadron test beam data provided by MINERvA. Throughgoing muons are used to calibrate the energy scale for both the data and simulation.

CHAPTER 4

DEEP INELASTIC SCATTERING ANALYSIS

4.1 Overview of the Measurement

The focus of the analysis presented in this chapter is to measure the charge current (CC) muon-neutrino double differential deep inelastic scattering (DIS) cross section on different nuclear targets (A) like Iron (^{56}Fe), Lead (^{208}Pb), Carbon (^{6}C), and Hydrocarbons (CH). The DIS scattering process is given by:

$$\nu_\mu + N \rightarrow \mu + X,$$

where the final state has a charged muon μ and a bunch of hadrons represented by X. The kinematical regions are isolated based on the definition of the four momentum transfer squared Q^2 and the invariant mass W in order to choose the DIS sample for for the cross section measurement. The four momentum transfer squared Q^2 has the dimensions $\left(\frac{\text{length}\times\text{mass}}{time}\right)^2$ while the invariant mass W has the dimensions of mass in natural units. In this chapter, unit used for the four momentum transfer squared Q^2 is (GeV/c)^2 and for the invariant mass W is (GeV/c^2). The background will comprise the contributions from the different regions of Q^2 and W than the canonical Q^2 > 1.0 (GeV/c)^2 and W >2.0 (GeV/c^2).

4.1.1 Cross Section

As explained in detail in the following sections, the standard formula to calculate the total cross section is given as [73]:

$$\sigma_{ij} = \frac{U_{ijk}\ \ (d_{ij} - b_{jk})}{\Delta_{ij}\ \epsilon_{ij}\ \Phi\ N} \tag{4.1}$$

where σ is the total cross section, U_{ijk} is the smearing matrix, d_{ij} is the number of the data events in the reconstructed energy bin ij, b_{jk} is the number of background events in the reconstructed energy bin jk, Δ_{ij} is the width of the bin, ϵ_{ij} is the total efficiency of the event sample, Φ is the integrated neutrino flux, and N is the number of nucleons in a particular target i.e. Fe, Pb, C or CH. The expression for the double differential cross section is given by:

$$\left(\frac{d^2\sigma}{dxdy}\right)_{\alpha\beta} = \frac{\sum_{ij} U_{ij\alpha\beta}\left(N_{data,ij} - N_{ij}^{bkgd}\right)}{A_{\alpha\beta}(\phi_{ij}T)(\Delta x \Delta y)} \tag{4.2}$$

In the high energy tail of the neutrino energy, the uncertainties on the flux calculation are large and this is the region where most of the DIS events originate. Hence, the ratios of the cross sections from different nuclei like Fe, Pb, C with respect to CH is calculated. In the past analysis, the direct evidence of the Bjorken scaling variable x_{bj} dependent nuclear effects have been observed while taking the ratio of the differential cross section on the nuclei Fe, Pb, C to CH. The effects are well known in electron scattering but have not been measured systematically in neutrino scattering. In a DIS interaction, x_{bj} is defined as the fraction of the total momentum carried by the struck quark. It is the ratio of the four momentum transfer squared Q^2 to the nucleon mass and the recoil energy (hadronic energy):

$$x_{bj} = \frac{Q^2}{2M_N E_{had}} \tag{4.3}$$

where, M_N is the mass of the nucleons.

The double differential DIS cross section measurements presented in this thesis are evaluated in terms of Bjorken scaling variable x_{bj} and inelasticity y. The subsequent sections of this chapter will elaborate on different steps and methods used to calculate the cross section. The signal selection as well as the sample purity and efficiency are given in Sec. 4.2. The background classifications and estimation for the selected sample are presented in Sec. 4.3. The systematic uncertainties associated with the measurements are discussed in Sec. 4.4. The unfolding or unsmearing method is given in Sec. 4.5 that explains the measurements independent of detector effects. For the unfolded sample, the efficiency correction and target normalization are discussed Sec 4.6. The DIS cross section measurement is discussed in Sec. 4.7.

4.2 Event Reconstruction and Efficiency

In this section, there will be a discussion about the event sample passing the selection cuts used to measure the cross section. The DIS event sample is isolated with the selection cuts from the other events reconstructed in the detector. These events are then distributed in various bins of physics variables. The event selection populates, d_{ij} from the following equation:

$$\sigma_{ij} = \frac{U_{ijk}\ (d_{ij} - b_{jk})}{\Delta_{ij}\ \epsilon_{ij}\ \Phi\ N} \tag{4.4}$$

where, d_{ij} is the number of DIS events selected after passing the selection cuts.

4.2.1 Sample selection cuts

The target analysis presented in this thesis inherits a set of selection cuts (CCInclusive cuts) from the previously published DIS analysis [68, 69]. The description of the CCInclusive cuts inherited are as follows:

- Only those muons are analyzed and reconstructed which have a clear track in the MINOS detector.

- In order to have a ν_μ event, the muons matched in MINOS must have a negative curvature in the MINOS magnet to ensure a negatively charged muon.
- The interaction vertex of the event must be inside the 850 mm hexagonal fiducial area.
- There should be at least a separation of 25 mm between the barrier of the materials and the interaction vertex in passive target materials 1, 2, 3, 5.
- There is a filter for the rock muons to remove them from the sample.
- There should be at least a 5σ curvature significance for the muons reconstructed in the MINOS magnetic field.
- In MINOS, the endpoints of muon tracks should lie within 201 $<$ R $<$ 2500 mm of the magnetic coil.
- The muon angle θ_μ must be less than 17° due to the acceptance in the MINOS detector.
- Muon energy should be in the range $2 \leq E_\mu \leq 50$ GeV.

The kinematical cut used to isolate the DIS sample from the inclusive sample is applied on reconstructed Q^2 and W. If the reconstructed $Q^2 \geq 1$ (GeV/c)^2 and the reconstructed W $\geq$ 2 GeV/c^2, the reconstructed event is considered as a DIS event. A true DIS event is a signal event if it passes a true generated $Q^2 \geq 1$ (GeV/c)^2 and a true generated W $\geq$ 2 GeV/c^2. Also, the GENIE channel number for a true DIS event should be 3 in order to eliminate the charge current quasi elastic (CCQE) events which produce a charm quark and could potentially pass the Q^2 and the W cuts. Reconstructed events pass reconstructed Q^2 and W cuts while the "signal events" pass true Q^2 and W cuts. Events which pass both true as well as reconstructed Q^2 and W cuts are called as "true reconstructed events". MC event sample may have all of the three types.

4.2.2 Event selection and Efficiency

In order to isolate the DIS sample we apply the selection cuts, and to correct for those cuts, two quantities are considered. The first efficiency is defined as the fraction of the number of events in the true material passing the reconstructed and true DIS cuts along with the reconstructed CCInclusive cuts to the number of events in the true material passing the truth DIS cut and the reconstructed CCInclusive cuts. The efficiency depends on the muon and hadronic resolutions because Q^2 and W are derived from the hadronic energy. This will be referred to as the "inelastic efficiency" throughout the rest of the text.

The inelastic efficiency has a quantity related to it called "inelastic purity". It is defined as the fraction of the number of events in the true material passing the reconstructed and true DIS cuts along with the reconstructed CCInclusive cuts to the number of events in the true material passing the reconstructed DIS cut and the reconstructed CCInclusive cuts. Both the purity and efficiency quantify the efficacy of the DIS cuts.

The second efficiency used to isolate the DIS sample is called "overall efficiency". It has a similar definition for the numerator as that of the inelastic efficiency but the denominator is defined as the number of CC DIS events generated in the true fiducial volume with true muon angle ($\theta_\mu < 17^\circ$). This quantity explains the overall efficiency of the MINOS matching, the DIS cut, and the algorithm responsible to locate the vertices in the nuclear targets. This efficiency is always less than the inelastic efficiency because the denominator of the overall efficiency takes into more events than the inelastic efficiency. This efficiency is used to calculate the total and differential cross sections.

In a similar way as inelastic purity, the overall purity is related to the overall efficiency. It is the ratio of the events in the true material passing the reconstructed and true DIS cut along with CCInclusive cuts to the number of the events passing

Target / Z	Inelastic Efficiency (%)	Overall Efficiency (%)
1/26	25.92	18.14
1/82	26.32	18.48
2/26	26.49	19.64
3/6	25.60	21.54
3/26	26.04	19.49
4/82	2.18	23.55
14/82	29.97	29.62

Table 4.1: The overall and inelastic efficiencies of the DIS cut for different nuclear targets and a few tracker modules. These numbers are scaled to represent the size of the data sample, 1.06×10^{21}

the reconstructed DIS and the CCInclusive cut. It accounts for the loss of the mis-reconstructed events in the fiducial volume which were not taken into account in the inelastic purity. Table 4.1 lists the inelastic and overall efficiencies of the DIS cut. The events with the inelastic efficiency are given in Table 4.2. The contamination defined as 1 minus the inelastic purity is given in Table 4.3.

4.2.3 Data and MC event sample

The Data and MC sample in the present analysis uses the inclusive events (tuples) produced by the algorithm developed for the Data preservation project of the MINERvA experiment. The algorithm works in two stages: first, the lattice information describing the event is created which then serves as an input for the machine learning algorithm [70]. The machine learning algorithm then produces predictions of the vertex location of the events which contains all the information about the events and especially how confident is the algorithm about the prediction of the event vertex location. In the second stage, the machine learning vertex

Target	Target Z	True Events	True Reconstructed Events	Overall Efficiency (%)
1	26	70875	12858	18.14
1	82	58798	10866	18.48
2	26	69513	13658	19.64
3	06	36413	7843	21.54
3	26	34625	6749	19.49
4	82	4449	1048	23.55
14	82	129346	38318	29.62

Table 4.2: The number of true DIS events, the number of events passing true as well as reconstruct DIS cuts and overall efficiency for different nuclear targets and a few modules of tracker. These numbers are scaled to represent the size of the data sample, $1.06{\times}10^{21}$.

Target	Target Z	Reconstructed Events	True Reconstructed Events	Contamination (%)
1	26	49600	12858	74.07
1	82	41274	10866	73.67
2	26	51559	13658	73.50
3	06	30628	7843	74.39
3	26	25916	6749	73.95
4	82	47986	1048	97.82
14	82	127831	38318	70.00

Table 4.3: The number of true DIS events, the number of events passing reconstruct DIS cuts and Inclusive cuts, and contamination for different nuclear targets and a few modules of tracker. These numbers are scaled to represent the size of the data sample, $1.06{\times}10^{21}$

location predictions are used to run the algorithm again where it now adjusts the location of the event vertex to the vertex location predicted with the machine learning algorithm. To account for the loss or the gain of the energy due to the vertex location adjustment, the energy-related to a muon and hadronic system must be corrected. The MasterAnaDev ntuples produced divide the sample into different samples depending upon the predicted z-vertex of the event. Machine learning sorts the events by most probable module/target, and the tracker which are then classified based on the (x,y) position of the vertex in each target.

For the nuclear targets and the tracker modules, histograms are produced and analyzed separately. Figures [4.1, 4.2], [4.3, 4.4] and [4.5,4.6] shows the data and simulation plots for the DIS sample in the Fe of all targets, Pb of all targets, and C of target 3, respectively, along with the systematic uncertainities as well as statistical uncertainty. As this is the two-dimensional analysis, for each pair of variables, there will be two projections. From these plots, it can be seen that when we use heavy nuclear targets like Fe, Pb we have a huge sample of events in comparison to the single C nuclear target. But at the same time, we have to deal with the least understood nuclear medium effects. The Data/simulation ratio plots along with the other individual target plots are shown in Appendix B. Figure 4.8 shows the contributions from different systematic uncertainities discussed in Sec. 4.4 for different variables.

4.3 Background: Estimation and Subtraction

The background contamination to our DIS sample comes from the fact that the DIS cut will take into account the events with a reconstructed $Q^2 \geq 1.0$ GeV^2 and $W \geq 2.0$ GeV but with the true $Q^2 < 1.0$ GeV^2 and $W < 2.0$ GeV. This contamination must be separated from the DIS event sample before doing the cross section calculations. In the cross section expression shown below, the background

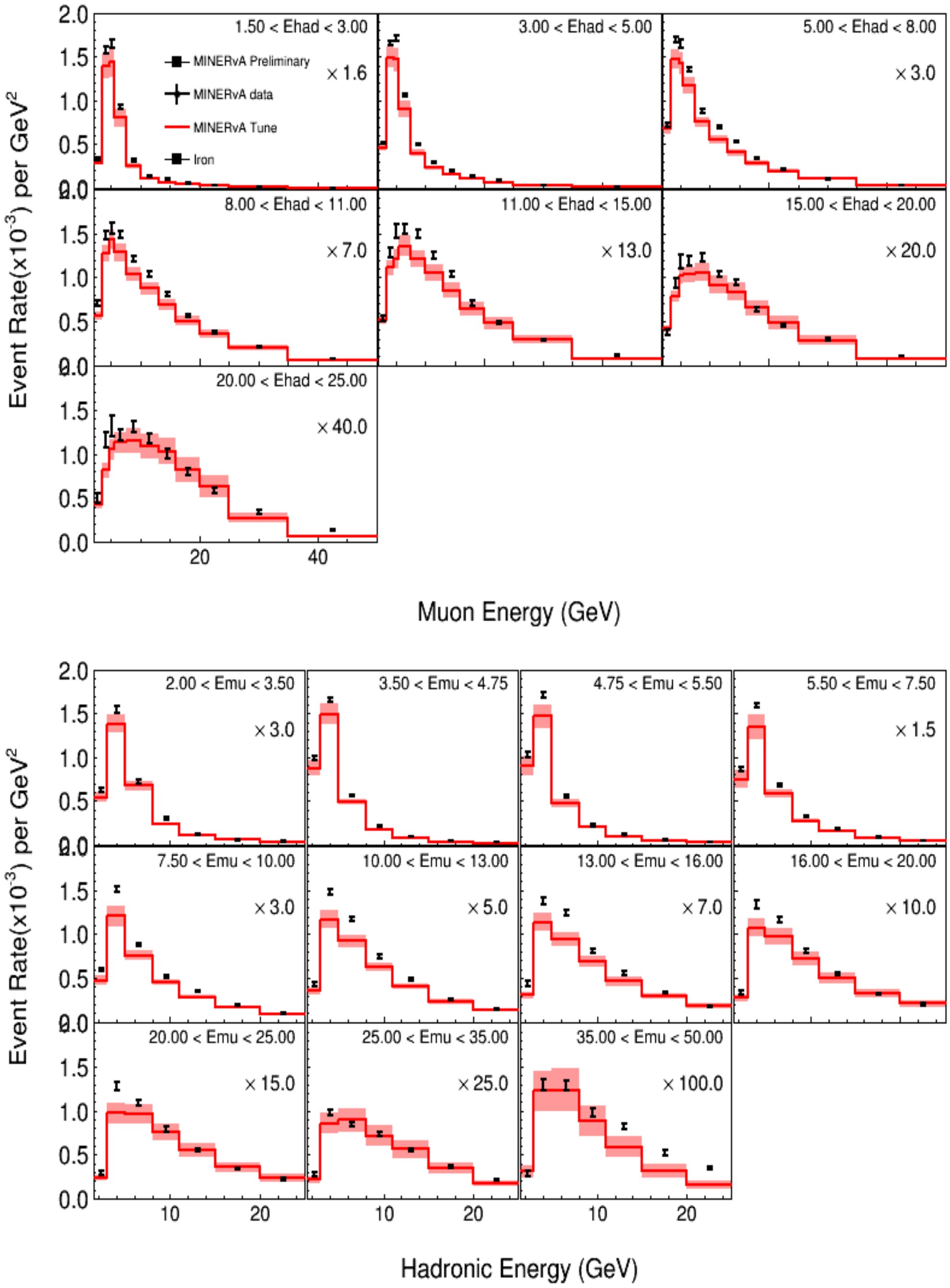

Figure 4.1: The Data and simulation plots for the combined Fe of all targets. The plots are for Muon energy vs Hadronic Energy. The pink band around the simulation represents the systematic uncertainities as well as the statistical uncertainty on the simulation where as the data points have the statistical uncertainty only.

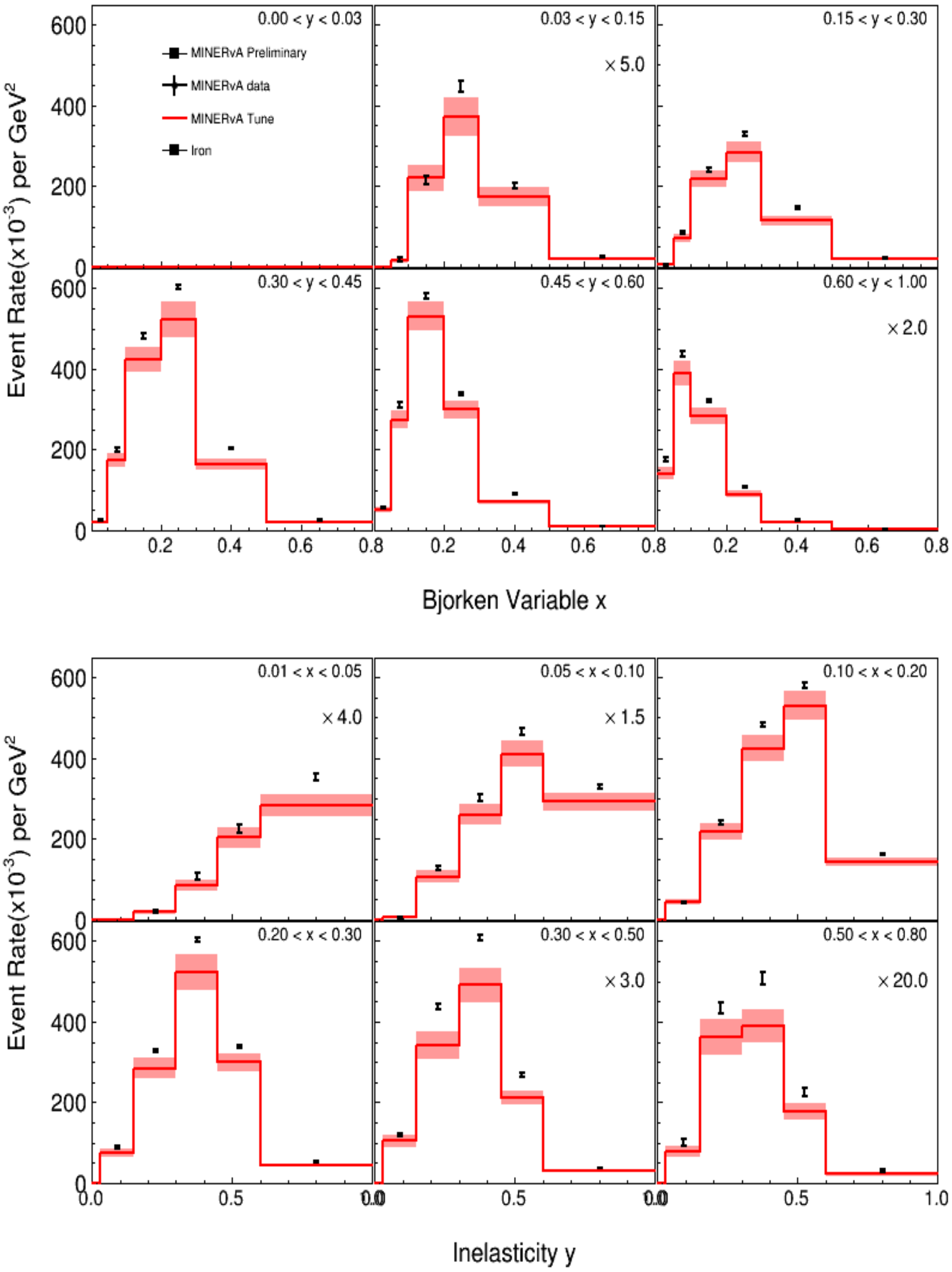

Figure 4.2: The Data and simulation plots for the combined Fe of all targets. The plots are for Bjorken variable x and Inelasticity y. The pink band around the simulation represents the systematic uncertainities as well as the statistical uncertainty on the simulation where as the data points have the statistical uncertainty only.

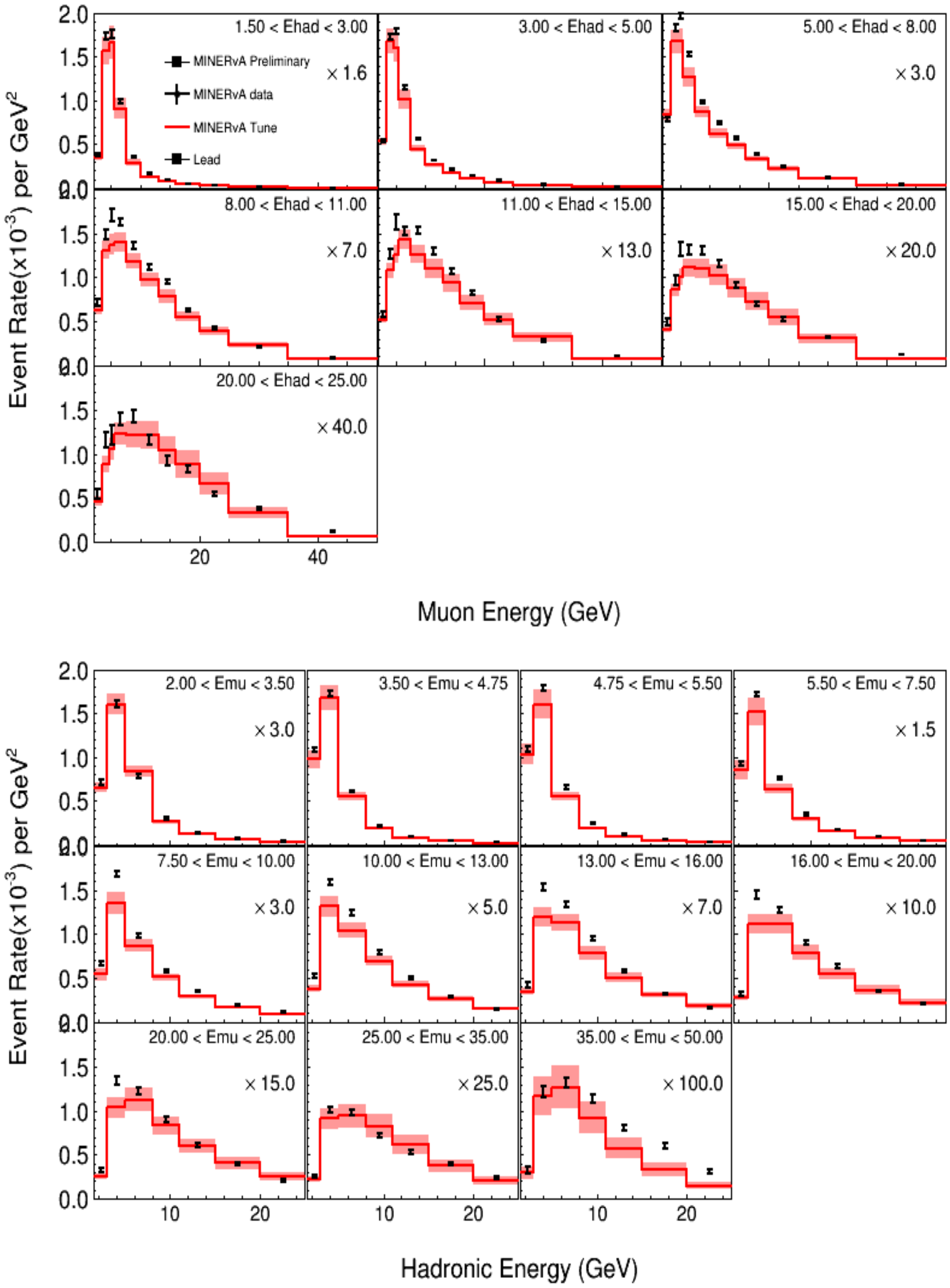

Figure 4.3: The Data and simulation plots for the combined Pb of all targets. The plots are for Muon energy vs Hadronic Energy. The pink band around the simulation represents the systematic uncertainities as well as the statistical uncertainty on the simulation where as the data points have the statistical uncertainty only.

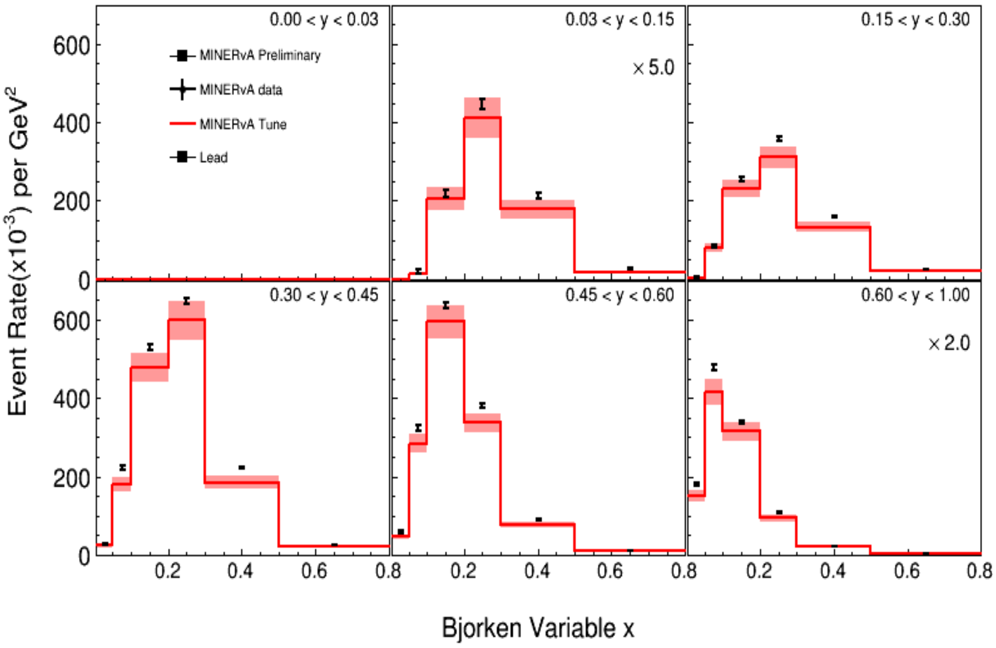

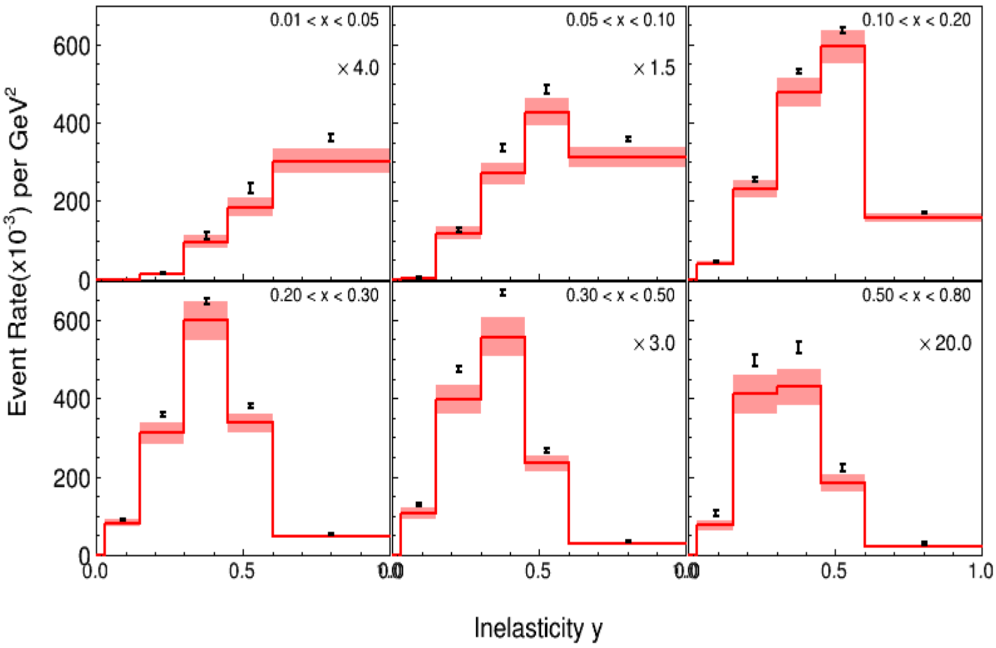

Figure 4.4: The Data and simulation plots for the combined Pb of all targets. The plots are for Bjorken variable x and Inelasticity y. The pink band around the simulation represents the systematic uncertainities as well as the statistical uncertainty on the simulation where as the data points have the statistical uncertainty only.

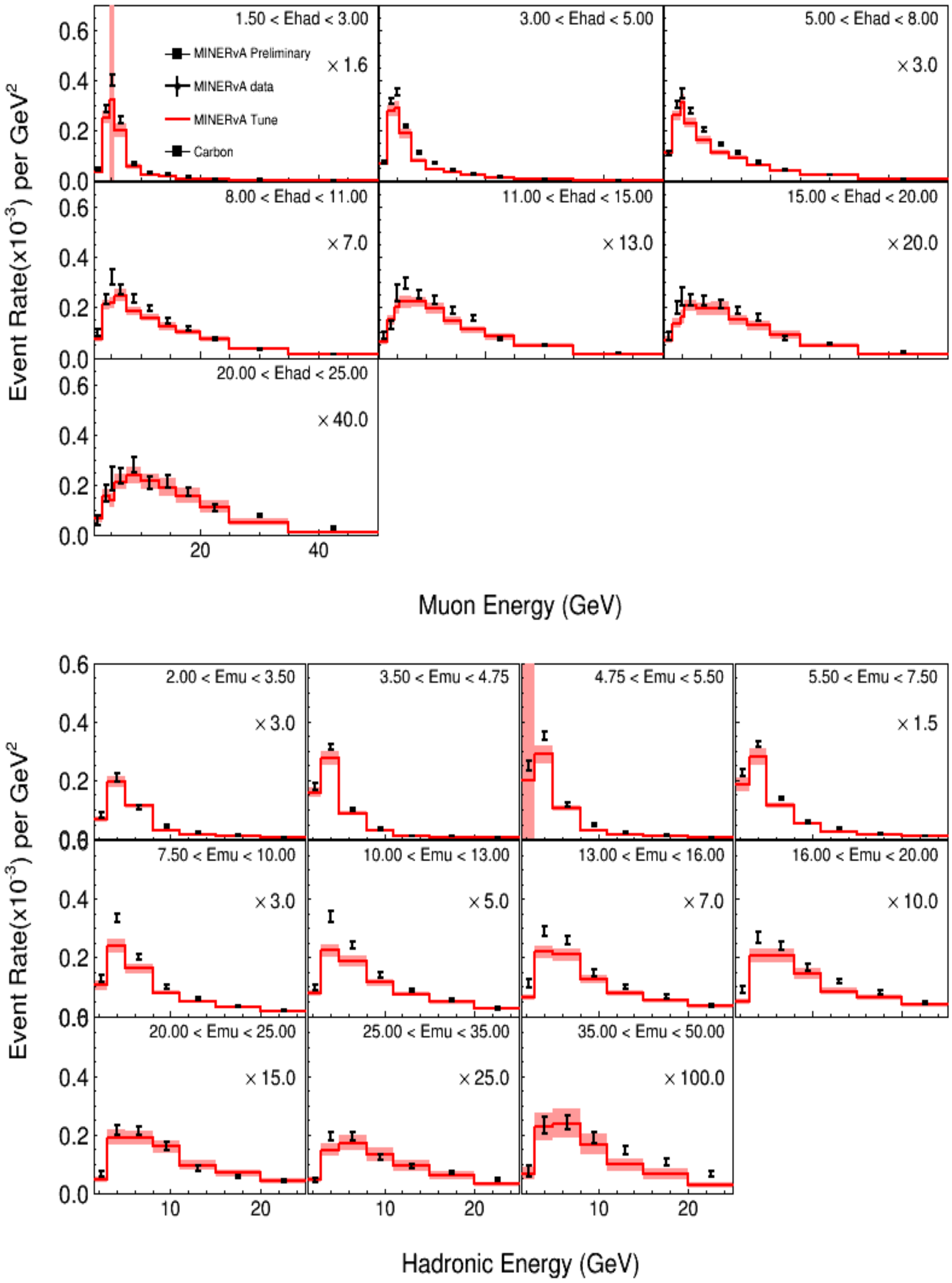

Figure 4.5: The Data and simulation plots for the combined C of target 3. The plots are for Muon energy vs Hadronic Energy. The pink band around the simulation represents the systematic uncertainities as well as the statistical uncertainty on the simulation where as the data points have the statistical uncertainty only.

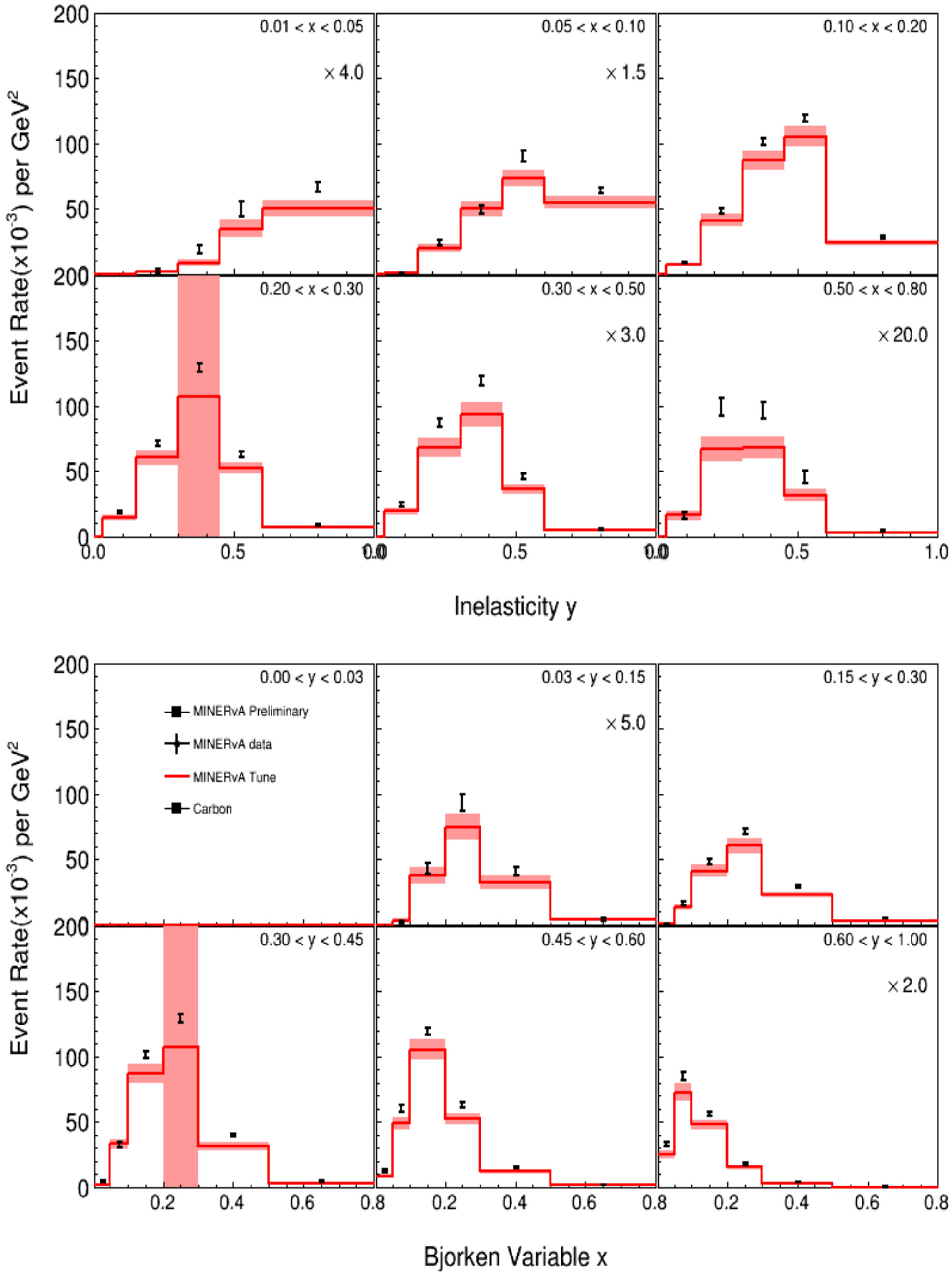

Figure 4.6: The Data and simulation plots for the combined C of target 3. The plots are for Bjorken variable x and Inelasticity y. The pink band around the simulation represents the systematic uncertainities as well as the statistical uncertainty on the simulation where as the data points have the statistical uncertainty only.

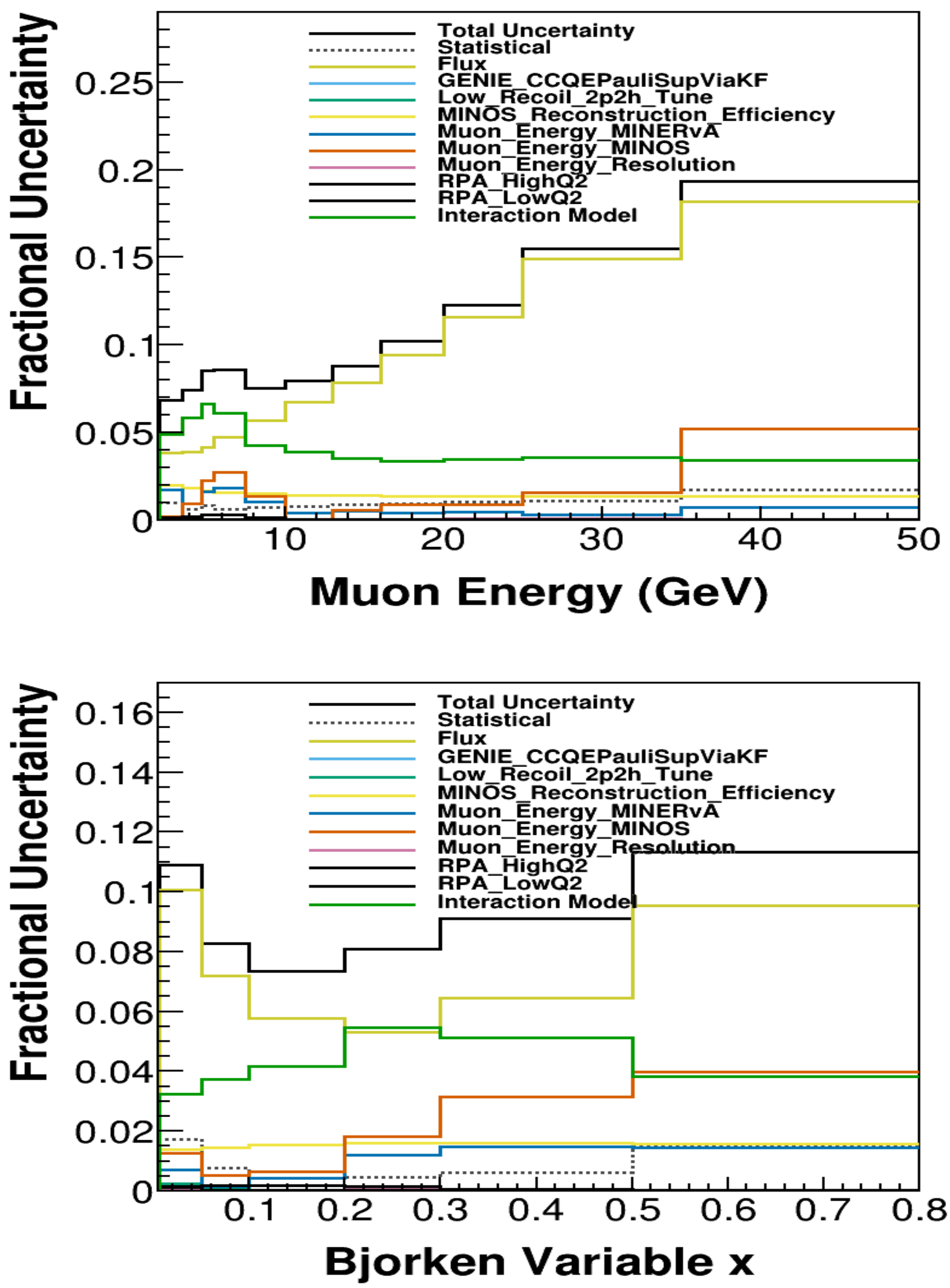

Figure 4.7: The contribution of the statistical and the systematic uncertainities on the event rate plots for the combined Fe of all targets. The plots are included for two variables: (i) Muon energy and (ii) Bjorken variable x.

is accounted through b_{jk} as

$$\sigma_{ij} = \frac{U_{ijk}\ (d_{ij} - b_{jk})}{\Delta_{ij}\ \epsilon_{ij}\ \Phi\ N} \tag{4.5}$$

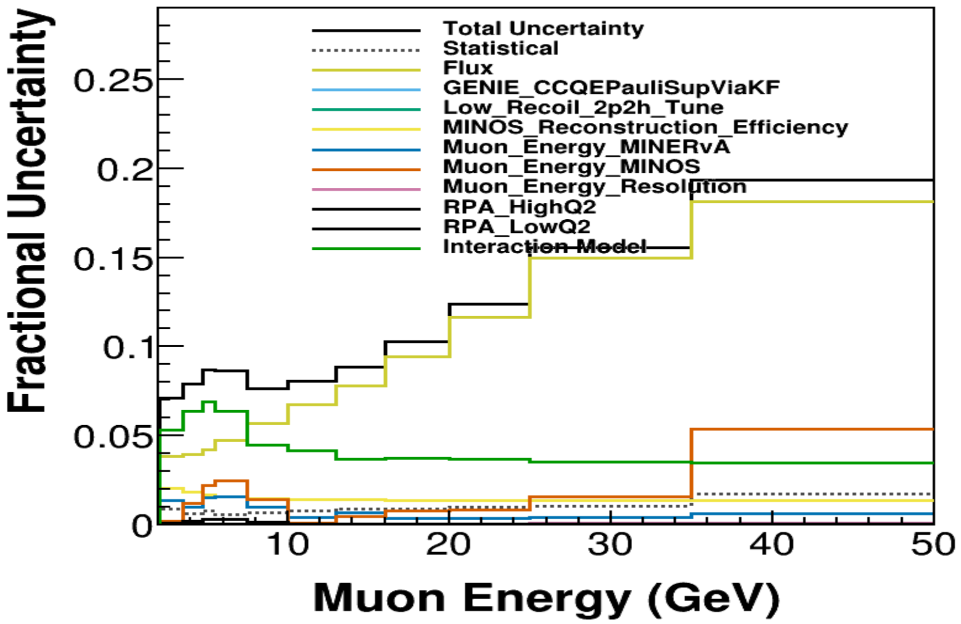

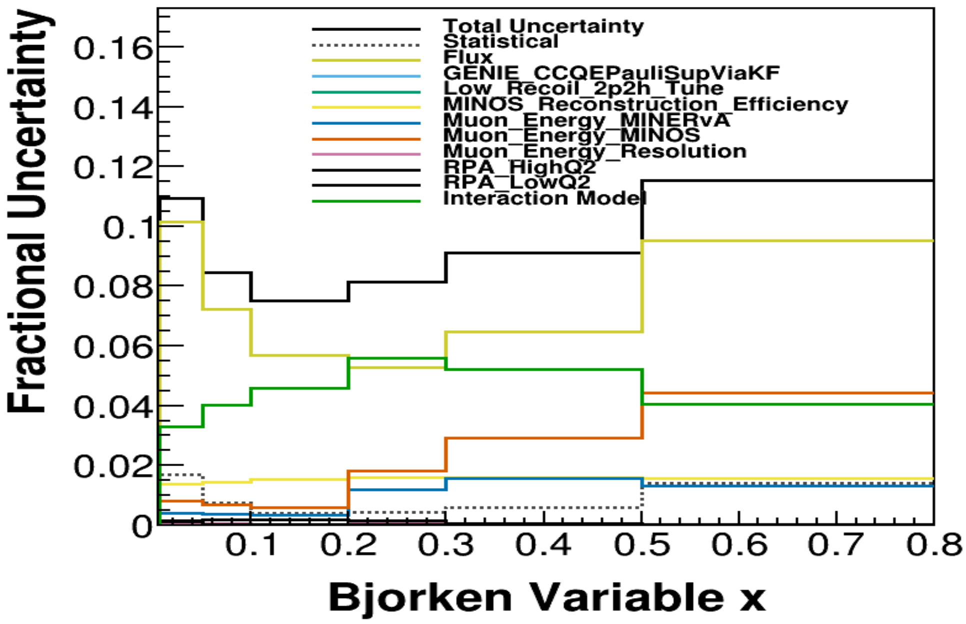

Figure 4.8: The contribution of the statistical and the systematic uncertainities on the event rate plots for the combined Pb of all targets. The plots are included for two variables: (i) Muon energy and (ii) Bjorken variable x.

The background is first estimated using the simulation sample and then subtracted from the data sample. Also, in order to minimize model dependency in the background measurement, the simulation background is constrained to data before subtraction. The model dependence of the background is critical for any low purity analysis, so additional background enhanced samples also called as sidebands are used to make sure that the background is properly taken care of. Sidebands are used to constrain the background under the peak of some variable as they are regions to the side of the peak.

The goal is to eliminate background contamination from the sample and obtain a pure DIS sample. The reconstructed DIS event sample may contain events that truly originate in the plastic scintillator but are taken as events coming from the nuclear targets. Kinematically, the DIS sample may also contain events that don't pass the true Q^2 and W cut. Hence, the background subtraction is complicated in the analysis performed in the nuclear target region. The classification of the background events in the present analysis is done according to the target where the interaction happened and according to the kinematics. Figure 4.9 illustrates the background estimation and subtraction process presented in this thesis.

4.3.1 Plastic or wrong target background

Construction of Sidebands

To subtract the plastic background from the non-DIS sample and to avoid discrimination on the basis of kinematics, the sideband sample is computed from inclusive sample instead of DIS sample. The background contamination from individual targets is statistically limited so targets are combined to obtain a more precise measurement. This is done by looping over all the passive targets for specific nuclei. Also, the histograms for the true material of the vertex are made for the events where the vertex is predicted originating from the downstream (6

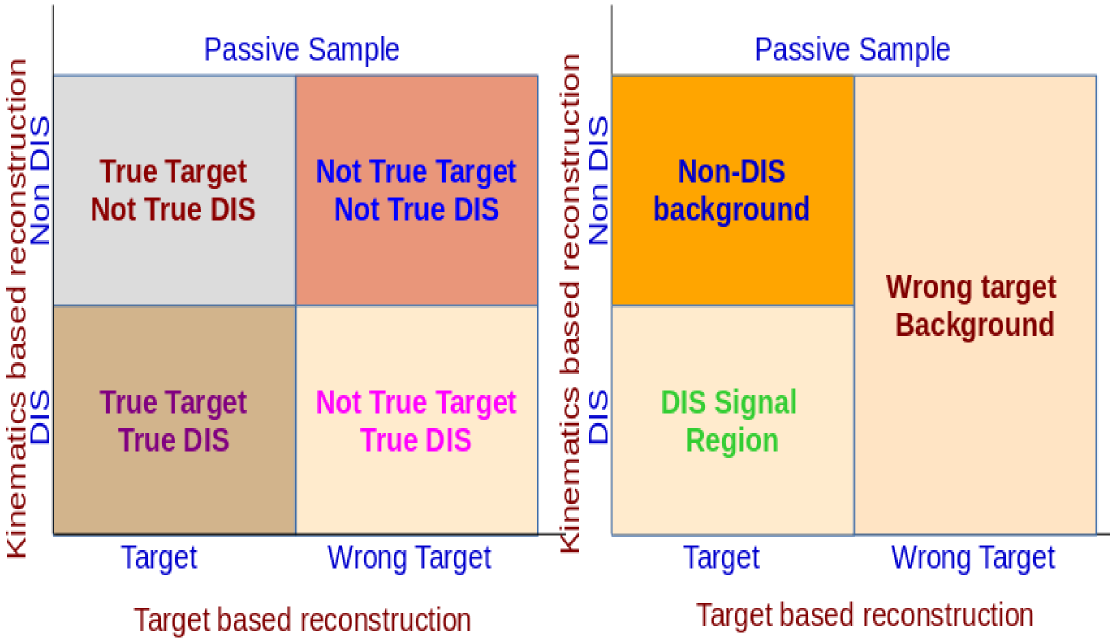

Figure 4.9: The plastic and physics background for the DIS analysis.

planes only) or the upstream (6 planes only) sideband of the target.

The scintillator planes upstream of target 1 are not included in the background construction process. This exclusion is done because in that region the data is statistically limited due to the rock muon cut which rejects the muons having the interaction vertex in the first two modules of the detector. Figure 4.9 shows the sideband distribution for the plastic sidebands.

Fitting Prescription

There are two simulation plastic background templates used to fit the data for the inclusive sample events. The first template contains all of those events which have the interaction vertex reconstructed in the plastic region which is upstream of the passive nuclear target. The second template contains all of those events which have the interaction vertex reconstructed in the plastic region downstream of the nuclear target. A χ^2 minimization is used to fit the two templates simultaneously to the data in both sidebands for each plane number bin i,

$$\chi^2 = \Sigma_{\text{bin i}} \frac{(N_{DATA} - N_{MC})^2}{\sigma^2_{DATA}}. \tag{4.6}$$

The fits are performed for each nuclear target between plane number 11 to 65 which includes the plastic scintillator tracker just downstream of passive target 1 through four scintillator modules downstream of target 5. The results of the χ^2 minimization for each material are the scale factors. The scale factors are obtained as follows:

- Use the ROOT Minuit2Minimizer function [71] to extract upstream plastic scale factors. This is done by keeping the signal, downstream plastic events and the events from other passive targets upstream of the reconstructed target fixed while allowing the events occurring in the upstream plastic to float.
- Repeat the first step but by allowing the events occurring in the downstream plastic to float while keeping rest fixed.
- Simulation is scaled to data using POT normalization, then data to simulation ratio is compared before the tuning and after the tuning. This procedure is considered acceptable if the χ^2 is close to 1,

$$\begin{aligned} \chi^2 &= \Sigma_{\text{bin i, bin j}}(N_{\text{bin i, DATA}} - N_{\text{bin i, MC}}) \\ &\times \sigma M_{\text{bin i, bin j}} \times (N_{\text{bin j, DATA}} - N_{\text{bin j, MC}}). \end{aligned} \tag{4.7}$$

Tuning

The scale factors obtained with the prescription explained above are applied to the upstream plastic background templates and downstream plastic background templates in each of the nuclei in the passive targets. After the plastic background tuning, the tuned background is subtracted from the data.

4.3.2 Non-DIS background

The DIS sample events are selected by applying the DIS cut with reconstructed $Q^2 > 1$ $(GeV/c)^2$ and reconstructed $W > 2$ GeV/c^2 . The events which are not truly DIS but got passed the kinematic DIS cut are termed as non-DIS background events. These backgrounds can be classified into two categories: (i) continuum region, where the events have true $W > 2$ GeV/c^2 , but true $Q^2 < 1$ $(GeV/c)^2$, (ii) transition region, where the events have true $W < 2$ GeV/c^2.

The true DIS events truly coming from a nucleus N are calculated as:

$$T_N = (R_N - R_{CH}) - C_N \tag{4.8}$$

where, R_N is the number of DIS events reconstructed in a nucleus, R_{CH} reconstructed DIS events coming truly from plastics and C_N true non-DIS events reconstructed in the nucleus. The reconstructed signal region is very close to the reconstructed sideband region in low Q^2 and low W due to the higher statistics in the ME. Hence, the sidebands better model the background in the signal region. The sidebands are adjusted on the basis of low Q^2 and low W to search for the true contamination in the signal region.

Fitting Prescription

We use the χ^2 technique to fit the transition and continuum background templates to the data after the plastic background is subtracted from each template. The χ^2 fitting function used is defined as:

$$\chi^2 = \Sigma_{\text{bin i}} \frac{(N_{DATA} - N_{MC})^2}{\sigma^2_{DATA}}. \tag{4.9}$$

The output of the fits are the scale factors α and β which are used to scale both the templates, respectively. The fits are performed for each passive nuclear target and also for the combination of the target material and the active tracker region. The scale factors are calculated for the combination of the target materials because of the limited statistics of the sidebands.

Fit results

The scale factors extracted using the above technique are applied to non-DIS simulation events which pass the DIS cut. The plastic background is subtracted prior to the non-DIS subtraction. The background is then subtracted using the re-weighted simulation from the DIS events in data.

4.4 Systematics

The lack of understanding about the measurement tools at a very good precision and the models employed to compare the observed data results in systematic uncertainties. Due to the insufficient theoretical knowledge, to explain these uncertainties, they are associated with one measurement to another. There are three types of systematic errors on the cross section measurements in MINERvA: flux, reconstruction, and the theoretical cross section applied in the simulation. These uncertainties are further split into various error categories: Detector Resolution, Flux and Mass, Interaction Models, and FSI Models. The systematic uncertainty allocated to the predicted simulation by the DIS analysis is equally valid for the data. However, the statistical error is relatively small on the simulation as compared to data because we generate simulation 10 times larger than the data sample.

4.4.1 Calculation of Systematic Uncertainties

The DIS analysis calculates the systematic uncertainty on the distribution of any parameter "x" by the standard MINERvA method. The baseline simulation is employed to generate a "central value" distribution as a function of parameter x. To compute the systematic uncertainty, the model parameters are changed with a known covariance matrix to produce shifted distribution. The uncertainty is defined as the difference between the central value distribution in a bin and the mean of the varied distribution in that bin. The effect of model uncertainties on any distribution influenced by the model is represented by the error band. In MINERvA experiment, a multi-universe approach is used to determine the uncertainty with many correlated parameters, such as flux. Each parameter is varied randomly within a $\pm 1\sigma$ Gaussian width distribution to assure the precise measurement of uncertainty. This goes till "n" number of times to produce "n" shifted distributions of x, also called as universe. A new simulated distribution is produced for every set of parameters in every universe. So, the uncertainty on x in a bin is the RMS of the resulting "n" universes in that bin. The total uncertainty includes the quadrature sum of the uncertainties on each parameter, and the correlation between parameters are also considered when appropriate.

4.4.2 GENIE systematics

The cross section estimation method depends on the Monte Carlo simulation to estimate background fractions, unfolding, efficiency correction, and flux estimation. There are two ways by which GENIE uncertainties can impact the cross section model: a) Initial-state interaction rate uncertainties b) Final-state interaction rate uncertainties. Data from earlier experiments has been used to estimate the uncertainty on each GENIE parameters. The model dependency of the background estimate that goes into cross section measurements provides large uncertainties on the measurement. But, background model dependency can be lower down by creating background enhanced control regions (sideband method), although the extrapolation of the background constraint into the signal region still depends somewhat on the model. The sideband regions are created with similar underlying kinematics to the background in the signal region.

4.4.3 GENIE FSI

To model the final-state interactions (FSI), the GENIE event generator utilizes the INTRANUKE (hA) intranuclear hadron transport model. Few quantum effects like Pauli blocking and nucleon correlations are included in the model and briefly described in Ref. [72]. There are two types of uncertainties that can influence the INTRANUKE (hA) intranuclear hadron transport model:

- Uncertainties in the sum of the rescattering probabilities (mean free path) for hadrons when they pass within the nuclear medium.
- When the rescattering takes place, uncertainties arise from each of the hadron rescattering mode probabilities. The rescattering modes contain the pion production and absorption, charge exchange, inelastic, elastic, and other rescattering modes.

For cross section measurements, all the GENIE parameters correlated with final state interactions are given a $\pm 1\sigma$ systematic uncertainty.

4.4.4 Reweightable GENIE

The probability for a certain type of interaction to happen depends on the GENIE uncertainties in the interaction model, so, the uncertainties for a physics quantity "x" need to be determined through event reweighting procedure. As stated earlier, in the GENIE framework of MINERvA experiment, the systematic parameter is changed by $\pm 1\sigma$. Hence, the corresponding physics quantity "x" is altered by $\pm \delta x$. For the error calculation in cross section measurement, the standard GENIE $\pm 1\sigma$ uncertainty is added. Two different universes are determined using the two different pre-calculated GENIE weights that correspond to the positive and negative variations in question. The uncertainty is calculated from the mean deviation of the two universes. The details to estimate the GENIE cross section uncertainties in MINERvA are explained in Ref. [73] and for GENIE weights are given in Ref. [72]. For uncertainty calculations, every GENIE knob is altered independently. The GENIE systematic uncertainties are estimated on the efficiency, wrong target, non-DIS background events, and the reconstructed signal.

4.4.5 Non-Reweightable GENIE

When the particle passes through the nuclear medium, some GENIE uncertainties can alter its outcome due to which they cannot be modeled easily by the reweighting method or by specifying the error band as in the case of FSI. So for these specific cases, a particular generation of GENIE is needed to assess the systematic uncertainties on the model. To estimate the uncertainty coming from the hadronization model, the inclusive analysis is carried out on the regenerated samples between an E_{had} of 2 and 20 GeV as most of the DIS events come into this energy range. The uncertainty calculation requires the shifted sample and then determines the ratio of the shifted sample to the default GENIE model in each bin of E_{had} [74]. This ratio is taken as the $\pm 1\sigma$ uncertainty. This systematic was estimated separately for the passive and faux targets. The shifted GENIE samples contain:

- Varying the effective radius of the interacting nucleus (ENuc).
- Altering the formation length of hadrons (hadronization).
- An alternate tuning of the hadronization model GENIE employs to simulate intermediate energy hadron showers, AGKY. The detailed method to measure the systematic associated to the hadronization model is explained in Ref. [74] .

4.4.6 Flux

The things that contribute to flux uncertainty are: beam focusing with the magnetic horns, tertiary particle production, and CERN's NA49 experiment [37]. The first uncertainty that comes from beam focusing is defined as, how well the particles are focused into the beam at each energy. The second thing is tertiary particle production is defined as when the particles pass through the long target, there are chances of re-interaction of particles produced in the target which counts for the second source of flux uncertainty. The third source of uncertainty is the error proposed by the interaction of the proton beam and the target to generate pions and kaons. The production rate is computed by utilizing the data from CERN's NA49 experiment that has its own uncertainty, but since it must be extrapolated from their energy range to MINERvA's range of energy, it leads to additional uncertainties.

Each of the components of the flux error is calculated by altering the flux model parameters to create 100 different universes for beam focusing, tertiary hadron production, and NA49 uncertainties. In every universe, the underlying model parameters are modified and the flux prediction is computed again creating 100 different weights for each uncertainty. The RMS of these variations are used to get the systematic uncertainty and added together in quadrature giving a single systematic uncertainty. For the DIS nuclear target analysis, the flux uncertainty is allotted to the yield of events in each bin because of the traditional reasons as the inclusive framework that this analysis inherits from used to serve as a cross-check on detector calibrations and reconstruction algorithms. Once the flux uncertainty is given to the event distribution, it helps to examine if the discrepancy observed in normalization could be assigned to the flux model.

4.5 Unfolding

Unfolding is the procedure to remove the effect of a measuring device from a measurement. The procedure takes the reconstructed variable in bins j, and produces a result in bins of the true variable, i. Mathematically, the process is to describe the mapping between true and reconstructed variables through an unfolding matrix U_{ij}. The measurement of any physics observable will introduce deviations or smearing because we measure the reconstructed value of the observable instead of the true variable. The physics analyses must unfold their distributions by removing the detector effects like losses due to efficiency (acceptance) of the detector, smearing due to the finite resolution of the device in order to make a way for comparison with theoretical models and between experiments.

Due to the imperfect reconstruction and detection process, physical quantities reconstructed and computed are offset from their true values. The true and reconstructed variable quantities are then related through a migration matrix M_{ij}:

$$x_i = M_{ij} x_j. \tag{4.10}$$

The migration matrix is computed separately for each target and also for the combined targets in this thesis. The goal is to find the inverse of the M_{ij} called as an unfolding matrix:

$$x_j = M_{ji}^{-1} x_i. \tag{4.11}$$

Inverting the migration matrix is not direct and may introduce the statistical uncertainty in the reconstructed variable bins to inflate, hence large fluctuations. Also, directly inverting the matrix may introduce model dependence into the measurement. The complete description of the method used is in [75] and will be briefly summarized in the next section. As this is two dimensional analysis, the two pairs of variables selected for unfolding are Bjorken variable x, Inelastic y and Muon energy, hadronic energy. Another aspect to be careful with unfolding studies is the choice of the bin width. The unfolded distribution loses the sensitivity to the high-frequency components of the true distribution if the bin size is too large and if it is too small compared to resolution, the matrix will have large off diagonal elements. Hence, binning is chosen carefully by starting with a large bin size and then decreasing it in subsequent steps until the correlation between adjusted bins becomes too big. This procedure is valid for all the variables taken into account in this thesis except the Bjorken variable x_{bj} for which the bins are chosen based on the regions of the nuclear medium effects in DIS like shadowing ($0.01 < x_{bj} < 0.1$), anti-shadowing ($0.1 < x_{bj} < 0.3$) and the EMC effect ($0.3 < x_{bj} < 0.8$).

4.5.1 Procedure for Unfolding

The D'Agostini unfolding technique used by MINERvA is characterized as an algorithm for maximum-likelihood estimation with early stopping. The result of this technique is equivalent to an inversion of the matrix in the Gaussian limit when the algorithm converges. The bias is introduced due to uncertainties in the underlying theoretical models of our simulation because the unfolding is based on the Bayesian statistics. The matrix is calculated based on Bayes theorem [75]:

$$P(C_i|E) = \frac{P(C_i|E)\dot{P}(C_i)}{\Sigma_{l=1}^{n_e} P(E|C_i)\dot{P}(C_i)} \tag{4.12}$$

where, C$_i$ is the ith cause producing an effect E and represents the true kinematic variables, and the effect is the measured kinematic observable. The probability P (E|C_i), that an event is truly coming from a true bin i is reconstructed in bin j is same as M$_{ij}$ in Equation 4.10. This method can be used for several effects or several reconstructed variable bins:

$$P(C_i|E_j) = \frac{P(E_j|C_i)\dot{P}(C_i)}{\Sigma_{l=1}^{n_e} P(E_j|C_i)\dot{P}(C_i)} \tag{4.13}$$

where, the reconstructed variable bin j is represented by E$_j$. The unfolding should yield the number of events in each true bin $\hat{n}C_i$ or the reconstructed variable spectrum should yield the true spectrum. The events in each bin must be given by:

$$\hat{n}(C_i) = \Sigma_{j=1}^{N_j} P(E_j|C_i)\dot{n}(E_j)). \tag{4.14}$$

The following procedure is used to obtain $\hat{n}(C_i)$:

- Start with an initial guess at the unfolded distribution $P_0(C_i)$ subject to the following constraint:

  $$\Sigma_{j=1}^{N_j} = 1. \tag{4.15}$$

  In this analysis, the best intial guess at the spectrum is the true simulation distribution (true signal distribution). This guess also provides the initial expected number of events $\hat{n}_0 = P_0(C_i)\dot{N}_{obs}$.

- Obtain $\hat{n}(C_i)$ and $P(C_i)$.

- Do a χ^2 comparison between $\hat{n}(C_i)$ and $\hat{n}_0(C_i)$.

- Replace $P_0(C_i)$ with $P(C_i)$ and $\hat{n}_0(C_i)$ with $\hat{n}(C_i)$ and repeat the process again. Stop the interation if the $\chi^2 < 0.001$, otherwise repeat step 2.

There are various advantages to using the Bayesian method for unfolding over the other methods. The method is independent of the shape of the distribution being unfolded. The method provides a satisfactory result from a uniform initial distribution. Also, this method of unfolding does not require matrix inversion, which could be a problem if the matrix is singular. In order to cover the signal dependence, a systematic error will be assigned which is calculated by varying the migration matrix by changing systematics so uncertainties in the signal cross section are part of the final error. This technique will fail if M_{ij} is highly non-diagonal.

The migration matrix is built with the reconstructed simulation events that are truly DIS and truly originating from the measured target. For each target and material combination, the migration matrices are constructed from the reconstructed and true (generated) values of the combination of the variables like (x_{bj}, y), and (E_μ, E_{had}). Figure 4.10 shows the migration matrices for the Iron of nuclear target 1. The plots are included for four different combination of variables.

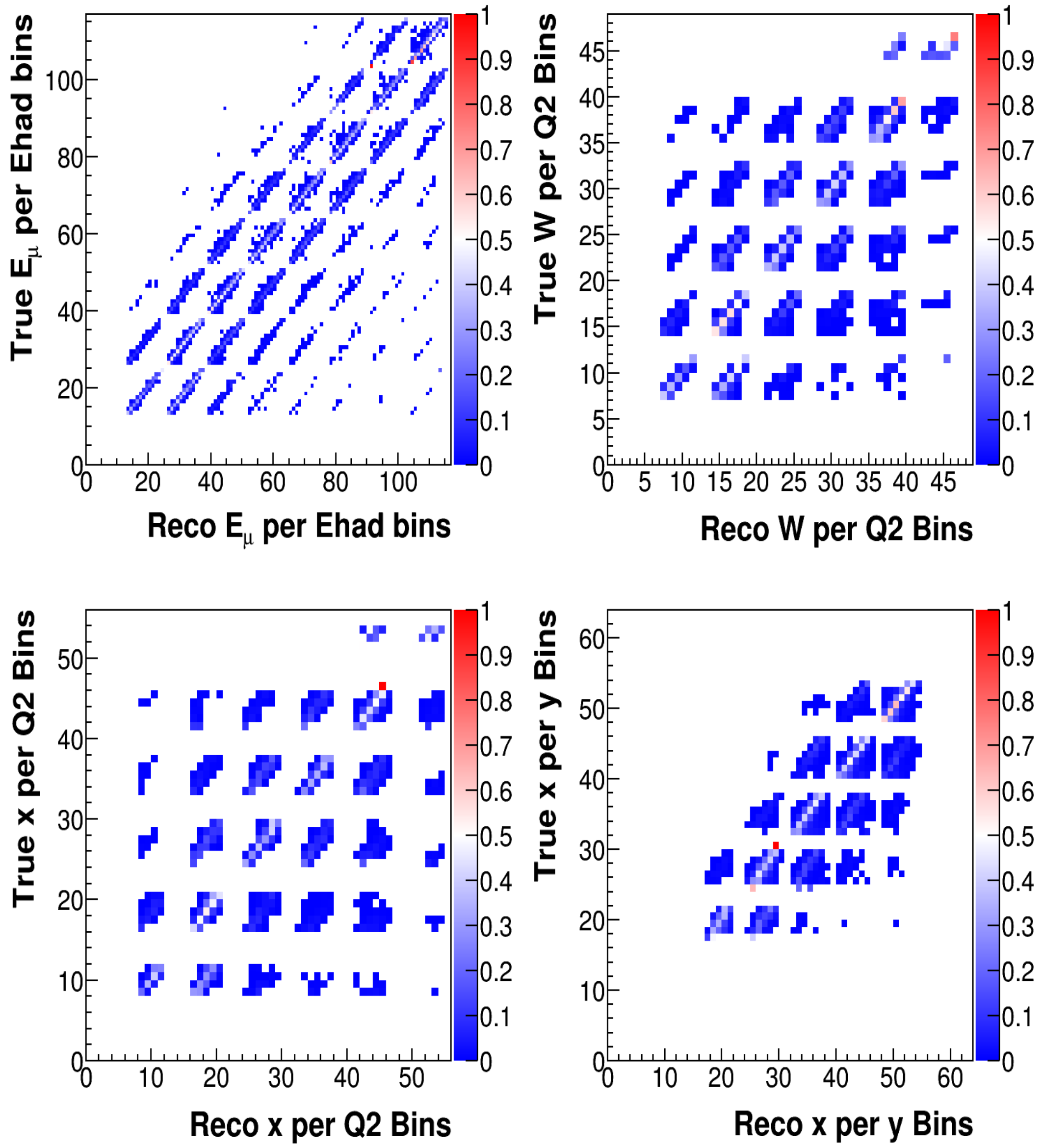

Figure 4.10: The migration matrices for different combination of variables. This panel is for the Iron of nuclear target 1. This shows the mapping of true and reconstructed events.

In order to unfold the matrix, the number of unfolded iterations is fixed using warping fake data studies discussed in the next section. The MinervaUnfold package with Bayesian unfolding is then used to unfold the reconstructed data from each target combination. The events that fill the migration matrix pass all the reconstruction cuts with true material as well as the true DIS cuts.

4.5.2 Warping studies

A fake data study, before the unfolding, is conducted to monitor for any biases and also to obtain the optimal number of unfolding iterations. The study uses the migration matrices reconstructed with the procedure described above and reweights the non-DIS background data tuned simulation. A sample of fake data is generated by re-weighting the simulation according to a re-weighting fit function f(x,y), which is obtained after fitting the data/simulation ratio in each bin. The complete procedure is given in [76]. The analysis presented in this thesis generates 100 universes and unfolds the fake data. The difference between the true number of events and mean unfolded events is calculated for each iteration. The mean tends to stay constant with the increase in the number of iterations. Increasing statistical uncertainty is introduced to the distribution with each successive iteration. The fake data study shows that using one iteration as a minimum number of iterations is sufficient to stabilize the unfolding.

4.5.3 Event yields before Unfolding

The present analysis measures the DIS events for the combination of the variables (x_{bj}, y) and (E_{μ}, E_{had}) for the different target nuclei like C, CH, Fe, and Pb after finalizing all selection cuts, the background estimations (CH and non-DIS) and unfolding. The event rate plots are included for the targets summed material-by-material. The contribution in the events for the Fe comes from the nuclear targets 1, 2, 3, 5, while for the Pb from nuclear targets 1, 2, 3, 4, and 5, for C events, come from nuclear target 3, and the CH from tracker modules 26 through 80. Figures 4.1, 4.2 and 4.3 show the DIS event distributions for C, Fe, and Pb as a function of reconstructed (x_{bj}, y) and (E_{μ}, E_{had}) before the background subtraction. In each case, the sample includes the non-DIS events and CH events, which are being estimated and will be subtracted in later stages of analysis. A systematic error band is included for each plot. There is a complete section for the discussion of the different systematic errors included in this thesis in Section 4.4.

4.6 Efficiency correction and Flux division

In order to convert the event yields to cross sections, the yields are divide by the overall efficiency, flux, and the number of targets.

The cuts used to separate the DIS sample are not able to reconstruct all the signal events and missed some of the signal events. Therefore, in order to recover the true signal distribution, efficiency correction is applied to the cross section calculation. Two true signal distributions are used to do the efficiency correction. The one distribution is the true distribution for all the signal events and the second is the true distribution for the reconstructed signal events. Simulation is used to calculate the efficiency as defined in the previous sections. The overall efficiency is defined as the ratio of the reconstructed events which pass the true DIS cuts, truly in a nuclear target A over the total number of events generated in that nuclear target A. For each nuclear target, there is a separate efficiency correction as a function of the combination of variables. Figures 4.11 shows the efficiencies for the Fe of nuclear target 1 for different combinations of the variables. Also, the efficiency plots for the Pb of nuclear target 1 are shown in Figure 4.12.

In order to calculate the total cross section, the flux must be averaged over

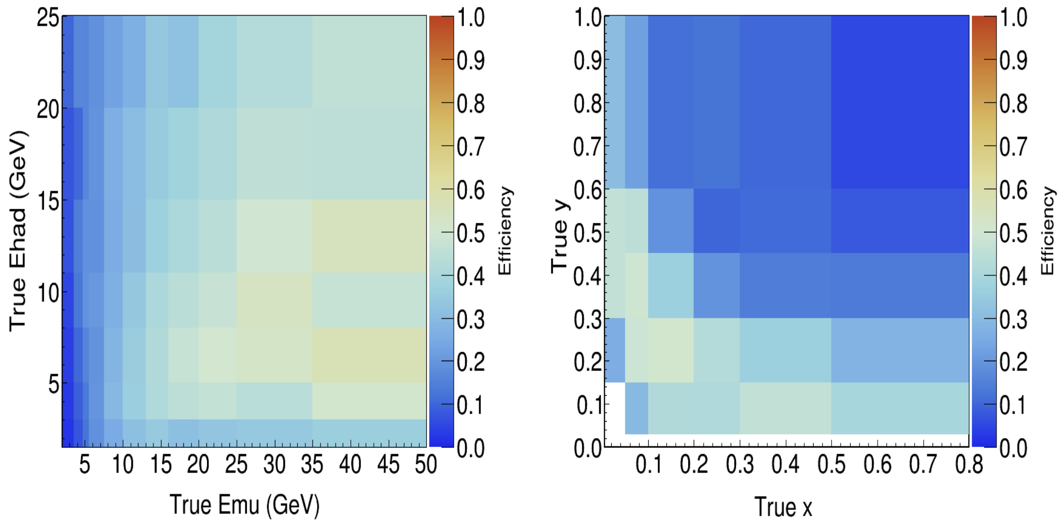

Figure 4.11: The efficiency plots for the Fe of nuclear target 1. The plots are for two combination of variables:(i) E_μ vs E_{had} and Bjorken variable x vs Inelasticity y.

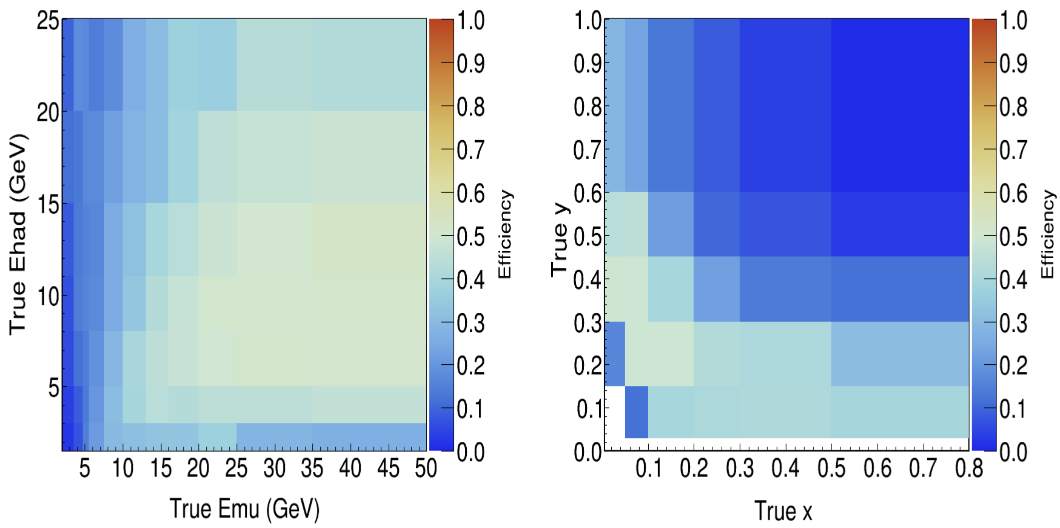

Figure 4.12: The efficiency plots for the Pb of nuclear target 1. The plots are for two combination of variables:(i) E_μ vs E_{had} and Bjorken variable x vs Inelasticity y.

each bin:

$$\sigma_{ij} = \frac{U_{ijk}\ (d_{ij} - b_{jk})}{\Delta_{ij}\ \epsilon_{ij}\ \Phi\ N} \tag{4.16}$$

The binning of the flux distribution is matched with the binning of the combination of the variables. For the the differential cross section, integrated flux in the range $2 \leq E_\nu < 120$ GeV is used for the measurement, and each bin is divided by its bin width (Δ_{ij}) to express the result in the proper units:

$$\left(\frac{d^2\sigma}{dxdy}\right)_{\alpha\beta} = \frac{\sum_{ij} U_{ij\alpha\beta}\left(N_{data,ij} - N_{ij}^{bkgd}\right)}{A_{\alpha\beta}(\Phi T)(\Delta x \Delta y)} \tag{4.17}$$

The other things which are to be taken care of are the normalization factors like flux normalization, the target number normalization, the bin width normalization and they appear in the denominator of the Equations 4.16 and 4.17. The cross section is calculated per nucleon. The calculation includes division by the number of nucleons inside the fiducial volume computed from the measured density of each material. The nucleon number is converted into a mass by multiplying the thickness of each target by the fiducial area.

4.7 Cross Section Results

4.7.1 Closure tests

The internal consistency of the analysis is validated through a procedure called a closure test. The analysis treats the analyzed simulation events as fake data and compares them with the truth values at different steps of analysis. The first test is done at the background estimation where a sample of reconstructed simulation events is used as fake data to estimate the non-DIS and plastic background and then compared with the true simulation distribution. Then, the second test is done at the background subtraction stage repeating the same process. The next test is done at the unfolding stage where the result of the unfolding is compared with the sample of truth distribution of events. Last step is done at the efficiency correction step where the fake data is efficiency corrected and compared with the truth distribution of sginal events. The closure test will be done for each combination of the variables like (x_{bj}, y) and (E_μ, E_{had}) and for all passive nuclear targets as well as for the tracker. The ratio between the simulation and the fake data should be close to one in each closure test.

4.7.2 Total Cross section

The cross section per nucleon is calculated for different passive nuclear targets like C, CH, Fe, and Pb. The data is compared to the simulation in each of the nuclear targets and in the tracker. The analysis is yet to reach the stage of completion, therefore, there are no plots included for the cross section measurements.

4.7.3 Differential Cross section

The differential cross section per nucleon as a function of (x_{bj}, y) is calculated for the nuclear targets C, Fe, and Pb and for the tracker CH. Similar to the previous measurement, the data is compared to the simulation for each nucleus.

Part III

INO Experiment

CHAPTER 5

DIFFERENCES IN OSCILLATION PARAMETERS AT THE INO-ICAL EXPERIMENT

5.1 Introduction

In the last few decades, neutrino oscillation experiments have provided many model independent evidences of neutrino oscillations. It all started in 1998 when Super-Kaimokande observed that the atmospheric muon neutrinos are changing flavor as they traverse through the atmosphere [77, 78]. In 2001, the Sudbury Neutrino Observatory experiment obtained direct evidence of a flavor change of solar neutrinos due to neutrino oscillations [79]. Next, the KamLand experiment observed the same effect with reactor neutrinos in 2002 [80]. There are now multiple next generation experiments aimed at studying neutrino oscillation using different neutrino sources. The neutrino oscillations within the three flavor framework are well established from solar, atmospheric and reactor neutrino experiments, and the oscillation parameters are getting measured with better precision. The evidence of non-zero masses of neutrinos establish the fact that the three flavors of neutrinos are mixed. In the three-flavor oscillation paradigm, neutrino mixing can be described by a 3×3 unitary mixing matrix known as Pontecorvo-Maki-Nakagawa-Sakata (PMNS) matrix [25, 81]. The three flavor eigenstates of neutrinos are mixtures of three mass eigenstates according to the PMNS matrix. Under the standard parameterization of PMNS matrix, the neutrino oscillation probabilities are defined in terms of three mixing angles θ_{12}, θ_{23}, θ_{13}; two mass-squared differences Δm^2_{21}, Δm^2_{32} and a Dirac CP-violation phase δ_{CP}. The current best fit values and errors in these oscillation parameters on the basis of global neutrino analysis is given in Table 1 of Ref. [82]. The resulting oscillation probabilities depend on these oscillation parameters (mixing angles and mass squared differences). For a given neutrino of energy E_ν and the propagation length L, the survival probability for ν_μ is given by

$$P(\nu_\mu \to \nu_\mu) \simeq 1 - 4\cos^2\theta_{13}\sin^2\theta_{23} \times [1 - \cos^2\theta_{13}\sin^2\theta_{23}]\sin^2\left(\frac{1.267|\Delta m^2_{32}|L}{E_\nu}\right), \tag{5.1}$$

and similarly the survival probability for $\overline{\nu}_\mu$ is given by

$$P(\overline{\nu}_\mu \to \overline{\nu}_\mu) \simeq 1 - 4\cos^2\overline{\theta}_{13}\sin^2\overline{\theta}_{23} \times [1 - \cos^2\overline{\theta}_{13}\sin^2\overline{\theta}_{23}]\sin^2(\frac{1.267|\Delta\overline{m^2}_{32}|L}{E_{\overline{\nu}}}), \tag{5.2}$$

where the symbols $(|\Delta\overline{m^2}_{32}|, \overline{\theta}_{13}, \overline{\theta}_{23})$ are used for the respective parameters for the anti-neutrino oscillations.

In the Standard Model (SM) of particle physics, the parameters for particles and antiparticles are identical because of CPT symmetry. Hence, under the CPT symmetry, the mass splittings and mixing angles are identical for neutrinos and anti-neutrinos, implying $P(\nu_\mu \to \nu_\mu) = P(\overline{\nu}_\mu \to \overline{\nu}_\mu)$. Any inequality between these disappearance probabilities of neutrinos and antineutrinos could, therefore, provide a hint for new physics. Also, any difference between the parameters governing the oscillation probabilities of neutrinos and antineutrinos could provide a possible hint for CPT violation. We investigate the prospects for the measurement of such a difference in $|\Delta m^2_{32}|$ and $|\Delta\overline{m^2}_{32}|$ in Iron-Calorimeter (ICAL) experiment at the India-based Neutrino Observatory (INO) [83, 84]. Similar work has been carried out by MINOS [85] and Super-Kamiokande [86] experiments. However, we show the INO-ICAL experimental sensitivity for the difference in $|\Delta m^2_{32}|$ and $|\Delta\overline{m^2}_{32}|$ irrespective of the theoretical mechanism responsible for the difference in the neutrino and antineutrino parameters.

The INO-ICAL experiment is an atmospheric neutrino experiment meant to study neutrino oscillations with muon disappearance channel. The ICAL experiment is sensitive to the atmospheric muon type neutrinos and antineutrinos through their interactions with the iron target producing muons and hadrons via the Charged Current (CC) interactions. The ν_μ and $\overline{\nu}_\mu$ particles are identified by the production of μ^- and μ^+, respectively, through their CC interaction ($\nu_\mu(\overline{\nu}_\mu) + X \to \mu^-(\mu^+) + X'$). The energy and direction of the incoming neutrinos/antineutrinos have to be measured accurately for the precise measurement of oscillation parameters. The energy and direction of these interacting neutrinos/antineutrinos can be determined from the reconstructed energy and direction of muons and hadrons. The muons deposit their energy in iron target forming a clear track-like pattern while hadrons form a shower-like pattern. Further details of the INO-ICAL experiment are provided in Sec. 5.2.

In this Chapter, we present the sensitivity of separate measurement of neutrino and antineutrino oscillation parameters. The INO-ICAL detector has a unique ability to distinguish between μ^- and μ^+ events with their bendings in a magnetic field, and hence can easily separate neutrinos and antineutrinos. Earlier ICAL analysis has shown its potential for measurement of oscillation parameters and mass hierarchy with combined neutrino and anti-neutrino events [87, 88, 89, 90]. The reach of INO-ICAL experiment for CPT violation has also been studied in the literature [91, 92]. Here, we will analyze neutrino and antineutrino events separately and compare their oscillation parameters in order to find any signature of new physics including CPT violation [93, 94].

The analysis is performed with the construction of a χ^2 function with 3D binning in muon energy, muon direction and hadron energy [Sec. 5.3.1]. We calculate

χ^2 for neutrinos and antineutrinos separately and minimize it to constraint the experimental parameter spaces ($|\Delta m^2_{32}|$, θ_{23}) and ($|\Delta\overline{m^2}_{32}|$, $\overline{\theta}_{23}$) [Sec. 5.3.2] assuming that the true parameters of ν_μ and $\overline{\nu}_\mu$ are identical. Next, we study the possibility that the true values of $|\Delta m^2_{32}|$ and $|\Delta\overline{m^2}_{32}|$ can be different. In Sec. 5.3.3, we consider 4 theoretical scenarios when $|\Delta m^2_{32}|$ and $|\Delta\overline{m^2}_{32}|$ take different set of values in order to obtain the $\Delta\chi^2$ contours for different experimental values of $|\Delta m^2_{32}|$ and $|\Delta\overline{m^2}_{32}|$. This gives us the INO-ICAL sensitivity in the ($|\Delta m^2_{32}|$-$|\Delta\overline{m^2}_{32}|$) parameter space for these hypothetical scenarios.

The main aim of the work is to find the sensitivity of INO-ICAL for the measurement of the difference ($|\Delta m^2_{32}| - |\Delta\overline{m^2}_{32}|$). If the true values of the $|\Delta m^2_{32}|$ and $|\Delta\overline{m^2}_{32}|$ are different, at what confidence level the null hypothesis i.e. $|\Delta m^2_{32}|$=$|\Delta\overline{m^2}_{32}|$, can be ruled out? This is addressed in Sec. 5.3.4.

In this chapter, we have demonstrated the potential of INO-ICAL for the separate measurement of ν_μ and $\overline{\nu}_\mu$ oscillation parameters.

5.2 The INO experiment

After the proposal of neutrinos by Pauli, Bethe and Pierels calculated the neutrino interaction cross section to be of the order of 10^{-44} cm^2. With this small cross section, in order to observe neutrinos directly in an experiment very high flux of neutrinos or very large detectors were required. At that time it was difficult to construct such huge detectors. However, in the year 1953 Reines and Cowan [95, 96], as well as Davis and collaborators [97] in 1964, tried to observe neutrino experimentally in the reactor and solar neutrinos, respectively. For the first time, the observation of the neutrino events coming from the cosmic ray interactions with the earth's atmosphere at the Kolar Gold Field (KGF), some 50 years back, encouraged the Indian scientific community to explore the field of neutrino oscillations. The KGF was a deep underground laboratory situated at about 870m above sea level near the city of Bangalore in South India and provides a depth of around 3000 m below the surface of the earth to carry out the experiments. The neutrino experiments in the KGF mine were conducted by a collaboration consisting of groups from Durham University (UK), Osaka City University (Japan) and TIFR in India. The laboratory which was setup in KGF mines later put up an experiment to investigate proton decay. Unfortunately, the KGF mines were closed and there was a brief halt in the progress of neutrino research in India. But the Indian scientific community never stopped and kept looking for another option to keep neutrino research going. With the immense efforts of the many scientists and institutions, the proposal was put forward to perform the underground neutrino studies under the name India-based Neutrino Observatory (INO), and it was approved by the government of India. A large number of scientists from many institutions and universities are a part of the INO collaboration and are growing further. In this section, we will explain some salient features of the INO facility and then introduce the Iron Calorimeter detector, which will be used by the INO experiment.

INO, an approved mega-science project, will be built underground to study the atmospheric neutrino oscillations. The present location of the facility is Pottipuram in Bodi West hills in the Theni district of South India. The facility will host a huge 50 kiloton Iron Calorimeter (ICAL) detector with the magnetized iron target as the main detector and several small experiments like neutrinoless double beta decay (NDBD) and dark matter searches (DINO). One of the important features of the INO facility is that the ICAL detector will be protected from the cosmic background by a 1 km rock overburden above the site acting as a natural shield. In order to access the INO facility, there is a 2100 m long and 7.5 m wide tunnel. The schematic of the INO facility and its location is shown in the Figure 5.1. Initially, INO was planned to carry out the studies related to the atmospheric neutrinos but the scope of looking at solar and supernova studies can't be ruled out. Also, the ICAL detector can act as the far detector for the neutrinos coming from the accelerators situated in Japan and LHC in CERN.

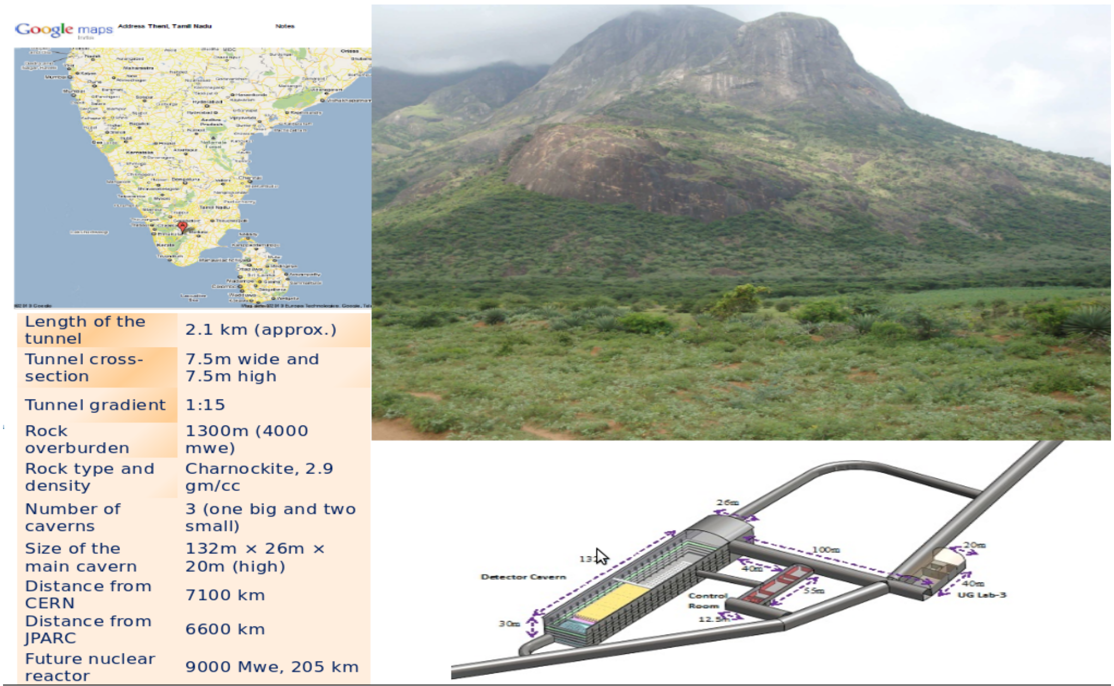

Length of the tunnel	2.1 km (approx.)
Tunnel cross-section	7.5m wide and 7.5m high
Tunnel gradient	1:15
Rock overburden	1300m (4000 mwe)
Rock type and density	Charnockite, 2.9 gm/cc
Number of caverns	3 (one big and two small)
Size of the main cavern	132m × 26m × 20m (high)
Distance from CERN	7100 km
Distance from JPARC	6600 km
Future nuclear reactor	9000 Mwe, 205 km

Figure 5.1: The location and the schematic of the INO experiment.

5.2.1 The ICAL experiment

The INO laboratory will host a large magnetised Iron Calorimeter detector to study the atmospheric neutrinos and antineutrinos and may reveal many unsolved mysteries in the weak interactions. The schematic design of the ICAL detector is shown in the Figure 5.2.

The ICAL detector will be rectangular with dimensions of 48m $\times$ 16m $\times$ 14.5m having three modules. Each module weighs about 17 kiloton with the dimensions 16m $\times$ 16m $\times$ 14.5m in x, y, and z-direction, respectively. Each module will consist of 151 layers of 5.6 cm thick iron plates with alternate gaps of 4 cm where the active detector element will be placed. The ICAL experiment will use Resistive Plate Chambers (RPCs) as active detector elements to detect the charged particles produced in the neutrino interaction with the iron nuclei. Since the INO experiment is expected to take data for several years to collect a statistically significant number of interactions, the RPC's are a good choice because of their long lifetime[20].

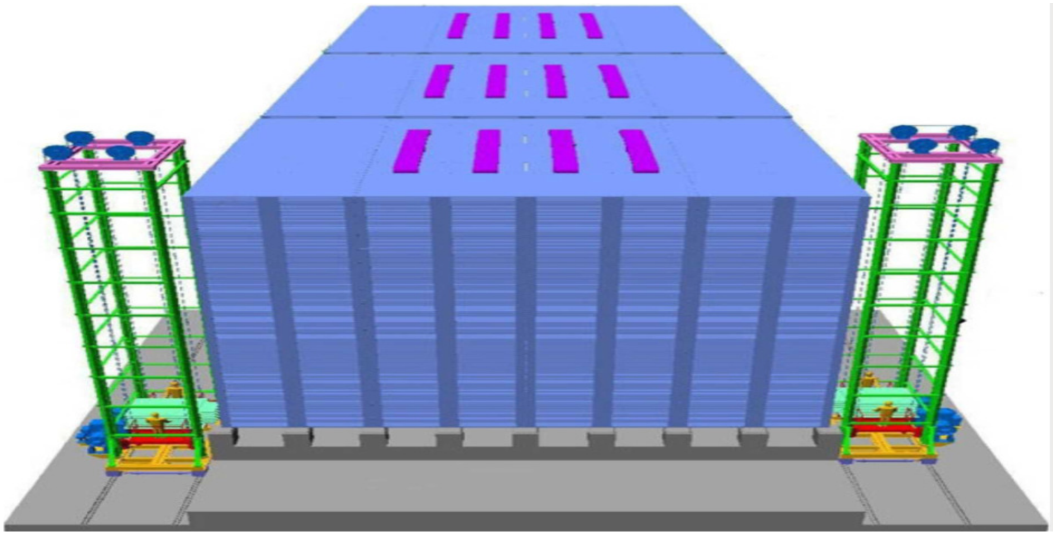

Figure 5.2: The schematic view of the ICAL detector.

Also, RPC's are gaseous detectors hence have good spatial and time resolution. The RPC's will give (X, Y) hit information with 0.96 cm spatial resolution. There will be a total of 30,000 RPC's of dimension 2m $\times$ 2m in the ICAL detector. Another important feature of the INO-ICAL experiment is the application of a magnetic field of 1.5 T uniformly applied throughout the detector that will help in distinguishing the charge of the interacting particles. Due to this magnetic field, the ICAL detector can distinguish μ^+ and μ^- by bending their tracks in opposite directions which may lead to pure neutrino and antineutrino event samples. This distinction is crucial for the precise determination of the relative ordering of neutrino mass states (neutrino mass hierarchy) and other parameters. There will be an external layer of scintillator or gas proportional counters which will be used for the identification of the external muons entering the detector from outside. The magnetic field will enable to estimate the momentum of the particle by using the curvature of the charged particle's track. The precision in the measurement of the momentum of the particle improves with the increasing magnetic field. For better performance, the design of the ICAL magnet is made in such a way that there will be uniform magnetic field inside the detector and minimal field leakage outside.

The INO-ICAL experiment is sensitive to atmospheric muons only. Hence, it will observe interactions of muon type neutrinos. The detector is not suitable for the detection of electrons because of the large thickness of iron plates (5.6 cm) compared to the radiation length of iron (17.6 cm). Also, tau lepton production is limited because of the high threshold of tau production (4 GeV). The ICAL experiment will also measure the energy of hadron shower to improve the energy reconstruction of events, and hence the overall sensitivity to neutrino parameters[98, 89].

The INO-ICAL resolutions for muon energy and direction as well as hadron energy are available from the GEANT4 [67] simulation studies [99, 100]. The simulation studies provide us a reasonable characterization of the detector.

5.3 Analysis procedure

The magnetized ICAL detector is primarily designed to differentiate the neutrino and anti-neutrino interactions of atmospheric muon neutrinos with excellent charge identification [99]. Since the events at ICAL can easily be separated into samples of ν_μ and $\overline{\nu}_\mu$, they can be used to study oscillations separately in neutrinos and anti-neutrinos. We exploit this feature of ICAL experiment to measure the oscillation parameters independently using ν_μ and $\overline{\nu}_\mu$ events assuming $|\Delta m^2_{32}| = |\Delta\overline{m^2}_{32}|$. Next, we explore the ICAL ability to find out any non-zero difference in the atmospheric mass squared differences of neutrinos and antineutrinos i.e. $|\Delta m^2_{32}| - |\Delta\overline{m^2}_{32}|$.

For performing the analysis, we generated the atmospheric neutrino data set using Honda et al.[101] 3-D neutrino flux with ICAL detector specifications using NUANCE event generator [102]. For final χ^2 analysis, 1000 years equivalent data of 50kt ICAL detector has been scaled down to 10 years exposure to normalize the statistical fluctuations. The ICAL detector is highly sensitive for the CC interactions of ν_μ and $\overline{\nu}_\mu$ events in the energy range 0.8-12.8 GeV. Therefore, full

Muon energy bins ($E_{\mu^\pm}$ in GeV)	Range	Bin width
12	0.8-4.8	0.34
4	4.8-6.8	0.5
3	6.8-9.8	1
1	9.8-12.8	3
Hadron energy bins (E_{hadron} in GeV)		
2	0.0-2.0	1
2	2.0-8.0	3
1	8.0-13	5
Muon angle bins ($\cos\theta_{\mu^\pm}$)		
20	-1 - +1	0.1

Table 5.1: Optimized 3D binning scheme used for analyses.

event spectrum comprises the CC ν_μ (and $\overline{\nu}_\mu$) events coming from $\nu_\mu(\overline{\nu}_\mu) \to \nu_\mu(\overline{\nu}_\mu)$ survival channel and from $\nu_e(\overline{\nu}_e) \to \nu_\mu(\overline{\nu}_\mu)$ oscillation channel. Initially, each event is generated without introducing oscillations, to reduce the computational time. The effect of oscillations has been incorporated separately using the Monte Carlo re-weighting algorithm described in earlier studies [88, 90, 89]. For each neutrino/antineutrino event of a given energy (E_ν or $E_{\overline{\nu}}$) and zenith direction θ_z, three flavor oscillation probabilities are calculated taking earth matter effects into account. The matter density profile of the Earth is taken from the Preliminary Reference Earth Model [103], which divides the earth into several layers according to their matter densities.

In order to introduce the detector effects, we use the realistic detector resolutions and efficiencies of the ICAL detector based on GEANT4 simulations. The reconstruction of a neutrino (or anti-neutrino) event requires the measurement of the secondary particles like muons (or anti-muon) and hadrons. The muons give a clear track of hits inside the magnetized detector. Therefore, the energy of these particles can be easily reconstructed using a track fitting algorithm. The complete details of ICAL response for μ^+ or μ^- e.g. energy and direction resolutions, reconstruction and charge identification efficiencies are available in Ref [99]. The ICAL has an excellent charge identification efficiency (more than 98%) and good direction resolution for muons ($\sim 1^\circ$) in the energy region of interest. Hadrons deposit their energies in a shower like pattern in the detector. So, total energy deposited by the hadron shower ($E'_{had} = E_\nu - E_\mu$) is used to calibrate the detector response. The details of energy resolution and efficiency for hadrons at ICAL can be found in Ref [100].

5.3.1 The χ^2 Function

The oscillation parameters of the atmospheric neutrinos have been extracted with a χ^2 analysis. The re-weighted events, with detector resolutions and efficiencies folded in, are binned into the observed muon energy, muon direction, and hadron energy. An optimized bin width has been used for these observables to get statistically significant event rates. The data has been divided into a total of 20 muon energy bins and 5 hadron energy bins with varying bin widths. A total of 20 muon direction bins for $\cos\theta_\mu$ in the range of -1 to 1, with equal bin width, has been chosen. The above mentioned binning scheme is applied for both ν_μ and $\overline{\nu}_\mu$ events. The details of the binning scheme are shown in Table 5.1.

A "pulled" χ^2 [104] method based on Poisson probability distribution is used to compare the expected and observed data with the inclusion of systematic errors. Five systematic errors used in the analysis are: a 20% error on atmospheric neutrino flux normalization, 10% error on neutrino cross section, an overall 5% statistical error, a 5% uncertainty due to zenith angle dependence of the fluxes, and an energy dependent tilt error, as considered in earlier ICAL analyses [88, 89].

In the method of pulls, systematic uncertainties and the theoretical errors are parameterized in terms of a set of variables ζ, called pulls. Due to the fine binning,

Oscillation parameters	True values	Marginalization range
$\sin^2(2\theta_{12})$	0.86	Fixed
$\sin^2(\theta_{23})$	0.5	0.4-0.6
$\sin^2(\theta_{13})$	0.0234	Fixed
Δm^2_{21} (eV^2)	7.6×10^{-5}	Fixed
$\|\Delta m^2_{32}\|$ (eV^2)	2.4×10^{-3}	(2.1-2.6) $\times 10^{-3}$
δ	0.0	Fixed

Table 5.2: True values of the neutrino oscillation parameters used in the analysis. We vary $\sin^2\theta_{23}$ and $|\Delta m^2_{32}|$ in their 3σ range whereas the other variables are kept fixed.

some bins may have very small number of entries. Therefore, we use the Poissonian definition of χ^2 given as

$$\chi^2(\nu_\mu) = min \sum_{i,j,k} \left(2(N^{th'}_{ijk}(\nu_\mu) - N^{ex}_{i,j,k}(\nu_\mu)) + 2N^{ex}_{i,j,k}(\nu_\mu)(\ln \frac{N^{ex}_{i,j,k}(\nu_\mu)}{N^{th'}_{i,j,k}(\nu_\mu)}) \right) + \sum_n \zeta_n^2, \tag{5.3}$$

where

$$N^{th'}_{ijk}(\nu_\mu) = N^{th}_{i,j,k}(\nu_\mu) \left(1 + \sum_n \pi^n_{ijk}\zeta_n \right). \tag{5.4}$$

Here, N^{ex}_{ijk} are the observed number of reconstructed events, generated using true values of the oscillation parameters in i^{th} muon energy bin, j^{th} muon direction bin and k^{th} hadron energy bin. In Eq.(6.5), N^{th}_{ijk} are the number of theoretically predicted events generated by varying oscillation parameters, $N^{th'}_{ijk}$ show modified events spectrum due to different systematic uncertainties, π^n_{ijk} are the systematic shift in the events of the respective bins due to n^{th} systematic error. The variable ζ_n, the univariate pull variable, corresponds to the π^n_{ijk} uncertainty. An expression similar to Eq.(6.4) can be obtained for $\chi^2(\overline{\nu}_\mu)$ using reconstructed μ^+ event samples.

The functions $\chi^2(\nu_\mu)$ and $\chi^2(\overline{\nu}_\mu)$ are calculated separately for the independent measurement of neutrino and anti-neutrino oscillation parameters. The two χ^2

can be added to get the combined $\chi^2(\nu_\mu + \overline{\nu}_\mu)$ as

$$\chi^2(\nu_\mu + \overline{\nu}_\mu) = \chi^2(\nu_\mu) + \chi^2(\overline{\nu}_\mu). \tag{5.5}$$

5.3.2 Same True oscillation parameters for neutrinos and antineutrinos

We investigate the scenario where the neutrino and antineutrino oscillations are different. However, we begin with the case where neutrinos and antineutrinos have identical oscillation parameters ($|\Delta m^2_{32}| = |\Delta\overline{m^2}_{32}|$, $\sin^2\theta_{23} = \sin^2\overline{\theta}_{23}$). The central true values of the oscillation parameters and their marginalization range used in the analysis are shown in Table 5.2. The χ^2 have been calculated as the function of the atmospheric oscillation parameters ($|\Delta m^2_{32}|$ and $\sin^2\theta_{23}$) while all other oscillation parameters are kept fixed at their central values. The solar oscillation parameters Δm^2_{21} and $\sin^2\theta_{12}$ are fixed as they do not show significant impact on the results. Since θ_{13} is now known quite precisely, it has been kept fixed as well. Since, ICAL is not sensitive to the δ_{CP} [105], it is kept fixed at 0°.

In order to obtain the experimental sensitivity for $\sin^2\theta_{23}$ and $|\Delta m^2_{32}|$, we independently minimize the $\chi^2(\nu_\mu)$, $\chi^2(\overline{\nu}_\mu)$ and combined $\chi^2(\nu_\mu + \overline{\nu}_\mu)$ function by varying oscillation parameters within their allowed ranges with all systematic uncertainties folded in. The precision on the oscillation parameters can be defined as the ratio of $(P_{max} - P_{min})$ to the $(P_{max} + P_{min})$, where P_{max} and P_{min} are the maximum and minimum values of the concerned oscillation parameters at the given confidence level.

Figure5.3 shows the resulting contours at 3σ confidence level (C.L.) obtained for the ($|\Delta m^2_{32}|$, $\sin^2\theta_{23}$) or ($|\Delta\overline{m^2}_{32}|, \sin^2\overline{\theta}_{23}$) planes. These results are also compared with combined results of neutrino and antineutrino events.

Table 5.3 shows the precision values at the 3σ C.L. obtained from neutrino

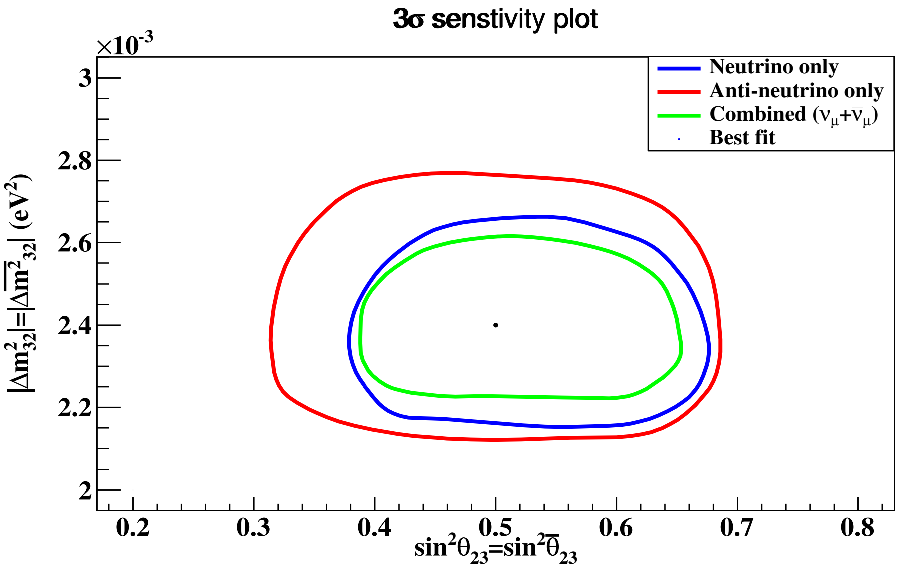

Figure 5.3: The 3σ sensitivity plot on ($\sin^2\theta_{23}$=$\sin^2\overline{\theta}_{23}$, $|\Delta m^2_{32}|$=$|\Delta\overline{m^2}_{32}|$) parameter space from the χ^2 analyses separately for neutrino only events, antineutrino only events and combined neutrino and antineutrino ($\nu_\mu + \overline{\nu}_\mu$) events

only events, anti-neutrino only events and with the combined ($\nu_\mu + \overline{\nu}_\mu$) events. It can be observed that combined ν_μ and $\overline{\nu}_\mu$ analysis gives more precise values of the oscillation parameters, as expected. The major contribution to this precision comes from the higher statistics of the combined neutrino events. However, the ICAL detector can also measure $|\Delta m^2_{32}|$ very precisely from neutrino and antineutrino events, separately. It can be noted that the allowed parameter space of anti-neutrino analysis is wider than the neutrino only events analysis due to their

Analysis	$\sin^2\theta_{23}$	$\lvert\Delta m^2_{32}\rvert$ (eV^2)
Neutrino events	27.1%	10.4%
Anti-neutrino events	38.0%	13.4%
Combined($\nu_\mu + \overline{\nu}_\mu$)	25.0%	8.3%

Table 5.3: Precision values at the 3σ C.L. considering $\sin^2\theta_{23} = \sin^2\overline{\theta}_{23}$ and $|\Delta m^2_{32}|$=$|\Delta\overline{m^2}_{32}|$ (eV^2) obtained from neutrino only events, anti-neutrino only events and with the combined ($\nu_\mu + \overline{\nu}_\mu$) events.

low statistics.

5.3.3 Different True values of $|\Delta m^2_{32}|$ and $|\Delta\overline{m^2}_{32}|$

The INO has good sensitivity to $|\Delta m^2_{32}|$ as compared to θ_{23} [Table 6.3]. This better sensitivity for $|\Delta m^2_{32}|$ motivates us to examine a scenario when true values of $|\Delta m^2_{32}|$ and $|\Delta\overline{m^2}_{32}|$ are different while true values of θ_{23} and $\overline{\theta}_{23}$ are identical. Using better analysis techniques, the INO's sensitivity to θ_{23} can be utilized for studying a scenario when θ_{23} is different for neutrinos and antineutrinos. However, in this section, we demonstrate the INO's good ability to differentiate between $|\Delta m^2_{32}|$ and $|\Delta\overline{m^2}_{32}|$ only. The present analysis will allow us to either establish or rule out the hypothesis that neutrinos and antineutrinos have same true value of $|\Delta m^2_{32}|$.

In this analysis we assume that neutrinos and antineutrinos have different true values of mass squared differences ($|\Delta m^2_{32}|$, $|\Delta\overline{m^2}_{32}|$), whereas θ_{23} and $\bar{\theta}_{23}$ are kept fixed at 45°. All other oscillation parameters are the same as in the previous section. We take different representative cases of the true values of $|\Delta m^2_{32}|$ and $|\Delta\overline{m^2}_{32}|$ and estimate χ^2 as a function of the $|\Delta m^2_{32}|$ and $|\Delta\overline{m^2}_{32}|$. For each case, the true values of all oscillation parameters are fixed and $\chi^2(\nu + \overline{\nu})$ have been estimated as a function of observed values of $|\Delta m^2_{32}|$ and $\Delta\overline{m^2}_{32}|$. The χ^2 contours at 68%, 90% and 99% C.L. have been plotted on the ($|\Delta m^2_{32}|$, $|\Delta\overline{m^2}_{32}|$) parameter space. The straight line corresponding to the null hypothesis ($|\Delta\overline{m^2}_{32}|$=$|\Delta m^2_{32}|$) is also shown. If the null hypothesis line is nσ away from the χ^2 minimum, it can be concluded that the null hypothesis ($|\Delta\overline{m^2}_{32}|$=$|\Delta m^2_{32}|$) is ruled out at n$\sigma$ C.L. The four plots in Figure 5.4 correspond to the true values of $|\Delta m^2_{32}|$ and $|\Delta\overline{m^2}_{32}|$ as shown in Table 5.4.

Figure 5.4(a) shows the contours when the true values of $|\Delta m^2_{32}|$ and $|\Delta\overline{m^2}_{32}|$ are exactly equal (i.e. $|\Delta m^2_{32}| - |\Delta\overline{m^2}_{32}| = 0$). In this case, the null hypothesis

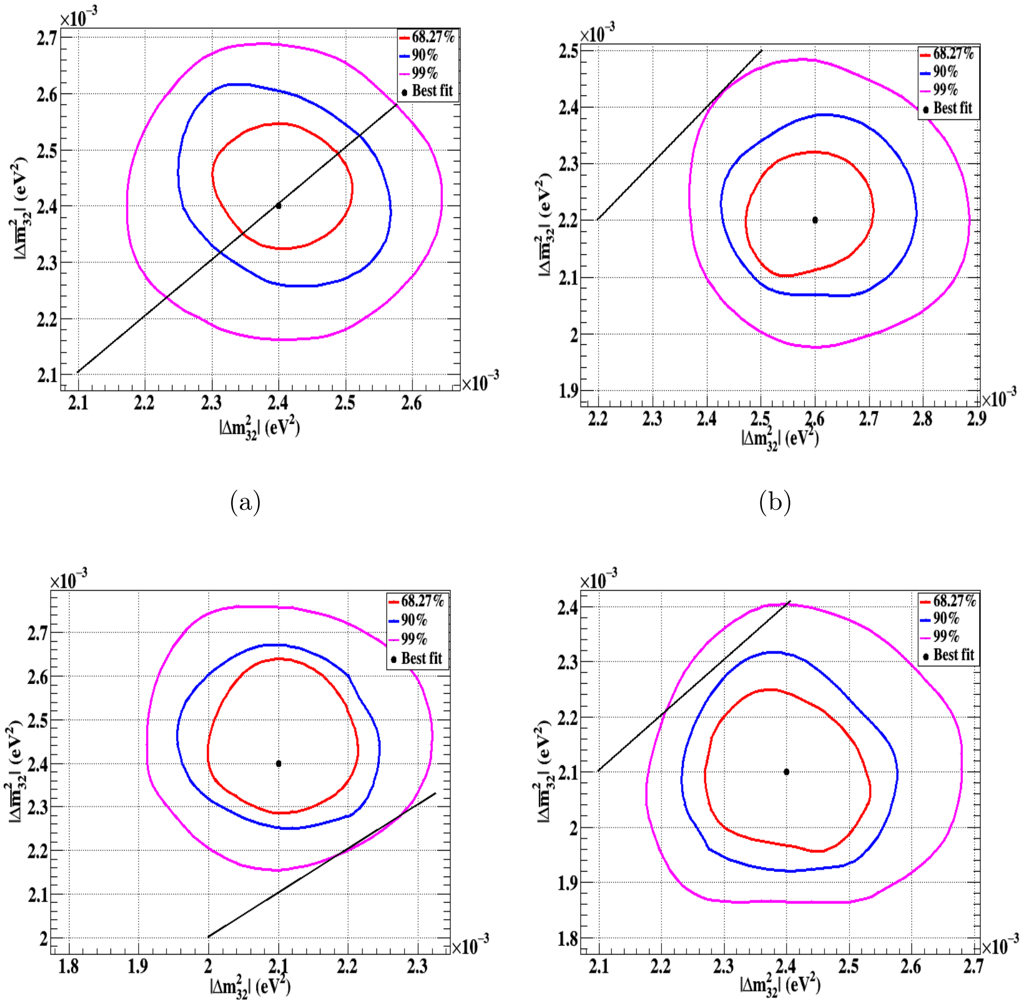

(a) (b)

(c) (d)

Figure 5.4: Contour plots at 68%, 90% and 99% C.L. for different true values of $|\Delta m^2_{32}|$ and $|\Delta\overline{m^2}_{32}|$ as mentioned in Table 5.4. Here, X-axis corresponds to $|\Delta m^2_{32}|$ values and Y-axis corresponds to $|\Delta\overline{m^2}_{32}|$ values.

line (solid black line) crosses the central best fit point. In Figure 5.4(b), 5.4(c) and 5.4(d) the difference (i.e. $|\Delta m^2_{32}| - |\Delta\overline{m^2}_{32}|$) is non-zero, and hence the best fit point shifts away from the null hypothesis line. Figure5.4(b) correspond to the case when true values of $|\Delta m^2_{32}| = 2.6\times10^{-3}eV^2$ and $|\Delta\overline{m^2}_{32}| = 2.2\times10^{-3}eV^2$ (i.e. $|\Delta m^2_{32}| - |\Delta\overline{m^2}_{32}| = 0.4\times10^{-3}eV^2$). Here, the null hypothesis line is tangential to 3σ contour. So, the tangential point is 3σ away from the central best fit value. Thus, it can be concluded that null hypothesis is ruled out at 3σ C.L. Similarly,

Fig2.No.	$\lvert\Delta m^2_{32}\rvert$ (eV^2)	$\lvert\Delta\overline{m^2}_{32}\rvert$ (eV^2)	$\lvert\Delta m^2_{32}\rvert$-$\lvert\Delta\overline{m^2}_{32}\rvert$ (eV^2)
(a)	2.4×10^{-3}	2.4×10^{-3}	0.0×10^{-3}
(b)	2.6×10^{-3}	2.2×10^{-3}	0.4×10^{-3}
(c)	2.1×10^{-3}	2.4×10^{-3}	-0.3×10^{-3}
(d)	2.4×10^{-3}	2.1×10^{-3}	$+0.3\times10^{-3}$

Table 5.4: Different combinations of $|\Delta m^2_{32}|$ and $|\Delta\overline{m^2}_{32}|$ values used in Fig 6.5.

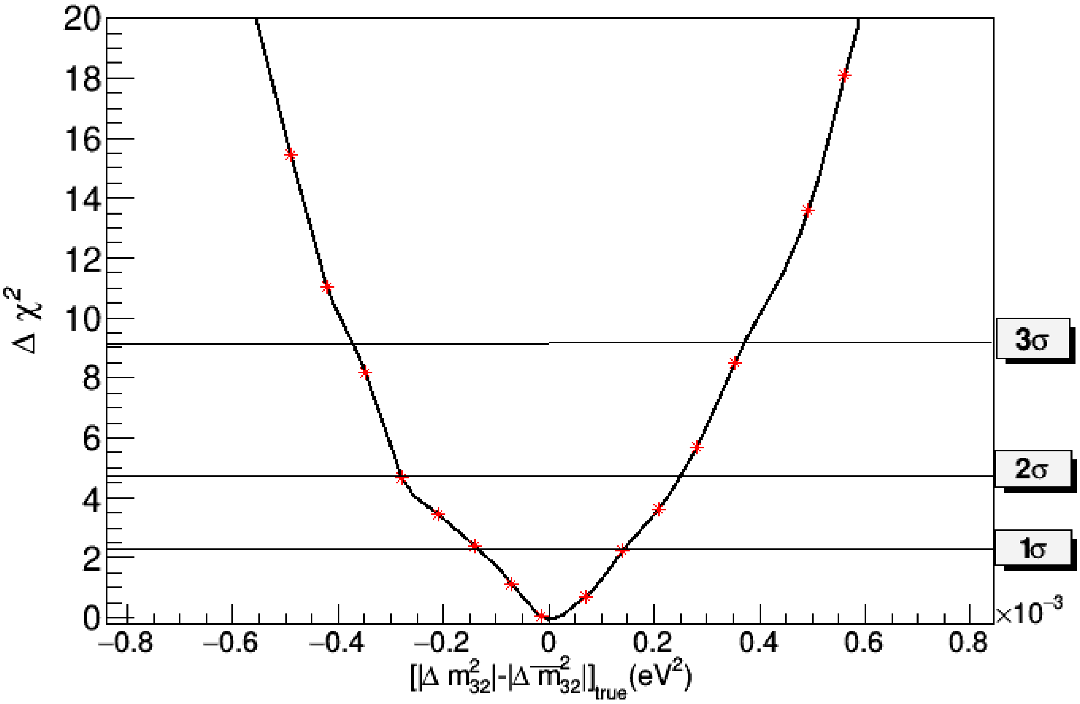

Figure 5.5: The INO-ICAL sensitivity for $(|\Delta m^2_{32}| - |\Delta\overline{m^2}_{32}|)_{True}(eV^2)$ at 1σ, 2σ and 3σ confidence levels.

Figure 5.4(c) shows that null hypothesis is tangential to 3σ CL when true values of $|\Delta m^2_{32}| = 2.1\times10^{-3}eV^2$ and $|\Delta\overline{m^2}_{32}| = 2.4\times10^{-3}eV^2$ (i.e. $|\Delta m^2_{32}| - |\Delta\overline{m^2}_{32}| = -0.3\times10^{-3}eV^2$). Figure 5.4(d) shows that the null hypothesis could be ruled out at roughly 2.5σ CL when true value of $|\Delta m^2_{32}| = 2.4\times10^{-3}eV^2$ and $|\Delta\overline{m^2}_{32}| = 2.1\times10^{-3}eV^2$ (i.e. $|\Delta m^2_{32}| - |\Delta\overline{m^2}_{32}| = +0.3\times10^{-3}eV^2$).

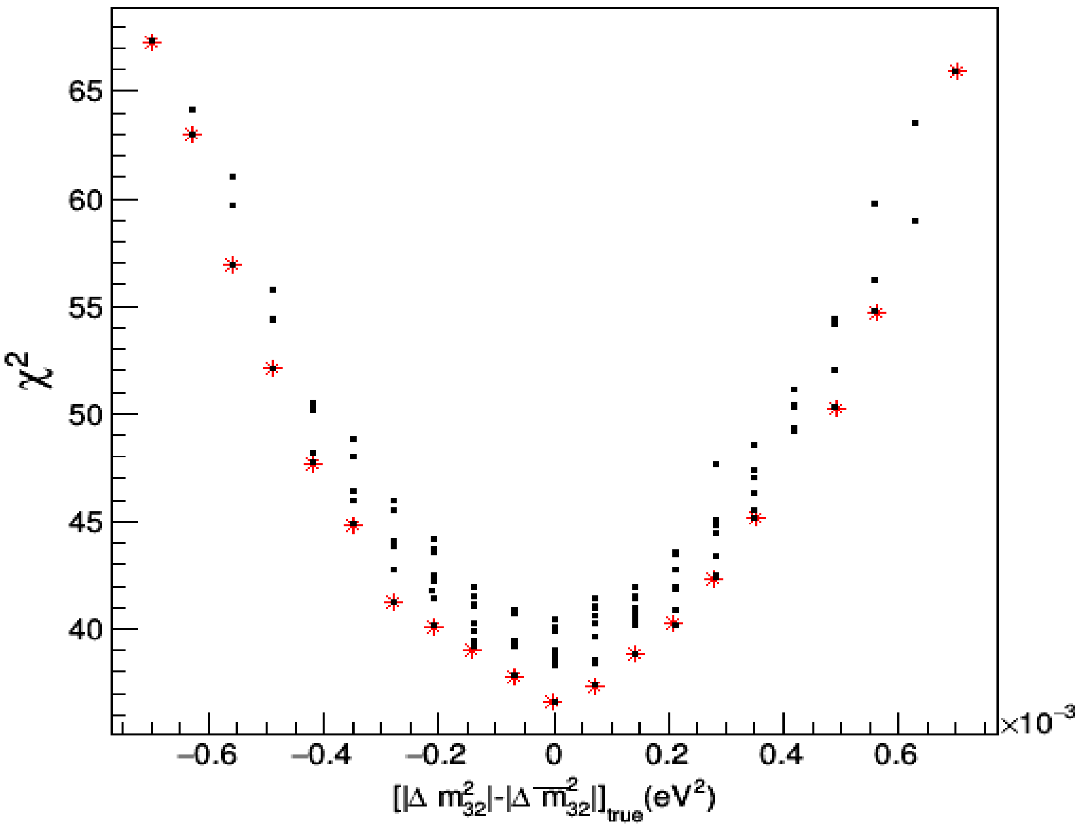

Figure 5.6: χ^2 versus $(|\Delta m^2_{32}| - |\Delta \overline{m^2}_{32}|)_{True}(eV^2)$ plot, black dots represents the several minimum χ^2 for a common $(|\Delta m^2_{32}| - |\Delta \overline{m^2}_{32}|)$ difference and red stars depicts the smallest χ^2 value among all of them.

For each value of $(|\Delta m^2_{32}| - |\Delta \overline{m^2}_{32}|)$, we calculate $\Delta\chi^2 = \chi^2 - \chi^2_{min}$ assuming $\chi^2_{min} = 37$ and plot it as the functions of $|\Delta m^2_{32}| - |\Delta \overline{m^2}_{32}|$ in Fig 5.5. This figure depicts the INO-ICAL potential for ruling out the null hypothesis $|\Delta m^2_{32}| = |\Delta \overline{m^2}_{32}|$ and is our final result of the present study.

5.3.4 ICAL sensitivity for $|\Delta m^2_{32}| - |\Delta \overline{m^2}_{32}| \neq 0$

In order to check the ICAL sensitivity for a non-zero value of the difference between $|\Delta m^2_{32}|$ and $|\Delta \overline{m^2}_{32}|$, the true values of $|\Delta m^2_{32}|$ and $|\Delta \overline{m^2}_{32}|$ have been varied independently in a range (0.0021 − 0.0028eV^2). But, we estimate the $\chi^2(\nu + \overline{\nu})$

only when the observed values of $|\Delta m^2_{32}|$ and $|\Delta \overline{m^2}_{32}|$ are equal. In other words, the $\chi^2(\nu + \overline{\nu})$ is being estimated on the null hypothesis line where the $|\Delta m^2_{32}|$ and $|\Delta \overline{m^2}_{32}|$ values are equal. The minimum value of χ^2 is chosen on this line that corresponds to the tangential point where the null hypothesis line coincides with the corresponding contour. Finally, this minimum χ^2 is binned as a function of difference in the true values of ($|\Delta m^2_{32}|$-$|\Delta \overline{m^2}_{32}|$). This will result in several χ^2 points corresponding to a common ($|\Delta m^2_{32}| - |\Delta \overline{m^2}_{32}|$) difference, depicted as dots in Figure 5.6. From all such candidate points, we pick those points that have the smallest χ^2 values and depict them as stars [see Figure 5.6].

CHAPTER 6

INDEPENDENT MEASUREMENT OF MUON NEUTRINO AND ANTI-NEUTRINO OSCILLATIONS AT THE INO-ICAL EXPERIMENT

6.1 Introduction

The phenomenon of neutrino oscillations is well established by many experiments involving solar [79], atmospheric [77, 78], accelerator [106], and reactor neutrinos [80]. It exhibits that neutrino flavor eigenstates $(\nu_e, \nu_\mu, \nu_\tau)$ are indeed quantum superpositions of mass eigenstates (ν_1, ν_2, ν_3) with definite masses (m_1, m_2, m_3) represented mathematically as

$$|\nu_i\rangle \quad = \sum_\alpha U_{\alpha i} \, |\nu_\alpha\rangle \,, \tag{6.1}$$

where, $|\nu_i\rangle$ represents a neutrino with a definite mass m_i (i=1,2,3), $|\nu_\alpha\rangle$ represents a neutrino with a definite flavor, and $U_{\alpha i}$ is the famous Pontecorvo Maki Nakagawa-Sakata (PMNS) lepton mixing matrix [25, 81]. The oscillation probability depends on three mixing angles, $\theta_{12}, \theta_{13}, \theta_{23}$; two mass differences, $\Delta m^2_{21}{=}m^2_2 - m^2_1$, and $\Delta m^2_{31}{=}m^2_3 - m^2_1$, and a CP phase δ_{CP}.

Although, remarkable progress has been made by several neutrino experiments to measure these oscillation parameters with reasonable accuracy [82, 107, 108, 109], still there are several physics concerns that perhaps lie beyond the paradigm of the three-massive-neutrinos scheme. The particles and their antiparticles are assumed to have equal masses and their different couplings are closely related as a consequence of the CPT-theorem. Therefore, parameters governing neutrino and antineutrino oscillation probabilities are considered to be identical. But, there is a possibility that neutrino and antineutrino may behave differently [110, 111, 112, 113, 91, 114, 92]. The survival probability for muon neutrinos at a particular energy E_ν and propagation length L is given by

$$P(\nu_\mu \to \nu_\mu) \simeq 1 - 4\cos^2\theta_{13}\sin^2\theta_{23} \times [1 - \cos^2\theta_{13}\sin^2\theta_{23}]\sin^2(\frac{1.267|\Delta m^2_{32}|L}{E_\nu}). \tag{6.2}$$

Similarly, the survival probability for muon antineutrino i.e., P$(\bar{\nu}_\mu \to \bar{\nu}_\mu)$ can be written by replacing the neutrino parameters by the corresponding antineutrino parameters, which are denoted mathematically by placing a bar on neutrino parameters.

Comparing the oscillation parameters of neutrinos and antineutrinos could, therefore, be a particular test of CPT-conservation as any difference between them may indicate a sign of new physics. Some experiments such as MINOS [115, 116, 117] and Super-Kamiokande (SK) [118] have performed some analyses with their experimental data assuming non-identical parameters for neutrinos and anti-neutrinos and found that neutrino and antineutrinos oscillation parameters are in agreement within uncertainties. Also, the magnetized Iron Calorimeter (ICAL) detector of the India-based Neutrino Observatory (INO)[84] will be able to easily distinguish an atmospheric ν_μ and $\overline{\nu}_\mu$ events on an event by event basis with its excellent charge identification capability due to the presence of a strong magnetic field. This chapter presents the future ICAL sensitivity for the measurement of muon neutrino and antineutrino oscillation parameters assuming that neutrinos and antineutrinos have different atmospheric mass-squared splittings and mixing angles assuming Normal mass Hierarchy (NH) is true. We study the prospects of the scenario when both the differences ($|\Delta m^2_{32}| - |\Delta\overline{m^2}_{32}|$) and ($\sin^2\theta_{23}$-$\sin^2\overline{\theta}_{23}$) are non-zero. Earlier INO study as in Ref [119] shows the ICAL detector sensitivity to measure the difference ($|\Delta m^2_{32}| - |\Delta\overline{m^2}_{32}|$) when only mass square splittings of neutrinos and anti-neutrinos are different with the assumption that ν_μ and $\bar{\nu}_\mu$ mixing angles are identical i.e. ($\sin^2\theta_{23}$-$\sin^2\overline{\theta}_{23}$=0). In this chapter, with the realistic detector resolutions and efficiencies of the ICAL, we vary all the four atmospheric oscillation parameters ($|\Delta m^2_{32}|, |\Delta\overline{m^2}_{32}|, \sin^2\theta_{23}$, $\sin^2\overline{\theta}_{23}$) simultaneously for neutrinos and antineutrinos to get a four dimensional fit. Using the results of this four parameters fit analysis, we show the ICAL detector potential to observe the difference between the neutrino and antineutrino mass-squared splittings ($|\Delta\overline{m^2}_{32}| - |\Delta m^2_{32}|$) and its sensitivity for ruling out the identical oscillation parameter hypothesis.

6.2 Methodology

The magnetized ICAL detector enables the separation of neutrino and antineutrino interactions for atmospheric events, allowing independent measurement of the neutrino and antineutrino oscillation parameters. Here, we analyze the reach of the ICAL for neutrino and antineutrino oscillations separately using a three-flavor analysis including the Earth's matter effects. We use a large number of unoscillated NUANCE [102] generated neutrino events, with an exposure of 50 kt $\times$ 1000 years of the ICAL detector, and then finally normalize to 500 kt-yr. We use HONDA [101] atmospheric neutrino fluxes for event generation. Each CC neutrino event is characterized by its energy and zenith angle.

Table 6.1 shows the oscillation parameters which are kept fixed throughout the analyses presented in this chapter. The solar oscillation parameters (Δm^2_{21} and $\sin^2\theta_{12}$) are kept fixed, as they do not show any significant impact on the results. As θ_{13} is now known quite precisely, it has been fixed as well. Since, the

ICAL is insensitive to the variation of δ_{CP} phase [105], hence it is also fixed at 0°. Oscillation effects have been introduced via a Monte-Carlo reweighting algorithm as described in earlier works [89, 88, 90]. Figure 6.1 shows oscillograms for ν_{μ} and $\bar{\nu}_{\mu}$ survival probabilities assuming NH. It is clear from the figure that due to the presence of the matter effect, ν_{μ} and $\bar{\nu}_{\mu}$ oscillations are different. The charge sensitive ICAL detector can easily distinguish the ν_{μ} and $\bar{\nu}_{\mu}$ oscillations and hence can easily measure their oscillation parameters separately with good precision.

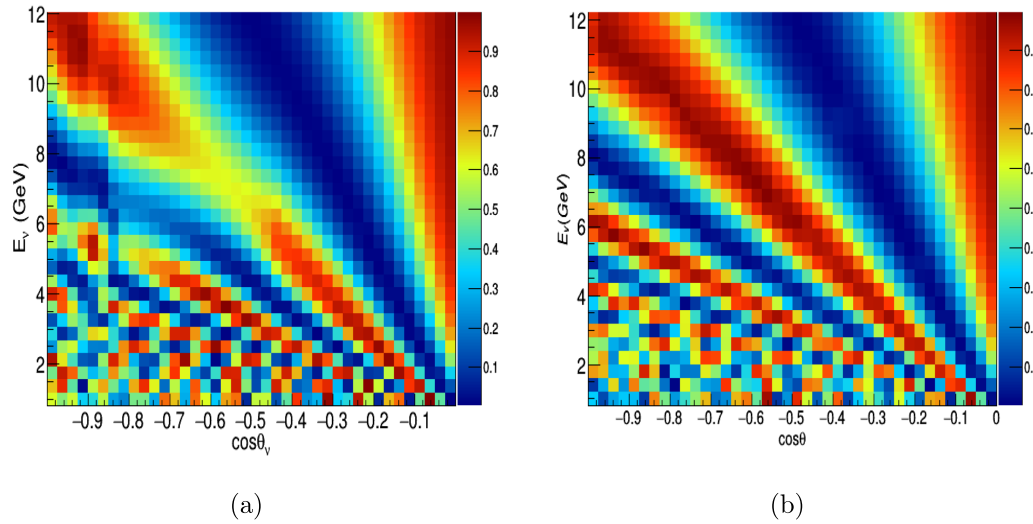

Figure 6.1: Oscillograms for muon neutrino (Left) and antineutrino (Right) survival probabilities on E-$\cos\theta$ palne including the earth matter effects using $|\Delta m^2_{23}|$ (or $|\Delta \bar{m}^2_{23}|$) $= 2.4 \times 10^{-3} eV^2$ and $\sin^2\theta_{23}$ $(or\, \sin^2\bar{\theta}_{23}) = 0.5$.

Oscillation parameters	True values	Marginalization range
$\sin^2\theta_{13}$	0.0234	Fixed
$\sin^2\theta_{12}(or\,\sin^2\bar{\theta}_{12})$	0.313	Fixed
$\Delta m^2_{12}(or \Delta\bar{m}^2_{12})$ (eV^2)	7.6×10^{-5}	Fixed
δ_{CP}	0.0	Fixed

Table 6.1: True values of the neutrino/antineutrino oscillation parameters used in the analysis.

Each oscillated neutrino or antineutrino event is divided as a function of twenty muon energy bins (E_μ), twenty muon zenith angle ($\cos\theta_\mu$), and five hadron energy bins (E_{hadron}) of optimized bin width as mentioned in Ref. [119]. These binned data are then folded with detector efficiencies and resolution functions as provided by the INO collaboration [99, 100] for the reconstruction of neutrino and antineutrino events separately.

Though the INO-ICAL has a very good charge identification efficiency, it is still possible that some muon events (say μ^-) are misidentified as opposite charge particles (say μ^+) and vice versa. This misidentification of events has been taken care of using following procedure as mentioned in references [88, 84]. Due to the misidentification, the total number of events, reconstructed as μ^- will increase by

$$N^{\mu^-} = N_{RC}^{\mu^-} + (N_R^{\mu^+} - N_{RC}^{\mu^+}), \tag{6.3}$$

where N^{μ^-} is the number of total reconstructed μ^- events. $N_{RC}^{\mu^-}$ is the number of μ^- events reconstructed and correctly identified in charge and $N_{RC}^{\mu^+}$ is the same for μ^+ events with their respective reconstruction and charge identification efficiencies folded in; whereas $N_R^{\mu^+}$ is the number of reconstructed μ^+ events. Hence, $N_R - N_{RC}$ gives the fraction of reconstructed events that have their charge wrongly identified. All the quantities given in Eq. 6.3 are function of E_μ and $\cos\theta_\mu$ and are determined bin wise. Total correctly identified reconstructed μ^+ events can be obtained using a similar expression with charge reversed.

We use a "pulled" χ^2 [104, 120, 121] method based on Poisson probability distribution to compare the expected and observed data with inclusion of systematic errors (a 20% error on atmospheric neutrino flux normalization, a 10% error on neutrino cross section, an overall 5% systematic error, a 5% uncertainty due to zenith angle dependence of the fluxes, and an energy-dependent tilt error), as considered in earlier ICAL analyses [84, 88, 90, 122]. All systematic uncertainties are correlated and the first two listed should cover the difference between neutrinos and anti-neutrinos.

The systematic uncertainties and the theoretical errors are parameterized in terms of a set of variables ζ, called pulls. Due to the fine binning, we use the poissonian log likelihood ratio given as,

$$\chi^2(\nu_\mu) = min \sum_{i,j,k} \left(2(N^{T'}_{ijk}(\nu_\mu) - N^{E}_{i,j,k}(\nu_\mu)) + 2N^{E}_{i,j,k}(\nu_\mu)(\ln \frac{N^{T}_{i,j,k}(\nu_\mu)}{N^{T'}_{i,j,k}(\nu_\mu)}) \right) + \sum_n \zeta_n^2, \tag{6.4}$$

where

$$N^{T'}_{ijk}(\nu_\mu) = N^{T}_{i,j,k}(\nu_\mu) \left(1 + \sum_n \pi^n_{ijk}\zeta_n \right). \tag{6.5}$$

Here, N^E_{ijk} are the observed number of reconstructed events, generated using true values of the oscillation parameters in i^{th} muon energy bin, j^{th} muon direction bin and k^{th} hadron energy bin, N^T_{ijk} are the number of theoretically predicted events generated by varying oscillation parameters, $N^{T'}_{ijk}$ show modified events spectrum due to different systematic uncertainties, π^n_{ijk} are the systematic shift in the events of the respective bins due to n^{th} systematic error. The univariate pull variable ζ_n, corresponds to the π^n_{ijk} uncertainty. An expression similar to Eq.(6.4) can be obtained for $\chi^2(\overline{\nu}_\mu)$ using reconstructed μ^+ event samples.

The functions $\chi^2(\nu_\mu)$ and $\chi^2(\overline{\nu}_\mu)$ are calculated separately for the independent measurement of neutrino and antineutrino oscillation parameters. All the systematic uncertainities are correlated and applied to neutrino and anti-neutrino events separately. Each χ^2 is fitted with 20 muon energy bins, 20 muon angle bins and 5 hadron energy bins via $20 \times 20 \times 5 = 2000$ binning scheme for neutrino as well as for antineutrinos. The two χ^2 can be added to get the combined $\chi^2(\nu_\mu + \overline{\nu}_\mu)$ as

$$\chi^2(\nu_\mu + \overline{\nu}_\mu) = \chi^2(\nu_\mu) + \chi^2(\overline{\nu}_\mu). \tag{6.6}$$

To estimate the ICAL sensitivity for the measurement of oscillation parameters, in the full parameter space, we vary all atmospheric oscillation parameters ($|\Delta m^2_{32}|, |\Delta\overline{m^2}_{32}|, \sin^2\theta_{23}$ and $\sin^2\overline{\theta}_{23}$) in their allowed ranges as mentioned in Table 6.2. The CC ν_μ and $\overline{\nu}_\mu$ events spectrum are separately binned into direction and energy bins. The χ^2 function is minimized with respect to these four parameters along with the five nuisance parameters to take into account the systematic uncertainties for different energy and direction bins.

After performing the feasibility study, we perform our analysis in two steps:
(1) Observed values of all four oscillation parameters ($|\Delta m^2_{32}|$, $\sin^2\theta_{23}$, $|\Delta\overline{m^2}_{32}|$, $\sin^2\overline{\theta}_{23}$) are varied within an experimentally allowed range as given in Table 6.2 keeping their true values fixed and non-identical.
(2) The true values of all the four oscillation parameters ($|\Delta m^2_{32}|$, $\sin^2\theta_{23}$, $|\Delta\overline{m^2}_{32}|$, $\sin^2\overline{\theta}_{23}$) are varied in a wide range and a χ^2 has been calculated to find out sensitivity for non-identical mass-squared splittings and mixing angles of ν_μ and $\overline{\nu}_\mu$.

oscillation parameters	Range
$\lvert\Delta m^2_{32}\rvert$ (eV^2)	(2.0-3.0) $\times 10^{-3}$
$\lvert\Delta\overline{m^2}_{32}\rvert$ (eV^2)	(2.0-3.0) $\times 10^{-3}$
$\sin^2\theta_{23}$	0.3-0.7
$\sin^2\overline{\theta}_{23}$	0.3-0.7

Table 6.2: The neutrino and antineutrino oscillation parameters and their experimentally allowed range used in the analysis.

6.2.1 Feasibility study

Lets consider a scenario where neutrino and antineutrino have different oscillation parameters. We generate the INO-ICAL events for the oscillation parameters as shown in Table 6.1 with the assumption that neutrinos and antineutrinos have different mass-squared splittings. We use ($|\Delta m^2_{32}| = 2.6\times10^{-3}(eV^2)$ and $|\Delta\overline{m^2}_{32}| = 2.2\times10^{-3}(eV^2)$. These ν and $\overline{\nu}$ events are then binned into $\cos\theta_\mu$, and E_μ and E_{hadron} bins separately. Further, $\chi^2(\nu)$ and $\chi^2(\overline{\nu})$ have been calculated separately and we show the 99% C.L. contours for ($|\Delta m^2_{32}|$, $\sin^2\theta_{32}$) and ($|\Delta\overline{m^2}_{32}|$, $\sin^2\overline{\theta}_{32}$) in Figure 6.2. The contours in blue and magenta show the sensitivity of INO for ν_μ and $\overline{\nu}_\mu$, respectively, for the scenario where they have different atmospheric mass-squared splittings.

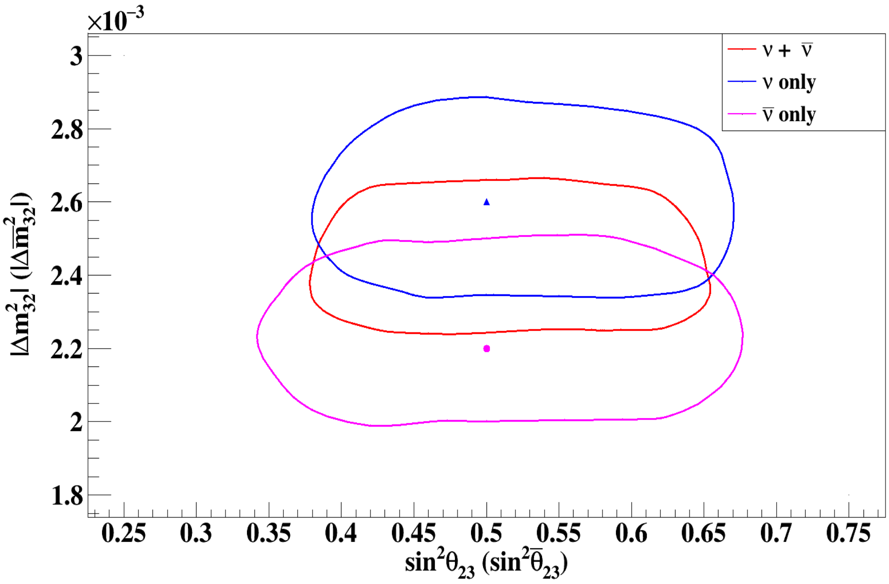

Figure 6.2: 99% C.L. contours obtained from $\chi^2(\nu)$, $\chi^2(\overline{\nu})$ separately and with combined χ^2 using non-identical true values of mass splittings for neutrinos ($|\Delta m^2_{32}| = 2.6 \times 10^{-3} eV^2$) and for antineutrino ($|\Delta\overline{m^2}_{32}| = 2.2 \times 10^{-3} eV^2$).

However, if the combined χ^2 is calculated as mentioned in Eq. 6.6, with the observation that neutrino and antineutrino have identical oscillation parameters, although their true values are different, then this sensitivity is shown with a red contour in Figure 6.2. It is clear that such a combined χ^2 analysis will give a best fit value that is more precise compared to that obtained from χ^2_ν and $\chi^2_{\overline{\nu}}$ separate analyses. We calculate the precision as $\frac{P_{max}-P_{min}}{P_{max}+P_{min}}$, where P_{max} and P_{min} are the maximum and minimum limits at the given CL of the corresponding oscillation parameters on the given axis. We find that the precision of the combined analysis is improved as expected ([Table 6.3]). But, it is highly likely that in this case the unrealistic sensitivity may be obtained when the difference between ν_μ and $\overline{\nu}_\mu$ is ignored. As it is clear from Figure 6.2 that the best fit obtained from combined χ^2 analyses is roughly an average value between the true values of Δm^2 and $\Delta\overline{m}^2$, which is less than 2σ away from the given true values of neutrino and antineutrino

Analysis	$\sin^2\theta_{23}$	$\|\Delta m^2_{32}\|$ (eV^2)
Neutrino events	28.84%	10.66%
Anti-neutrino events	32.66%	14.51%
Combined($\nu_\mu + \overline{\nu}_\mu$)	26.57%	8.57%

Table 6.3: Precision values at the 99% C.L. considering different oscillation parameters for neutrino, antineutrino and with the combined ($\nu_\mu + \overline{\nu}_\mu$) events [as shown in Figure 6.2] assuming $\sin^2\theta_{23} = \sin^2\overline{\theta}_{23}$ and $|\Delta m^2_{32}|$=$|\Delta\overline{m^2}_{32}|$ (eV^2) for χ^2 calculations

mass squared splittings.

Thus, in order to achieve the accurate sensitivity without ignoring the difference between oscillation parameters, or to test the hypothesis that neutrinos and antineutrinos share identical parameters, we should allow for the possibility of different true values of ν_μ and $\overline{\nu}_\mu$ parameters in nature. For this, we need to vary the true as well as observed values of all four parameters i.e. ($|\Delta m^2_{32}|$, $\sin^2\theta_{23}$, $|\Delta\overline{m^2}_{32}|$, $\sin^2\overline{\theta}_{23}$) in the analyses.

6.2.2 Measurement with the Non-identical, fixed true values

Four-parameter fit and extraction of two-parameter fit

This study has been performed to extract the sensitivity of the ICAL detector on a four parameter space assuming non identical parameters for ν_μ and $\overline{\nu}_\mu$. Here, χ^2 have been calculated as a function of four atmospheric oscillation parameters ($|\Delta m^2_{32}|$, $\sin^2\theta_{23}$, $|\Delta\overline{m}^2_{32}|$, $\sin^2\overline{\theta}_{23}$) while all other oscillation parameters are kept fixed at their central values.

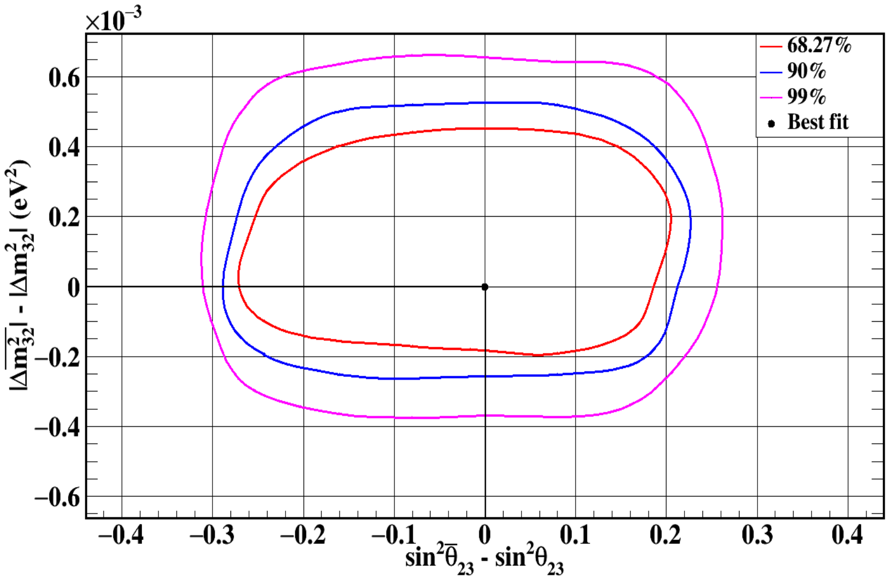

Figure 6.3: The ICAL sensitivity on ($\delta_m = |\Delta\overline{m^2}_{32}| - |\Delta m^2_{32}|$)) and ($\delta_\theta = \sin^2\overline{\theta}_{23} - \sin^2\theta_{23}$) plane at 68%, 90% and 99% confidence levels. The origin is the point where, neutrino and antineutrino parameters are identical.

We start with the assumption that neutrino and antineutrinos have different mass-squared splittings but identical mixing angles as $|\Delta m^2_{32}|$=2.38 $\times 10^{-3}(eV^2)$, $|\Delta\overline{m}^2_{32}|$=2.5 $\times 10^{-3}(eV^2)$ such that the difference $|\Delta\overline{m^2}_{32}| - |\Delta m^2_{32}| = 0.12$, and $\sin^2\theta_{23}$= $\sin^2\overline{\theta}_{23}$=0.5 such that ($\sin^2\overline{\theta}_{23} - \sin^2\theta_{23} = 0$). A fake dataset is generated at the given fixed true values of oscillation parameters ($|\Delta m^2_{32}|$, $\sin^2\theta_{23}$, $|\Delta\overline{m}^2_{32}|$, $\sin^2\overline{\theta}_{23}$). A four dimensional grid search ($10 \times 5 \times 10 \times 5$) is performed for the predicted dataset. χ^2 is calculated between the fake dataset and predicted dataset for each set of oscillation parameters.

The χ^2 for neutrino and antineutrino has been calculated separately, and a combined χ^2 sensitivity is considered for the estimation of the differences in mass-squared splittings ($\delta_m = |\Delta\overline{m^2}_{32}| - |\Delta m^2_{32}|$) and mixing angles ($\delta_\theta = \sin^2\overline{\theta}_{23} - \sin^2\theta_{23}$) of neutrinos and antineutrinos. Figure 6.3 plots the differences between the oscillation parameters on ($\delta_m = |\Delta\overline{m^2}_{32}| - |\Delta m^2_{32}|$) and ($\delta_\theta = \sin^2\overline{\theta}_{23} - \sin^2\theta_{23}$) plane at 68%, 90% and 99% CL. In general, there will be several points from the four dimensional χ^2 surface but a minimum χ^2 has been chosen among those points

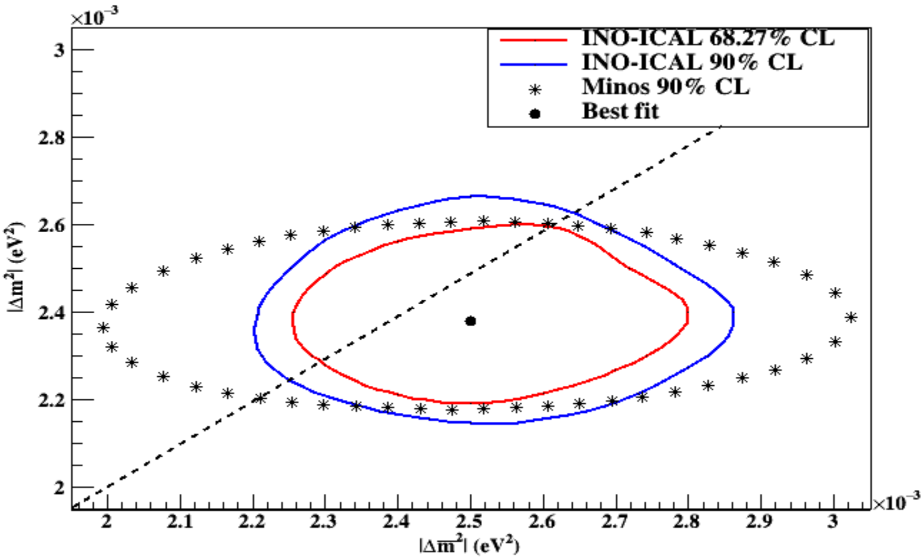

Figure 6.4: The 68% and 90% confidence level contours on the $|\Delta m^2_{32}|$ and $|\Delta \overline{m^2}_{32}|$ parameter space showing the sensitivity of the ICAL experiment using atmospheric data only and MINOS experiment using combined beamline and atmospheric data as given in Ref.[117]. Dashed line shows $|\Delta m^2_{32}| = |\Delta \overline{m^2}_{32}|$

.

to take the final single value in that bin.

A set of two parameters profile can also be extracted from the four parameters χ^2 data set by minimizing with respect to pairs of remaining oscillation parameters. Figure 6.4 shows the ICAL sensitivity for atmospheric mass-squared splitting on $|\Delta m^2_{32}|$ and $|\Delta \overline{m^2}_{32}|$ parameter space by minimizing over $\sin^2 \overline{\theta}_{23}$ and $\sin^2 \theta_{23}$ at different confidence intervals. It is clear from the figure that the ICAL can measure $|\Delta m^2_{32}|$ and $|\Delta \overline{m^2}_{32}|$ with a precision of about 10.41% and 12.87% at 90% Confidence Levels, respectively. The diagonal dashed line in Figure 6.4 indicates the case of identical mass splittings and mixing angles for neutrinos and antineutrinos, respectively. The neutrino mass-squared splittings on the $|\Delta m^2_{32}|$ and $|\Delta \overline{m^2}_{32}|$ parameter space at different confidence intervals obtained from MINOS detector using both beamline and atmospheric data has been shown in Figure 4 of Ref. [117], having similar fixed true values as mentioned in Table 6.4. Figure 6.4 shows that using similar oscillation parameters, the ICAL sensitivity for neutrinos is almost comparable to that of MINOS as shown in Ref. [117] while qualitatively, the ICAL is more sensitive than MINOS for the antineutrinos.

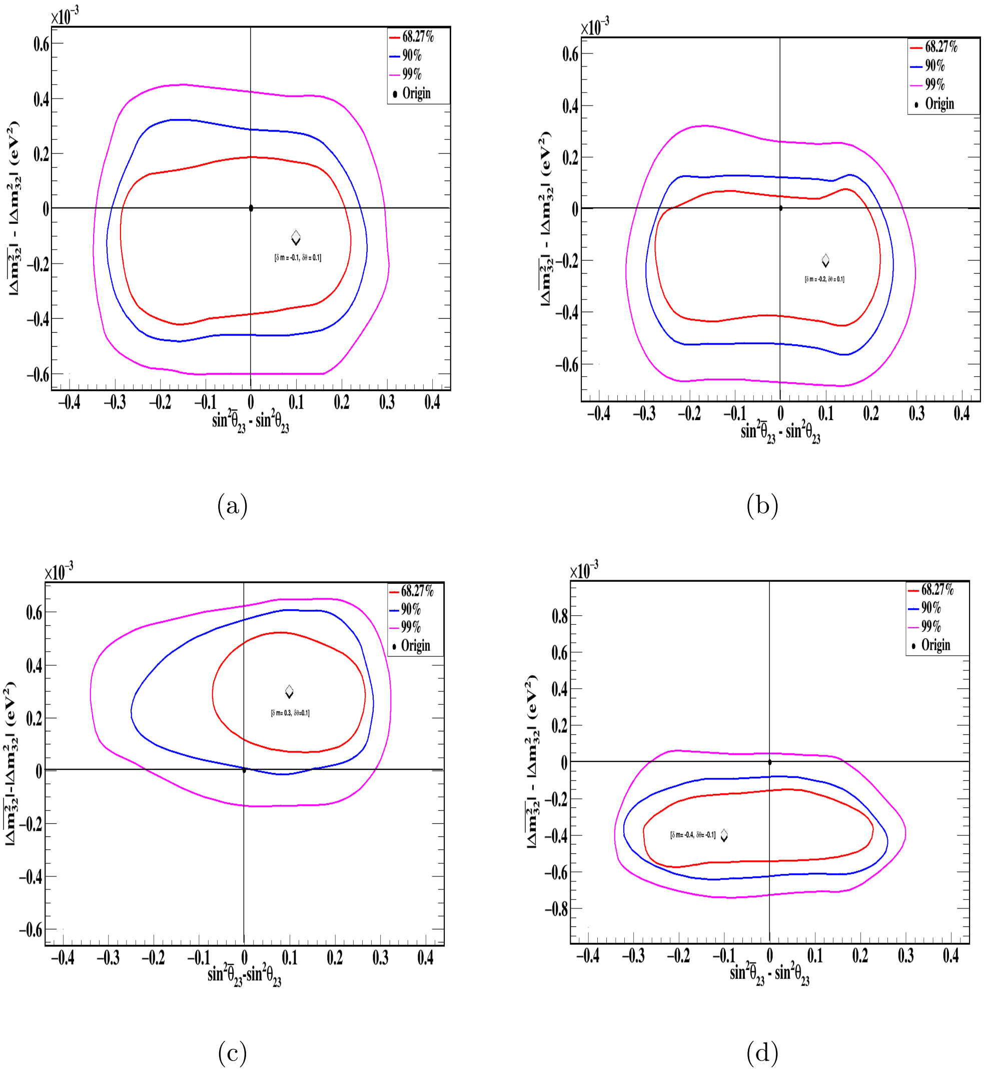

(a) (b) (c) (d)

Figure 6.5: Contour plots at 68%, 90% and 99% C.L. for different true values of $|\Delta m^2_{32}|$ and $|\Delta \overline{m^2}_{32}|$ as mentioned in Table 6.4. Here, x-axis corresponds to the differences of $\sin^2\theta_{23}$ and $\sin^2\overline{\theta}_{23}$ and y-axis corresponds to differences in $|\Delta m^2_{32}|$ and $|\Delta \overline{m^2}_{32}|$ values. In these plots diamond shows the best fit value of the observed parameters.

ICAL sensitivity in δ_m and δ_θ plane with non-identical true parameters

We performed the similar four fit χ^2 study for different sets of fixed, but non-identical true values of atmospheric oscillation parameters to check the ICAL sensitivity to rule out the hypothesis that neutrinos and antineutrinos have identical oscillation parameters. Figure 6.5 shows the sample sensitivity plots for different combinations of oscillation parameters as shown in Table 6.4 as a function of (δ_m) and (δ_θ) at different C.L. In these plots, the origin point shows the null hypothesis where neutrino and antineutrino parameters could be identical or in other words ($\delta_m = \delta_\theta = 0$). It can be seen from these figures that as δ_m and δ_θ move away from the origin point either in the positive or negative direction (as shown in Table 6.4), the ICAL sensitivity to the null hypothesis varies significantly. For example, Figure 6.5(a) and 6.5(b) having $[\delta_m, \delta_\theta]$ as $[-0.1 \times 10^{-3}$, 0.1] and $[-0.2 \times 10^{-3}$, 0.1] shows that using the corresponding mass-squared splitting and mixing angles for ν and $\overline{\nu}$, the ICAL can rule out the null hypothesis only at less than 1σ (68%)level. Similarly, Figure 6.5(c) and 6.5(d) having $[\delta_m, \delta_\theta]$ as $[0.3 \times 10^{-3}$, 0.1] and $[-0.4 \times 10^{-3}$, -0.1] shows the same at 2σ (90%) and more than 2σ level. Hence, to estimate the real significance of the ICAL detector for ruling out the null hypothesis or to reveal any mismatch in the ν and $\overline{\nu}$ parameters, it is pertinent to vary the true values of all four oscillation fit parameters rather than fixing them at any certain value, as is done in the next section.

Set No.	$\lvert\Delta m^2_{32}\rvert(eV^2)$	$\lvert\Delta\overline{m^2}_{32}\rvert(eV^2)$	$\sin^2\theta_{23}$	$\sin^2\overline{\theta}_{23}$	$\delta_m(eV^2)$	δ_θ
Set-1	2.6×10^{-3}	2.5×10^{-3}	0.5	0.6	-0.1×10^{-3}	0.1
Set-2	2.6×10^{-3}	2.4×10^{-3}	0.5	0.6	-0.2×10^{-3}	0.1
Set-3	2.2×10^{-3}	2.5×10^{-3}	0.4	0.5	0.3×10^{-3}	0.1
Set-4	2.4×10^{-3}	2.0×10^{-3}	0.5	0.4	-0.4×10^{-3}	-0.1

Table 6.4: True values of the neutrino and antineutrino mass-squared splittings, mixing angles and their differences used in the analysis

6.3 ICAL potential for non-identical mass-squared splittings

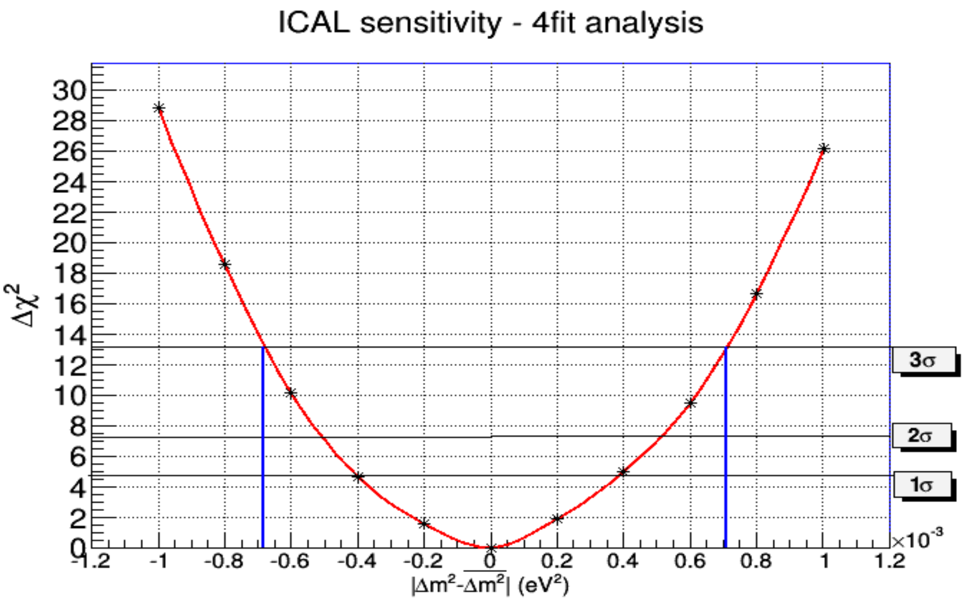

Figure 6.6: The INO-ICAL sensitivity for the difference between true values of mass-squared splittings of neutrinos and anti-neutrinos $(|\Delta m^2_{32}| - |\overline{\Delta m^2}_{32}|)_{True}$ (eV^2) at 1σ (68%), 2σ (90%) and 3σ (99%) obtained with minimising over true values of other two oscillation parameters (i.e. $\sin^2\theta_{23}, \sin^2\overline{\theta}_{23}$).

In this section, the true as well as observed values of atmospheric oscillation parameters (i.e. $|\Delta m^2_{32}|$, $|\overline{\Delta m^2}_{32}|, \sin^2\theta_{23}$ and $\sin^2\overline{\theta}_{23}$) have been allowed to vary independently as given in Table 6.2. The ICAL sensitivity to validate a non-zero value of the differences in ν and $\overline{\nu}$ mass-squared splittings ($\delta_m \neq 0$), true values of oscillation parameters are set to be non-identical. These true values are also varied simultaneously in a grid of 6×5 for neutrino plane and 6×5 for anti-neutrino plane. Further, we assume the identical parameters for neutrinos and antineutrinos (δ_m $=0$) and (δ_θ $=0$) as our null hypothesis. To test this null hypothesis, we estimate the $\chi^2(\nu+\overline{\nu})$ only for observed ($|\Delta m^2_{32}|$=$|\overline{\Delta m^2}_{32}|$) and ($\sin^2\theta_{23} = \sin^2\overline{\theta}_{23}$) values. The χ^2 is calculated for each set of true values of $|\Delta m^2_{32}|$, $\sin^2\theta_{23}$, $|\overline{\Delta m^2}_{32}|$, and

$\sin^2 \overline{\theta}_{23}$.

A minimum χ^2 has been binned as a function of difference in the true values of $[\delta_m]_{True}$ keeping marginalization over $[\sin^2 \theta_{23}$ and $\sin^2 \overline{\theta}_{23}]_{True}$. This results in several χ^2 points corresponding to a common set of differences of mass-squared splittings. For each set of difference $[\delta_m]_{True}$ and, we calculate $\Delta\chi^2 = \chi^2 - \chi^2_{min}$ and plot it as the functions of set of differences. Figure 6.6 represents the sensitivity of the ICAL for $[|\Delta m^2_{32}| - |\Delta \overline{m^2}_{32}|]_{True}$ with minimisation over true values of other two oscillation parameters $(\sin^2 \theta_{23},\ \sin^2 \overline{\theta}_{23})$. This represents the INO-ICAL potential for ruling out the null hypothesis $|\Delta m^2_{32}| = |\Delta \overline{m^2}_{32}|$.

Part IV

Inelastic processes

CHAPTER 7

ELECTROMAGNETIC PRODUCTION OF ASSOCIATED PARTICLES OFF THE NUCLEON TARGET

7.1 Introduction

The theoretical and the experimental study of the associated photoproduction of kaon-hyperon KY; $(Y = \Lambda, \Sigma)$ system on the proton was started almost 60 years ago [123, 124, 125, 126, 127, 128]. Out of the three isospin channels of the kaon-hyperon photoproduction from the proton, *viz.* $\gamma + p \longrightarrow K^+ + \Lambda$, $K^+ + \Sigma^0$, $K^0 + \Sigma^+$, the $K\Lambda$ production is the most studied one. The experimental measurements of the cross section and the polarization observables, although initially being scarce with large uncertainties [128, 124, 125, 126], are now available with improved statistics and better precision [129, 130, 131, 132, 133, 134, 135, 136, 137, 138]. Since the threshold for the $K\Lambda$ production is 1.61 GeV, therefore, the study of this process (and in general, the study of KY production), gives important information about the nucleon resonances, lying even in the third and higher resonance regions, which is not available from the study of $N\pi$ and $N\eta$ production processes. Unlike the $N\pi$ and $N\eta$ productions where $P_{33}(1232)$ [139] and $S_{11}(1535)$ [140, 141, 142] resonances, respectively, make the dominant contribution, there is no dominant resonance contributing to the $K\Lambda$ production and a large number of resonances may couple to this channel [143, 144, 145, 146, 147, 148, 149]. There are many resonances predicted in various quark models which are not observed in the pion-nucleon or electron-nucleon scattering processes [150, 151, 152], and one may get information about these resonances from the study of the $K\Lambda$ production process. Along with the real photons, the $K\Lambda$ production has also been studied using electrons, where the virtual photon interacts with the proton. Experimentally, the measurements of the cross sections, response functions and the polarization observables for the electron induced $K\Lambda$ production process have been done by CLAS [153, 154, 155], MAINZ A1 [156], JLab Hall-C [157] collaborations and several theoretical calculations for this process exist in the literature [158, 159, 160, 161, 162, 145, 148, 149].

With the availability of high intensity photon and electron beams at the Electron Stretcher System (ELSA) Germany, Thomas Jefferson National Accelerator Facility (TJNAF) US, Super Photon Ring – 8 GeV (SPring-8) Japan, European Synchrotron Radiation Facility (ESRF) France and Mainz Microtron (MAMI) Germany, it has been possible to precisely measure the cross sections and the polarization observables of the $K\Lambda$ channel in SAPHIR [131, 130], CLAS [132, 133, 134], LEPS [135], GRAAL [136, 137] and MAMI-C [138] experiments. There exists some disagreement between the CLAS and the SAPHIR data in the differential cross section especially in the forward angle region as well as in the total cross section in the center of mass (CM) energy range $W \geq 1.7$ GeV. Moreover, the forward angle data from CLAS 2006 [132] and CLAS 2010 [134] also do not agree with each other in the kinematic region of $W < 1.84$ GeV. On the other hand, the data from SAPHIR 1998 [130], SAPHIR 2004 [131] and MAMI-C [138] are fairly consistent with each other in this energy region.

The experiments LEPS [135] and GRAAL [136, 137] have studied the associated production of the strange particles with polarized photon beams and made measurements on the beam asymmetry and other polarization observables of the final hyperon. Notwithstanding, the importance of studying these observables in which a considerable amount of data is available, we have not included them in the present work. This is due to our immediate aim of finding a simple model with a minimal number of parameters to describe the total cross section and angular distributions in the photoproduction, which can be extended to weak production of strange particles induced by (anti)neutrinos in $\Delta S = 0$ sector by benchmarking the contribution of the vector currents. It is, therefore, appropriate time that the cross sections of these processes are calculated to complement the current efforts to model the neutrino nucleon cross sections in the few GeV energy region. A theoretical understanding of the total cross section and angular distributions in these weak processes induced by charged current (CC) and neutral current (NC) is currently of immense topical interest in modeling the (anti)neutrino cross section in the analysis of the present day neutrino oscillation experiments [163, 164] and no work has been done on these processes in the last 40 years [165, 166, 167, 168] except the work of Adera *et al.* [169]. However, keeping in mind, the important role of the measurements made on the various polarization observables in the study of associated production of strange particles induced by the unpolarized and polarized photons, we plan to study them in future.

Theoretically $\gamma(\gamma^*)p \longrightarrow K^+\Lambda$ process has been studied in various models, for example, the quark model [150, 151, 152, 170, 171, 172, 173, 174], chiral perturbative model [175], chiral unitary model [176], coupled channel model [177, 178, 179, 180, 181, 174], isobar model [182, 162, 158, 160, 183, 184, 185, 146, 159, 186, 187, 161, 188, 189, 190, 143, 191, 192, 144, 145, 193, 194, 195, 196, 197, 198, 149], isobar-Regge hybrid model [199, 200, 201, 202], or purely Regge models [203]. Among these models, one widely-studied model is the isobar model developed by various groups, for example, Saclay-Lyon (SL) [158, 160], Kaon-MAID (KM) [185], Ghent-Isobar [146, 186, 187], BS1 [144], BS3 [145], Mart [184, 147, 148, 183, 143, 161] and others [193, 194, 195, 197, 198, 188, 182, 191, 192]. The quark model is based on the quark degrees of freedom and assumes the extended structure of the baryons, in which the resonance contribution is taken through the excited states of the quarks. Hence, the quark model requires limited number of parameters. In the chiral models, the application of the chiral symmetry treats the pseudoscalar meson as the Goldstone boson and the Lagrangians for the meson-baryon system are obtained in the chiral limit. These models are best suited to calculate the $K\Lambda$ production in the threshold region but can be extended to higher energies using chiral unitary models. In the coupled channel models, the meson-baryon final state interactions are also included. For example, the photoproduction of $K\Lambda$ may take place through the primary production of the intermediate states *i.e.* $\gamma p \to \pi N,\ \eta N$, etc., leading to the $K\Lambda$ in the final state through the rescattering process. Therefore, the intermediate state can be any strangeness conserving meson-baryon system like $N\pi,\ N\eta,\ K\Lambda,\ K\Sigma$, etc. In the isobar models, mostly using an effective Lagrangian approach, the hadronic current consists of the non-resonant Born terms (s, t and u channels) and the resonance exchanges in s, t and u channels. In some versions of the isobar models, in which the pseudovector coupling is used for describing the meson-nucleon interactions, the contact term also appears. The final state interactions are not considered in most of the isobar models as they are based on the effective Lagrangians, except in a few calculations. This is because most of the isobar models make use of the phenomenological values for the various electromagnetic and strong couplings, which are assumed to simulate the effect of the final state interaction. However, in some versions of the isobar models in which a coupled channel analysis is used to treat the final particles, the final state interactions are taken into account [180, 177, 178, 179]. The various isobar models are different from each other in many ways and are classified on the basis of their treatment of the non-resonant terms and the resonance terms.

In the case of non-resonant terms considered in the s, t and u channels, the various models based on the effective Lagrangian differ in describing the meson-nucleon-hyperon interactions using either the pseudoscalar or the pseudovector coupling and the way in which the requirement of gauge invariance is implemented. The extensive studies made in the photo- and electro- productions of pions in a wide energy range extending from the threshold to high energies have demonstrated that the pseudovector coupling is to be preferred over the pseudoscalar coupling as it reproduces the low energy theorems (LET) predicted by the partially conserved axial vector current (PCAC) hypothesis and current algebra as a consequence of the chiral symmetry of strong interactions and are consistent with the experimental observations [204]. Moreover, the choice of the pseudovector coupling generates a contact term in the presence of electromagnetic interactions in a natural way, which facilitates the understanding of LET and helps to implement the requirement of gauge invariance. However, in the presence of hadronic form factors at the strong vertex, the implementation of gauge invariance necessitates additional assumptions about the momentum dependence of the hadronic form factors. On the other hand, in the case of the associated photoproduction of KY, both the pseudoscalar and pseudovector couplings have been used in many calculations in the absence of any theoretical preference for the pseudovector coupling. This is due to the inadequacy of the low energy theorems implied by the pseudovector coupling arising from the slow convergence of the low energy expansion [205].

In the case of resonance terms, the difference between various calculations arises mainly due to the number of resonances taken into account in the intermediate states and the determination of their electromagnetic couplings to the photons and their strong couplings to the meson-nucleon-hyperon systems *i.e.* RKY. For example, the Saclay-Lyon model [158, 160] has taken into consideration, spin $\frac{1}{2}$, $\frac{3}{2}$ and $\frac{5}{2}$ nucleon resonances in the s channel, K^* and K_1 in the t channel and spin $\frac{1}{2}$ Λ^* and Σ^* resonances in the u channel. The Kaon-MAID model [185] uses spin $\frac{1}{2}$ and $\frac{3}{2}$ nucleon resonances in the s channel, K^* and K_1 in the t channel and no hyperon resonance in the u channel. The Ghent model [146, 186, 187] uses three different ways to fit the experimental data from SAPHIR [131] for the $K\Lambda$ channel: (i) assuming SU(3) symmetry and without considering the hyperon resonances, (ii) assuming SU(3) symmetry and with hyperon resonances, and (iii) without assuming SU(3) symmetry and without hyperon resonances. In all the three prescriptions, spin $\frac{1}{2}$ and $\frac{3}{2}$ nucleon resonances are taken in the s channel. In BS1 and BS3 models [144, 145], spin $\frac{1}{2}$, $\frac{3}{2}$ and $\frac{5}{2}$ nucleon resonances are taken in the s channel, K^* and K_1 in the t channel and spin $\frac{1}{2}$ and $\frac{3}{2}$ Λ^* and Σ^* resonances in the u channel.

Other than these models, Regge model [203, 206], where particles are replaced by their Regge trajectories to extend the model to higher energies, is also used to study the $K\Lambda$ production, but its applicability is restricted to higher energies (3 GeV $\leq E_\gamma \leq$ 16 GeV). Also, there are hybrid models that combine the Regge and resonance models to study the photo- and electro- production of strange particles, which describes the data both in the resonance region as well as at high energies [207, 208, 202].

In this work, we present an isobar model to study the photon induced $K\Lambda$ production on the proton. In this model, an effective Lagrangian based on the chiral SU(3) symmetry has been used to obtain the non-resonant terms consisting of s, t and u channel diagrams and the Lagrangian also generates the contact term as a requirement of the underlying symmetry. The electromagnetic couplings are described in terms of the charge and magnetic moment of the baryons like p, Λ and Σ occurring in the s, t and u channel diagrams. The strong couplings of the meson-nucleon-baryon system like $g_{K\Lambda p}$, $g_{K\Sigma p}$, $g_{\gamma K\Lambda p}$, $g_{\gamma K\Sigma p}$ are described in terms of f_π, D and F which are determined from the electroweak phenomenology of nucleons and hyperons, where f_π is the pion decay constant and D and F, respectively, are the axial vector current couplings of the baryon octet in terms of the symmetric and antisymmetric couplings. Therefore, the contribution of the non-resonant terms is calculated without any free parameters except the cut-off parameter used to define the form factors at the strong vertex which is taken to be the same for all the background terms i.e. non-resonant terms and the resonance terms in the t and u channels. The form factor of the contact term is fixed in terms of the other form factors according to the well known prescription given by Davidson and Workman [209]. The non-linear sigma model with chiral SU(2) symmetry has been earlier used in the calculations of single pion production induced by electron, neutrino and antineutrino [210, 211, 30], and has been extended to the chiral SU(3) symmetry to calculate the single kaon production induced by electron and neutrino [212, 213], single antikaon production induced by positron and antineutrino [213, 31], eta production induced by neutrino and antineutrino [214].

In the resonance sector, we have considered various nucleon, hyperon and kaon resonances giving rise to $K\Lambda$ in the final state. Only those nucleon resonances R are taken in the s channel, which are well established and are referred by $***{*}$ and $***$ status in the particle data group (PDG), having spin $\leq \frac{3}{2}$, mass in the range $1.6 - 1.9$ GeV and non-vanishing ($> 4 - 5\%$) branching ratio in the $K\Lambda$ decay mode (see Table 7.1). In the case of nucleon resonances, the electromagnetic couplings γNR, are determined in terms of the helicity amplitudes and the strong $RK\Lambda$ couplings are determined by the partial decay width of the resonance decaying to $K\Lambda$ using an effective Lagrangian. A form factor of the general dipole form with a cut-off parameter Λ_R taken to be the same for all nucleon resonances in the s channel has been used to describe the $R\Lambda K$ vertex.

In the u channel, two spin $\frac{1}{2}$ hyperon resonances *viz.* $\Lambda^*(1405)$ and $\Lambda^*(1800)$ and in the t channel, two kaon resonances of spin 1 *viz.* $K^*(892)$ and $K_1(1270)$ are taken into account. The t and u channel resonances along with the non-resonant contributions constitute the background part of the hadronic current which are calculated using the effective Lagrangians. Due to the lack of the experimental data on the kaon and hyperon resonances, the strong and electromagnetic couplings of u and t channel resonances are not well determined phenomenologically and are, therefore, varied by fitting the data from CLAS [132, 134] and SAPHIR [130, 131] experiments. While doing this fitting, a form factor is taken into account, to be of a general dipole form with a cut-off parameter Λ_B, to describe the strong

$R\Lambda K$ vertex. This cut-off parameter Λ_B is taken to be the same as that has been considered for the Born terms as both contribute to the background terms.

The calculation of various terms contributing to the background term is done in the lowest order tree-level approximation using the effective Lagrangians for the non-resonant s, t and u channel diagrams and the contact terms as well as the resonance contribution from all the t channel and u channel resonances while the calculations of the different resonance terms is done using the effective Lagrangians for all the s channel nucleon resonances. The present calculation, and the many earlier calculations [215, 158, 159, 216, 217, 218] done for this process, in the tree level approximation are known to suffer from lack of unitarity as they do not consider the rescattering effects in the $K\Lambda$ channel or other channels produced in the γp interaction. There are some prescriptions described in the literature to restore the unitarity [219], in the multichannel coupled channel models [220, 221, 222, 223, 224, 225] and the Watson's treatment method [226, 227, 228]. We have examined the effect of restoring unitarity using the energy dependent width of the resonances weighted by the branching ratios of the various decay channels of the considered resonances following the prescription of Bennhold *et al.* [215], Mart and Bennhold [183, 184] and Skoupil and Bydzovsky [145]. The numerical results for the total and differential cross sections with fixed as well as energy dependent decay widths of the nucleon resonances are presented and compared with the experimental results available from SAPHIR 1998 [130], SAPHIR 2004 [131], CLAS 2006 [132] and CLAS 2010 [134]. We have also compared the results of the present work for the total and differential cross sections with the various theoretical models available in the current literature, like the Regge model [203, 206], chiral perturbation model [175], Saclay-Lyon model [158, 160], Kaon-MAID model [185], Ghent model [146, 186, 187], BS1 model [144], BS3 model [145], Bonn-Gatchina model [229, 180, 230, 231, 232, 233], Bonn-Julich model [234], and KSU model [235, 236].

The major advantage of the formalism developed in the present model is that, it makes use of many physics inputs available from various experimental observations on the electroweak and strong interaction phenomenology of mesons and baryons and involves very few parameters to reproduce the data. Specifically, the model has the following features:

i) The contact term in the non-resonant contribution occurs naturally in the model with the strength of its coupling predicted by the model.

ii) A general dipole form is used in all the form factors appearing at the strong meson-nucleon-hyperon vertices for all the background terms with a common cut-off parameter Λ_B. The background terms consist of the s, t and u channel Born terms, contact term as well as the t and u channel resonance terms.

iii) All the resonances included in the s channel, *viz.* $S_{11}(1650)$, $P_{11}(1710)$, $P_{13}(1720)$, $P_{11}(1880)$, $S_{11}(1895)$ and $P_{13}(1900)$, are the well established resonances with definite mass, decay width, branching ratio in $K\Lambda$ channel given in PDG [237].

iv) The partial decay width of the resonances (R) for decaying into $K\Lambda$ channel from the PDG [237] is used to determine the strength of the strong couplings of the resonance (R) to the $K\Lambda$ channel, using an effective Lagrangian approach. We have chosen those resonances which have a branching ratio for decaying in the $K\Lambda$ channel greater than $4-5\%$.

v) The helicity amplitudes of the resonances $S_{11}(1650)$ and $P_{13}(1720)$ are taken from MAID [139], and for the rest of the s channel resonances, the helicity amplitudes are taken from PDG [237] (Table 7.2). These amplitudes are used to determine the strength of the electromagnetic couplings at the γNR vertex.

vi) A common cut-off parameter Λ_R is used to describe the hadronic form factors at the strong $RK\Lambda$ vertex in the case of the nucleon resonances constituting the resonance terms in the s channel.

vii) The coupling strengths of the t and u channel resonances (see Table 7.3) are fitted to reproduce the experimental results, keeping the same cut-off parameter Λ_B. The cut-off parameters Λ_B and Λ_R are varied to reproduce the experimental results on the total cross sections specially in the low energy region where the data from the SAPHIR and CLAS agree with each other. The total cross sections at higher energies (W >1.72 GeV) as well as the angular distributions as function of W and $\cos\theta_K^{CM}$ are predictions of the model.

In Sect. 7.2, the formalism for the $K\Lambda$ production induced by the real photons on the proton has been presented, where we discuss the contribution to the hadronic current arising due to the non-resonant and resonance diagrams. Sect. 7.2.2 focuses on the non-resonant terms, determined by the non-linear sigma model assuming the chiral SU(3) symmetry. The structure of the nucleon, hyperon and kaon resonances and their couplings are discussed in Sect. 7.2.3. The results and their discussions are presented in Sect. 7.3, and Sect. 8 gives a summary and concludes the present findings.

7.2 Formalism

In this work, we have studied the $K\Lambda$ photoproduction on the proton,

$$\gamma(q) + p(p) \longrightarrow K^+(p_k) + \Lambda(p'), \tag{7.1}$$

where the quantities in the parentheses represent the four momenta of the corresponding particles. In Sect. 7.2.1, we give the general discussion for the evaluation of the transition matrix element and cross section in the CM frame. The transition matrix element is written in terms of the photon polarization state vector and the hadronic current. The hadronic current receives contribution from the background and resonance terms. Following the standard terminology, the background terms consist of all the non-resonant terms contributing in the s, t and u channels and the contact term as well as the contributions from the resonance terms in the t and u channels. The non-resonant terms are determined using the non-linear sigma model and the chiral SU(3) symmetry, discussed in Sect. 7.2.2 while the contributions from the hyperon and kaon resonances are discussed in Sects. 7.2.3 and 7.2.3, respectively. The nucleon resonances with spin $\frac{1}{2}$ and $\frac{3}{2}$ in the s channel constitute the resonance contribution of the hadronic current and are discussed in Sects. 7.2.3 and 7.2.3, respectively.

7.2.1 Matrix element and cross section

The differential cross section for the photoproduction process given in Eq. (A.1) is written as

$$d\sigma = \frac{1}{4(q\cdot p)}(2\pi)^4\delta^4(q+p-p_k-p')\frac{d\vec{p}_k}{(2\pi)^3(2E_k)}\frac{d\vec{p}\,'}{(2\pi)^3(2E_\Lambda)}\overline{\sum_r\sum}|\mathcal{M}^r|^2 \tag{7.2}$$

where E_k and E_Λ, respectively, are the energies of the outgoing kaon and lambda. $\overline{\sum}\sum|\mathcal{M}^r|^2$ is the square of the transition matrix element $\mathcal{M}^r$, for photon polarization state r, averaged and summed over the initial and final spin states. $\mathcal{M}^r$ is written in terms of the real photon polarization vector ϵ^r_μ and the matrix element of the electromagnetic current taken between the hadronic states of $|p\rangle$ and $|K\Lambda\rangle$, *i.e.*

$$\mathcal{M}^r = e\epsilon^r_\mu(q)\,\langle\Lambda(p')K^+(p_k)|\,J^\mu\,|p\rangle\,, \tag{7.3}$$

where $e=\sqrt{4\pi\alpha}$ is the strength of the electromagnetic interaction, with $\alpha = \frac{1}{137}$ being the fine-structure constant. In the case when the photon polarization remains undetected, the summation over all the polarization states is performed which gives

$$\sum_{r=\pm1}\epsilon^{*(r)}_\mu\epsilon^{(r)}_\nu \longrightarrow -g_{\mu\nu}. \tag{7.4}$$

In the case when the polarization states of the initial and the final baryon also remain unmeasured, the hadronic tensor $\mathcal{J}^{\mu\nu}$ is written in terms of the hadronic current J^μ as

$$\mathcal{J}^{\mu\nu} = \overline{\sum}\sum_{spins} J^{\mu\dagger} J^\nu = \mathrm{Tr}\left[(\not{p} + \mathrm{M})\tilde{\mathrm{J}}^\mu(\not{p}' + \mathrm{M}_\Lambda)\mathrm{J}^\nu\right], \qquad \tilde{\mathrm{J}}^\mu = \gamma_0(\mathrm{J}^\mu)^\dagger\gamma_0, \quad (7.5)$$

where M and M_Λ are the masses of the proton and lambda, respectively. The hadronic matrix element of the electromagnetic current J^μ receives the contribution from the background terms and resonance terms.

Using Eqs. (7.4) and (7.5), the transition matrix element squared is obtained as

$$\overline{\sum_r}\sum_{spin} |\mathcal{M}^r|^2 = -\frac{1}{4} g_{\mu\nu}\mathcal{J}^{\mu\nu}. \quad (7.6)$$

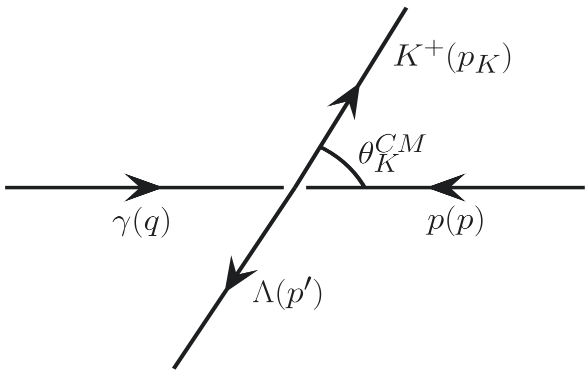

Figure 7.1: Diagrammatic representation of the process $\gamma(q) + p(p) \rightarrow K^+(p_k) + \Lambda(p')$ in the center of mass frame. The quantities in the parentheses represent the four momenta of the corresponding particles. θ_k^{CM} is the angle between photon and kaon in the CM frame.

Following the above expressions, the differential cross section $\frac{d\sigma}{d\Omega}$ in the CM frame is written as

$$\left.\frac{d\sigma}{d\Omega}\right|_{CM} = \frac{1}{64\pi^2 s}\frac{|\vec{p}\,'|}{|\vec{p}|}\overline{\sum_r}\sum_{spin}|\mathcal{M}^r|^2, \quad (7.7)$$

where s is the CM energy squared obtained as

$$s = W^2 = (q+p)^2 = M^2 + 2ME_\gamma, \quad (7.8)$$

E_γ is the energy of the incoming photon in the laboratory frame. The center of mass energies of the initial and the final particles are obtained as

$$\begin{aligned} E_\gamma^{CM} &= \frac{s-M^2}{2\sqrt{s}}, & E_p^{CM} &= \frac{s+M^2}{2\sqrt{s}}, \\ E_k^{CM} &= \frac{s+M_k^2-M_\Lambda^2}{2\sqrt{s}}, & E_\Lambda^{CM} &= \frac{s+M_\Lambda^2-M_k^2}{2\sqrt{s}}. \end{aligned} \tag{7.9}$$

In the CM frame as shown in Figure 7.1, $|\vec{q}| = |\vec{p}|$ and $|\vec{p}_k| = |\vec{p}\,'|$ which are given by [237]:

$$|\vec{q}| = \frac{\lambda^{1/2}(s,0,M^2)}{2\sqrt{s}}, \qquad |\vec{p}\,'| = \frac{\lambda^{1/2}(s,M_k^2,M_\Lambda^2)}{2\sqrt{s}}, \tag{7.10}$$

with $\lambda(a,b,c)$ being the Callan function, expressed as

$$\lambda(a,b,c) = a^2+b^2+c^2-2ab-2bc-2ca.$$

Assuming the incoming photon to be along the z-axis, the energy and three momentum of the incoming and the outgoing particles are expressed as:

$$\begin{aligned} \text{photon} &: \quad (E_\gamma^{CM}, 0, 0, |\vec{q}|) \\ \text{proton} &: \quad (E_p^{CM}, 0, 0, -|\vec{q}|) \\ \text{kaon} &: \quad (E_k^{CM}, 0, |\vec{p}_k|\sin\theta_k^{CM}, |\vec{p}_k|\cos\theta_k^{CM}) \\ \text{lambda} &: \quad (E_\Lambda^{CM}, 0, -|\vec{p}_k|\sin\theta_k^{CM}, -|\vec{p}_k|\cos\theta_k^{CM}), \end{aligned}$$

where θ_k^{CM} is the angle between the photon and kaon measured in the CM frame.

7.2.2 Non-resonant contribution

The non-resonant contributions are obtained using the non-linear sigma model assuming the chiral SU(3) symmetry, which involves the low-lying baryons and mesons. This model implements spontaneous breaking of chiral symmetry [238, 239, 240, 241]. In the SU(3) version of the model, it generates the octet of pseudoscalar mesons π, K and η as well as the interaction Lagrangians for the meson-meson and meson-baryon interactions [238, 239]. The details for the non-linear sigma model are given in Appendix C.

In order to get the Lagrangian which describes the dynamics of these pseudoscalar mesons, we need continuous fields which are described in terms of these Goldstone modes. The elements of $SU(3)$ pseudoscalar meson fields are written in terms of a unitary matrix

$$U(\Theta) = \exp\left(-i\Theta_k \frac{\lambda_k}{2}\right) , \tag{7.11}$$

where Θ_k; $(k = 1-8)$ are the real set of parameters and λ_k are the traceless, Hermitian 3×3 Gell-Mann matrices.

Each Goldstone boson corresponds to the x-dependent Cartesian component of the fields, $\phi_k(x)$, which in turn, is expressed in terms of the physical fields as

$$\Phi(x) = \sum_{k=1}^{8} \phi_k(x)\lambda_k = \begin{pmatrix} \pi^0 + \frac{1}{\sqrt{3}}\eta & \sqrt{2}\pi^+ & \sqrt{2}K^+ \\ \sqrt{2}\pi^- & -\pi^0 + \frac{1}{\sqrt{3}}\eta & \sqrt{2}K^0 \\ \sqrt{2}K^- & \sqrt{2}\bar{K}^0 & -\frac{2}{\sqrt{3}}\eta \end{pmatrix} . \tag{7.12}$$

For the baryons, we follow the same procedure as we do for the mesons. However, unlike the pseudoscalar mesons where the fields are real, in the case of baryon fields, represented by a B matrix, each entry is a complex-field and the general representation is given by,

$$B(x) = \sum_{k=1}^{8} \frac{1}{\sqrt{2}} b_k(x)\lambda_k = \begin{pmatrix} \frac{1}{\sqrt{2}}\Sigma^0 + \frac{1}{\sqrt{6}}\Lambda & \Sigma^+ & p \\ \Sigma^- & -\frac{1}{\sqrt{2}}\Sigma^0 + \frac{1}{\sqrt{6}}\Lambda & n \\ \Xi^- & \Xi^0 & -\frac{2}{\sqrt{6}}\Lambda \end{pmatrix} . \tag{7.13}$$

After getting the parameterization of pseudoscalar meson fields octet $\Phi(x)$ in Eq.(7.12) and baryon fields octet $B(x)$ in Eq. (7.13), we now discuss the construction of Lagrangian for meson-meson, baryon-meson interactions and their interaction with the external fields.

Meson - Meson Interaction

The lowest-order $SU(3)$ chiral Lagrangian describing the pseudoscalar mesons in the presence of an external current is obtained as [238, 239]

$$\mathcal{L}_M = \frac{f_\pi^2}{4}\mathrm{Tr}[D_\mu U (D^\mu U)^\dagger], \tag{7.14}$$

where $f_\pi (= 92.4$ MeV) is the pion decay constant obtained from the weak decay of pions, *i.e.*, $\pi^\pm \to \mu^\pm \nu_\mu(\bar{\nu}_\mu)$. The covariant derivatives $D^\mu U$ and $D^\mu U^\dagger$ appearing in Eq. (7.14) are expressed in terms of the partial derivatives as

$$\begin{aligned} D^\mu U &\equiv \partial^\mu U - i r^\mu U + i U l^\mu, \\ D^\mu U^\dagger &\equiv \partial^\mu U^\dagger + i U^\dagger r^\mu - i l^\mu U^\dagger, \end{aligned} \tag{7.15}$$

where U is the SU(3) unitary matrix given as

$$U(x) = \exp\left(i\frac{\Phi(x)}{f_\pi}\right), \tag{7.16}$$

where $\Phi(x)$ is given by Eq. (7.12) and the left-(l^μ) and right-(r^μ) handed currents appearing in Eq. (7.15) are expressed as

$$l_\mu = -e\hat{Q}\mathcal{A}_\mu, \qquad r_\mu = -e\hat{Q}\mathcal{A}_\mu. \tag{7.17}$$

$\mathcal{A}^\mu$ is the electromagnetic four-vector potential and $\hat{Q}$ is the $SU(3)$ quark charge.

Baryon - Meson Interaction

To incorporate baryons in the theory, we have to take care of their masses which do not vanish in the chiral limit [242]. However, if we take nucleons as massive matter fields which couples to external currents and the pseudoscalar mesons, we have to then expand the Lagrangian according to their increasing number of momenta. Here, we shall present in brief the extension of the formalism to incorporate the heavy matter fields.

The lowest-order chiral Lagrangian for the baryon octet in the presence of an external current may be written in terms of the $SU(3)$ matrix B as [238, 239],

$$\mathcal{L}_{MB} = Tr\left[\bar{B}\left(i\not{D} - M\right)B\right] - \frac{D}{2}Tr\left(\bar{B}\gamma^\mu\gamma_5\{u_\mu, B\}\right) - \frac{F}{2}Tr\left(\bar{B}\gamma^\mu\gamma_5[u_\mu, B]\right), \tag{7.18}$$

where M denotes the mass of the baryon octet, $D = 0.804$ and $F = 0.463$ are the axial vector coupling constants for the baryon octet determined from the semileptonic decays of neutron and hyperons [243], the matrix B is given in Eq. (7.13) and the Lorentz vector u^μ is given by [239]:

$$u^\mu = i\left[u^\dagger(\partial^\mu - ir^\mu)u - u(\partial^\mu - il^\mu)u^\dagger\right]. \tag{7.19}$$

In the case of meson-baryon interactions, the unitary matrix for the pseudoscalar field is expressed as

$$u = \sqrt{U} \equiv \exp\left(\mathrm{i}\frac{\Phi(\mathrm{x})}{2\mathrm{f}_\pi}\right),$$

and the covariant derivative of B is given by

$$D_\mu B = \partial_\mu B + [\Gamma_\mu, B], \qquad \text{with} \qquad \Gamma^\mu = \frac{1}{2}\left[u^\dagger(\partial^\mu - ir^\mu)u + u(\partial^\mu - il^\mu)u^\dagger\right]. \tag{7.20}$$

Using Eqs. (7.12), (7.13), (7.19) and (7.20) in the general expression of the Lagrangian given in Eq. (7.18), the Lagrangians for the desired vertices involved in the meson-baryon interactions among themselves and with the external fields are obtained. The Lagrangians using chiral SU(3) symmetry relevant for the present work, are derived to be:

$$\mathcal{L}_{\gamma pp} = -ee_p\bar{\psi}_p\gamma_\mu\psi_p A^\mu \tag{7.21}$$

$$\mathcal{L}_{\gamma\Lambda\Lambda} = -ee_\Lambda\bar{\psi}_\Lambda\gamma_\mu\psi_\Lambda A^\mu \tag{7.22}$$

$$\mathcal{L}_{K\Lambda p} = \left(\frac{D+3F}{2\sqrt{3}f_\pi}\right)\bar{\psi}_\Lambda\gamma_\mu\gamma_5\psi_p\partial^\mu K^\dagger \tag{7.23}$$

$$\mathcal{L}_{\gamma K\Lambda p} = -ie\left(\frac{D+3F}{2\sqrt{3}f_\pi}\right)\bar{\psi}_\Lambda\gamma_\mu\gamma_5\psi_p K^\dagger A^\mu \tag{7.24}$$

$$\mathcal{L}_{\gamma KK} = -ie\left(K^\dagger\partial_\mu K - K\partial_\mu K^\dagger\right)A^\mu \tag{7.25}$$

where e_p and e_Λ, respectively, represents the electric charge of proton and lambda, $\bar{\psi}_p$ and $\bar{\psi}_\Lambda$ represent the outgoing proton and lambda fields, ψ_p and ψ_Λ represent the incoming proton and lambda fields, A_μ represents the electromagnetic field with e being the strength of the electromagnetic field, and $K^\dagger$ and $\partial_\mu K^\dagger$ represent the kaon field and covariant derivative of kaon field, respectively.

The above Lagrangians are obtained assuming the baryons to be point particles. Since the baryons are composite particles, therefore, there is a charge distribution and the magnetic coupling appears as this is due to a structure. Moreover, in the case of virtual photons, these electric and magnetic couplings acquire q^2 dependence.

Current for the non-resonant terms

The hadronic currents for the various non-resonant terms shown in Fig 7.2(a)–(d) are obtained using the non-linear sigma model described in the above sections. The expressions of the hadronic currents for the different channels are obtained using the Lagrangians given in Eqs. (7.21)–(7.25) and are expressed as [210, 30]:

$$J^\mu|_s = ieA_s\, F_s(s)\bar{u}(p')\not{p}_k\gamma_5\frac{\not{p}+\not{q}+M}{s-M^2}\left(\gamma^\mu e_p + i\frac{\kappa_p}{2M}\sigma^{\mu\nu}q_\nu\right)u(p), \tag{7.26}$$

$$J^\mu|_t = ieA_t\, F_t(t)\bar{u}(p')\left[(\not{p}-\not{p}')\cdot\gamma_5\right]u(p)\frac{(2p_k^\mu - q^\mu)}{t-M_k^2}, \tag{7.27}$$

$$J^\mu|_{u\Lambda} = ieA_u^\Lambda\, F_u^\Lambda(u)\bar{u}(p')\left(\gamma^\mu e_\Lambda + i\frac{\kappa_\Lambda}{2M_\Lambda}\sigma^{\mu\nu}q_\nu\right)\frac{\not{p}'-\not{q}+M_\Lambda}{u-M_\Lambda^2}\not{p}_k\gamma_5 u(p), \tag{7.28}$$

$$J^\mu|_{u\Sigma^0} = ieA_u^{\Sigma^0}\, F_u^{\Sigma^0}(u)\bar{u}(p')\left(\gamma^\mu e_{\Sigma^0} + i\frac{\kappa_{\Sigma^0}}{2M_{\Sigma^0}}\sigma^{\mu\nu}q_\nu\right)\frac{\not{p}'-\not{q}+M_{\Sigma^0}}{u-M_{\Sigma^0}^2} \times \not{p}_k\gamma_5 u(p), \tag{7.29}$$

$$J^\mu|_{CT} = -ieA_{CT}\, F_{CT}\bar{u}(p')\,\gamma^\mu\gamma_5\,u(p), \tag{7.30}$$

where CT stands for the contact term and $s,\ t,\ u$ are the Mandelstam variables defined as

$$t = (p-p')^2, \qquad u = (p'-q)^2, \tag{7.31}$$

and s is defined in Eq. (7.8). A_i's; $i = s,t,u,CT$ are the coupling strengths of s, t, u channels and the contact term, respectively, and are obtained as

$$A_s = A_t = A_u^\Lambda = A_{CT} = -\left(\frac{D+3F}{2\sqrt{3}f_\pi}\right) = -6.85\ \text{GeV}^{-1}, \tag{7.32}$$

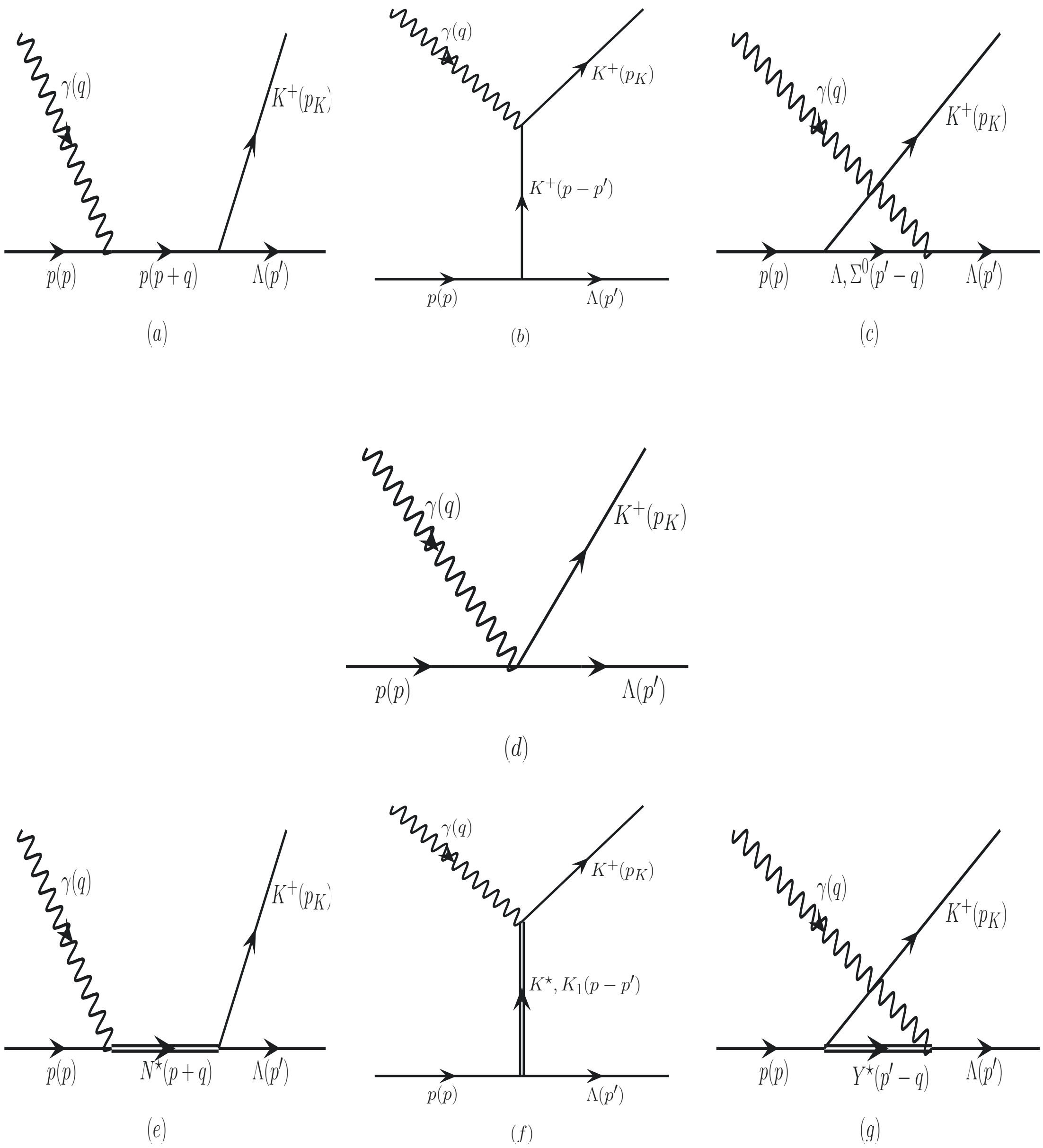

Figure 7.2: Feynman diagram for the various channels possible for the process $\gamma(q) + p(p) \rightarrow K^+(p_k) + \Lambda(p')$. (a) s channel, (b) t channel, (c) u channel and (d) contact term constitute the non-resonant terms. (e) nucleon resonances in the s channel, (f) kaon resonances in the t channel and (g) hyperon resonances in the u channel. The quantities in the bracket represent four momenta of the corresponding particles.

$$A_u^{\Sigma^0} = \left(\frac{D-F}{2f_\pi}\right) = 1.85 \text{ GeV}^{-1}. \tag{7.33}$$

All these couplings of non-resonant terms are generated by the chiral symmetry and are fixed by the low energy electroweak phenomenology consistent with experimental data.

The values of e and κ for proton, lambda and sigma are

$$\begin{aligned} e_p &= 1, & e_\Lambda &= 0, & e_{\Sigma^0} &= 0, \\ \kappa_p &= 1.793, & \kappa_\Lambda &= -0.613, & \kappa_{\Sigma^0} &= 1.61. \end{aligned} \tag{7.34}$$

In order to take into account the hadronic structure, the form factors $F_s(s)$, $F_t(t)$, $F_u(u)$ and F_{CT}, are introduced at the strong vertices. Various parameterizations of these form factors are available in the literature [144], however, we use the most general dipole form, parameterized as [143]:

$$F_x(x) = \frac{\Lambda_B^4}{\Lambda_B^4 + (x - M_x^2)^2}, \qquad x = s, t, u \tag{7.35}$$

where $\Lambda_B = 0.505$ GeV is the cut-off parameter taken to be same for all the background terms, whose value is fitted to the experimental data, x represents the Mandelstam variables $s,\ t,\ u$ and $M_x = M,\ M_k,\ M_Y$, corresponds to the mass of the baryons or mesons exchanged in the $s,\ t,\ u$ channels.

One of the most important properties of the electromagnetic current is the gauge invariance which corresponds to the current conservation. The total hadronic current for the non-resonant terms is given by

$$J^\mu = J^\mu|_s + J^\mu|_t + J^\mu|_{u\Lambda} + J^\mu|_{u\Sigma^0} + J^\mu|_{CT}. \tag{7.36}$$

The condition to fulfill gauge invariance is

$$q_\mu J^\mu = 0. \tag{7.37}$$

In the absence of the hadronic form factors ($F_s = F_t = F_u = F_{CT} = 1$), if we consider only the $s,\ t,\ u$ channel Born terms in the expression of the hadronic current

$$J^\mu = J^\mu|_s + J^\mu|_t + J^\mu|_{u\Lambda} + J^\mu|_{u\Sigma^0}, \tag{7.38}$$

then the condition given in Eq. (7.37) is applied to J^μ as defined in Eq. (7.38) in which the individual currents are defined in Eqs. (7.26)–(7.29). Using the coupling strengths obtained in our model from Eqs. (7.32) and (7.34), we obtain

$$q_\mu J^\mu = -\frac{D+F}{2\sqrt{3}f_\pi}\bar{u}(p')\left[(\not{p}_k + \not{p}' - \not{p})\gamma_5\right]u(p). \tag{7.39}$$

The above expression shows that in the presence of only s, t, u channel contributions, the hadronic current is not gauge invariant. However, when the contribution from the contact term *i.e.* $J^\mu|_{CT}$ is added, we obtain $q_\mu J^\mu = 0$ and J^μ satisfies the gauge invariance. The present model, thus, predicts the strength of the coupling of the contact term in such a way that the gauge invariance is satisfied in a natural way. On the other hand, in most of the effective Lagrangian used in the other isobar models with pseudoscalar and/or pseudovector interactions, the coupling strengths are modulated to obtain the gauge invariance.

As the hadronic form factors are taken into account in the hadronic current, the condition for gauge invariance gives

$$q_\mu J^\mu = -\frac{D+F}{2\sqrt{3}f_\pi}\bar{u}(p')\left[(\not{p}_k F_s + (\not{p}' - \not{p})F_t - \not{q}F_{CT})\gamma_5\right]u(p). \tag{7.40}$$

From the above equation, it is evident that due to the presence of hadronic form factor, the hadronic current is not gauge invariant. Therefore, in order to restore gauge invariance, the following term is added to Eq. (7.40)

$$q_\mu J^\mu_{add} = -\frac{D+F}{2\sqrt{3}f_\pi}\bar{u}(p')\left[\not{p}_k(F_{CT} - F_s) + (\not{p}' - \not{p})(F_{CT} - F_t)\right]\gamma_5 u(p). \tag{7.41}$$

Thus, the presence of the additional terms given in Eq. (7.41) implies that the gauge invariance can be achieved if the hadronic current J^μ defined through Eq. (7.36) is supplemented by adding an additional term J^μ_{add} given by

$$J^\mu_{add} = -\frac{D+F}{2\sqrt{3}f_\pi}\bar{u}(p')\left[\frac{2\not{p}_k p^\mu}{s-M^2}(F_{CT} - F_s) + \frac{2p_k^\mu}{t-M_k^2}(\not{p} - \not{p}')(F_{CT} - F_t)\right]u(p). \tag{7.42}$$

In order to take into account the effect of the form factor for the contact term, there are different prescriptions available in the literature, for example that of Ohta [217], Haberzettl *et al.* [244], Davidson and Workman [209], etc. In the present work, we have followed the prescription of Davidson and Workman [209], where F_{CT} is given by:

$$F_{CT} = F_s(s) + F_t(t) - F_s(s) \times F_t(t). \tag{7.43}$$

7.2.3 Resonance contribution

In this section, we discuss the contributions of the different nucleon, kaon and hyperon resonances.

Spin $\frac{1}{2}$ nucleon resonances

The hadronic current for the spin $\frac{1}{2}$ resonance state is given by

$$j^\mu_{\frac{1}{2}} = \bar{u}(p')\Gamma^\mu_{\frac{1}{2}} u(p), \tag{7.44}$$

where $u(p)$ and $\bar{u}(p')$ are, respectively, the Dirac spinor and adjoint Dirac spinor for spin $\frac{1}{2}$ particles and $\Gamma^\mu_{\frac{1}{2}}$ is the vertex function. For a positive parity state, $\Gamma^\mu_{\frac{1}{2}^+}$ is given by

$$\Gamma^\mu_{\frac{1}{2}^+} = V^\mu_{\frac{1}{2}}, \tag{7.45}$$

and for a negative parity resonance, $\Gamma^\mu_{\frac{1}{2}^-}$ is given by

$$\Gamma^\mu_{\frac{1}{2}^-} = V^\mu_{\frac{1}{2}} \gamma_5, \tag{7.46}$$

where $V^\mu_{\frac{1}{2}}$ represents the vector current parameterized in terms of $F_2^{R^+}$, as

$$V^\mu_{\frac{1}{2}} = \left[\frac{F_2^{R^+}}{2M} i\sigma^{\mu\alpha} q_\alpha \right]. \tag{7.47}$$

The coupling F_2^{R+} is derived from the helicity amplitudes extracted from the real photon scattering experiments. The explicit relation between the coupling F_2^{R+} and the helicity amplitude $A^p_{\frac{1}{2}}$ is given by [245]

$$A^p_{\frac{1}{2}} = \sqrt{\frac{2\pi\alpha}{M}\frac{(M_R \mp M)^2}{M_R^2 - M^2}}\left[\frac{M_R \pm M}{2M}F_2^{R^+}\right], \tag{7.48}$$

where the upper (lower) sign stands for the positive (negative) parity resonance. M_R is the mass of corresponding resonance. The value of the helicity amplitude $A^p_{\frac{1}{2}}$ for $S_{11}(1650)$ resonance is taken from MAID [139] while for the other spin $\frac{1}{2}$ nucleon resonances, these values are taken from PDG [237] and are quoted in Table 7.2.

The most general form of the hadronic currents for the s channel processes where a resonance state $R^{\frac{1}{2}}$ with spin $\frac{1}{2}$ is produced and decays to a kaon and a lambda in the final state, are written as [211, 246]

$$j^\mu\big|_R^{\frac{1}{2}\pm} = ie\ \bar{u}(p')\frac{g_{R^{\frac{1}{2}}K\Lambda}}{M_K}\not{p}_k\Gamma_s\frac{\not{p} + \not{q} + M_R}{s - M_R^2 + iM_R\Gamma_R}\Gamma^\mu_{\frac{1}{2}\pm}u(p), \tag{7.49}$$

where Γ_R is the decay width of the resonance, $\Gamma_s = 1(\gamma_5)$ stands for the positive (negative) parity resonances. $\Gamma_{\frac{1}{2}^+}$ and $\Gamma_{\frac{1}{2}^-}$ are, respectively, the vertex function for the positive and negative parity resonances, as defined in Eqs. (7.45) and (7.46). $g_{R^{\frac{1}{2}}K\Lambda}$ is the coupling strength for the process $R^{\frac{1}{2}} \to K\Lambda$, given in Table 7.1.

Due to the lack of experimental data, there is a large uncertainty associated with $RK\Lambda$ coupling at the $R^{\frac{1}{2}} \to K\Lambda$ vertex. We determine the $RK\Lambda$ coupling using the value of branching ratio and decay width of these resonances from PDG [237] and use the expression for the decay rate which is obtained by writing the most general form of $RK\Lambda$ Lagrangian [245],

$$\mathcal{L}_{R_{\frac{1}{2}}K\Lambda} = \frac{g_{R^{\frac{1}{2}}K\Lambda}}{M_K}\bar{\Psi}_{R_{\frac{1}{2}}}\ \Gamma_s^\mu\ \partial_\mu K^i\tau_i\,\Psi, \tag{7.50}$$

where $g_{R^{\frac{1}{2}}K\Lambda}$ is the $RK\Lambda$ coupling strength. Ψ is the nucleon field and $\Psi_{R_{\frac{1}{2}}}$ is the spin $\frac{1}{2}$ resonance field. K^i is the kaon field and τ is the isospin factor for the isospin

$\frac{1}{2}$ states. The interaction vertex $\Gamma_s^\mu = \gamma^\mu\gamma^5$ (γ^μ) stands for positive (negative) parity resonance states.

Using the above Lagrangian, one may obtain the expression for the decay width in the resonance rest frame as

$$\Gamma_{R_{\frac{1}{2}}\to K\Lambda} = \frac{\mathcal{C}}{4\pi}\left(\frac{g_{R\frac{1}{2}K\Lambda}}{M_K}\right)^2 (M_R \pm M_\Lambda)^2 \frac{E_\Lambda \mp M_\Lambda}{M_R}|\vec{p}_k^{\,\mathrm{cm}}|, \tag{7.51}$$

where the upper (lower) sign represents the positive (negative) parity resonance. The parameter $\mathcal{C}$ depends upon the charged state of R, $K\Lambda$ and is obtained from the isospin analysis and found out to be 1. $|\vec{p}_k^{\,cm}|$ is the outgoing kaon momentum measured from resonance rest frame and is given by,

$$|\vec{p}_k^{\,\mathrm{cm}}| = \frac{\sqrt{(W^2 - M_K^2 - M_\Lambda^2)^2 - 4M_K^2 M_\Lambda^2}}{2M_R} \tag{7.52}$$

and E_Λ, the lambda energy is

$$E_\Lambda = \frac{W^2 + M_\Lambda^2 - M_K^2}{2M_R}, \tag{7.53}$$

where W is the total center of mass energy carried by the resonance.

Using Eq. (7.51), the coupling for $R\frac{1}{2} \to K\Lambda$ is obtained and given in Table-7.1 for various spin $\frac{1}{2}$ resonances.

Spin $\frac{3}{2}$ nucleon resonances

Next, we discuss spin $\frac{3}{2}$ resonances exchanged in the s channel process. The general structure of the electromagnetic hadronic current for spin $\frac{3}{2}$ resonances describing the $\gamma N R_{\frac{3}{2}}$ excitations as well as the effective Lagrangian for describing the $R_{\frac{3}{2}}K\Lambda$ vertex is written in terms of the spin $\frac{3}{2}$ field $\Psi_\mu(p)$ using the Rarita-Schwinger formalism [247]. It is well known that the Rarita-Schwinger formalism is not unique for describing the spin $\frac{3}{2}$ field (as well as for the higher spin fields) and has a problem associated with the lower spin degrees of freedom. This leads to some ambiguities in describing the propagation of the off-shell spin $\frac{3}{2}$ fields using a propagator specially in the presence of interactions like the electromagnetic and strong interactions. The problem has been discussed extensively in literature for many years ever since the field theory of higher spins was developed using either the vector-spinor formalism [247] or the multi-spinor formalism [248]. Consequently there are various prescriptions for treating the propagator and the effective Lagrangians for the interacting fields of higher spin in a consistent way for describing the interaction of spin $\frac{3}{2}$ fields. One of the most popular prescriptions given Pascalutsa and Timmermans [249] has been investigated further in the latest works of Mart [250] and Vrancx *et al.* [251] and many other references cited there. However, in the present work, we follow the prescription used by us [212, 31, 213, 30, 214, 253, 254, 255, 256, 252, 257, 258] and many others [210, 211, 245, 246, 160, 259, 260] in the past to study the photo, electro and weak interaction induced pion, eta and kaon productions.

The general structure for the hadronic current for spin three-half resonance excitation is determined by the following expression

$$J_\mu^{\frac{3}{2}} = \bar{\psi}^\nu(p')\Gamma_{\nu\mu}^{\frac{3}{2}} u(p), \tag{7.54}$$

where $u(p)$ is the Dirac spinor for the nucleon, $\psi^\mu(p)$ is the Rarita-Schwinger spinor for spin three-half particle and $\Gamma_{\nu\mu}^{\frac{3}{2}}$ has the following general structure for the positive and negative parity resonance states [210, 245]:

$$\begin{aligned} \Gamma_{\nu\mu}^{\frac{3}{2}^+} &= V_{\nu\mu}^{\frac{3}{2}}\gamma_5 \\ \Gamma_{\nu\mu}^{\frac{3}{2}^-} &= V_{\nu\mu}^{\frac{3}{2}}, \end{aligned} \tag{7.55}$$

where $V_{\mu\nu}^{\frac{3}{2}}$ is the vector current for spin three-half resonances and is given by [261, 262]

$$V_{\nu\mu}^{\frac{3}{2}} = \left[\frac{C_3^p}{M}(g_{\mu\nu}\not{q} - q_\nu\gamma_\mu) + \frac{C_4^p}{M^2}(g_{\mu\nu}q\cdot p' - q_\nu p'_\mu) + \frac{C_5^p}{M^2}(g_{\mu\nu}q\cdot p - q_\nu p_\mu)\right] \tag{7.56}$$

with C_i^p being the γNR couplings. The couplings $C_i^p;\ i = 3, 4, 5$ are related with the helicity amplitudes $A_{\frac{1}{2}}$, $A_{\frac{3}{2}}$ and $S_{\frac{1}{2}}$ by the following relations [245]:

$$\begin{aligned} A^p_{\frac{3}{2}} &= \sqrt{\frac{\pi\alpha}{M}\frac{(M_R \mp M)^2}{M_R^2 - M^2}}\left[\frac{C_3^p}{M}(M \pm M_R) \pm \frac{C_4^p}{M^2}\frac{M_R^2 - M^2}{2}\right. \\ &\pm \left.\frac{C_5^p}{M^2}\frac{M_R^2 - M^2}{2}\right] \end{aligned} \tag{7.57}$$

$$\begin{aligned} A^p_{\frac{1}{2}} &= \sqrt{\frac{\pi\alpha}{3M}\frac{(M_R \mp M)^2}{M_R^2 - M^2}}\left[\frac{C_3^p}{M}\frac{M^2 + MM_R}{M_R} - \frac{C_4^p}{M^2}\frac{M_R^2 - M^2}{2}\right. \\ &- \left.\frac{C_5^p}{M^2}\frac{M_R^2 - M^2}{2}\right] \end{aligned} \tag{7.58}$$

$$\begin{aligned} S^p_{\frac{1}{2}} &= \pm\sqrt{\frac{\pi\alpha}{6M}\frac{(M_R \mp M)^2}{M_R^2 - M^2}}\frac{\sqrt{(M_R^2 - M^2)^2}}{M_R^2}\left[\frac{C_3^p}{M}M_R + \frac{C_4^p}{M^2}M_R^2\right. \\ &+ \left.\frac{C_5^p}{M^2}\frac{M_R^2 + M^2}{2}\right], \end{aligned} \tag{7.59}$$

where $A_{\frac{3}{2},\frac{1}{2}}$ and $S_{\frac{1}{2}}$ are the amplitudes corresponding to the transverse and longitudinal polarizations of the photon, respectively. Since in the present work, we have considered $K\Lambda$ production induced by the real photon, therefore, the amplitude corresponding to the longitudinal polarization vanishes. Thus, in the numerical calculations, we have taken $S_{\frac{1}{2}} = 0$. The fitted values of $A_{\frac{1}{2}}$ and $A_{\frac{3}{2}}$ have been taken from MAID [139] and PDG [237] for $P_{13}(1720)$ and $P_{13}(1900)$ resonance, respectively, and are quoted in Table 7.2. The upper (lower) sign in Eqs. (7.57)–(7.59) represents the positive (negative) parity resonance states.

The most general expression of the hadronic current for the s channel where a resonance state with spin $\frac{3}{2}$, $R^{\frac{3}{2}}$ (with positive or negative parity) is produced and decays to a kaon and a lambda in the final state may be written as [211, 246]:

$$j^\mu\Big|_R^{\frac{3}{2}\pm} = ie\,\frac{g_{RK\Lambda}}{M_K}\frac{p_k^\alpha \Gamma_s}{s - M_R^2 + iM_R\Gamma_R}\bar{u}(p')P^{3/2}_{\alpha\beta}(p_R)\Gamma^{\beta\mu}_{\frac{3}{2}\pm}u(p), \quad p_R = p + q, \tag{7.60}$$

where $\Gamma_s = 1(\gamma_5)$ for positive (negative) parity resonances, $g_{RK\Lambda}$ is the coupling strength for $R \to K\Lambda$ (R can be any spin $\frac{3}{2}$ resonance given in Table 7.1), determined from partial decay widths. M_R is the mass of the resonance and Γ_R is its decay width. For the sake of unitarity restoration, we have considered the energy dependent decay width of the nucleon resonances, which will be discussed in Section 7.2.3.

In Eq. (7.60), $P^{3/2}_{\alpha\beta}$ is spin three-half projection operator and is given by

$$P^{3/2}_{\alpha\beta}(p') = -(\not{p}' + M_R)\left(g_{\alpha\beta} - \frac{2}{3}\frac{p'_\alpha p'_\beta}{M_R^2} + \frac{1}{3}\frac{p'_\alpha \gamma_\beta - p'_\beta \gamma_\alpha}{M_R} - \frac{1}{3}\gamma_\alpha\gamma_\beta\right). \quad (7.61)$$

The coupling strength $g_{RK\Lambda}$ is determined using the data of branching ratio and decay width of these resonances from PDG [237].

The expression for the decay rate is obtained by writing the most general form of $RK\Lambda$ Lagrangian [245],

$$\mathcal{L}_{R_{\frac{3}{2}}K\Lambda} = \frac{g_{RK\Lambda}}{M_K}\bar{\Psi}^\mu_{R_{\frac{3}{2}}}\ \Gamma_s\ \partial_\mu K^i \tau_i\ \Psi \quad (7.62)$$

where $g_{RK\Lambda}$ is the $RK\Lambda$ coupling strength. Ψ is the nucleon field and $\Psi^\mu_{R_{\frac{3}{2}}}$ are the fields associated with the spin $\frac{3}{2}$ resonances. K^i is the kaon field and τ is isopin factor. The interaction vertex Γ_s is 1 for positive parity state and γ_5 for negative parity state. Using the above Lagrangian, one may obtain the expression for the decay width in the resonance rest frame as

$$\Gamma_{R_{\frac{3}{2}}\to K\Lambda} = \frac{\mathcal{C}}{12\pi}\left(\frac{g_{RK\Lambda}}{M_K}\right)^2 \frac{E_\Lambda \pm M_\Lambda}{M_R}|\vec{p}_k^{\,cm}|^3, \quad (7.63)$$

where the upper (lower) sign represents the positive (negative) parity resonance state. The parameter $\mathcal{C}$ is obtained from the isospin analysis and found out to be 1 for isospin $\frac{1}{2}$ state. The expressions for $|\vec{p}_k^{\,cm}|$ and E_Λ are given in Eqs. (7.52) and (7.53), respectively.

Using the above expressions for decay width, the couplings for $R\frac{3}{2} \to K\Lambda$ are obtained and given in Table-7.1 for the spin $\frac{3}{2}$ resonances considered in this work.

Energy dependent decay widths of the nucleon resonances

As already discussed in the introduction that the unitarity can be restored, even at the tree level, if widths for the various nucleon resonances are taken to be energy

Table 7.1: Properties of the resonances included in the present model, with Breit-Wigner mass M_R, spin J, isospin I, parity P, the total decay width Γ, the branching ratio into $K\Lambda$ and $g_{RK\Lambda}$ stands for the coupling strength at the $RK\Lambda$ vertex.

Resonances R_{2I2J}	M_R [GeV]	I	J	P	Γ (GeV)	$K\Lambda$ branching ratio (%)	$g_{RK\Lambda}$
$S_{11}(1650)$	1.655 ± 0.015	$\frac{1}{2}$	$\frac{1}{2}$	$-$	0.135 ± 0.035	10 ± 5	0.45
$P_{11}(1710)$	1.700 ± 0.020	$\frac{1}{2}$	$\frac{1}{2}$	$+$	0.120 ± 0.040	15 ± 10	-0.61
$P_{13}(1720)$	1.675 ± 0.015	$\frac{1}{2}$	$\frac{3}{2}$	$+$	$0.250\pm^{0.150}_{0.100}$	4.5 ± 0.5	1.73
$P_{11}(1880)$	1.860 ± 0.040	$\frac{1}{2}$	$\frac{1}{2}$	$+$	0.230 ± 0.050	20 ± 8	0.52
$S_{11}(1895)$	1.910 ± 0.020	$\frac{1}{2}$	$\frac{1}{2}$	$-$	0.110 ± 0.030	18 ± 5	0.28
$P_{13}(1900)$	1.920 ± 0.020	$\frac{1}{2}$	$\frac{3}{2}$	$+$	0.150 ± 0.050	11 ± 9	-0.62

dependent. In the present work, we have considered the energy dependent decay widths to be of the following form [145]

$$\Gamma_R(W) = \Gamma_R \frac{W}{M_R} \sum_i \left[x_i \left(\frac{|\vec{q}_i|}{|\vec{q}_i^R|} \right)^{2l+1} \frac{D_l(|\vec{q}_i|)}{D_l(|\vec{q}_i^R|)} \right], \tag{7.64}$$

where the sum i runs over all possible meson-baryon decay modes, with the relative orbital momentum l. Γ_R and x_i denote the total decay width, and the branching ratio of a resonance into different meson-baryon channels [237], respectively. The momenta $|\vec{q}_i|$ and $|\vec{q}_i^R|$ have the following form:

$$|\vec{q}_i^R| = \sqrt{\frac{(M_R^2 - M_B^2 + M_m^2)^2}{4M_R^2} - M_m^2}, \tag{7.65}$$

$$|\vec{q}_i| = \sqrt{\frac{(W^2 - M_B^2 + M_m^2)^2}{4W^2} - M_m^2}, \quad \textit{and} \tag{7.66}$$

$$D_l(x) = exp\left(-\frac{x^2}{3\alpha^2} \right), \tag{7.67}$$

which is consistent with the value of $\alpha = 400$ MeV taken in Ref. [145], and $x = |\vec{q}_i|$ or $|\vec{q}_i^R|$.

In the case of energy dependent widths, Λ_B and Λ_R are taken to be $\Lambda_B = 0.505$

GeV and $\Lambda_R = 1.32$ GeV, respectively while in the case of fixed widths, these values are $\Lambda_B = 0.525$ GeV and $\Lambda_R = 1.1$ GeV.

Spin $\frac{1}{2}$ hyperon resonances

Along with the nucleon resonance exchange contributions in the s channel, we have also taken into account the hyperon resonances exchanged in the u channel. In the present work, we have taken two lambda resonances, $\Lambda^*(1405)$ and $\Lambda^*(1800)$ with $J^P = \frac{1}{2}^-$ in the u channel. The Lagrangians for the strong and the electromagnetic vertices in the case of Λ^* exchange are given as [160, 263, 264, 265]:

$$\mathcal{L}_{\gamma\Lambda\Lambda^*} = e\frac{\kappa_{\Lambda\Lambda^*}}{2(M_{\Lambda^*} + M_\Lambda)}\bar{\psi}_{\Lambda^*}\sigma_{\mu\nu}\Gamma_s\psi_\Lambda F^{\mu\nu} + h.c., \tag{7.68}$$

$$\mathcal{L}_{pK\Lambda^*} = \frac{g_{pK\Lambda^*}}{f_\pi}(\partial^\mu K^\dagger)\bar{\psi}_p\Gamma_\mu\psi_{\Lambda^*} + h.c., \tag{7.69}$$

with $\kappa_{\Lambda\Lambda^*}$, the transition magnetic moment between Λ and Λ^*. $g_{pK\Lambda^*}$ is the coupling strength at $pK\Lambda^*$ vertex. $\Gamma_s = 1(\gamma_5)$ and $\Gamma_\mu = \gamma_\mu(\gamma_\mu\gamma_5)$ for the positive (negative) parity resonances.

Using the above Lagrangians, the hadronic current for the Λ^* resonance exchange may be written as

$$\begin{aligned} J_\mu\big|_{\Lambda^*\pm} &= ie\bar{u}(p')\frac{g}{M_\Lambda + M_{\Lambda^*}}\sigma_{\mu\nu}q^\nu\Gamma_s\left(\frac{\not{p}' - \not{q} + M_{\Lambda^*}}{u - M_{\Lambda^*}^2 + iM_{\Lambda^*}\Gamma_{\Lambda^*}}\right) \\ &\times \not{p}_k\gamma_5\Gamma u(p), \end{aligned} \tag{7.70}$$

with $g = \kappa_{\Lambda\Lambda^*}g_{pK\Lambda^*}/f_\pi$, M_{Λ^*} and Γ_{Λ^*} being the mass and the decay width of Λ^*. Unlike the nucleon resonances where the strong and electromagnetic couplings are determined phenomenologically by the partial decay width and the helicity amplitudes, respectively, the experimental data is not adequate in the case of hyperon resonances, to determine these couplings. Therefore, the parameter g is treated as a free parameter to be fitted to the experimental data. The values of the different parameters of the Λ^* taken in the present model are summarized in Table 7.3.

Table 7.2: Values of the helicity amplitude $A_{\frac{1}{2}}$ and $A_{\frac{3}{2}}$ for the different nucleon resonances. The values for $S_{11}(1650)$ and $P_{13}(1720)$ are taken from MAID [139]. For the rest of the resonances, the parameterization of $A_{\frac{1}{2}}$ and $A_{\frac{3}{2}}$ are not available in MAID and are taken from PDG [237].

Resonance	Helicity amplitude	
	$A_{\frac{1}{2}}$ (10^{-3} GeV$^{-1/2}$)	$A_{\frac{3}{2}}$ (10^{-3} GeV$^{-1/2}$)
$S_{11}(1650)$	33.3	-
$P_{11}(1710)$	50	-
$P_{13}(1720)$	73	-11.5
$P_{11}(1880)$	21	-
$S_{11}(1895)$	-16	-
$P_{13}(1900)$	24	-67

Spin 1 kaon resonances

In the present work, we have considered two kaon resonances in the t channel: a vector meson $K^*(892)$ and an axial vector meson $K_1(1270)$. The Lagrangians for the electromagnetic and strong vertices, when a vector kaon is exchanged in the t channel, are given by [160, 263, 264, 265]:

$$\mathcal{L}_{\gamma KK^*} = i\frac{e\kappa_{KK^*}}{4\mu}\epsilon_{\mu\nu\lambda\sigma}F^{\mu\nu}V^{\lambda\sigma}K, \tag{7.71}$$

$$\mathcal{L}_{K^*\Lambda p} = -\left(g^v_{K^*\Lambda p}\bar{\psi}_\Lambda\gamma_\mu\psi_p V^\mu - \frac{g^t_{K^*\Lambda p}}{2(M+M_\Lambda)}\bar{\psi}_\Lambda\sigma_{\mu\nu}V^{\mu\nu}\psi_p\right) + h.c., \tag{7.72}$$

where κ_{KK^*} is the coupling strength of the γKK^* vertex, μ is an arbitrary mass factor which is introduced to make the Lagrangian dimensionless. μ is chosen to be 1 GeV. The vector meson tensor $V^{\mu\nu}$ is defined as $V^{\mu\nu} = \partial^\nu V^\mu - \partial^\mu V^\nu$, with V^μ, the vector kaon field. $g^v_{K^*\Lambda p}$ and $g^t_{K^*\Lambda p}$ are the vector and the tensor couplings, respectively, at the strong $K^*\Lambda p$ vertex.

Using the Lagrangians given in Eqs. (7.71) and (7.72), the hadronic current

Table 7.3: Properties of the hyperon and the kaon resonances included in the present model, with mass M_R, spin J, isospin I, parity P, the total decay width Γ, the coupling parameter g for the hyperon resonances, and the vector G_K^v and tensor G_K^t couplings for the kaon resonances. It is to be noted that these couplings g, G_K^v and G_K^t contains both the electromagnetic as well as the strong coupling strengths.

Resonances	M_R [GeV]	J	I	P	Γ (GeV)	g	G_K^v	G_K^t
Λ^* (1405)	$1.405\pm^{0.0013}_{0.001}$	$\frac{1}{2}$	0	$-$	0.0505 ± 0.002	-10.18	-	-
Λ^* (1800)	$1.800\pm^{0.080}_{0.050}$	$\frac{1}{2}$	0	$-$	0.300 ± 0.100	-4.0	-	-
$K^*(892)$	0.89166 ± 0.00026	1	$\frac{1}{2}$	$-$	0.0508 ± 0.0009	-	-0.18	0.02
$K_1(1270)$	1.272 ± 0.007	1	$\frac{1}{2}$	$+$	0.090 ± 0.020	-	0.28	-0.28

for the K^* exchange is obtained as

$$
\begin{aligned}
J_\mu\big|_{K^*} &= ie\bar{u}(p')\epsilon_{\mu\nu\rho\sigma}q^\rho(p'-p)^\sigma \left(\frac{-g^{\nu\alpha}+(p-p')^\nu(p-p')^\alpha/M_{K^*}^2}{t-M_{K^*}^2+iM_{K^*}\Gamma_{K^*}}\right) \\
&\times \left[G_{K^*}^v\gamma_\alpha + \frac{G_{K^*}^t}{M+M_\Lambda}(\not{p}'-\not{p})\gamma_\alpha\right]u(p), \qquad (7.73)
\end{aligned}
$$

with $G_{K^*}^v = \kappa_{KK^*}g_{K^*\Lambda p}^v/\mu$ and $G_{K^*}^t = \kappa_{KK^*}g_{K^*\Lambda p}^t/\mu$. M_{K^*} and Γ_{K^*} are the mass and width of the K^* resonance, respectively. Due to the lack of the experimental data on the K^* and K_1 resonances, the values of $G_{K^*}^v$ and $G_{K^*}^t$ can not be determined phenomenologically and are treated as free parameters to be fitted to the experimental data of the $K\Lambda$ production and are quoted in Table 7.3.

The Lagrangian for the electromagnetic and strong vertices, when an axial vector kaon resonance is exchanged in the t channel, is given by [160, 263, 264, 265]:

$$
\mathcal{L}_{\gamma KK_1} = i\frac{e\kappa_{KK_1}}{\mu}\partial_\mu A_\nu \mathcal{V}_p^{\mu\nu}K, \qquad (7.74)
$$

$$
\mathcal{L}_{K_1\Lambda p} = -\left(g_{K_1\Lambda p}^v\bar{\psi}_\Lambda\gamma_\mu\gamma_5\psi_p\mathcal{V}_p^\mu - \frac{g_{K_1\Lambda p}^t}{2(M+M_\Lambda)}\bar{\psi}_\Lambda\sigma_{\mu\nu}\gamma_5\mathcal{V}_p^{\mu\nu}\psi_p\right) + h.c. \qquad (7.75)
$$

where κ_{KK_1} is the coupling strength of the electromagnetic γKK_1 vertex. The axial vector meson tensor $\mathcal{V}_p^{\mu\nu}$ is defined as $\mathcal{V}_p^{\mu\nu} = \partial^\nu\mathcal{V}_p^\mu - \partial^\mu\mathcal{V}_p^\nu$, with $\mathcal{V}_p^\mu$, the axial vector kaon field. $g^{v}_{K_1\Lambda p}$ and $g^{t}_{K_1\Lambda p}$ are the vector and the tensor couplings, respectively, at the strong $K_1\Lambda p$ vertex.

The hadronic current for the axial vector kaon K_1 exchange in the t channel is obtained, using Eqs. (7.74) and (7.75), as

$$\begin{aligned} J_\mu\big|_{K_1} &= ie\bar{u}(p')[g_{\alpha\mu}q\cdot(p-p') - q_\alpha(p-p')_\mu]\left(\frac{-g^{\alpha\rho}+(p-p')^\alpha(p-p')^\rho/M^2_{K_1}}{t-M^2_{K_1}+iM_{K_1}\Gamma_{K_1}}\right) \\ &\times \left[G^{v}_{K_1}\gamma_\rho\gamma_5 + \frac{G^{t}_{K_1}}{M+M_\Lambda}(\not{p}'-\not{p})\gamma_\rho\gamma_5\right]u(p), \end{aligned} \tag{7.76}$$

with $G^{v}_{K_1} = \kappa_{KK^*}g^{v}_{K_1\Lambda p}/\mu$ and $G^{t}_{K_1} = \kappa_{KK^*}g^{t}_{K_1\Lambda p}/\mu$. M_{K_1} and Γ_{K_1} are the mass and width of the K_1 resonance, respectively. The values of $G^{v}_{K_1}$ and $G^{t}_{K_1}$ are treated as free parameters to be fitted to the experimental data of the $K\Lambda$ production and are quoted in Table 7.3.

In analogy with the non-resonant terms, in the case of resonances we have considered the following form factors at the strong vertex, in order to take into account the hadronic structure:

$$F^*_x(x) = \frac{\Lambda^4_R}{\Lambda^4_R + (x - M^2_x)^2}, \tag{7.77}$$

where Λ_R is the cut-off parameter whose value is fitted to the experimental data, x represents the Mandelstam variables $s,\ t,\ u$ and $M_x = M_R,\ M_{K^*},\ M_{K_1},\ M_{Y^*}$, corresponding to the mass of the nucleon, kaon or hyperon resonances exchanged in the $s,\ t,$ and u channels. In the case of nucleon resonances, the value of the cut-off parameter Λ_R is fitted to be $\Lambda_R = 1.32$ GeV, while in the case of kaon and hyperon resonances, the value of Λ_R is taken to be $\Lambda_R = \Lambda_B = 0.505$ GeV.

7.3 Results and discussions

We have used Eq. (7.7) to numerically evaluate the differential cross section $\frac{d\sigma}{d\cos\theta_k}\Big|_{CM}$ and the total cross section σ is obtained by integrating Eq. (7.7) over the polar angle *i.e.*

$$\sigma = \int_{\cos\theta_k^{min}}^{\cos\theta_k^{max}} \frac{1}{32\pi s}\frac{|\vec{p}\,'|}{|\vec{p}|}\overline{\sum_r}\sum |\mathcal{M}^r|^2 d\cos\theta_k, \tag{7.78}$$

where $\cos\theta_k^{min}$ ($\cos\theta_k^{max}$) is taken to be -1 ($+1$) in order to cover the full range of the scattering angle.

In the expression for the transition amplitude $\mathcal{M}^r$ in the aforementioned equation, we have taken the contributions from the background and the resonance terms and added them coherently. Therefore, the hadronic current of the full model is expressed as:

$$\begin{aligned} J^\mu|_{Full} &= J^\mu|_s + J^\mu|_t + J^\mu|_{u\Lambda} + J^\mu|_{u\Sigma} + J^\mu|_{CT} + J^\mu|_{add} + J^\mu|_R + J^\mu|_{\Lambda^*} \\ &+ J^\mu|_{K^*} + J^\mu|_{K_1}, \end{aligned} \tag{7.79}$$

where $J^\mu|_{add}$ (given in Eq. (7.42)) ensures the gauge invariance of the total hadronic current, and $J^\mu|_R$ and $J^\mu|_{\Lambda^*}$ are expressed as

$$\begin{aligned} J^\mu|_R &= J^\mu|_{S_{11}(1650)} + J^\mu|_{P_{11}(1710)} + J^\mu|_{P_{13}(1720)} + J^\mu|_{P_{11}(1880)} \\ &+ J^\mu|_{S_{11}(1895)} + J^\mu|_{P_{13}(1900)}, \end{aligned} \tag{7.80}$$

$$J^\mu|_{\Lambda^*} = J^\mu|_{\Lambda^*(1405)} + J^\mu|_{\Lambda^*(1800)}. \tag{7.81}$$

The expressions of J^μ appearing in the above equations are given explicitly in Section 7.2.

The background terms consist of the non-resonant *i.e.* s, t, u and contact terms as well as the kaon and hyperon resonances exchanged in the t and u channels. The nucleon resonances exchanged in the s channel constitute the resonance contribution. This nomenclature for the resonance and the background terms is used because all the terms used in calculating the background contribution do not resonate in the physical region while the s channel resonances do so. The strong and electromagnetic couplings of the non-resonant terms are predicted by the non-linear sigma model with the chiral SU(3) symmetry. For the s, t and u channels, a dipole parameterization of the hadronic form factors (Eq. (7.35)) is

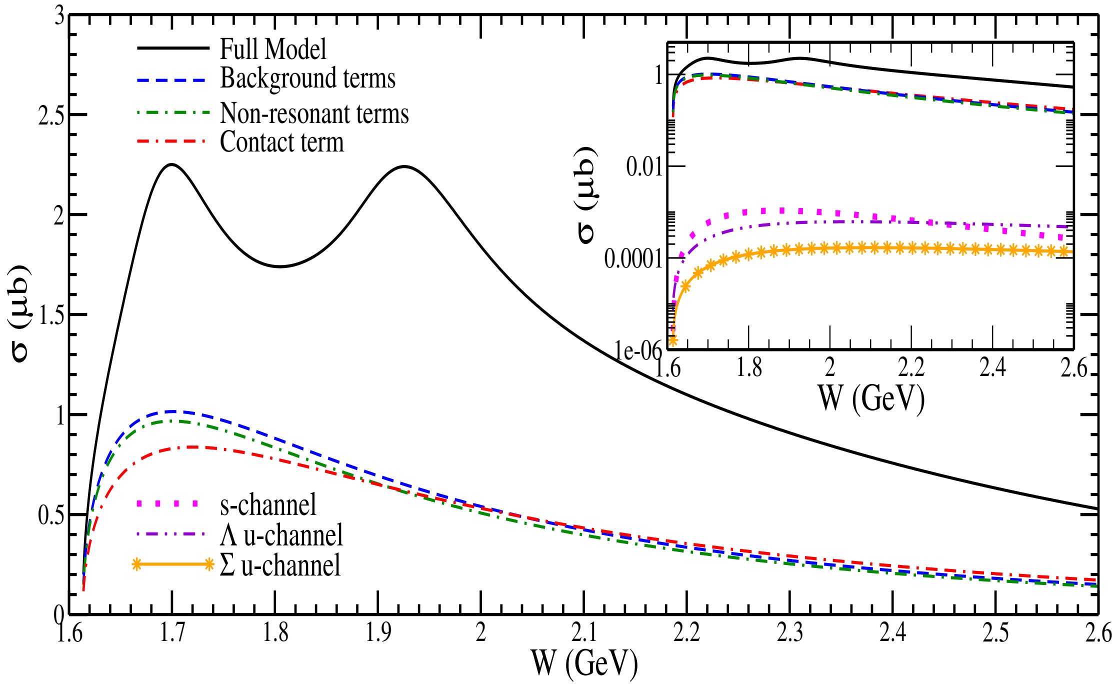

Figure 7.3: Total cross section σ as a function of CM energy W for the process $\gamma + p \rightarrow K^+ + \Lambda$. Solid line represents the results of the full model of the present work by taking into account the W dependent decay widths of the nucleon resonances as discussed in Section 7.2.3. Dashed line, dashed-dotted line, double-dashed-dotted line represents the results of the background terms, non-resonant terms and the contact term, respectively. In addition to the aforementioned four cases, in the inset (note the log scale), the individual contribution from the nucleon exchanged in the s channel, Λ exchanged in the u channel and Σ exchanged in the u channel have been shown, respectively, by the dotted line, double-dotted-dashed line and solid line with star symbol.

used while for the contact term, the prescription given by Davidson and Workman [209] (Eq. (7.43)) is used. In the case of nucleon resonances, the energy dependent decay widths (unless stated otherwise) of the different resonances as discussed in Section 7.2.3, are taken into account. The electromagnetic (γNR) and strong ($RK\Lambda$) couplings of the s channel resonances (R) are deduced, respectively, from the helicity amplitudes of the $\gamma N \rightarrow R$ transitions and the partial decay width of the resonances (R) to $K\Lambda$ channel and those of the u channel (Y^*) and t channel ($K^*,\ K_1$) resonances are fitted to reproduce the current experimental data available in this energy region. For the numerical calculations, we have taken the cut-off parameter for the background and resonance terms, respectively, to be $\Lambda_B = 0.505$ GeV and $\Lambda_R = 1.32$ GeV for the energy dependent decay widths of the nucleon resonances, while, for comparison, we have also taken the fixed widths, for which the best fit for the total scattering cross section (Figure 7.5) is obtained with $\Lambda_B = 0.525$ GeV and $\Lambda_R = 1.1$ GeV, whereas in other calculations, these parameters are taken as $\Lambda_B = 1.235$ GeV and $\Lambda_R = 1.864$ GeV in Ref. [202], and $\Lambda_B = 0.70$ GeV and $\Lambda_R = 1.31$ GeV in Ref. [266]. The numerical results are presented for the total and differential cross sections and are compared with the available experimental data from CLAS and SAPHIR as well as with some of the recent theoretical models.

In the following, we present the results of the total cross section σ as a function of CM energy W in section 7.3.1 and the results of the differential cross section $\left.\frac{d\sigma}{d\cos\theta_k}\right|_{CM}$ as a function of $\cos\theta_k^{CM}$ for fixed W as well as a function of W for fixed $\cos\theta_k^{CM}$ in section 7.3.2.

7.3.1 Total cross section

Discussion of theoretical results

In Figure 7.3, we have presented the results of σ *vs.* W for the $K\Lambda$ production induced by the photon beam off the proton target. The results have been presented separately showing the contributions from the background terms as well as the total contributions by including the well established nucleon resonances in the s channel with spin- 1/2 and 3/2 lying below $W = 2$ GeV, which have been considered in this work (Table 7.1). The individual contribution from the non-resonant terms i.e. individual contribution of s, t and u channel Born terms as well as the contact term, are also shown separately. It may be observed that the contact term is the dominant one among the non-resonant terms. At low and intermediate W *i.e.* from threshold up to 2 GeV, the contact term has smaller contribution than the total non-resonant contribution, however, at high W, beyond 2 GeV, the contact term has a larger contribution than the contribution from the total non-resonant terms. For example, in the peak region, $W = 1.7$ GeV, individually the contact term is $\sim 15\%$ smaller than the non-resonant terms while at $W = 2.6$ GeV, the contact term contributes $\sim 20\%$ more than the non-resonant terms. The contributions of the hyperon and the kaon resonances are small but increase the value of the total cross section. In the inset of this figure, we have also shown the incoherent contribution from the s and u channel Born terms. It may be observed from the figure that the incoherent contributions of the s and u channels are very small as compared to the results of the full model, however, their interference with the contact term and with the different resonances considered in the s channel when all the amplitudes are added coherently, has a significant contribution to the cross section (not explicitly shown here). It is worth mentioning that in the present model, the contribution of the non-resonant terms including the contact term is relatively small as compared to the other isobar model using SU(3) symmetry, even though the value of the coupling constants are similar. This is mainly because of the smaller value of the cut-off parameter Λ_B. Moreover, the smaller value of Λ_B used in the strong form factors of t and u channel diagrams mediated by the kaon and hyperon resonances also suppresses their contribution. Both these effects prevent the cross section from rising and obtain better agreement with the experiments in the region of low energy.

The impact of each resonance considered in this work on the total contribution has been explicitly discussed in Figure 7.4, where we have depicted the effect of individual contributions from the various s channel resonances considered in the present work. The incoherent contribution of the individual resonances is comparatively low as compared to the total cross section but the interference of the s channel resonance with the background terms when all the amplitudes

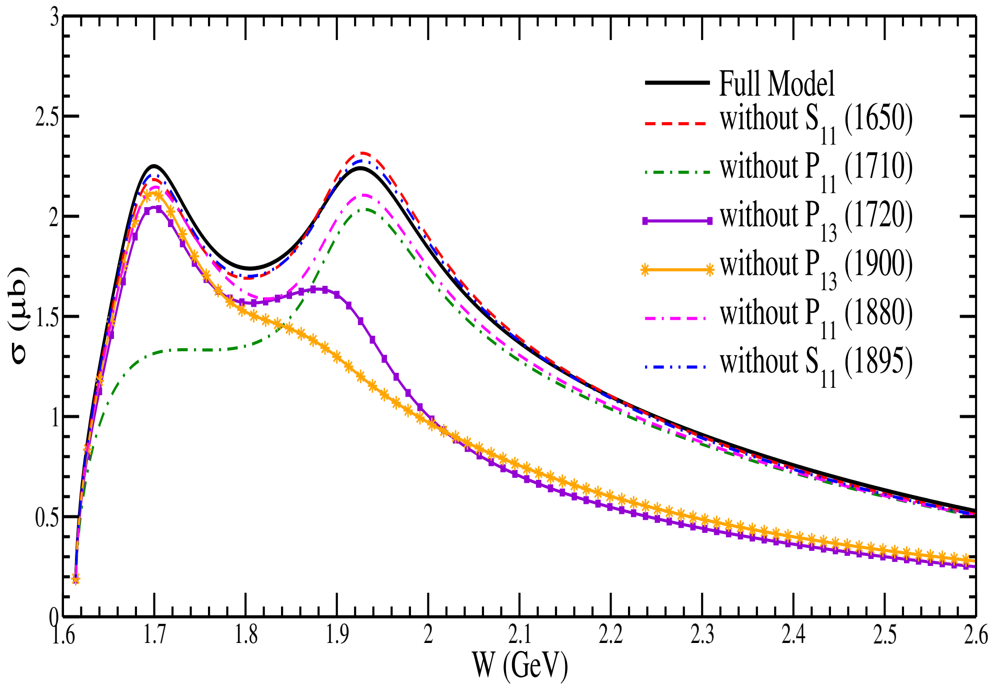

Figure 7.4: σ *vs.* W for the process $\gamma+p \rightarrow K^{+}+\Lambda$. Solid line represents the results of the full model of the present work, dashed line, dashed-dotted line, solid line with square, solid line with star, double-dashed-dotted line and double-dotted-dashed line represents the results of the full model when $S_{11}(1650)$, $P_{11}(1710)$, $P_{13}(1720)$, $P_{11}(1880)$, $S_{11}(1895)$ and $P_{13}(1900)$ resonance, respectively, is not taken into account.

are added coherently, contributes significantly to the total cross section. In this figure, we have presented the results of the full model when a particular resonance is switched off. The comparison of the results of the full model with the result when a particular resonance is switched off shows the significance (without the experimental data) of that particular resonance.

One may observe from the figure that $P_{11}(1710)$ resonance has a significant effect on the total cross section in the region $W = 1.61 - 2.3$ GeV which becomes small for $W > 2.3$ GeV. The absence of $P_{11}(1710)$ reduces the first peak by $\sim 42\%$ while the second peak is reduced by $\sim 9\%$. In the dip region, the total cross section in the absence of $P_{11}(1710)$ is reduced by $\sim 22\%$. The contribution of $P_{13}(1720)$

and $P_{13}(1900)$ resonances are important for the $K\Lambda$ production at all values of W. It must be noted that when the contribution from $P_{13}(1720)$ or $P_{13}(1900)$ resonance is excluded, the results beyond $W = 2$ GeV are suppressed significantly. Although the first peak and the dip region are not much affected (reduced by about 10%) by the absence of the $P_{13}(1720)$ resonance, the second peak is suppressed by $\sim 20\%$ as well as it is shifted from $W = 1.92$ GeV to $W = 1.88$ GeV. In the absence of $P_{13}(1900)$ resonance, the cross section in the first peak is reduced by about 6%, while it is reduced by 13% in the dip region and the second peak in the energy region of W around 1.9 GeV does not appear. It must be pointed out that beyond $W > 1.7$ GeV, $P_{13}(1900)$ has the most dominant contribution followed by $P_{13}(1720)$ resonance. At $W = 2.6$ GeV, by switching $P_{13}(1720)$ or $P_{13}(1900)$ resonance off, the total cross section is reduced by $\sim 53\%$ and 47%, respectively. The effect of $P_{11}(1880)$ is small in the entire range of W in which the cross section reduces to $\sim 5-10\%$, if this resonance is switched off. The two S_{11} resonances, *viz.* $S_{11}(1650)$ and $S_{11}(1895)$, have very small effect on the total cross section in the entire range of W.

Comparison with the experimental data

In Figs. 7.5 and 7.6, we have shown the results for the total scattering cross section σ *vs.* W obtained for the full model (Eq. (7.79)) by taking both energy dependent as well as fixed decay widths of the nucleon resonances into account and compared them with the experimental results available from CLAS 2006 [132], SAPHIR 2004 [131] and SAPHIR 1998 [130]. To show the significance of the present model in the threshold region, we have presented in Figure 7.6 our results in the range 1.6 GeV $< W <$ 1.72 GeV. Before we compare our results with the experimental results from CLAS and SAPHIR, the main features of the data on the total cross section can be classified with some distinct features in three kinematic regions summarized as:

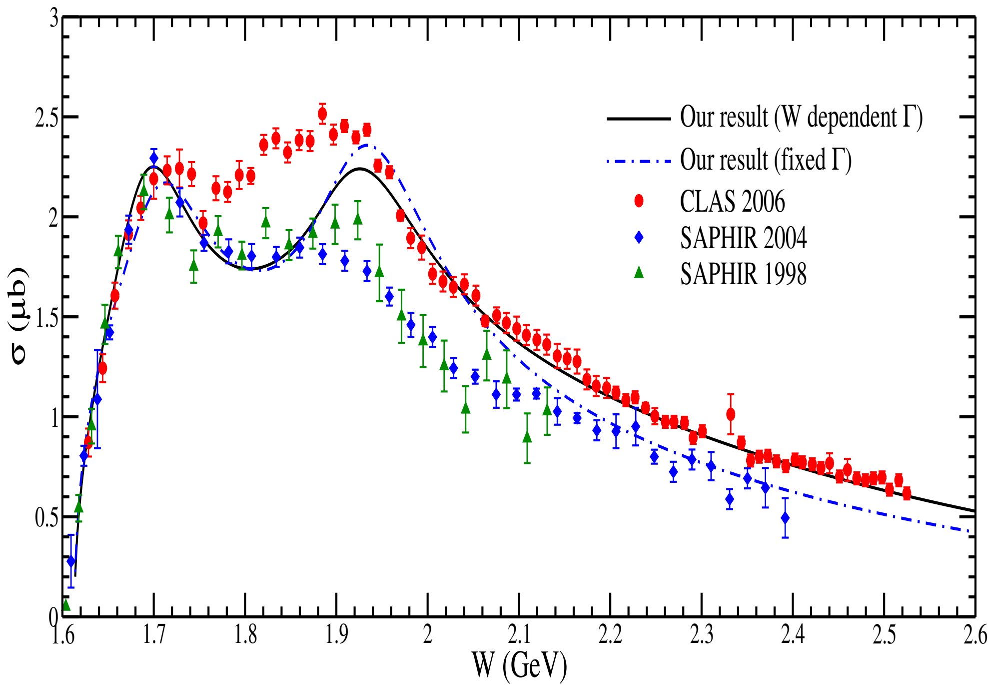

Figure 7.5: σ *vs.* W for the process $\gamma+p \rightarrow K^{+}+\Lambda$. Solid and dashed-dotted lines, respectively, show the results of the the present model taking the W dependent decay widths of the nucleon resonances as discussed in Sect. 7.2.3 and the fixed values of the decay widths as listed in Table 7.1. The experimental data has been taken from the CLAS 2006 [132] (solid circle), SAPHIR 2004 [131] (solid diamond) and SAPHIR 1998 [130] (solid triangle).

(i) $W < 1.72$ GeV

In the region of $W < 1.72$ GeV, all the experimental data show a continuous rise with W in the kinematic region from threshold up to 1.72 GeV.

(ii) 1.72 GeV $< W <$ 1.92 GeV

In this region of W, the data from SAPHIR 1998 and SAPHIR 2004 are fairly consistent with each other, both being lower than the data from CLAS 2006. All the three data show double peaks at around $W \simeq 1.7$ and 1.9 GeV with a minimum around $W = 1.75$ GeV in the CLAS 2006 data and at $W = 1.8$ GeV in the SAPHIR data. In both of the SAPHIR data, the later peak at

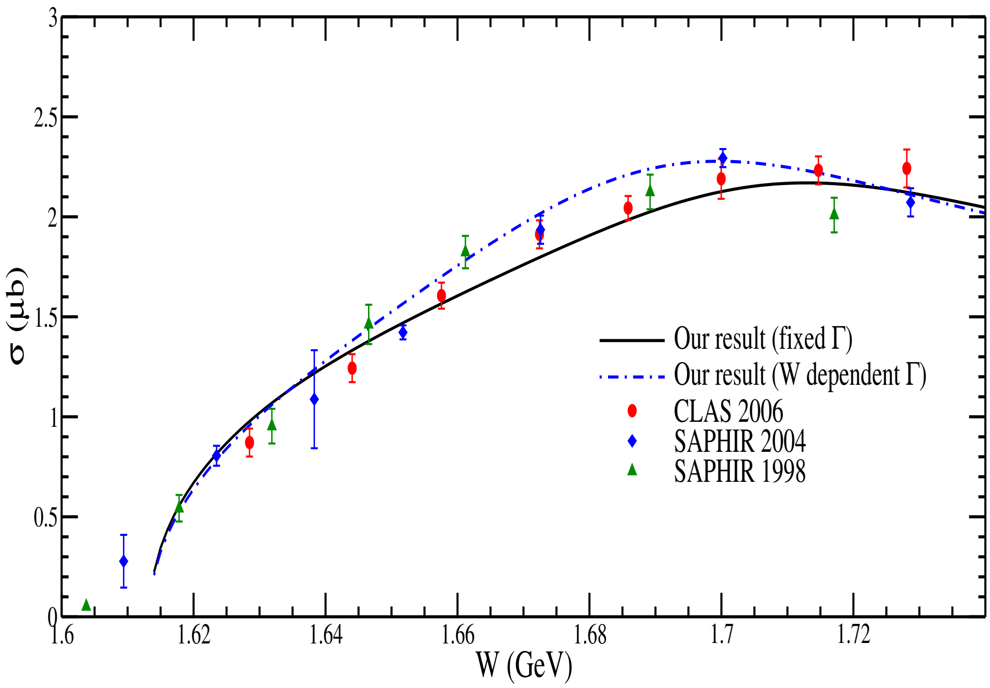

Figure 7.6: σ *vs.* W for the process $\gamma + p \rightarrow K^+ + \Lambda$ in the threshold region. Lines and points have the same meaning as in Figure 7.5.

$W = 1.9$ GeV is lower than the earlier peak at $W = 1.7$ GeV while the CLAS 2006 data show a moderate two peak structure at $W = 1.7$ and 1.9 GeV, in which the minimum is considerably mild and shifted to lower W, i.e., at $W = 1.74$ GeV. Moreover, unlike the SAPHIR data, the second peak at $W = 1.9$ GeV is higher than the first peak at $W = 1.7$ GeV.

(iii) $W \geq 1.92$ GeV

In the region of $W \geq 1.92$ GeV, the CLAS 2006 data are fairly in agreement with both the SAPHIR data in shape but are significantly higher than both the SAPHIR data in the entire range of 1.92 GeV $\leq W \leq$ 2.4 GeV while both the SAPHIR data are reasonably consistent with each other.

We see from Figure 7.5 that our results with energy dependent decay widths are in good agreement with the SAPHIR 1998 and SAPHIR 2004 data (which are consistent with each other) in the range $W = 1.61 - 1.9$ GeV as well as with CLAS data in the range $W = 1.61 - 1.73$ GeV and $W = 1.94 - 2.52$ GeV. Although, the results for energy dependent as well as fixed widths of the resonances are almost consistent with each other in the region of W from threshold up to 1.9 GeV, in the region of W from 1.9 GeV to 2.1 GeV, the present results obtined with fixed widths are consistent with CLAS 2006 data while in the region of $W = 2.1$ GeV to 2.4 GeV, these results are consistent with SAPHIR 1998 and SAPHIR 2004 data. For the region $W = 1.75 - 1.9$ GeV, our results show a prominent dip at $W \approx 1.8$ GeV, which is consistent with SAPHIR but not with CLAS. However, in the energy region of $W > 1.9$ GeV, our results with energy dependent decay widths are in agreement with the CLAS data and are higher than both the SAPHIR data. It must be pointed out that we have considered only those nucleon resonances which are well established and are present in PDG and have known branching ratios for decay in $K\Lambda$ mode. Therefore, the region of $W \approx 1.8$ GeV may indicate the existence of some other resonances which are yet to be observed experimentally.

When our results are compared with the experimental data, we observe that:

i) In the threshold region (Figure 7.6) before the first peak, our numerical results are in a very good agreement with the experimental results available from the CLAS 2006 [132], SAPHIR 2004 [131] and SAPHIR 1998 [130], where the data from all the three experiments are also in agreement among themselves. To fix the unknown parameters (Λ_B, Λ_R and the couplings of the t and u channel resonances) in our model, we have performed a Chi-square fit with the results of the present model using the energy dependent decay widths and obtained the best $\chi^2/N_{d.o.f}$ to be 1.3.

ii) Beyond the second peak region, there is a disagreement between the CLAS and the SAPHIR data and our numerical results both with energy dependent as well as with fixed decay widths are consistent with CLAS data.

iii) At high W region, CLAS and SAPHIR data are in a reasonably agreement

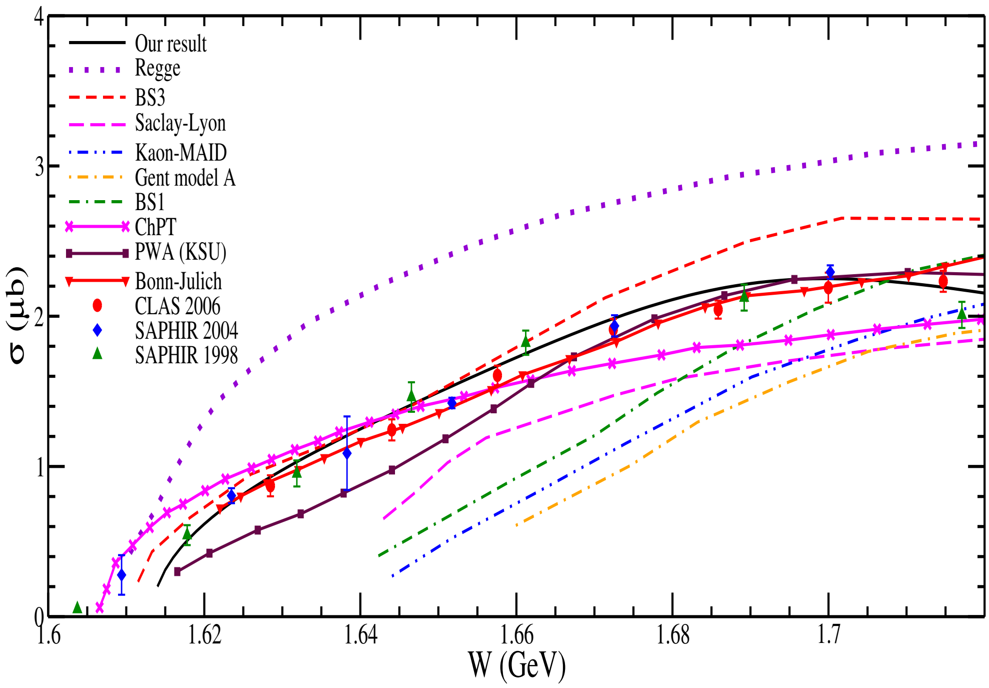

Figure 7.7: σ *vs.* W for the process $\gamma + p \rightarrow K^+ + \Lambda$ in the threshold region. Solid line represents the results of the present work taking the W dependent decay widths of the nucleon resonances, which are compared with other theoretical models like Regge model [203, 206] (dotted line), BS3 model [145] (short dashed line), Saclay-Lyon model [158, 160] (long dashed line), Kaon-MAID model [185] (double-dotted-dashed line), Ghent model A [146, 186, 187] (dashed-dotted line), BS1 model [144] (double-dashed-dotted line), partial wave analysis (PWA) available from Kent State University (KSU) [236] (squares with solid line), chiral perturbation theory (ChPT) [175] (cross with solid line) and Bonn-Julich model [234] (down triangle with solid line).

with each other in shape but not in the absolute values and the present results in our model with energy dependent decay widths explain the CLAS data very well in shape as well as in absolute magnitude while the present results with fixed widths explain the SAPHIR data very well in shape as well as in absolute magnitude.

iv) As the CM energy increases from $W = 1.75$ to $W = 1.9$ GeV, where CLAS and SAPHIR data are not consistent with each other, the results of the present work are in good agreement with the SAPHIR data.

v) We emphasize that the present model with energy dependent decay widths reproduces all the experimental results in the threshold region $W < 1.75$ (Figs. 7.6 and 7.7) and the data from CLAS 2006 in the region 1.9 GeV $< W <$ 2.54 GeV.

Comparison with other theoretical results

To compare our results with some of the theoretical results available in the literature in Figs. 7.7 and 7.8, we have presented the results for σ *vs.* W for the process $\gamma + p \rightarrow K^+ + \Lambda$, where we have shown the results from the different models like Regge model [203, 206], model based on chiral perturbation theory [175], BS3 model [145], Saclay-Lyon model [158, 160], Kaon-MAID model [185], Ghent model A [146, 186, 187], BS1 model [144], Bonn-Julich model [234] and model based on the partial wave analysis [236]. For completeness, we have also shown the experimental data from CLAS 2006 [132], SAPHIR 2004 [131] and SAPHIR 1998 [130].

In Figure 7.7, we have compared the results with energy dependent decay widths of the present model with the other theoretical and experimental results available in the literature, in the threshold region. A very good agreement between the numerical results obtained using the present model with the experimental results from CLAS 2006 [132], SAPHIR 2004 [131] and SAPHIR 1998 [130] may be observed in the region of $W <$ 1.72 GeV. Other than the present model, the threshold region is explained only by the model based on the chiral perturbation theory (ChPT) up to $W =$ 1.66 GeV and by the model based on the partial wave analysis, *i.e.*, the KSU model beyond $W =$ 1.66 GeV. Moreover, the Bonn-Julich model explains the experimental data quite well in the threshold region.

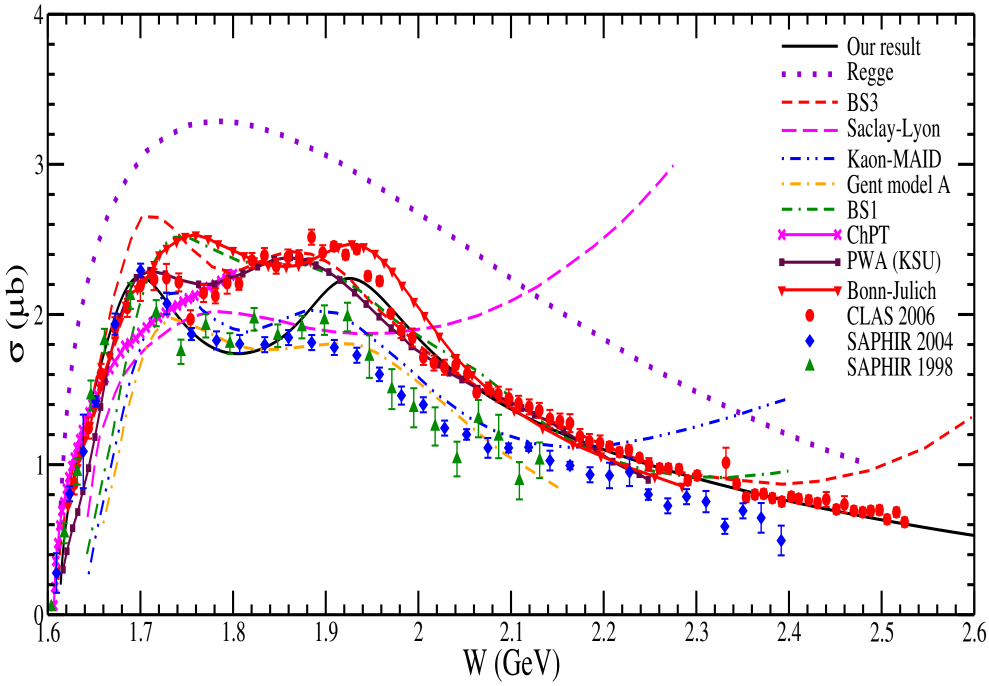

Figure 7.8: σ *vs.* W for the process $\gamma + p \rightarrow K^+ + \Lambda$. Line and points have the same meaning as in Figure 7.7

In Figure 7.8, we have compared our results with with the other theoretical and experimental results in the entire range of W. It may be observed from Figure 7.8, the Regge model over predicts the experimental data at all values the of W from 1.61 to 2.6 GeV. There is only one broad peak at $W \sim 1.8$ GeV in the Regge model and the model does not explain the experimental data from CLAS as well as from SAPHIR which show two peaks at $W = 1.7$ and 1.9 GeV. The model based on the chiral perturbation theory explains the experimental data very well in the threshold region but the model is not applicable at high W. However, the model based on the partial wave analysis explains the experimental data available from the CLAS very well in the intermediate and high W region, the threshold region (Figure 7.7) is not well explained by this model. Except the Ghent model A, all the other models like Saclay-Lyon, Kaon-MAID, BS1 and BS3 show that, at high W, the cross section increases with W, which is not supported by the experimental data. However, the Ghent model A as well as the present work (even at $W = 2.6$ GeV) do not show any such increase. As pointed out in Ref. [144], this increase comes mainly from the background part of the amplitude. Also, this increase of the total cross section is model dependent. For example, the Saclay-Lyon [158, 160] model starts increasing from $W \sim 2$ GeV while the Kaon-MAID model starts increasing beyond $W \sim 2.1$ GeV. In the BS1 and BS3 models, the cross section increases for $W > 2.3$ GeV.

In comparison with other theoretical models, the success of the present model in describing the data except in the energy region of 1.75 GeV $< W <$ 1.9 GeV is due to the physical input parameters used in calculating the contribution from the resonance terms which dominate in this energy region. Moreover, the use of a small value of the cut-off parameter in the form factors in the calculation of the non-resonant Born and the contact terms as well as the t and u channel resonances suppresses the contribution of the background terms preventing the rise of the cross section in the low energy region as compared to other models. We would like to emphasize that the present model is very economical version of isobar models used in the literature as it uses a minimal number of resonances and highlights the importance of a few resonances like $S_{11}(1650)$, $P_{11}(1710)$, $P_{13}(1720)$, $P_{11}(1880)$, $S_{11}(1895)$ and $P_{13}(1900)$ in explaining the total cross section data. The results of the present model are in agreement with many elaborate calculations available in literature (Bonn-Gatchina [230, 231, 232], Bonn-Julich [234], KSU [236], Skoupil-Bydzovsky [144, 145, 202], Mart [250, 149, 148, 143], Ghent model [199, 200, 201]).

7.3.2 Differential cross section

We have presented our results for the differential cross sections and compared them with the experimental data available from CLAS, SAPHIR and MAMI as well as with the models based on the partial wave analysis [236], Saclay-Lyon model [158, 160], Kaon-MAID model [185] and BS3 model [145].

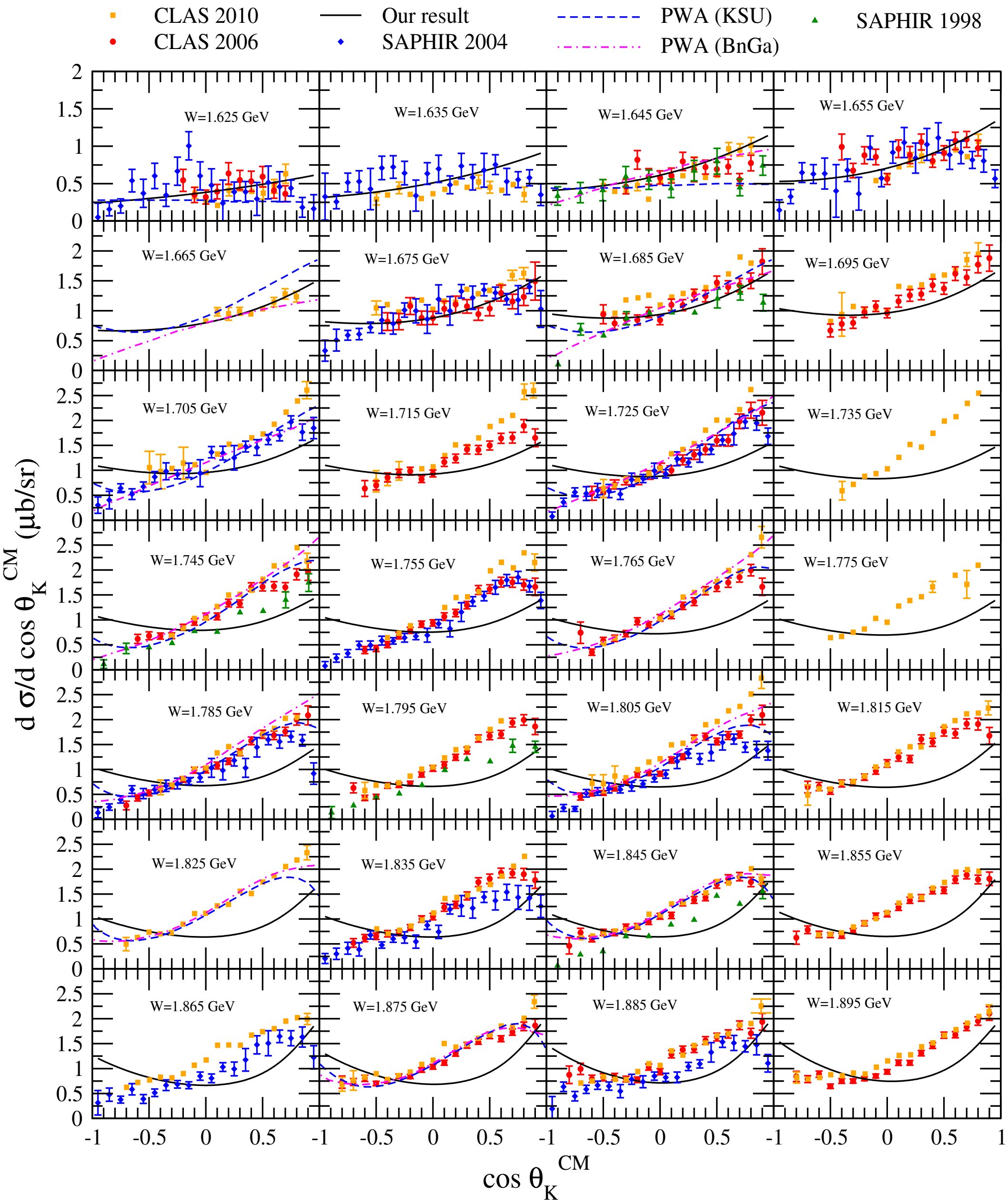

Figure 7.9: $d\sigma/d\cos\theta_k^{CM}$ *vs.* $\cos\theta_k^{CM}$ at fixed W ranging from $1.625-1.895$ GeV, for the process $\gamma+p\rightarrow K^{+}+\Lambda$. The experimental data has been taken from CLAS 2010 [134] (solid square), CLAS 2006 [132] (solid circle), SAPHIR 2004 [131] (solid diamond) and SAPHIR 1998 [130] (solid triangle). Solid line represents the results of the full model taking W dependent decays width of the nucleon resonance. Dashed (Dashed-dotted) line shows the results obtained using the partial wave analysis done by the Kent State University (KSU) (Bonn-Gatchina (BnGa)) model [236].

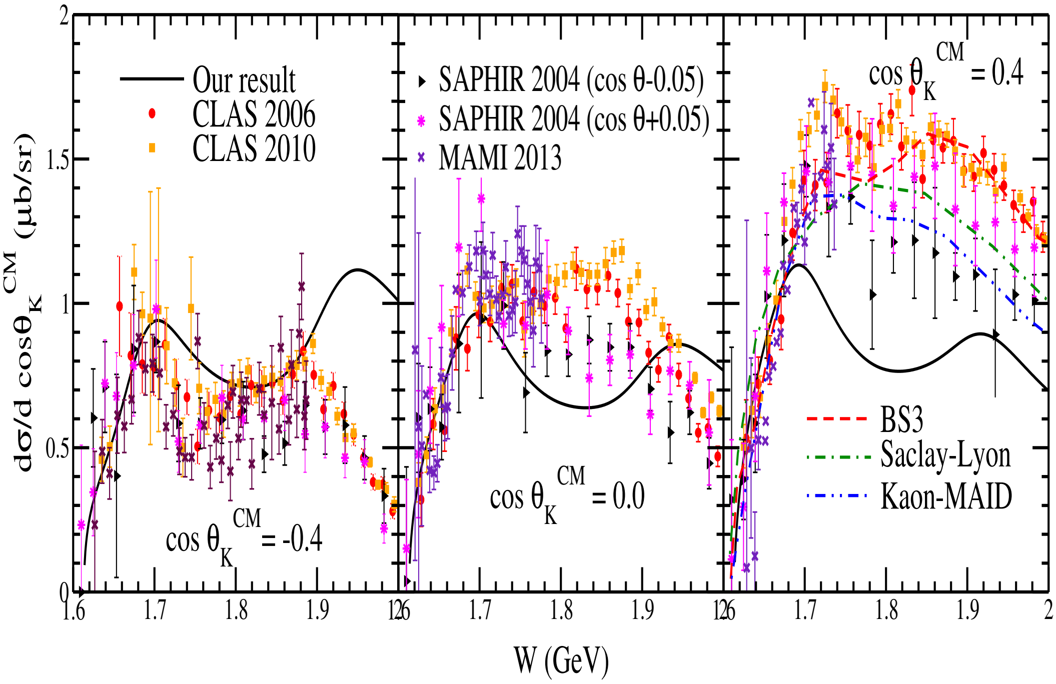

Figure 7.10: $d\sigma/d\cos\theta_k^{CM}$ *vs.* W at fixed $\cos\theta_k^{CM} = -0.4$, 0 and 0.4, for the process $\gamma + p \to K^+ + \Lambda$. The experimental data has been taken from CLAS 2010 [134] (solid square), CLAS 2004 [132] (solid circle), MAMI 2013 [138] (cross symbol), SAPHIR 2004 ($\cos\theta - 0.05$) [131] (right triangle) and SAPHIR 2004 ($\cos\theta + 0.05$) (diamond). Solid line represents the results of the full model of the present work taking the energy dependent decay widths of the nucleon into account. Dashed line, dashed-dotted line, dashed-double-dotted line show the results of BS3 [145], Saclay-Lyon [158, 160] and Kaon-MAID [185] models, respectively.

In Figure 7.9, we have presented the results for $d\sigma/d\cos\theta_k^{CM}$ as a function of $\cos\theta_k^{CM}$ at fixed W ranging from $1.625 - 1.895$ GeV in the interval of 10 MeV obtained using the energy dependent decay width of the various resonances considered in the present work, for the $K\Lambda$ photoproduction process. The present results are also compared with the experimental results available from CLAS 2010 [134], CLAS 2006 [132], SAPHIR 2004 [131] and SAPHIR 1998 [130] as well as with the theoretical results obtained by the Kent State University (KSU) [236] and the Bonn-Gatchina (BnGa) [236] groups, using the partial wave analysis. In the low W region, *i.e.*, from the threshold up to $W = 1.695$ GeV, our results are in a good agreement with the available experimental data as well as with the models based on the partial wave analysis. In the intermediate and high region of W, our results in the backward region are fairly in agreement with KSU and BnGa models, however, this is not the case at the forward angle region. In the region of W from $1.705 - 1.895$ GeV, our results in the forward region are in agreement with SAPHIR data but not with CLAS data. CLAS 2006 and CLAS 2010 data are not in agreement with each other and the results obtained using the model discussed in this work favor SAPHIR experimental observations.

To show the energy dependence of the differential cross section, in Figure 7.10, we have presented our results for $d\sigma/d\Omega_k^{CM}$ *vs.* W at $\cos\theta_k^{CM} = -0.4$, 0 and $+0.4$, obtained using the fixed decay width of the resonances. We have compared our results with the experimental data available from SAPHIR 2004 [131], CLAS 2006 [132], CLAS 2010 [134] and MAMI 2013 [138] as well as with the theoretical models like BS3 model [145], Saclay-Lyon model [158, 160] and Kaon-MAID model [185]. It may be observed from the figure that in the threshold region, at all values of $\cos\theta_k^{CM}$, our results are in a very good agreement with the available experimental data. In the backward region, our results are in a reasonable agreement with the experimental data up to $W = 1.9$ GeV. However, our results in the forward region emphasize the need for a missing resonance in order to explain the experimental data.

Part V

Conclusions

CHAPTER 8

SUMMARY AND CONCLUSION

In this thesis, I have presented the work that I am performing at the MINERvA collaboration over the last two years. My analysis goal is to obtain the double differential deep inelastic scattering cross section in the neutrino mode using the MINERvA detector. Also, the plan is to obtain the total cross section for the different nuclei used in the detector like helium, carbon, oxygen, iron and lead and to obtain the ratio of these cross sections to the cross sections obtained using the hydrocarbons and to extract the information on the structure functions using these ratios in the neutrino and antineutrino modes. In the case of electromagnetic interactions, the structure functions are well studied while in the case of weak interactions, the information on the structure functions are limited, therefore, our plan is to extract the weak structure functions using the MINERvA data. As the MINERvA detector uses moderate to heavy nuclear targets, therefore, it provides an opportunity to understand the effect of nuclear medium in the different nuclei. In order to obtain the experimental cross sections, we have to perform various steps like event selection, efficiency, background estimation and subtraction, etc. and most of these steps are already completed and the results have been presented.

In the second part of my thesis, I have presented the work that I did in the INO analysis. The INO experiment is dedicated to study the atmospheric neutrino and antineutrino oscillations in the muon disappearance channel. The INO-ICAL detector uses high magnetic field applied uniformly throughout the detector which helps in the distinguishing μ^- and μ^+ events separately, therefore, the neutrino and antineutrino events are separated easily. We have performed the study of oscillation parameters at the INO experiment analyzing the neutrino and antineutrino events separately in order to fing the signature of new physics like the CPT violation.

Third, the theoretical work that I have performed at the Aligarh Muslim University. This work has been performed keeping in mind the theoretical development of a model that will describe the associated particle production induced by photons, electrons, neutrinos, and antineutrinos. We have studied the associated particle production induced by photons which receives the contributions from the non-resonant terms as well as from the nucleon, hyperon, and kaon resonances.

After introducing the topic and discussing the plan of the thesis in Chapter-1, in Chapter-2, we have introduced the Fermilab's NuMI beam and the MINERvA detector. NuMI beam is providing neutrinos to the MINERvA, MINOS, and NOvA detectors for the cross section and oscillation measurements. We have discussed and explained the functioning of the different components of the NuMI beam like beam design, NuMI target, magnetic horns (required to select the polarity of the particles passing through them) and, hadron absorbers, etc. NuMI beam is predominantly composed of muon neutrinos in the neutrino mode with a small muon antineutrino percentage (5%) and electron neutrino/antineutrino components (total $< 1\%$). We have also discussed the design of the MINERvA detector and explained in detail the different components of the detector.

In Chapter 3, we have discussed the process of reconstruction and simulation used by the MINERvA experiment. We have given a complete description of various steps involved in the reconstruction process like time slices, cluster formation, track reconstruction, MINOS matching of the reconstructed tracks.

In Chapter-4, the details of the analysis procedure required to obtain the cross section in the MINERvA experiment are explained. Also, the chapter has discussed about the different systematics included in the cross section measurement. The steps which are required to obtain the cross section are event selection, background estimation and subtraction, efficiency correction, unfolding, and normalization. In the event selection, the data sample is selected by applying different cuts at the event-by-event level. The optimization of the cuts is done based on several criteria like the signal selection efficiency, purity, to minimize systematic uncertainties. This helps to put events into the kinematic bins and events are represented then as a histogram. The next step is the background subtraction which removes the events that pass selection cuts but are not in fact signal. The background events are estimated by Monte Carlo simulation after applying the selection cuts and then referring to the true properties to look at whether an event is a signal or background. A complete procedure of estimation and subtraction of the background events is discussed in the thesis. The shortcomings in detection and event reconstruction in the data result in the smearing of the measurement which is handled with a procedure called unfolding. Here, an unfolding matrix is constructed from the simulation's discrepancies between reconstructed and true quantities. This is basically a mapping of events between the reconstructed and true space. The matrix is then applied to the background-subtracted data distribution, transforming it from a reconstructed into a "true" variable. The background-subtracted and the unfolded sample is then repopulated with the signal events that were missed due to inefficiency of the selection cuts and to the detector acceptance or kinematic thresholds through a process called efficiency (and acceptance) correction. The efficiency and the acceptance are simulated together as the number of selected signal events, divided by the total number of signal events, all in bins of the variables of interest. The final step is to normalize the efficiency-corrected distributions and introduces cross section units of measure. We normalize the sample with the muon neutrino flux exposure of the dataset and the number of target protons and neutrons in the allowed neutrino interaction regions of the detector. We also do a bin width normalization to obtain a differential cross section measurement and giving the distribution a final unit of measure [cm^2 /target nucleon/[variable unit]].

The experimental confirmation of different oscillation parameters for neutrinos and antineutrinos will be a signature of any new physics like CPT symmetry in the neutrino sector. In chapter 5, we investigate this possibility by studying INO-ICAL potential for the separate measurements of neutrino and antineutrino oscillation parameters for 10 years of exposure. The CC ν_μ and $\overline{\nu}_\mu$ events are separated into muon energy, muon direction and hadron energy bins. A χ^2 analysis is used with realistic detector resolutions, efficiencies and systematic errors. The separate analysis for neutrino and antineutrino events having identical oscillation parameters ($|\Delta m^2_{32}| = |\Delta\overline{m^2}_{32}|, \sin^2\theta_{23} = \sin^2\overline{\theta}_{23}$) indicates that ICAL can measure the atmospheric neutrino parameters $|\Delta m^2_{32}|$ with a precision of 10.14% and $\sin^2\theta_{23}$ with a precision of 27.10%. The atmospheric antineutrino parameters $|\Delta\overline{m^2}_{32}|$ and $\sin^2\overline{\theta}_{23}$ can be measured with a precision of 13.4% and 38.0% at 3σ confidence level respectively. As expected, the combined $\nu_\mu + \overline{\nu}_\mu$ events show a better sensitivity with a precision of 8.7% for $|\Delta m^2_{32}|$ and 25.0% for $\sin^2\theta_{23}$ at same confidence level due to larger events in χ^2.

Further, we have investigated the scenario where the neutrino and antineutrino oscillation parameters have different values. We measure the ICAL sensitivity for ruling out the null hypothesis ($|\Delta m^2_{32}| = |\Delta\overline{m^2}_{32}|$) by estimating the difference between the true values of mass squared differences of neutrinos and antineutrinos i.e. ($|\Delta m^2_{32}| - |\Delta\overline{m^2}_{32}|$). We show that ICAL can rule out the null hypothesis of $|\Delta m^2_{32}| = |\Delta\overline{m^2}_{32}|$ at more than 3σ level if the difference of true values of $|\Delta m^2_{32}| - |\Delta\overline{m^2}_{32}| \geq +0.4 \times 10^{-3} eV^2$ or $|\Delta m^2_{32}| - |\Delta\overline{m^2}_{32}| \leq -0.4 \times 10^{-3} eV^2$.

In chapter 6, the INO-ICAL potential, in the frame of four-fit technique, for the distinct measurements of neutrino and antineutrino oscillation parameters for ten years of exposure have been investigated. It is shown that to get the accurate sensitivity of the ICAL detector and to test the hypothesis that neutrinos and antineutrinos share the identical parameters, the difference between oscillation parameters can not be ignored. Therefore, we allow the possibility of different true values of ν_μ and $\overline{\nu}_\mu$ parameters ($|\Delta m^2_{32}|$, $\sin^2\theta_{23}$, $|\Delta\overline{m^2}_{32}|$, $\sin^2\overline{\theta}_{23}$) in nature. With four parameters fitting analyses, using fixed but different true values of four oscillation parameters, we have shown the ICAL sensitivity for the measurement of the differences $|\Delta m^2_{32}|-|\Delta\overline{m^2}_{32}|$. Further, the extraction of two parameter plots from four parameters fit provides sensitivity for individual oscillation parameters. It has been found that ICAL can measure $|\Delta m^2_{32}|$ and $|\Delta\overline{m^2}_{32}|$ with a precision of about $\sim$ 10% and $\sim$ 13% at 90% CL, respectively. Qualitatively, we found that the ICAL is slightly better sensitive for the anti-neutrinos mass-squared splittings compared to the MINOS as presented in Ref. [117], by using the atmospheric events only while for the neutrinos mass-squared splitting, its sensitivity is almost similar to that of MINOS.

Further, we investigate the scenario where the neutrino and antineutrino oscillation parameters have different true values. We measure the ICAL sensitivity for ruling out the null hypothesis ($|\Delta m^2_{32}| = |\Delta\overline{m^2}_{32}|$) by estimating the difference between the true values of mass-squared differences of neutrinos and antineutrinos i.e. ($|\Delta m^2_{32}| - |\Delta\overline{m^2}_{32}|$). We find that ICAL can rule out the null hypothesis of $|\Delta m^2_{32}| = |\Delta\overline{m^2}_{32}|$ at more than 3σ (99%)level if the difference of true values of $|\Delta m^2_{32}| - |\Delta\overline{m^2}_{32}| \geq +0.7\times 10^{-3} eV^2$ or $|\Delta m^2_{32}| - |\Delta\overline{m^2}_{32}| \leq -0.7\times 10^{-3} eV^2$.

In chapter 7, we have presented a version of the isobar model based on the chiral SU(3) symmetry, to study the photoproduction of $K\Lambda$ from the proton. The results are presented for the total cross section as a function of CM energy W and the differential cross sections for various values of W in the region of few GeV of photon energy $E_\gamma \leq 3$ GeV. The results are compared with the experimental data available from CLAS [132, 134] and SAPHIR [131, 130] and are found to be in a good agreement with the experimental data, except for the region 1.75 GeV$<$ W $<$ 1.9 GeV. The results of the present model for the total cross sections are also compared with the results reported using various theoretical models available in the literature like Regge [203, 206], chiral unitary [175], Saclay-Lyon [158, 160], Kaon-MAID [185], Bonn-Julich model [234], Bonn-Gatchina model [230, 231, 232], KSU model [236], BS1 [144] and BS3 [145] models.

In this model, the non-resonant terms are obtained using the non-linear σ model in which the contact term appears quite naturally with the strength of its couplings predicted by the model. The different diagrams contributing to the non-resonant terms are the s, t and u channels and the contact term in which the various meson-nucleon-hyperon couplings *viz.* $g_{KN\Lambda}$ and $g_{KN\Sigma}$, are uniquely predicted in the model. The hadronic form factors at the strong vertices are introduced to account for the hadronic structure and a dipole parameterization is used, using a cut-off parameter Λ_B taken to be the same for all the diagrams. For the contact term, the prescription of the form factor given by Davidson and Workman [209] is used.

We have also considered nucleon, kaon and hyperon resonance exchanges in the s, t and u channels. The nucleon resonances with spin $\leq \frac{3}{2}$ and mass in the range $1.6-1.9$ GeV, which are well established, represented by $****$ and $***$ states in the PDG having branching ratio in $K\Lambda$ are included. The electromagnetic couplings of the various nucleon resonances are obtained in terms of the experimental helicity amplitudes given in MAID [139] and PDG [237]. The strong couplings at $RK\Lambda$ vertices are obtained from the observed partial decay width of the resonance decaying to $K\Lambda$. The unitary corrections are partially implemented by using the energy dependent widths for the various nucleon resonances [202]. The kaon resonances *viz.* K^* and K_1 having spin 1, are considered in the t channel and spin $\frac{1}{2}$ lambda resonances *viz.* $\Lambda^*(1405)$ and $\Lambda^*(1800)$ are considered in the u channel. Since the experimental information about the kaon and hyperon resonances is not adequate to determine its electromagnetic and strong couplings phenomenologically, therefore, the couplings for these resonances are fitted to reproduce the experimental data available from CLAS and SAPHIR.

We summarize the results of the present study in the following:

(i) Our results explain very well the threshold region and the role of the non-resonant terms are quite significant in the threshold region up to $W \sim 1.75$ GeV. Moreover, the contact term, which occurs quite naturally in our model, has the most dominant contribution and plays important role in explaining the data in this region.

(ii) The results of the full model for the total cross section are in good agreement with the experimental data of SAPHIR as well as CLAS experiments, in a wide region of W considered in this work, *i.e.,* from the threshold up to 1.75 GeV and from 1.9 to 2.6 GeV, except for a narrow range of W *i.e.* 1.75–1.9 GeV.

(iii) Among the resonance contribution, at low W, the contribution of $P_{11}(1710)$ is found to be significant although it is not considered in most of the isobar models. We find that both $P_{13}(1720)$ and $P_{13}(1900)$ resonances make significant contributions to the cross section for $W \gtrsim 1.8$ GeV. The S_{11} resonances *viz.* $S_{11}(1650)$ and $S_{11}(1895)$ have small contribution to the cross section in the entire range of W.

(iv) We would like to emphasise the important role of $P_{13}(1720)$ and $P_{13}(1900)$ resonances at higher energies specially in the region of $W > 2$ GeV. When these resonances are taken into account, the results are closer to CLAS data. The contribution of both resonances are almost equally important in the entire region of W considered in this work. However, in the region of 1.8 GeV $< W <$ 2.0 GeV, the $P_{13}(1900)$ resonance gives a significant enhancement in the total cross section leading to the appearance of second peak around $W = 1.9$ GeV seen in the data of CLAS 2006 and SAPHIR

1998.

(v) Our results for the angular distribution are in fair agreement with the experimental data especially in the threshold region.

(vi) When we take an energy dependent width in order to restore the unitarity partially, it has been found that the effect (energy independent *vs.* energy dependent width) on the results of the total cross section is generally small but could be up to $5 - 20\%$ in the region of $W > 2$ GeV leading to a better agreement with the CLAS 2006 data.

The present study of the $K\Lambda$ production induced by photons may be quite useful in the planned experiments at TJNAF, SPring-8 and MAMI in this energy region. In future, we plan to extend this model to study the electromagnetic and weak productions of associated particles (KY) induced by electrons and (anti)neutrinos relevant for future experiments at ESRF, MAMI, ELSA and TJNAF in the case of electrons and at MINERvA, NOvA, T2K and DUNE in the case of (anti)neutrinos. The strong and electromagnetic couplings determined from the photoproduction process as well as the Q^2 dependence of the vector form factors extracted from the electroproduction process will be used as inputs in the case of neutrino and antineutrino induced associated particle production. Our future plan is to perform theoretical calculations for the (anti)neutrino induced associated particle production off the nucleon and nuclear targets in the energy region of a few GeV by taking contributions from the non-resonant and resonant channels. This study may be quite useful in the future analysis of MINERvA experiment as well as in the proposed DUNE experiment where the identification of strange particle production would be neat and enough events are expected at the DUNE energies which is planning to use argon targets.

Appendices

APPENDIX A

DEEP INELASTIC SCATTERING CROSS SECTION

The basic reaction for the (anti)neutrino induced charged current deep inelastic scattering process on a free nucleon target is given by

$$\nu_l(k)/\bar{\nu}_l(k) + N(p) \to l^-(k')/l^+(k') + X(p') \quad l = e, \mu \tag{A.1}$$

where k and k' are the four momenta of incoming and outgoing lepton, p and p' are the four momenta of the target nucleon and the jet of hadrons produced in the final state, respectively. This process is mediated by the W-boson ($W^{\pm}$) and the invariant matrix element corresponding to the reaction given in Eq.A.1 is written as

$$-i\mathcal{M} = \frac{iG_F}{\sqrt{2}}\, l_\mu \left(\frac{M_W^2}{q^2 - M_W^2}\right) \langle X|J^\mu|N\rangle\ , \tag{A.2}$$

where G_F is the Fermi coupling constant, M_W is the mass of W boson, and $q^2 = (k-k')^2$ is the four momentum transfer square. l_μ is the leptonic current and $\langle X|J^\mu|N\rangle$ is the hadronic current for the neutrino induced reaction.

The general expression of the double differential scattering cross section (DCX) corresponding to the reaction given in Eq. A.1 (depicted in Figure A.1) in the

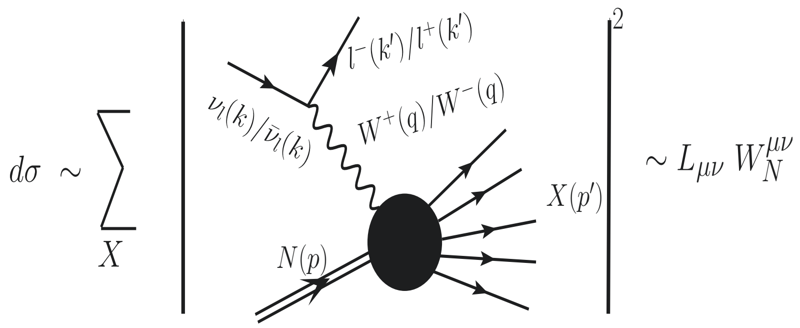

Figure A.1: $\nu_\mu(\bar{\nu}_\mu) - N$ inclusive scattering where the summation sign represents the sum over all the hadronic states such that the cross section($d\sigma$) for the deep inelastic scattering $\propto L_{\mu\nu} W_N^{\mu\nu}$.

laboratory frame is expressed as:

$$\frac{d^2\sigma}{dxdy} = \frac{yM_N}{\pi} \frac{E}{E'} \frac{|\mathbf{k}'|}{|\mathbf{k}|} \bar{\sum}\sum |\mathcal{M}|^2 \,, \tag{A.3}$$

where x and y are the scaling variables which lie in the ranges 0 to 1 in the limit $m_e, m_\mu \to 0$ and $\bar{\sum}\sum|\mathcal{M}|^2$ is the invariant matrix element square which is given in terms of the leptonic ($L_{\mu\nu}$) and hadronic ($W_N^{\mu\nu}$) tensors as

$$\bar{\sum}\sum |\mathcal{M}|^2 = \frac{G_F^2}{2} \left(\frac{M_W^2}{Q^2 + M_W^2}\right)^2 L_{\mu\nu} W_N^{\mu\nu}, \tag{A.4}$$

with $Q^2 = -q^2 \geq 0$. $L_{\mu\nu}$ is given by

$$L_{\mu\nu} = 8(k_\mu k'_\nu + k_\nu k'_\mu - k.k' g_{\mu\nu} \pm i\epsilon_{\mu\nu\rho\sigma} k^\rho k'^\sigma) \,. \tag{A.5}$$

Here the antisymmetric term arises due to the contribution from the axial vector components with +ve sign for antineutrino and -ve sign for neutrino. The hadronic tensor $W_N^{\mu\nu}$ is written in terms of the weak nucleon structure functions $W_{iN}(\nu, Q^2)$ $(i = 1-6)$ as

$$\begin{aligned} W_N^{\mu\nu} &= \left(\frac{q^\mu q^\nu}{q^2} - g^{\mu\nu}\right) W_{1N}(\nu,Q^2) + \frac{W_{2N}(\nu,Q^2)}{M_N^2}\left(p^\mu - \frac{p.q}{q^2}\, q^\mu\right) \\ &\times \left(p^\nu - \frac{p.q}{q^2}\, q^\nu\right) - \frac{i}{2M_N^2}\epsilon^{\mu\nu\rho\sigma} p_\rho q_\sigma W_{3N}(\nu,Q^2) + \frac{W_{4N}(\nu,Q^2)}{M_N^2} q^\mu q^\nu \\ &+ \frac{W_{5N}(\nu,Q^2)}{M_N^2}(p^\mu q^\nu + q^\mu p^\nu) + \frac{i}{M_N^2}(p^\mu q^\nu - q^\mu p^\nu) W_{6N}(\nu,Q^2)\,. \end{aligned} \tag{A.6}$$

The contribution of the term with $W_{6N}(\nu, Q^2)$ vanishes when contracted with the leptonic tensor and the contributions of the terms with $W_{4N}(\nu, Q^2)$ and $W_{5N}(\nu, Q^2)$ are proportional to charged lepton mass, therefore, it vanishes in the case of ν_e and ν_μ induced DIS process as $m_l \to 0$. When Q^2 and ν become large the structure functions $W_{iN}(\nu, Q^2)$; $(i = 1-3)$ are generally expressed in terms of the dimensionless nucleon structure functions $F_{iN}(x)$, $i = 1-3$ as:

$$\begin{aligned} F_{1N}(x) &= W_{1N}(\nu, Q^2), \qquad F_{2N}(x) = \frac{Q^2}{2xM_N^2} W_{2N}(\nu, Q^2) \\ F_{3N}(x) &= \frac{Q^2}{xM_N^2} W_{3N}(\nu, Q^2). \end{aligned}$$

Now the hadronic tensor may be written in terms of dimensionless nucleon structure functions $F_{iN}(x, Q^2)$ $(i = 1-3)$ as:

$$W_N^{\mu\nu} = -g_{\mu\nu} F_{1N}(x, Q^2) + \frac{p_\mu p_\nu}{p.q} F_{2N}(x, Q^2) - i\epsilon_{\mu\nu\rho\sigma} \frac{p^\rho q^\sigma}{2p_1 \cdot q} F_{3N}(x, Q^2). \quad (A.7)$$

The expression for the differential scattering cross section given in Eq. A.3 is written by using Eqs. A.5 and A.7 as:

$$\begin{aligned} \frac{d^2\sigma}{dxdy} &= \frac{G_F^2 M_N E_\nu}{\pi(1+\frac{Q^2}{M_W^2})^2} \Big\{ \Big[y^2 x + \frac{m_l^2 y}{2E_\nu M_N} \Big] F_{1N}(x, Q^2) + \Big[\Big(1 - \frac{m_l^2}{4E_\nu^2}\Big) - \Big(1 + \frac{M_N x}{2E_\nu}\Big) y \Big] F_{2N}(x, Q^2) \\ &\pm \Big[xy\Big(1 - \frac{y}{2}\Big) - \frac{m_l^2 y}{4E_\nu M_N} \Big] F_{3N}(x, Q^2) \Big\}. \end{aligned} \quad (A.8)$$

In general, the dimensionless nucleon structure functions are derived in the quark-parton model assuming Bjorken scaling in which they are written in terms of the parton distribution functions $q_i(x)$ and $\bar{q}_i(x)$ at the leading order as

$$F_2(x) = \sum_i x[q_i(x) + \bar{q}_i(x)] \; ; \; xF_3(x) = \sum_i x[q_i(x) - \bar{q}_i(x)] \quad (A.9)$$

In the case of $\nu(\bar{\nu})$-proton scattering above the charm production threshold, $F_{2,3}(x)$ are given by:

$$\begin{aligned} F_{2p}^{\nu}(x) &= 2x[d(x) + s(x) + \bar{u}(x) + \bar{c}(x)] \quad F_{2p}^{\bar{\nu}}(x) = 2x[u(x) + c(x) + \bar{d}(x) + \bar{s}(x)] \\ xF_{3p}^{\nu}(x) &= 2x[d(x) + s(x) - \bar{u}(x) - \bar{c}(x)] \quad xF_{3p}^{\bar{\nu}}(x) = 2x[u(x) + c(x) - \bar{d}(x) - \bar{s}(x)] \quad (A.10) \end{aligned}$$

and for the $\nu(\bar{\nu})$-neutron scattering $F_{2,3}(x)$ are given by

$$\begin{aligned} F_{2n}^{\nu}(x) &= 2x[u(x) + s(x) + \bar{d}(x) + \bar{c}(x)] \; ; \; F_{2n}^{\bar{\nu}}(x) = 2x[d(x) + c(x) + \bar{u}(x) + \bar{s}(x)] \\ xF_{3n}^{\nu}(x) &= 2x[u(x) + s(x) - \bar{d}(x) - \bar{c}(x)] \quad xF_{3n}^{\bar{\nu}}(x) = 2x[d(x) + c(x) - \bar{u}(x) - \bar{s}(x)]. \quad (A.11) \end{aligned}$$

For an isoscalar nucleon target, we use

$$F_{iN} = \frac{F_{ip} + F_{in}}{2}, \quad i = 1 - 3 \tag{A.12}$$

The structure functions $F_{1N}(x)$ at the leading order are written using Callan-Gross [267] relation as:

$$F_1(x) = \frac{F_2(x)}{2x}$$

The parton distribution functions (defined in Eqs.A.9, A.10 and A.11) for the nucleon have been determined by various groups and they are known in the literature by the acronyms MRST [268], GRV [269], GJR [270], MSTW [271], ABMP [272], ZEUS [273], HERAPDF [274], NNPDF [275], CTEQ [276], CTEQ-Jefferson Lab (CJ) [277], MMHT [278], etc.

APPENDIX B

DIS PLOTS

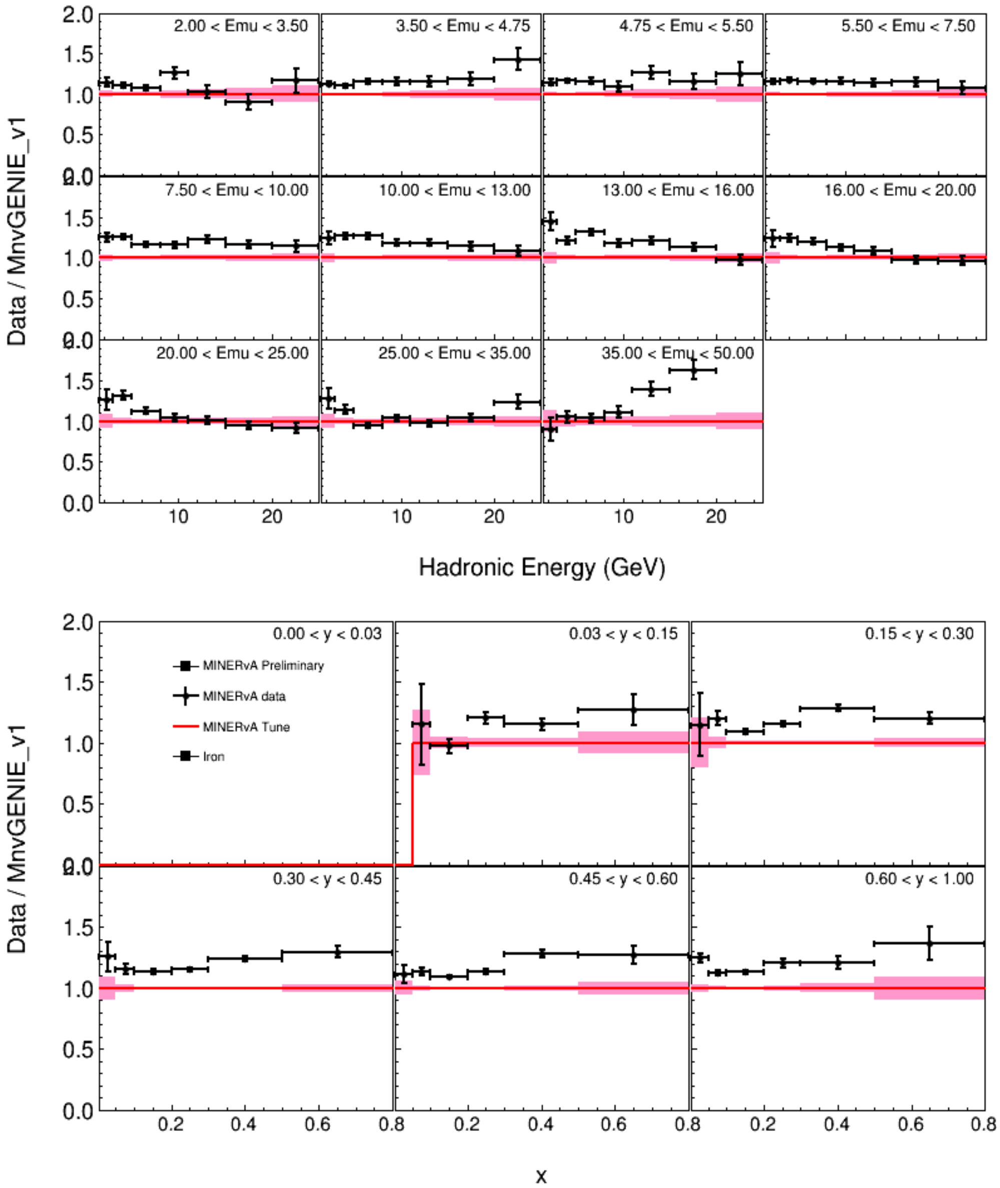

Figure B.1: The Data/simulation plots for the combined Fe of all targets. The plots are for two combinations: (i) Muon energy vs Hadronic Energy and (ii) Bjorken variable x and Inelasticity y. This is the first projection for the two pair of variables.

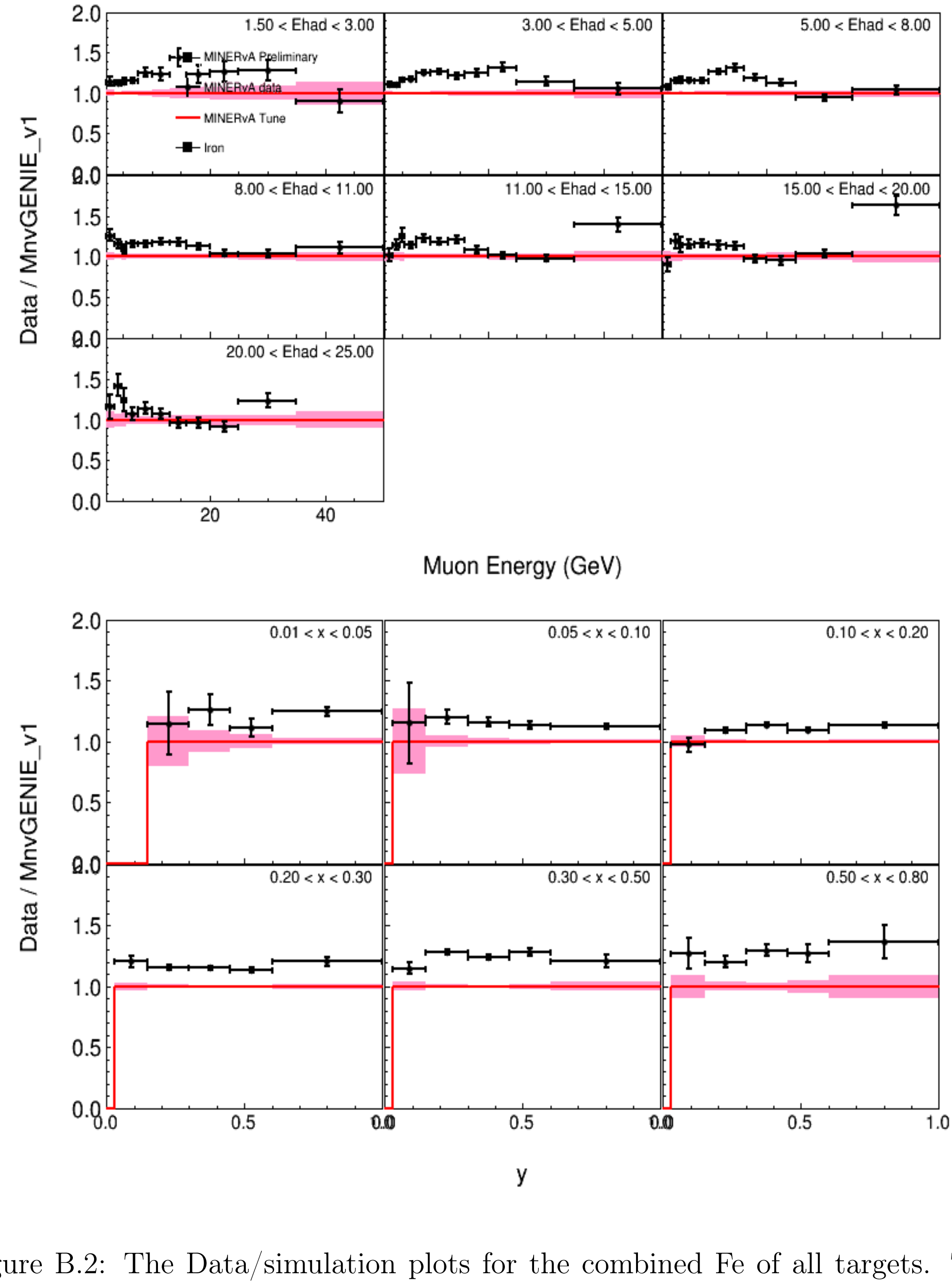

Figure B.2: The Data/simulation plots for the combined Fe of all targets. The second projection for the two pair of variables.

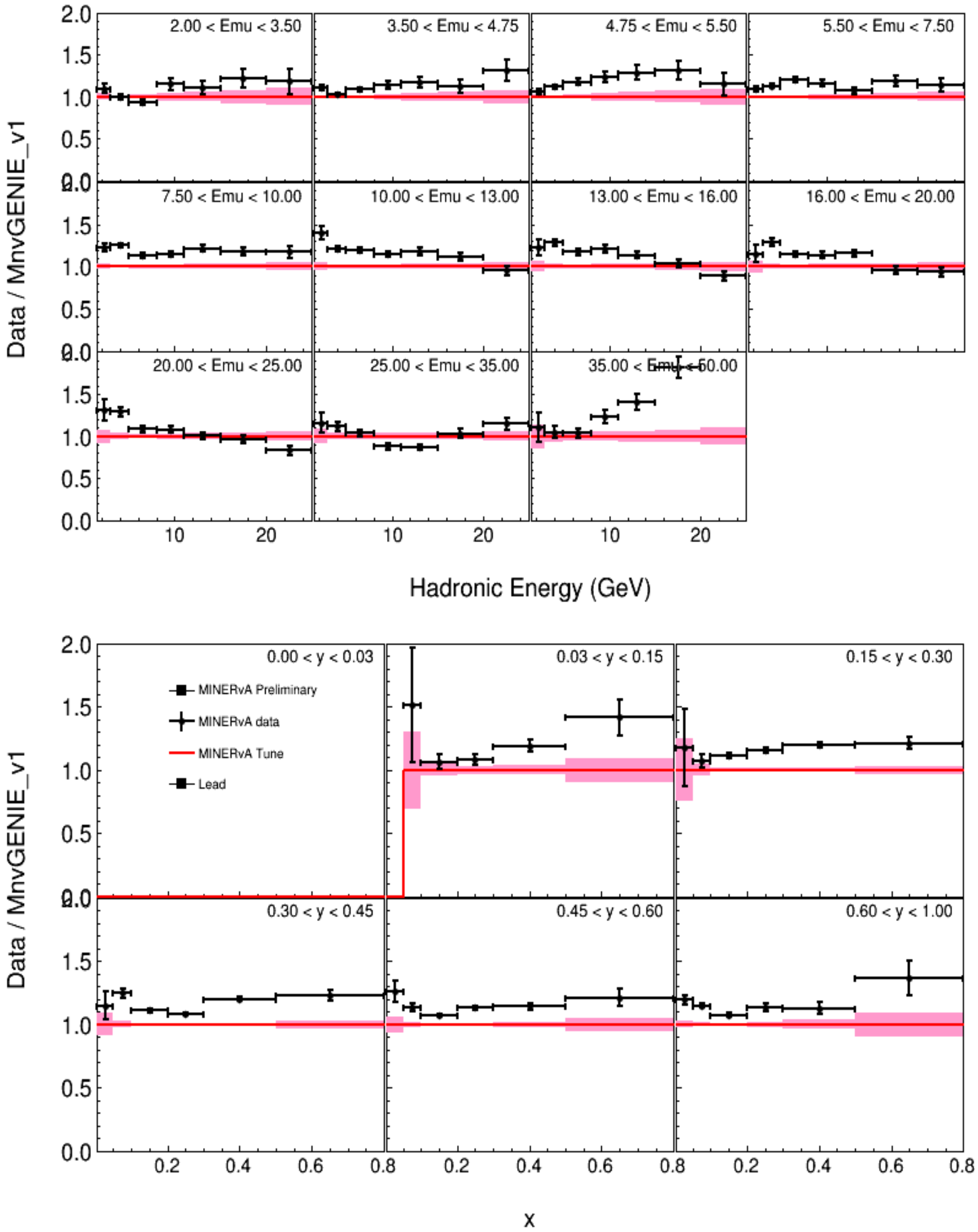

Figure B.3: The Data/simulation plots for the combined Pb of all targets. The plots are for two combinations: (i) Muon energy vs Hadronic Energy and (ii) Bjorken variable x and Inelasticity y. This is the first projection for the two pair of variables.

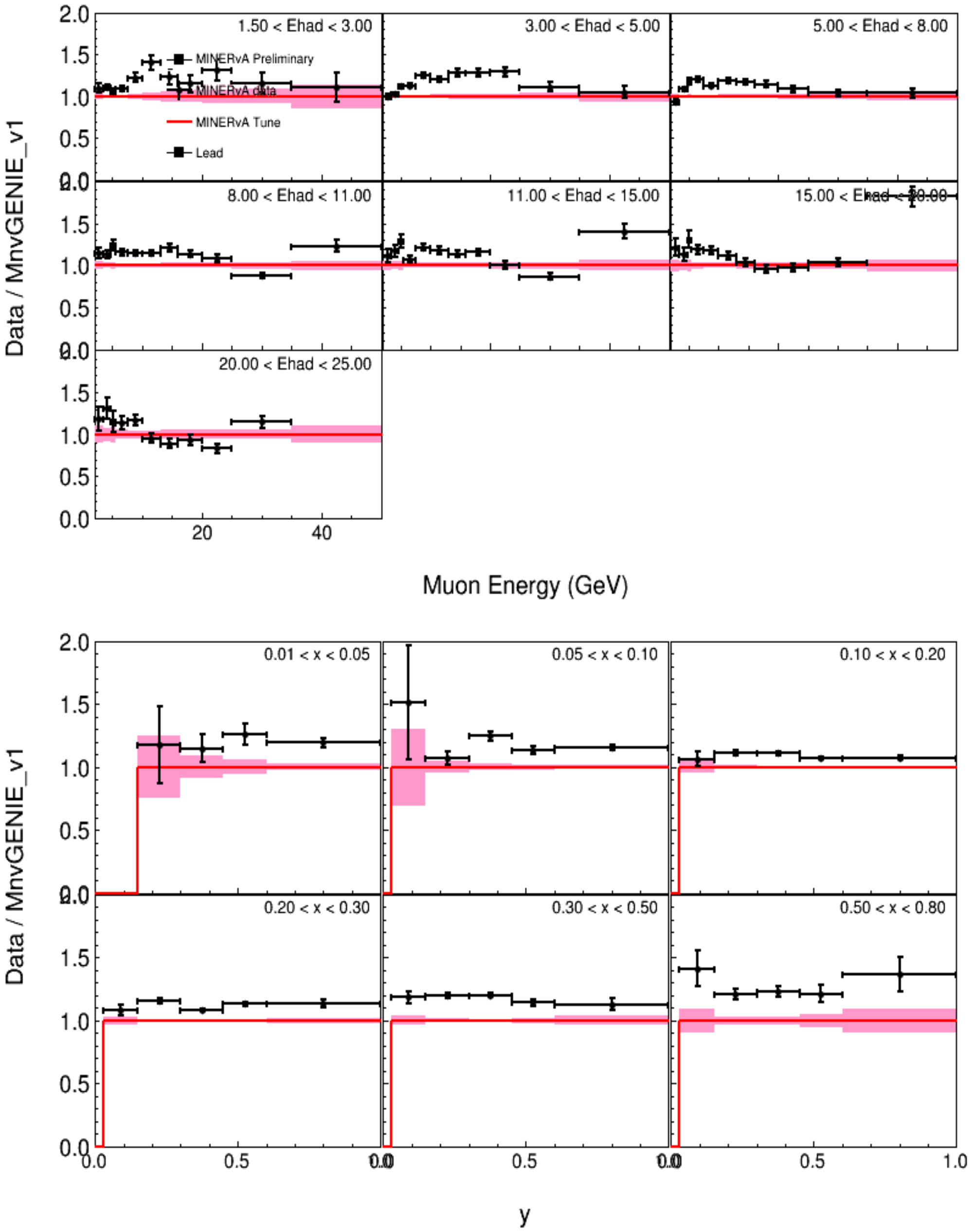

Figure B.4: The Data/simulation plots for the combined Pb of all targets. The second projection for the two pair of variables.

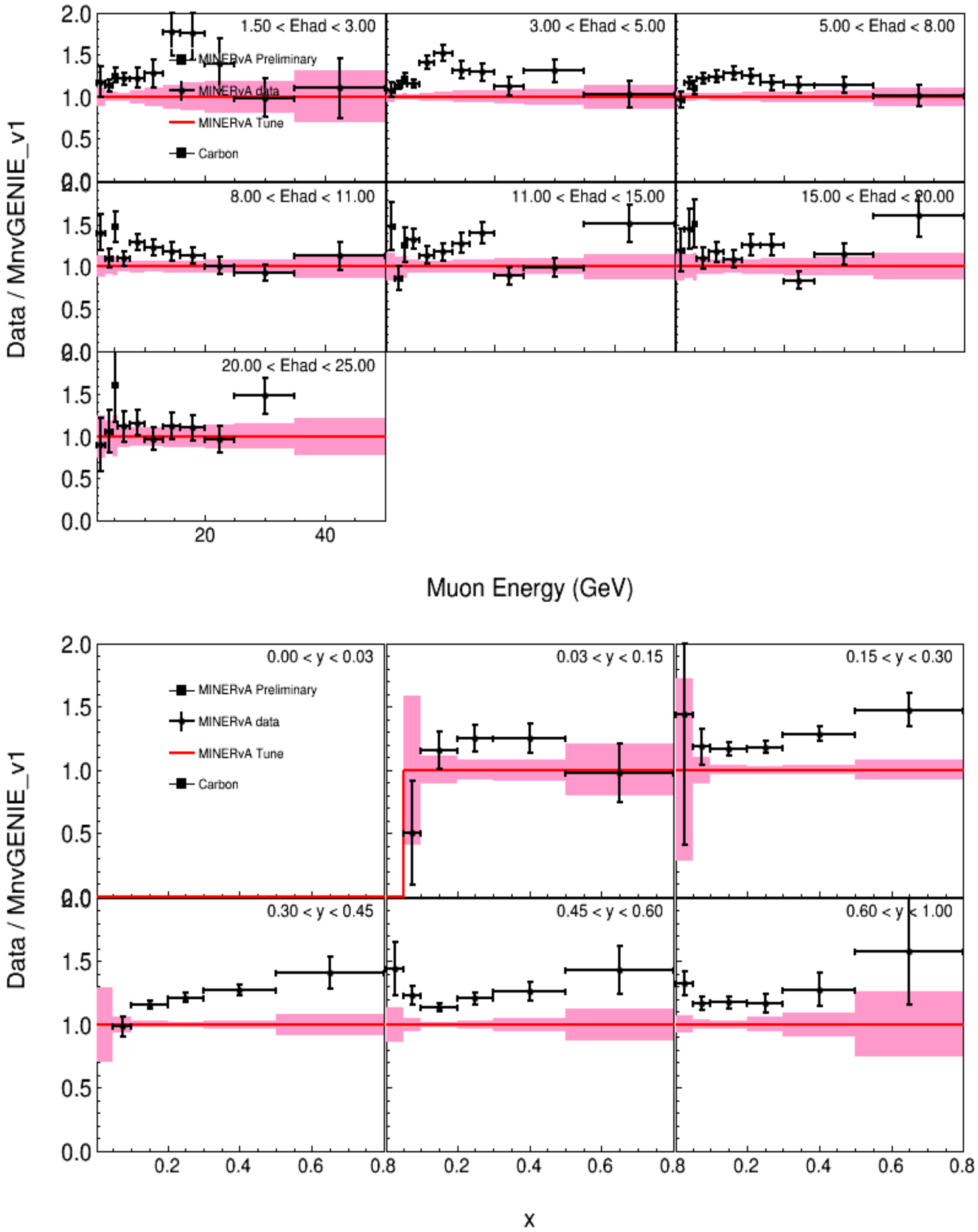

Figure B.5: The Data/simulation plots for the combined C of target 3. The plots are for two combinations: (i) Muon energy vs Hadronic Energy and (ii) Bjorken variable x and Inelasticity y. This is the first projection for the two pair of variables.

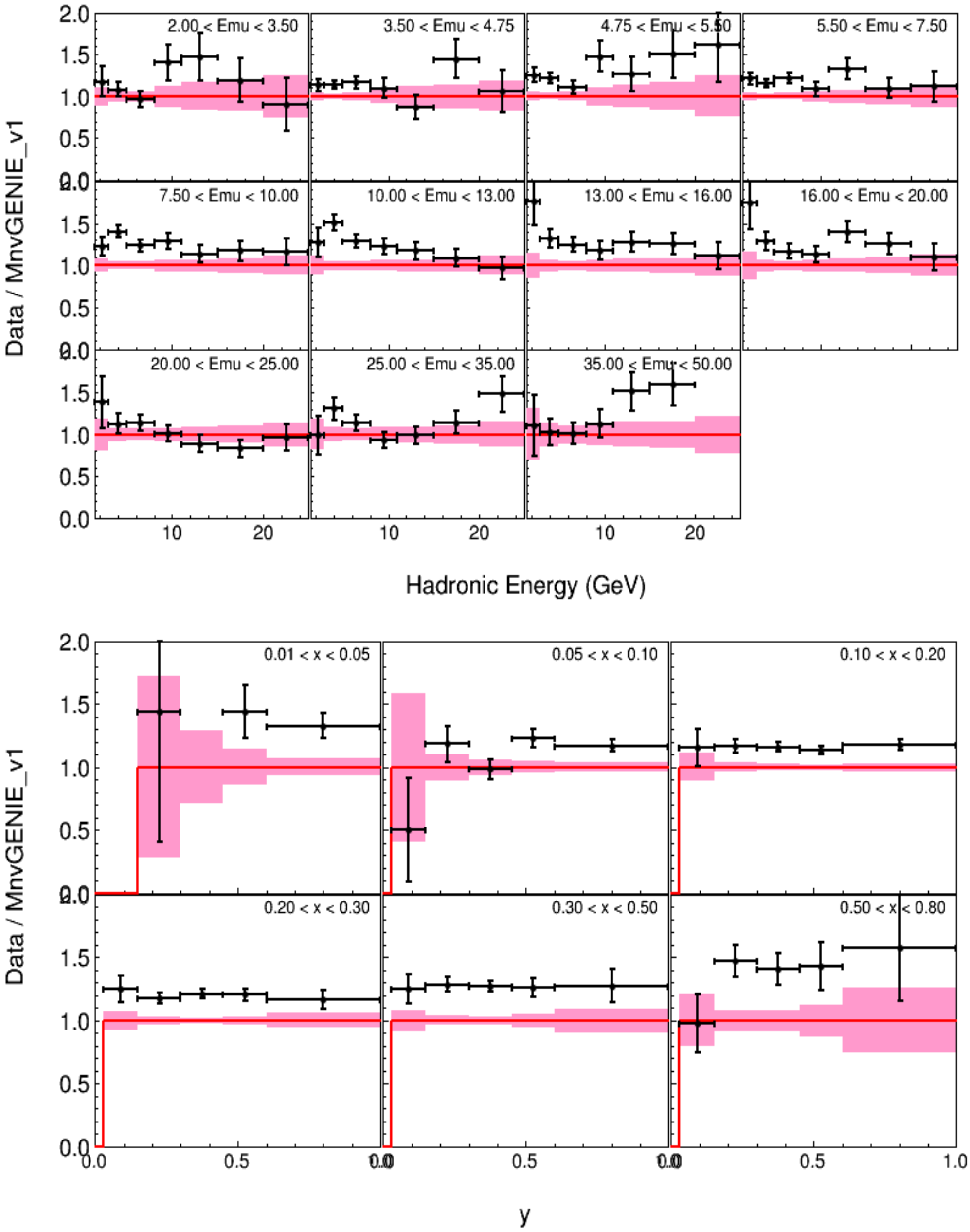

Figure B.6: The Data/simulation plots for the combined C of target 3. The second projection for the two pair of variables.

APPENDIX C

NON-RESONANT CONTRIBUTIONS

The non-resonant diagrams discussed in Chapter-7, give the essential contribution to the single meson production through the Born diagrams in s, t and u channels as shown in FigureC.1. While the s-channel diagrams consist of direct nucleon pole, the t-channel has meson poles and u-channel has the exchange baryon pole. Some phenomenological Lagrangians based on the pseudovector coupling or the effective Lagrangians based on the chiral symmetry also include, in addition to the Born terms, the contact diagram.

The contribution of all the Born diagrams corresponding to the non-resonant

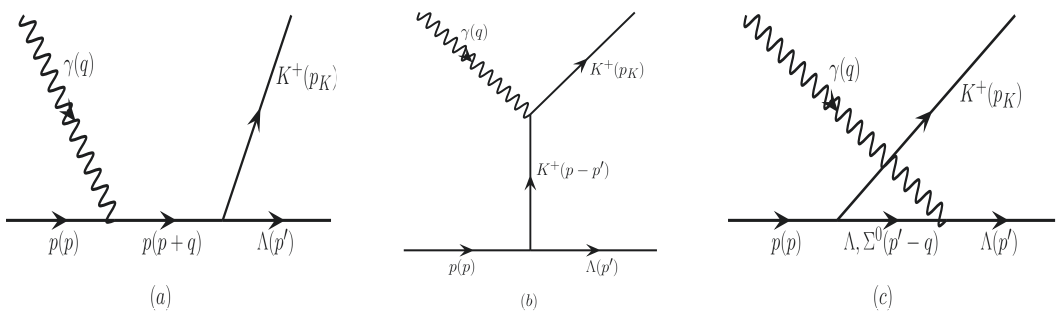

Figure C.1: Generic Feynman diagrams for the s, t and u-channels Born terms.

part are explicitly calculated using a phenomenological Lagrangian for πNN interaction. The contribution of the higher resonances are calculated using dispersion relation [279, 280, 281, 282]. Another method based on a dynamical model starting from the effective Lagrangian with bare pion-nucleon couplings obtained in the quark model, is used to construct a T matrix. Thereafter, a Lippmann-Schwinger equation is formulated and solved using coupled channel equations for pion production. In this way, it combines the effective Lagrangian with dynamical models [227, 224, 283]. In the case of effective Lagrangian approaches, the explicit contribution from the individual non-resonant Born diagrams and the higher resonances are explicitly calculated in terms of the parameters describing the effective Lagrangian.

Recently the effective Lagrangians based on the chiral symmetry have been used by many authors to calculate the inelastic reactions. One class of the models [284] uses Lagrangians containing nucleon, pion, σ, ω and ρ fields consistent with chiral symmetry while another class of models is based on the non-linear sigma model incorporating chiral symmetry [210, 285, 286, 287]. In the following sections, we outline the formalism to write an effective Lagrangian based on the chiral symmetry.

C.1 Chiral symmetry

The Lagrangian for QCD can be written as

$$\mathcal{L}_{QCD} = \overline{q}(i\not{D} - m_q)q - \frac{1}{4}G^{\alpha}_{\mu\nu}G^{\alpha\mu\nu} \tag{C.1}$$

where $q = \begin{pmatrix} u \\ d \\ s \end{pmatrix}$ denotes the quark field, $G^{\alpha}_{\mu\nu}$ is the gluon field-strength tensor with α as a color index and D_μ is defined as

$$D_\mu = \partial_\mu + ig\frac{\lambda^\alpha}{2}G_{\mu\alpha}, \tag{C.2}$$

where g is the quark-gluon coupling strength and $G_{\mu\alpha}$ is the vector gluon field. The Lagrangian written in Eq. (C.1) does not preserve chiral symmetry in its present form, however, in the limit when quark masses are assumed to be zero, the QCD Lagrangian preserves chiral symmetry. Today it is well established that all the quarks have non-zero mass although the current quark masses for u, d, s are small as compared to the nucleon mass. Thus, in the case of strong interactions, chiral symmetry is conserved in the limit of $m_u, m_d, m_s \to 0$. The consequence of the symmetries of the Lagrangian leads to the conserved currents. The vector current is conserved in nature due to the isospin symmetry. Similarly the axial vector current is conserved in the presence of the chiral symmetry. In case the chiral symmetry is broken spontaneously, it leads to the existence of massless Goldstone boson which are identified as the pion.

C.2 Transformation of mesons under chiral transformation

It is well known that the axial vector current is partially conserved and its consequences lead to the Goldberger-Treiman relation which relates the strong and weak couplings if it is broken spontaneously. The spectrum of mesons does not respect the chiral symmetry. Now we show the transformation of pion and rho mesons under the vector (Λ_V) and axial vector (Λ_V) transformations which are defined as

$$\Lambda_V \psi = e^{-i\frac{\vec{\tau}\cdot\vec{\Theta}}{2}}\psi = \left(1 - i\frac{\vec{\tau}\cdot\vec{\Theta}}{2}\right)\psi, \tag{C.3}$$

$$\Lambda_A \psi = e^{-i\gamma_5\frac{\vec{\tau}\cdot\vec{\Theta}}{2}}\psi = \left(1 - i\gamma_5\frac{\vec{\tau}\cdot\vec{\Theta}}{2}\right)\psi, \tag{C.4}$$

where $\psi = \begin{pmatrix} u \\ d \end{pmatrix}$ represents the quark doublet, Θ is the rotation angle, $\vec{\tau}$ represent the Pauli matrices. The pion and rho mesons can be expressed as

$$\vec{\pi} = i\bar{\psi}\vec{\tau}\gamma_5\psi, \qquad \vec{\rho}_\mu = \bar{\psi}\vec{\tau}\gamma_\mu\psi, \tag{C.5}$$

where $\vec{\pi}$, $\vec{\rho}$ represents the isovector pion and rho meson states, respectively. The subscript μ represents the vector mesons.

The vector transformation (Eq. (C.3)) when applied on the pion state yields

$$\begin{aligned}
\pi_i &= i\bar{\psi}\tau_i\gamma_5\psi = \Lambda_V^\dagger\bar{\psi}\tau_i\gamma_5\Lambda_V\psi, \\
&= i\bar{\psi}\left(1+\frac{i\tau_j\Theta^j}{2}\right)\tau_i\gamma_5\left(1-\frac{i\tau_j\Theta^j}{2}\right)\psi, \\
&= i\bar{\psi}\tau_i\gamma_5\psi + i\epsilon_{ijk}\Theta^j\bar{\psi}\tau_k\gamma_5\psi, \\
\vec{\pi} &= \vec{\pi} + \vec{\Theta}\times\vec{\pi}.
\end{aligned} \tag{C.6}$$

The above expression represents the rotation of the pion state through the isospin direction by the angle Θ. Similarly the vector transformation of the ρ mesons gives

$$\vec{\rho}_\mu = \vec{\rho}_\mu + \vec{\Theta}\times\vec{\rho}_\mu. \tag{C.7}$$

From Eqs. (C.6) and (C.7), it can be concluded that the vector transformation of the mesons leads to the rotation along the isospin direction, which means that the conservation of the vector current is associated with the isospin symmetry.

Next we see the axial vector transformation of theses meson states, starting with the pion state. For this, we start with Eq. (C.4) and obtain

$$\begin{aligned}
\pi_i &= i\bar{\psi}\tau_i\gamma_5\psi = \Lambda_A^\dagger\bar{\psi}\tau_i\gamma_5\Lambda_A\psi, \\
&= i\bar{\psi}\left(1-\frac{i\gamma_5\tau_j\Theta^j}{2}\right)\tau_i\gamma_5\left(1-\frac{i\gamma_5\tau_j\Theta^j}{2}\right)\psi, \\
&= i\bar{\psi}\tau_i\gamma_5\psi + \Theta^j\bar{\psi}(\delta_{ij})\psi,
\end{aligned}$$

$$\Rightarrow \qquad \vec{\pi} = \vec{\pi} + \vec{\Theta}\bar{\psi}\psi, \tag{C.8}$$

$$= \vec{\pi} + \vec{\Theta}\sigma, \tag{C.9}$$

if σ is identified with the scalar particle associated with $\bar{\psi}\psi$. Eq. (C.8) represents the rotation of the pion into linear combination of π and sigma meson when the axial vector transformation is applied on the pion state. Similarly, under axial vector transformation, a scalar meson σ $(= \bar{\psi}\psi)$ transforms as:

$$\begin{aligned} \sigma &= \bar{\psi}\psi = \Lambda_A \bar{\psi} \Lambda_A \psi, \\ &= \bar{\psi}\left(1 - i\gamma_5 \frac{\tau_j \Theta^j}{2}\right)\left(1 - i\gamma_5 \frac{\tau_j \Theta^j}{2}\right)\psi, \\ \Rightarrow \qquad \sigma &= \sigma - \vec{\Theta} \cdot \vec{\pi}. \end{aligned} \tag{C.10}$$

From Eqs. (C.8) and (C.10), it is inferred that the pion and sigma mesons, under the axial vector transformation, are rotated to each other.

Similarly, the transformation of the axial vector current on the ρ mesons gives

$$\begin{aligned} \rho_{\mu_i} &= \bar{\psi}\left(1 - i\gamma_5 \frac{\tau_j \Theta^j}{2}\right)\tau_i \gamma_\mu \left(1 - i\gamma_5 \frac{\tau_j \Theta^j}{2}\right)\psi, \\ \Rightarrow \qquad \vec{\rho}_\mu &= \vec{\rho}_\mu + \vec{\Theta} \times \vec{a}_{1_\mu}, \end{aligned} \tag{C.11}$$

where $\vec{a}_{1_\mu} = \bar{\psi}\vec{\tau}\gamma_\mu\gamma_5\psi$ represents vector meson a_1 with spin 1. The axial vector transformation of rho mesons shows the existence of a_1 meson. Also, the two i.e. rho and a_1 mesons are rotated into one another by the axial vector transformation.

Therefore, if the chiral symmetry is good, then $(\pi, \;\; \sigma)$ and $(\rho, \;\; a_1)$ should be degenerate which is not true experimentally. This is because we know that σ is not observed experimentally and in the case of ρ and a_1 meson states, the mass of ρ is $m_\rho = 0.77$ GeV while that of a_1 is $m_{a_1} = 1.23 \pm 0.04$ GeV. Since there is a large mass difference between the masses of ρ and a_1, therefore, the chiral symmetry is broken in nature at the nucleon level. However, if the chiral symmetry is broken spontaneously then the degeneracy of states is not a required consequence. Moreover, in this case, the massless Goldstone bosons can appear which are identified as pions. A small mass of pions can be generated by assigning a non zero but very small mass to the fermions in the theory which leads to an axial vector current consistent with PCAC [288, 289]. This degeneracy of mass spectrum is not present in the case of the spontaneous breaking of the symmetry, which generates the pion mass and leads to PCAC.

C.3 Linear sigma model

Linear sigma-model is an effective chiral model introduced by Gell-Mann and Levy in 1960 to study the chiral symmetry in the pion-nucleon system before the formulation of QCD. Spontaneous symmetry breaking and PCAC are the natural consequences of this model. The structure of the Lagrangian is Lorentz scalar and also is invariant under vector (Λ_V) and axial vector (Λ_A) transformations. We have studied in the earlier sections that the pion as well as sigma fields are not invariant under axial vector transformations. Our task is to first construct a field which is invariant under both Λ_V and Λ_A and then write the Lagrangian around it.

We have discussed in section C.2 that the vector transformation is nothing but the isospin rotation, thus, the squares of these fields are also invariant under vector transformation:

$$\pi^2 \xrightarrow{\Lambda_V} \pi^2 \qquad\qquad \sigma^2 \xrightarrow{\Lambda_V} \sigma^2, \tag{C.12}$$

while under the axial vector transformation, even the square of the meson fields are not invariant and yields the following expressions in the limit of small $\vec{\Theta}$:

$$\pi^2 \xrightarrow{\Lambda_A} \pi^2 + 2\sigma\vec{\Theta}\cdot\vec{\pi} \qquad\qquad \sigma^2 \xrightarrow{\Lambda_A} \sigma^2 - 2\sigma\vec{\Theta}\cdot\vec{\pi}. \tag{C.13}$$

Furthermore, from Eqs. (C.12) and (C.13), one may notice that the combination $\sigma^2+\pi^2$ is invariant under both vector and axial vector transformations. Also this combination is Lorentz invariant hence the Lagrangian for the linear sigma model can be constructed around $\sigma^2+\pi^2$.

The most general Lagrangian of the linear sigma model for the pion-nucleon

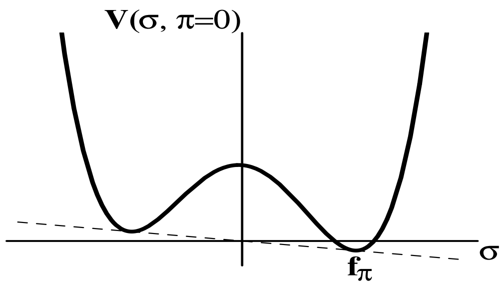

Figure C.2: Effect of explicit symmetry breaking.

interaction is written as [241, 290]:

$$\begin{aligned}\mathcal{L}_{LSM} &= i\bar{\psi}\partial_\mu\gamma^\mu\psi + \frac{1}{2}\partial_\mu\pi\partial^\mu\pi + \frac{1}{2}\partial_\mu\sigma\partial^\mu\sigma \\ &- g_\pi(i\bar{\psi}\gamma_5\vec{\tau}\psi\vec{\pi} + \bar{\psi}\psi\sigma) - \frac{\lambda}{4}\left((\pi^2+\sigma^2) - f_\pi^2\right)^2, \end{aligned} \tag{C.14}$$

where ψ, π and σ represents the nucleon, pion and sigma fields, respectively, g_π is the pion-nucleon coupling and f_π represents the pion decay constant. The first term in Eq. (C.14) represents the kinetic energy of the nucleon which is the Lagrangian of the massless nucleons. Second and third terms represent the kinetic energy of the pion and sigma mesons. The fourth term represents the pion-nucleon interaction term which is generally expressed by the term $g_\pi(i\bar{\psi}\gamma_5\vec{\tau}\psi)\vec{\pi}$ and transforms like π^2 under Λ_V and Λ_A transformations, while π^2 is not invariant under Λ_A transformation and one requires a term which transform like σ^2 to make the potential chiral invariant. The simplest choice for a Lagrangian which transforms like σ^2 is $g_\pi\bar{\psi}\psi\sigma$, thus, sigma is incorporated in the pion-nucleon potential to make it chiral invariant. The last term in Eq. (C.14) represents the pion-sigma potential. The vacuum expectation value of σ is generated by this potential, thus, the chiral invariance requires that the potential must be a function of $\pi^2+\sigma^2$. The simplest form of this potential is given by the last term in the above Lagrangian, where f_π represents the minimum of this potential.

In the Lagrangian given in Eq. (C.14), all the interaction terms between pion, nucleon and sigma are present except the mass terms. The mass term for the nucleon is generated without breaking the chiral symmetry, by its interaction with the sigma field which is given by the potential $g_\pi(\bar{\psi}\psi)\sigma$. This is achieved by giving a finite vacuum expectation value of the sigma fields

$$< \sigma >= \sigma_0, \tag{C.15}$$

which describes the spontaneous breaking of the chiral symmetry. By this mechanism the nucleon mass is generated. Due to the spontaneously broken chiral symmetry the pion remains massless and sigma obtains mass term through its coupling with the vacuum expectation value of the sigma field from the last terms in Eq. (C.14). Thus in the linear sigma model the pion is massless but sigma is massive.

C.4 Explicitly broken chiral symmetry

The chiral symmetry is a good symmetry in the limit of vanishing quark masses. In the presence of the quark mass terms in the Lagrangian, although being very small for the lowest lying $u,\ d,\ s$ quarks, the chiral symmetry is broken explicitly.

One can visualize the effect of the explicit symmetry breaking as shown in Figure C.2. In the case of the explicit symmetry breaking, the Hamiltonian and in turn, the potential is not symmetric under rotation. The ground state of the potential is shifted but the shift is very small such that the rotation along the pion axis and the radial excitation along the σ axis in the case of spontaneously breaking of the chiral symmetry remains almost undisturbed. The spontaneous and explicit symmetry breaking generate, respectively, the nucleon and the pion masses. Thus, in the limit of the small explicit breaking, the effect of the spontaneous breaking of the chiral symmetry still dominates the effect of the explicit breaking. This means that the chiral symmetry is good even in the limit of the small explicit symmetry breaking effect. The effect of the explicit symmetry breaking on the

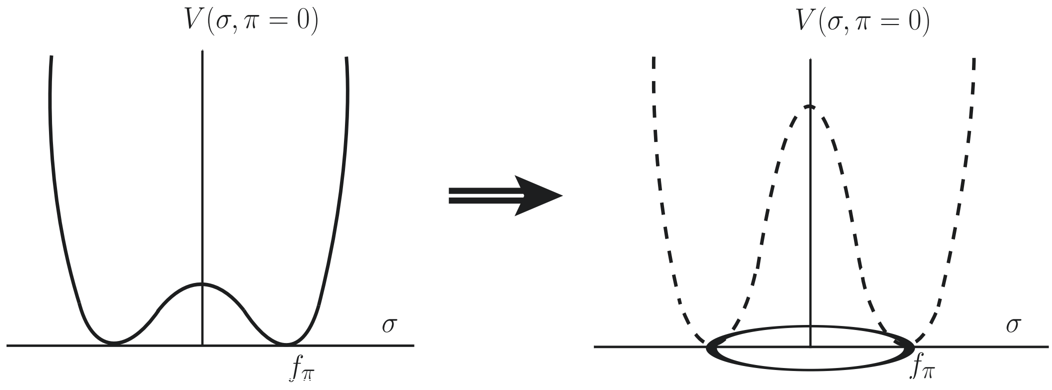

Figure C.3: Infinitely steep potential in the σ-direction.

linear sigma model makes the pion massive. However, the problem lies with the massive σ field, as the σ meson has not been observed experimentally and therefore non-linear sigma model was proposed which is discussed in the next section [241].

C.5 Non-linear sigma model

In the non-linear sigma model, this massive σ field is removed by taking an infinitely large coupling λ which results in the infinite mass of the σ meson and the potential gets infinitely steep in the sigma-direction as depicted in Figure C.3. Minimum of this potential defines a circle (known in the literature as the chiral circle but, in principle, it is a sphere not a circle) described by

$$\pi^2 + \sigma^2 = f_\pi^2. \tag{C.16}$$

The dynamics of the system is confined to the rotation along this circle. Thus, the pion and sigma meson fields can be expressed in terms of the pion fields $\vec{\Phi}(x)$ and the radius of the circle f_π, as

$$\begin{aligned} \sigma(x) &= f_\pi \cos\left(\frac{\Phi(x)}{f_\pi}\right), && \text{(C.17)} \\ \vec{\pi}(x) &= f_\pi \hat{\Phi} \sin\left(\frac{\Phi(x)}{f_\pi}\right), && \text{(C.18)} \end{aligned}$$

where $\Phi = \sqrt{\vec{\Phi}\vec{\Phi}}$ and $\hat{\Phi} = \frac{\vec{\Phi}}{\Phi}$.

The pion and sigma fields can be expressed in the complex form as

$$U(x) = e^{\frac{i\vec{\tau}\cdot\vec{\Phi}(x)}{f_\pi}} = \cos\left(\frac{\Phi(x)}{f_\pi}\right) + i\vec{\tau}\hat{\Phi}\sin\left(\frac{\Phi(x)}{f_\pi}\right) = \frac{1}{f_\pi}(\sigma + i\vec{\tau}\vec{\pi}), \tag{C.19}$$

where $U(x)$ is the unitary 2×2 matrix. In terms of the complex field, the chiral circle is expressed as

$$\frac{1}{2}\mathrm{Tr}(U^\dagger U) = \frac{1}{f_\pi}(\sigma^2 + \pi^2) = 1. \tag{C.20}$$

As in the case of the vector current, isospin symmetry corresponds to the rotational symmetry, analogously, the chiral symmetry corresponds to the rotational symmetry along the chiral circle.

The Lagrangian for the linear sigma model given in Eq. (C.14) is now expressed in terms of Φ or the complex representation $U(x)$.

Writing the kinetic energy terms of the mesons, in terms of $U(x)$, we get

$$\frac{1}{2}(\partial_\mu\sigma\partial^\mu\sigma + \partial_\mu\vec{\pi}\partial^\mu\vec{\pi}) = \frac{f_\pi^2}{4}(\partial_\mu U^\dagger\partial^\mu U). \tag{C.21}$$

Similarly, the nucleon-meson coupling term modifies as

$$\begin{aligned}
-g_\pi(\bar{\psi}\psi\sigma + i\bar{\psi}\gamma_5\vec{\tau}\psi\vec{\pi}) &= -g_\pi\bar{\psi}\left(f_\pi\cos\left(\frac{\Phi}{f_\pi}\right) + i\gamma_5\vec{\tau}f_\pi\hat{\Phi}\sin\left(\frac{\Phi}{f_\pi}\right)\right)\psi, \\
&= g_\pi f_\pi\bar{\psi}e^{\frac{i\gamma_5\vec{\tau}.\vec{\Phi}}{f_\pi}}\psi, \\
&= g_\pi f_\pi\bar{\psi}\Lambda\Lambda\psi
\end{aligned} \tag{C.22}$$

with $\Lambda = e^{\frac{i\gamma_5\vec{\tau}.\vec{\Phi}}{2f_\pi}}$.

Redefining the nucleon field ψ by

$$\psi_W = \Lambda\psi, \tag{C.23}$$

the nucleon-meson coupling strength becomes

$$-g_\pi(\bar{\psi}\psi\sigma + i\bar{\psi}\gamma_5\vec{\tau}\psi\vec{\pi}) = -g_\pi f_\pi\bar{\psi}_W\psi_W = -M\bar{\psi}_W\psi_W, \tag{C.24}$$

where the Goldberger-Treiman relation ($g_\pi = \frac{g_{\pi NN}}{\sqrt{2}}$; $g_\pi f_\pi = M$) is used. Thus, in the non-linear sigma model the nucleon-meson interaction term reduces to the nucleon mass term. In terms of the redefined nucleon field ψ_W, the nucleon kinetic energy term is modified as:

$$\begin{aligned} \bar{\psi}(i\partial\!\!\!/)\psi &= \bar{\psi}_W \Lambda^\dagger (i\partial^\mu \gamma_\mu) \Lambda^\dagger \psi_W, \\ &= \bar{\psi}_W (i\partial\!\!\!/ + \gamma_\mu V^\mu + \gamma_\mu \gamma_5 A^\mu) \psi_W \end{aligned} \tag{C.25}$$

where V^μ and A^μ are defined in terms of the unitary matrix u as

$$V^\mu = \frac{1}{2}[u^\dagger \partial^\mu u + u \partial^\mu u^\dagger], \tag{C.26}$$

$$A^\mu = \frac{i}{2}[u^\dagger \partial^\mu u - u \partial^\mu u^\dagger], \tag{C.27}$$

and

$$u = e^{\frac{i\vec{\tau}.\vec{\Phi}}{2f_\pi}}; \quad U = u^2. \tag{C.28}$$

The last term of the Lagrangian given in Eq. (C.14) vanishes as the potential between the pion and sigma fields vanishes in the chiral limit ($\pi^2 + \sigma^2 = f_\pi^2$). Thus, the Lagrangian for the non-linear sigma model in the chiral limit becomes

$$\mathcal{L}_{NLSM} = \bar{\psi}_W (i\partial\!\!\!/ + \gamma_\mu V^\mu + \gamma_\mu \gamma_5 A^\mu - M) \psi_W + \frac{f_\pi^2}{4} (\partial_\mu U^\dagger \partial^\mu U), \tag{C.29}$$

where the first term of the above Lagrangian represents the interaction between the nucleons and pions (in general, between baryons and mesons) and the second term represents the interaction between pions (in general mesons). The above Lagrangian can be expanded in terms of the single variable, $\vec{\Phi}(x)$, which represents the pion field. Noticeably the sigma field which was present in the linear sigma model has got disappeared in the Lagrangian for the non-linear sigma model. An important point to keep in mind regarding the Lagrangian given in Eq. (C.29) is that it represents only the interaction between pions and nucleons but not the interaction of these particles with the gauge bosons.

In reality all the interactions proceed via the exchange of gauge bosons. Thus, our next task is to incorporate the gauge bosons in the meson-meson and meson-baryon Lagrangians which be discussed in the next section. Also it is worth mentioning that the unitary matrix U is expressed in terms of the Pauli matrices $\vec{\tau}$ representing the SU(2) isospin symmetry, however, one may extend the Lagrangian given in Eq. (C.29) to the SU(3) isospin symmetry, i.e. through the inclusion of the octet of mesons and baryons.

C.6 Lagrangian for the meson-meson and meson-gauge boson interactions

The Lagrangian for the meson-meson interaction is given in Eq. (C.29) (second term), where in the unitary matrix $U = e^{\frac{i\vec{\tau}\vec{\Phi}(x)}{f_\pi}}$, $\vec{\tau}$ stands for the SU(2) isospin symmetry. In order to extend the meson-meson Lagrangian for the SU(3) symmetry (where the three massless quarks; u, d, s are considered), the Lagrangian remains the same while the only change is the modification of U, which in the SU(3) symmetry becomes

$$U(x) = e^{\frac{i\vec{\lambda}\cdot\vec{\Phi}(x)}{f_\pi}} = e^{\frac{i\lambda_i\Phi_i(x)}{f_\pi}}; \qquad i = 1-8, \tag{C.30}$$

where λ represents the Gell-Mann matrices and Φ_i represents the octet of the meson fields, expressed as

$$\begin{aligned}\vec{\lambda}\cdot\vec{\Phi} = \sum_{i=1}^{8}\lambda_i\Phi_i &= \begin{pmatrix} \Phi_3 + \frac{1}{\sqrt{3}}\Phi_8 & \Phi_1 - i\Phi_2 & \Phi_4 - i\Phi_5 \\ \Phi_1 + i\Phi_2 & -\Phi_3 + \frac{1}{\sqrt{3}}\Phi_8 & \Phi_6 - i\Phi_7 \\ \Phi_4 + i\Phi_5 & \Phi_6 + i\Phi_7 & -\frac{2}{\sqrt{3}}\Phi_8 \end{pmatrix} \\ &= \begin{pmatrix} \pi^0 + \frac{1}{\sqrt{3}}\eta & \sqrt{2}\pi^+ & \sqrt{2}K^+ \\ \sqrt{2}\pi^- & -\pi^0 + \frac{1}{\sqrt{3}}\eta & \sqrt{2}K^0 \\ \sqrt{2}K^- & \sqrt{2}\bar{K}^0 & -\frac{2}{\sqrt{3}}\eta \end{pmatrix}.\end{aligned} \tag{C.31}$$

With these modifications, the second term of the Lagrangian given in Eq. (C.29) gives the interaction among the octet of the pseudoscalar mesons. Using Eqs. (C.30) and (C.31) in the second term of the Lagrangian given in Eq. (C.29), one obtains the Lagrangians for the different meson-meson interactions. Here, for the sake of completeness, we write down the Lagrangians for the $\pi^+\pi^+ \to \pi^+\pi^+$ and

$\pi^+\pi^- \to K^+K^-$ interactions, as

$$\mathcal{L}_{\pi\pi\pi\pi} = \frac{\pi^+\partial_\mu\pi^-\pi^+\partial^\mu\pi^-}{2f_\pi^2}, \tag{C.32}$$

$$\mathcal{L}_{\pi\pi KK} = \frac{\pi^+\pi^-\partial_\mu K^-\partial^\mu K^+}{2f_\pi^2}. \tag{C.33}$$

However, in the real world, we need the interaction of these mesons with the gauge bosons. Therefore, the gauge boson fields are incorporated in the meson-meson Lagrangian by the replacing the partial derivative ∂_μ by the covariant derivative D_μ, i.e.,

$$\mathcal{L}_{MM} = \frac{f_\pi^2}{4}(D_\mu U^\dagger D^\mu U), \tag{C.34}$$

where $D_\mu U$ and $D_\mu U^\dagger$ written as

$$D_\mu U = \partial_\mu U - ir_\mu U + iUl_\mu, \tag{C.35}$$

$$D_\mu U^\dagger = \partial_\mu U^\dagger + iU^\dagger r_\mu - il_\mu U^\dagger. \tag{C.36}$$

r_μ and l_μ, respectively, represents the right and left handed currents, defined in terms of the vector (v_μ) and axial vector (a_μ) fields as

$$l_\mu = \frac{1}{2}(v_\mu - a_\mu), \qquad r_\mu = \frac{1}{2}(v_\mu + a_\mu). \tag{C.37}$$

The vector and axial vector fields are different for the interaction of the different gauge bosons with the meson fields. In the following, we explicitly discuss the interaction of the photon with the meson-meson Lagrangian for the electromagnetic processes.

C.6.1 Interaction with the photon field

Since we know that the electromagnetic interactions are purely vector in nature, therefore, the axial vector current does not contribute, thus, the left and right handed currents are identical and are expressed as

$$l_\mu = r_\mu = -e\hat{Q}A_\mu, \tag{C.38}$$

where $\hat{Q} = \begin{pmatrix} 2/3 & 0 & 0 \\ 0 & -1/3 & 0 \\ 0 & 0 & -1/3 \end{pmatrix}$ represents the charge of $u,\ d,\ s$ quarks, e is the electric charge and A_μ represents the photon field.

Using Eqs. (C.38), (C.35) and (C.36) in Eq. (C.34), one obtains the Lagrangian for the mesons interacting with the photons, for example, here we write the Lagrangians for the $\gamma\pi^+ \to \pi^+$ and $\pi^+\pi^- \to \gamma\gamma$ processes, as

$$\mathcal{L}_{\gamma\pi\pi} = -ie\pi^+\partial_\mu\pi^- A^\mu, \tag{C.39}$$

$$\mathcal{L}_{\gamma\gamma\pi\pi} = -e^2\pi^+\pi^- A_\mu A^\mu. \tag{C.40}$$

Similarly, Lagrangians for the different interactions are obtained.

C.7 Lagrangian for the meson-baryon-gauge boson interaction

The Lagrangian for the meson-baryon interaction is given as the first term of Eq. (C.29), where V_μ and A_μ are defined in terms of a unitary matrix u given in Eq. (C.28) for the SU(2) symmetry. The modification of u by the following expression:

$$u(x) = e^{\frac{i\vec{\Phi}\cdot\vec{\lambda}}{2f_\pi}}, \tag{C.41}$$

leads to the meson-baryon Lagrangian in the SU(3) symmetry. The Lagrangian for the meson-baryon interaction can be rewritten as

$$\mathcal{L}_{MB} = \mathrm{Tr}[\bar{B}(i\not{D} - M)B] - \frac{D}{2}\mathrm{Tr}[\bar{B}\gamma_\mu\gamma_5\{u^\mu, B\}] - \frac{F}{2}\mathrm{Tr}[\bar{B}\gamma_\mu\gamma_5[u^\mu, B]], \tag{C.42}$$

where M represents the baryon mass, D and F are the axial vector coupling constants for the baryons octet obtained from the analysis of the semileptonic decays of neutron and hyperons and B represents the baryon field, defined as

$$\begin{aligned} B(x) = \sum_{i=1}^{8} \frac{1}{\sqrt{2}} b_i \lambda_i &= \frac{1}{\sqrt{2}} \begin{pmatrix} b_3 + \frac{1}{\sqrt{3}} b_8 & b_1 - i b_2 & b_4 - i b_5 \\ b_1 + i b_2 & -b_3 + \frac{1}{\sqrt{3}} b_8 & b_6 - i b_7 \\ b_4 + i b_5 & b_6 + i b_7 & -\frac{2}{\sqrt{3}} b_8 \end{pmatrix} \\ &= \begin{pmatrix} \frac{1}{\sqrt{2}} \Sigma^0 + \frac{1}{\sqrt{6}} \Lambda & \Sigma^+ & p \\ \Sigma^- & -\frac{1}{\sqrt{2}} \Sigma^0 + \frac{1}{\sqrt{6}} \Lambda & n \\ \Xi^- & \Xi^0 & -\frac{2}{\sqrt{6}} \Lambda \end{pmatrix}, \end{aligned} \tag{C.43}$$

with b_i being the component of the baryon field. The quantities $D_\mu B$ and u^μ are defined as

$$D_\mu B = \partial_\mu B + [\Gamma_\mu, B], \tag{C.44}$$

$$u^\mu = i[u^\dagger(\partial^\mu - i r^\mu) u - u(\partial^\mu - i l^\mu) u^\dagger], \tag{C.45}$$

with

$$\Gamma_\mu = \frac{1}{2}[u^\dagger(\partial^\mu - i r^\mu) u - u(\partial^\mu - i l^\mu) u^\dagger] \tag{C.46}$$

and u defined in Eq. (C.28). r_μ and l_μ, respectively, represents the right and left handed currents, defined in terms of the vector (v_μ) and axial vector (a_μ) fields and are given in Eq. (C.37). These currents represent the interaction of the gauge bosons with the meson-baryon Lagrangian. Thus, the vector and axial vector fields are different for the interaction of the different gauge bosons. In the following section, we present the Lagrangians for the interaction of the photon with the mesons and baryon.

C.7.1 Interaction with the photon field

The left and right handed currents are given in Eq. (C.38) using Eqs. (C.38) and (C.43)–(C.46) in Eq. (C.42). The Lagrangian for the interaction of mesons and baryons among themselves and with the photon (γ) fields is obtained. For example, here we write the Lagrangians for the $\gamma p \to p$, $p \to p\pi^0$ and $\gamma p \to n\pi^+$

processes, as

$$\mathcal{L}_{\gamma pp} = -e\ \bar{p}\gamma_\mu p\ A^\mu, \tag{C.47}$$

$$\mathcal{L}_{pp\pi^0} = -\frac{(D+F)}{2f_\pi}\bar{p}\gamma_\mu\gamma_5 p\ \partial^\mu\pi^0, \tag{C.48}$$

$$\mathcal{L}_{\gamma pn\pi^+} = \frac{ie}{\sqrt{2}f_\pi}(D+F)\ \bar{n}\gamma_\mu\gamma_5 p\ A^\mu\pi^-. \tag{C.49}$$

In a similar manner, one may obtain the Lagrangians for the different possible interactions of the meson-baryon system with the photon field.

The Lagrangians which we have discussed in this Appendix are used to write the matrix element for specific processes in Chapter-7.

Bibliography

BIBLIOGRAPHY

[1] S. L. Glashow, Nucl. Phys. **22**, 579 (1961).

[2] The CMS collaboration, The CMS collaboration.

[3] A. Salam, Conf. Proc. C **680519**, 367 (1968).

[4] S. Weinberg, Phys. Rev. Lett. **19**, 1264 (1967).

[5] G. 't Hooft and M. J. G. Veltman, Nucl. Phys. B **44**, 189 (1972).

[6] B. W. Lee and J. Zinn-Justin, Phys. Rev. D **5**, 3121 (1972).

[7] S. L. Glashow, J. Iliopoulos and L. Maiani, Phys. Rev. D **2**, 1285-1292 (1970).

[8] W. Pauli, Letter to L. Meitner and her colleagues dated 4 December 1930 (letter open to the participants of the conference in Tübingen) (1930), recorded in W. Pauli, Wissenschaftlicher Briefwechsel mit Bohr, Einstein, Heisenberg u.a ., Band 11(Springer, Berlin, 1985) p. 39. A reference to 'neutrino' is seen in a letter from Heisenberg to Pauli on 1 December 1930: "Zu Deinen Neutronen möchte ich noch bemerken: ..." .

[9] E. Fermi, Nuovo Cim. **11**, 1 (1934).

[10] G. Gamow and E. Teller, Phys. Rev. **49**, 895 (1936).

[11] E. C. G. Sudarshan and R. E. Marshak, Phys. Rev. **109**, 1860 (1958).

[12] R. P. Feynman and M. Gell-Mann, Phys. Rev. **109**, 193 (1958).

[13] J. J. Sakurai, Nuovo Cim. **7**, 649 (1958).

[14] J. Orear, G. Harris, and S. Taylor. Phys. Rev. **102**, 1676 (1956).

[15] T. D. Lee and C. N. Yang, Phys. Rev. **104**, 254 (1956).

[16] C. S. Wu, E. Ambler, R. W. Hayward, D. D. Hoppes and R. P. Hudson, Phys. Rev. **105**, 1413 (1957).

[17] M. S. Athar and S. K. Singh, *"The Physics of Neutrino Interactions,"* Cambridge University Press (2020).

[18] F. Reines and C. L. Cowan, Nature **178**, 446 (1956).

[19] G. Danby, J. M. Gaillard, K. A. Goulianos, L. M. Lederman, N. B. Mistry, M. Schwartz and J. Steinberger, Phys. Rev. Lett. **9**, 36 (1962).

[20] K. Kodama *et al.* [DONUT Collaboration], Phys. Lett. B **504**, 218 (2001).

[21] N. Agafonova *et al.* [OPERA Collaboration], Phys. Lett. B **691**, 138 (2010).

[22] The Internal Constitution of the Stars, A. S. Eddington, The Scientific Monthly Vol. 11, No. 4 (Oct., 1920), pp. 297-303.

[23] R. Davis, Phys. Rev. Lett. **12**, 303 (1964); R. Davis, Jr., D. S. Harmer and K. C. Hoffman, Phys. Rev. Lett. **20**, 1205 (1968).

[24] J .N. Bahcall, *Neutrino Astrophysics*, Cambridge University Press, Cambridge (1989).

[25] B. Pontecorvo, Sov. Phys. JETP **6**, 429 (1957) [Zh. Eksp. Teor. Fiz. **33**, 549 (1957)].

[26] M. Gell-Mann and A. Pais, Phys. Rev. **97**, 1387 (1955).

[27] *“Single Charged Pion Production by Muon Neutrinos in the MINERvA Detector Using the NuMI Beam,”* http://d-scholarship.pitt.edu/38098/13/Messerly%20Final%20ETD.pdf.

[28] Z. Maki, M. Nakagawa and S. Sakata, Prog. Theor. Phys. **28**, 870 (1962).

[29] P. Lipari, M. Lusignoli and F. Sartogo, Phys. Rev. Lett. **74**, 4384 (1995).

[30] M. Rafi Alam, M. Sajjad Athar, S. Chauhan and S. K. Singh, Int. J. Mod. Phys. E **25**, 1650010 (2016).

[31] M. Rafi Alam, I. Ruiz Simo, M. Sajjad Athar and M. J. Vicente Vacas, Phys. Rev. D **85**, 013014 (2012).

[32] A. Fatima, Z. Ahmad Dar, M. Sajjad Athar and S. K. Singh, Int. J. Mod. Phys. E **29**, 2050051 (2020).

[33] M. Sajjad Athar, Jorge G. Morfin, FERMILAB-PUB-20-161-ND.

[34] L. Alvarez-Ruso *et al.* [NuSTEC], Prog. Part. Nucl. Phys. **100**, 1 (2018).

[35] T. Katori and M. Martini, J. Phys. G **45**, 013001 (2018).

[36] R. M. Zwaska, Accelerator Systems and Instrumentation for the NuMI Neutrino Beam (Page 5, Figure 1-2), Ph.D. thesis, Texas U. (2005). doi:10.2172/879065. URL http://lss.fnal.gov/cgi-bin/find paper.pl?thesis-2005-73

[37] L. Aliaga Soplin. “Neutrino Flux Prediction for the NuMI Beamline”. PhD thesis, William-Mary Coll., 2016.

[38] Nuruzzaman, “POT for the Medium Energy Run”, internal Document (2017). URL http://minerva-docdb.fnal.gov:8080/cgi-bin/ShowDocument?docid=12813

[39] P. Adamson *et al.*, Nucl. Instrum. Meth., A **806**, 279 (2016).

[40] A. Norrick, Approved me flux plots, internal Document (2017). URL https://minerva-docdb.fnal.gov/cgi-bin/private/ShowDocument?docid=9956

[41] Fermilab, Numi magnetic focusing horns (2017). URL http://targets.fnal.gov/NuMI horns.html

[42] L. Aliaga et al., Design, calibration, and performance of the minerva detector, Nucl. Instrum Meth. A **743**, 130 (2014).

[43] D.G. Michael *et al.*, Nucl. Instrum. Meth. A **596**, 190 (2008).

[44] P. Adamson *et al.*, Phys. Rev. D **81**, 072002 (2010).

[45] G. N. Perdue, Event Reconstruction in MINERvA (slide 15) , internal Document (2015). URL https://minerva-docdb.fnal.gov/cgi-bin/private/RetrieveFile?docid=10017

[46] R. Fruhwirth, Nucl. Instrum. Meth. A **262** (1987).

[47] W. D. Hulsbergen, Nucl. Instrum. Meth. A **552** (2005).

[48] R. Ospanov, A measurement of muon neutrino disappearance with the MINOS detectors and NuMI beam, Ph.D. thesis, The University of Texas at Austin (2008).

[49] T. M. Collaboration, Neutrino Oscillation Physics at Fermilab: The NuMI-MINOS Project, FERMILAB Technical Reports.

[50] L. Aliaga *et al.* (MINERvA), Nucl. Instrum. Meth. A **743**, 130 (2014).

[51] C. Andreopoulos *et al.*, Nucl. Instrum. Meth. A **614**, 87 (2010).

[52] A. Bodek and J. L. Ritchie, Phys. Rev. D **23**, 1070 (1981).

[53] R. Bradford, A. Bodek, H. S. Budd, and J. Arrington, Nucl. Phys. Proc. Suppl. **159**, 127 (2006).

[54] C. H. Llewellyn Smith, Phys. Rept. **3**, 261 (1972).

[55] D. Rein and L. M. Sehgal, Annals Phys. **133**, 79 (1981).

[56] A. Bodek, I. Park, and U.-k. Yang, Nucl. Phys. Proc. Suppl. **139**, 113 (2005).

[57] A. Bodek and U. K. Yang, J. Phys. **G29**, 1899 (2003).

[58] T. Yang, C. Andreopoulos, H. Gallagher, K. Hoffmann, and P. Kehayias, Eur. Phys. J. C **63**, 1 (2009).

[59] Z. Koba, H. B. Nielsen, and P. Olesen, Nucl. Phys. **B40**, 317 (1972).

[60] T. Sjostrand, S. Mrenna, and P. Z. Skands, JHEP **05**, 026 (2006).

[61] J. Nieves, I. Ruiz Simo, and M. J. Vicente Vacas, Phys. Lett. **B707**, 72 (2012).

[62] J. T. Sobczyk, Phys. Rev. C **86**, 015504 (2012).

[63] R. Gran, J. Nieves, F. Sanchez, and M. J. Vicente Vacas, Phys. Rev. D **88**, 113007 (2013).

[64] J. Schwehr, D. Cherdack, and R. Gran, arXiv:1601.02038 [hep-ph].

[65] J. Nieves, J. E. Amaro, and M. Valverde, Phys. Rev. C **70**, 055503 (2004), Phys. Rev. C **72**, 019902 (2005).

[66] S. A. Dytman and A. S. Meyer, AIP Conf. Proc. **1405**, 213 (2011).

[67] S. Agostinelli et al. (GEANT4), Nucl. Instrum. Meth. A **506**, 250 (2003).

[68] B. G. Tice *et al.*, Phys. Rev. Lett. **112** (23) (2014).

[69] J. Mousseau *et al.*, Phys. Rev. D **93**, 071101 (2016).

[70] G. N. Perdue *et al.*, Journal of Instrumentation, Volume 13, Number 11, 2018.

[71] F. James, M. Winkler, MINUIT Users Guide, http://seal.web.cern.ch/seal/documents/minuit/mnusersguide.pdf (2004).

[72] J. Mousseau, Genie cross section weight note, internal Document (2013). URL https://minerva-docdb.fnal.gov/cgi-bin/private/RetrieveFile?docid=7565

[73] C. Patrick, Measurement of the Antineutrino Double-Differential Charged-Current Quasi-Elastic Scattering Cross Section at MINERvA, Ph.D. thesis, Northwestern U. (2016). doi:10.1007/978-3-319-69087-2.

[74] B. Tice, Analysis of charged current neutrino interactions on nuclear targets, internal Document (2013). URL https://minerva-docdb.fnal.gov/cgi-bin/private/RetrieveFile?docid=8854

[75] G. D'Agostini, Nucl. Instrum. Meth. A **362**, 487 (1995).

[76] J. Mousseau, First Search for the EMC Effect and Nuclear Shadowing in Neutrino Nucleus Deep Inelastic Scattering at MINERvA, Ph.D. thesis, Florida U (2015). doi:10.1007/978-3-319-44841-1.

[77] Super-Kamiokande Collaboration, Y.Fukuda et al., Phys. Rev. Lett. **81**, 1562 (1998).

[78] Super-Kamiokande Collaboration, Y.Fukuda et al., Phys. Rev. Lett. **82**, 2644 (1999).

[79] SNO, Q. R. Ahmad et al., Phys. Rev. Lett. **89**, 011301 (2002).

[80] KamLAND, K. Eguchi et al., Phys. Rev. Lett. **90**, 021802 (2003).

[81] B. Pontecorvo, Sov. Phys. JETP **26**, 984 (1968) [Zh. Eksp. Teor. Fiz **53**, 1717 (1967)].

[82] Francesco Capozzi et al., arXiv:1703.04471v1 [hep-ph].

[83] INO Collaboration, S.Athar et al., *"The Technical Design Report of INO-ICAL Detector"* (2006).

[84] The ICAL Collaboration, arXiv:1505.07380v1 [physics.ins-det](2015).

[85] M. M. Medeiros et al., Braz.J.Phys. **44**, 415 (2014).

[86] K. Abe et al. (Super-Kamiokande Collaboration), Phys. Rev. Lett. **107**, 241801 (2011).

[87] A. Ghosh et al., JHEP **04**, 009 (2013).

[88] T. Thakore et al., JHEP **05**, 058 (2013).

[89] D. Kaur et al., Euro. Phys. J. C, **75**, 156 (2015).

[90] M. M. Devi et al., JHEP **10**, 189 (2014).

[91] Animesh Chatterjee, Raj Gandhi, Jyotsna Singh, JHEP **06**, 045 (2014).

[92] A. Dutta et al., Phys. Lett. B **597**, 356 (2004).

[93] M. C. Gonzalez-Garcia, M. Maltoni, and T. Schwetz, Phys. Rev. D **68**, 053007 (2003).

[94] G. Barenboim and J. Lykken, Phys. Rev. D **80**, 113008 (2009).

[95] F. Reines and C. L. Cowan, Phys. Rev. **92**, 830 (1953).

[96] C. L. Cowan, F. Reines, F. B. Harrison, E. C. Anderson and F. N. Hayes, Phys. Rev. **90**, 493 (1953).

[97] R. Davis, Phys. Rev. Lett. **12**, 303 (1964).

[98] A. Ghosh, S. Choubey, JHEP **2013**, 174 (2013).

[99] A. Chatterjee et al., JINST **9** P007001 (2014).

[100] M. M. Devi et al., JINST **8** P11003 (2013).

[101] M. Honda, T.Kajita et al, Phys. Rev. D **70**, (2004).

[102] D. Casper, Nucl.Phys. Proc.Suppl. **112**, 161 (2002).

[103] A. M. Dziewonski and D. L. Anderson, Phys. Earth Planet. Interior **25**, 297, (1981).

[104] M. C. Gonzalez-Garcia, *et al.*, Phys.Rev. D **70**, 033010 (2004).

[105] A. Ghosh *et al.*, JHEP **4**, 009 (2013).

[106] S. H. Ahn, *et al.* (The K2K Collaboration), Phys. Lett. B **511**, 178 (2001).

[107] J. Ahn *et al.* (RENO collaboration), Phys. Rev. Lett. **108**, 191802 (2012).

[108] F. An *et al.* (DAYA-BAY Collaboration), Phys. Rev. Lett. **108**, 171803 (2012).

[109] K. Abe *et al.* (T2K collaboration), Phys. Rev. Lett. **112**, 181801 (2014).

[110] G. Barenboim *et al.*, JHEP 0210, 001 (2002).

[111] G. Barenboim *et al.*, Phys. Lett. B **534**, 106 (2002).

[112] G. Barenboim *et al.*, Phys. Lett. B **537**, 227 (2002).

[113] G. Barenboim et al., Phys. Lett. B **554**, 73 (2003).

[114] Animesh Chatterjee, Raj Gandhi, Jyotsna Singh, JHEP **06**, 045 (2014).

[115] P. Adamson *et al.*, Phys. Rev. Lett. **107**, 021801 (2011).

[116] P. Adamson *et al.*, Phys. Rev. Lett. **108**, 191801 (2012).

[117] M.M.Medeiros *et al.*, Proceedings of 33rd International Cosmic Ray Conference, RIO DE JANEIRO (2013), http://www.cbpf.br/ icrc2013/papers/icrc2013-0958.pdf.

[118] K. Abe et al. Phys. Rev. Lett. **107**, 241801 (2011).

[119] D. Kaur, Zubair Ahmad Dar, S. Kumar, Md. Naimuddin, Phys. Rev. D **95**, 093005 (2017).

[120] G. L. Fogli, E. Lisi, A. Marrone, D. Montanino, and A. Palazzo, Phys. Rev.D **66**, 053010 (2002).

[121] G. L. Fogli, E. Lisi, A. Marrone, and D. Montanino, Phys. Rev.D**67**, 093006 (2003).

[122] R. Gandhi *et al.*, Phys. Rev. D **76**, 073012 (2007).

[123] M. Kawaguchi and M. J. Moravcsik, Phys. Rev. **107**, 563 (1957).

[124] B. D. McDaniel, A. Silverman, R. R. Wilson and G. Cortellessa, Phys. Rev. **115**, 1039 (1959).

[125] A. Silverman, R. R. Wilson and W. M. Woodward, Phys. Rev. **108**, 501 (1957).

[126] P. L. Donoho and R. L. Walker, Phys. Rev. **112**, 981 (1958).

[127] R. H. Capps, Phys. Rev. **114**, 920 (1959).

[128] D. E. Groom and J. H. Marshall, Phys. Rev. **159**, 1213 (1967).

[129] R. Erbe *et al.* (ABBHHM Collaboration), Phys. Rev. **188**, 2060 (1969); data tabulated in Numerical Data and Functional Relationships in Science and Technology, edited by H. Schopper, Landolt-Börnstein, New Series I/12b (Springer-Verlag, New York, 1988), p. 355.

[130] M. Q. Tran *et al.* [SAPHIR Collaboration], Phys. Lett. B **445**, 20 (1998).

[131] K.-H. Glander *et al.*, Eur. Phys. J. A **19**, 251 (2004).

[132] R. Bradford *et al.*, Phys. Rev. C **73** 035202 (2006).

[133] J. W. C. McNabb *et al.*, Phys. Rev. C **69**, 042201(R) (2004).

[134] M. E. McCracken *et al.*, Phys. Rev. C **81** 025201 (2010).

[135] M. Sumihama *et al.* [LEPS Collaboration], Phys. Rev. C **73**, 035214 (2006).

[136] A. Lleres *et al.*, Eur. Phys. J. A **31**, 79 (2007).

[137] A. Lleres *et al.*, Eur. Phys. J. A **39**, 149 (2009).

[138] T. C. Jude *et al.* [Crystal Ball at MAMI Collaboration], Phys. Lett. B **735**, 112 (2014).

[139] L. Tiator, D. Drechsel, S. S. Kamalov and M. Vanderhaeghen, Eur. Phys. J. ST **198**, 141 (2011).

[140] G. Knochlein, D. Drechsel and L. Tiator, Z. für Physik A, **352**, 327 (1995).

[141] L. Tiator, M. Gorchtein, V. Kashevarov, K. Nikonov, M. Ostrick, M. Hadžimehmedović, R. Omerović, H. Osmanović, J. Stahov and A. Švarc, Eur. Phys. J. A **54**, no.12, 210 (2018).

[142] W. T. Chiang, S. N. Yang, L. Tiator, M. Vanderhaeghen and D. Drechsel, Phys. Rev. C **68**, 045202 (2003).

[143] T. Mart and A. Rusli, PTEP **2017**, 123D04 (2017).

[144] D. Skoupil and P. Bydzovsky, Phys. Rev. C **93**, 025204 (2016).

[145] D. Skoupil and P. Bydzovsky, Phys. Rev. C **97**, 025202 (2018).

[146] S. Janssen, J. Ryckebusch, D. Debruyne, and T. Van Cauteren, Phys. Rev. C **65**, 015201 (2001).

[147] T. Mart and A. Sulaksono, Phys. Rev. C **74**, 055203 (2006).

[148] T. Mart and S. Sakinah, Phys. Rev. C **95**, 045205 (2017).

[149] T. Mart, Phys. Rev. D **100**, 056008 (2019).

[150] S. Capstick and W. Roberts, Prog. Part. Nucl. Phys. **45**, S241 (2000).

[151] U. Loring, B. C. Metsch, and H. R. Petry, Eur. Phys. J. A **10**, 395 (2001).

[152] U. Loring, B. C. Metsch, and H. R. Petry, Eur. Phys. J. A **10**, 447 (2001).

[153] P. Ambrozewicz *et al.* [CLAS Collaboration], Phys. Rev. C **75**, 045203 (2007).

[154] M. Gabrielyan *et al.* [CLAS Collaboration], Phys. Rev. C **90**, 035202 (2014).

[155] D. S. Carman *et al.* [CLAS Collaboration], Phys. Rev. C **87**, 025204 (2013).

[156] P. Achenbach *et al.* [A1 Collaboration], Eur. Phys. J. A **48**, 14 (2012).

[157] T. Gogami *et al.*, Few Body Syst. **54**, 1227 (2013).

[158] J. C. David, C. Fayard, G.-H. Lamot, and B. Saghai, Phys. Rev. C **53**, 2613 (1996).

[159] R. A. Williams, C. R. Ji and S. R. Cotanch, Phys. Rev. C **46**, 1617 (1992).

[160] T. Mizutani, C. Fayard, G.-H. Lamot, and B. Saghai, Phys. Rev. C **58**, 75 (1998).

[161] T. Mart, Phys. Rev. C **82**, 025209 (2010).

[162] S. Janssen, J. Ryckebusch and T. Van Cauteren, Phys. Rev. C **67**, 052201 (2003).

[163] N. Solomey [MINERvA Collaboration], Nucl. Phys. Proc. Suppl. **142**, 74 (2005).

[164] [MINERvA Collaboration], FERMILAB-DESIGN-2006-01, MINERVA-DOCUMENT-700.

[165] R. E. Shrock, Phys. Rev. D **12**, 2049 (1975).

[166] W. Mechlenburg. Acta Phys. Aust. **48**, (1976).

[167] A. A. Amer, Phys. Rev. D **18**, 2290 (1978).

[168] H. K. Dewan, Phys. Rev. D **24**, 2369 (1981).

[169] G. B. Adera, B. I. S. Van Der Ventel, D. D. van Niekerk and T. Mart, Phys. Rev. C **82**, 025501 (2010).

[170] Zhenping Li, Phys. Rev. C **52**, 1648 (1995).

[171] Zhenping Li, Hongxing Ye, Minghui Lu, Phys. Rev. C **56**, 1099 (1997).

[172] D. Lu, R. H. Landau, and S. C. Phatak, Phys. Rev. C **52**, 1662 (1995).

[173] G. R. Farrar, K. Huleihel, and H. Zhang, Nucl. Phys. B **349**, 655 (1991).

[174] B. Julia-Diaz *et al.*, Nucl. Phys. A **755**, 463 (2005).

[175] S. Steininger and U.-G. Meissner, Phys. Lett. B **391**, 446 (1997).

[176] B. Borasoy, P. C. Bruns, U.-G. Meissner, and R. Nissler, Eur. Phys. J. A **34**, 161 (2007).

[177] V. Shklyar, H. Lenske, and U. Mosel, Phys. Rev. C **72**, 015210 (2005).

[178] R. Shyam, O. Scholten, and H. Lenske, Phys. Rev. C **81**, 015204 (2010).

[179] B. Julia-Diaz, B. Saghai, T.-S. H. Lee, and F. Tabakin, Phys. Rev. C **73**, 055204 (2006).

[180] A. V. Anisovich *et al.*, Eur. Phys. J. A **34**, 243 (2007).

[181] B. Julia-Diaz, B. Saghai, T.-S. H. Lee and F. Tabakin, nucl-th/0512010.

[182] H. Thom, Phys. Rev. **151**, 1322 (1966).

[183] T. Mart and C. Bennhold, Phys. Rev. C **61**, 012201 (2000).

[184] T. Mart, Phys. Rev. C **62**, 038201 (2000).

[185] T. Mart, C. Bennhold, H. Haberzettl, and L. Tiator, http://www.kph.uni-mainz.de/MAID/kaon/kaonmaid.html.

[186] S. Janssen *et al.*, Eur. Phys. J. A **11**, 105 (2001).

[187] S. Janssen, D. G. Ireland, J. Ryckebusch, Phys. Lett. B **562**, 51 (2003).

[188] M. Sotona and S. Frullani, Prog. Theor. Phys. Suppl. **117**, 151 (1994).

[189] S. S. Hsiao, D. H. Lu, and S. N. Yang, Phys. Rev. C **61**, 068201 (2000).

[190] B. Han, M. Cheoun, K. Kim, and I.-T. Cheon, Nucl. Phys. A **691**, 713 (2001).

[191] O. V. Maxwell, Phys. Rev. C **76**, 014621 (2007).

[192] A. de la Puente, O. V. Maxwell, and B. A. Raue, Phys. Rev. C **80**, 065205 (2009).

[193] R. A. Adelseck, C. Bennhold and L. E. Wright, Phys. Rev. C **32**, 1681 (1985).

[194] R. A. Adelseck and L. E. Wright, Phys. Rev. C **39**, 580 (1989).

[195] R. A. Adelseck and B. Saghai, Phys. Rev. C **42**, 108 (1990).

[196] B. Saghai and F. Tabakin, AIP Conf. Proc. **339**, 521 (1995).

[197] R. A. Williams, C. R. Ji and S. R. Cotanch, Phys. Rev. C **43**, 452 (1991).

[198] R. A. Williams, C. R. Ji and S. R. Cotanch, Phys. Rev. D **41**, 1449 (1990).

[199] T. Corthals, J. Ryckebusch, and T. Van Cauteren, Phys. Rev. C **73**, 045207 (2006).

[200] T. Corthals, T. Van Cauteren, J. Ryckebusch, and D. G. Ireland, Phys. Rev. C **75**, 045204 (2007).

[201] T. Corthals *et al.*, Phys. Lett. **B656**, 186 (2007).

[202] P. Bydzovsky and D. Skoupil, Phys. Rev. C **100**, 035202 (2019).

[203] M. Guidal, J. M. Laget and M. Vanderhaeghen, Nucl. Phys. A **627**, 645 (1997).

[204] S. L. Adler and R. F. Dashen, Current Algebras and applications to particle physics, W. A. Benjamin (1968).

[205] S. Sakinah, S. Clymton and T. Mart, Acta Phys. Polon. B **50**, 1389 (2019).

[206] M. Guidal, J. M. Laget and M. Vanderhaeghen, Phys. Rev. C **61**, 025204 (2000).

[207] L. De Cruz, T. Vrancx, P. Vancraeyveld, and J. Ryckebusch, Phys. Rev. Lett. **108** 182002 (2012).

[208] L. De Cruz, J. Ryckebusch, T. Vrancx, P. Vancraeyveld, Phys. Rev. C **86**, 015212 (2012).

[209] R. M. Davidson and R. Workman, Phys. Rev. C **63**, 025210 (2001).

[210] E. Hernandez, J. Nieves and M. Valverde, Phys. Rev. D **76**, 033005 (2007).

[211] E. Hernandez, J. Nieves and M. J. Vicente Vacas, Phys. Rev. D **87**, 113009 (2013).

[212] M. Rafi Alam, I. Ruiz Simo, M. Sajjad Athar and M. J. Vicente Vacas, Phys. Rev. D **82**, 033001 (2010).

[213] M. Rafi Alam, I. Ruiz Simo, M. Sajjad Athar and M. J. Vicente Vacas, Phys. Rev. D **87**, 053008 (2013).

[214] M. Rafi Alam *et al.*, AIP Conf. Proc. **1680**, 020001 (2015).

[215] C. Bennhold *et al.*, nucl-th/9901066.

[216] C. Bennhold, T. Mart, and D. Kusno, Proceedings of the CEBAF/INT Workshop on N.Physics, Seattle, USA, 1996 (World Scientific, Singapore, 1997, T.- S. H. Lee and W. Roberts, editors), p.166.

[217] K. Ohta, Phys. Rev. C **40**, 1335 (1989).

[218] H. Haberzettl, Phys. Rev. C **56**, 2041 (1997).

[219] M. Benmerrouche, R. M. Davidson and N. C. Mukhopadhyay, Phys. Rev. C **39**, 2339 (1989).

[220] H. Kamano, S. X. Nakamura, T. S. H. Lee and T. Sato, Phys. Rev. C **94**, 015201 (2016).

[221] H. Kamano, B. Julia-Diaz, T.-S. H. Lee, A. Matsuyama and T. Sato, Phys. Rev. C **80**, 065203 (2009).

[222] B. Julia-Diaz, H. Kamano, T.-S. H. Lee, A. Matsuyama, T. Sato and N. Suzuki, Phys. Rev. C **80**, 025207 (2009).

[223] W. T. Chiang, B. Saghai, F. Tabakin and T. S. H. Lee, Phys. Rev. C **69**, 065208 (2004).

[224] H. Kamano, S. X. Nakamura, T.-S. H. Lee and T. Sato, Phys. Rev. D **86**, 097503 (2012).

[225] S. X. Nakamura, H. Kamano and T. Sato, Phys. Rev. D **92**, 074024 (2015).

[226] K. M. Watson, Phys. Rev. **88**, 1163 (1952).

[227] T. Sato, D. Uno and T. S. H. Lee, Phys. Rev. C **67**, 065201 (2003)

[228] L. Alvarez-Ruso, E. Hernández, J. Nieves and M. J. Vicente Vacas, Phys. Rev. D **93**, 014016 (2016).

[229] A. V. Anisovich *et al.*, Eur. Phys. J. A **48**, 88 (2012), https://pwa.hiskp.uni-bonn.de/

[230] A. Anisovich *et al.*, Eur. Phys. J. A **50**, 129 (2014).

[231] A. Anisovich *et al.*, Phys. Rev. Lett. **119**, 062004 (2017).

[232] A. Anisovich *et al.*, Eur. Phys. J. A **53**, 242 (2017).

[233] V. Nikonov *et al.*, Phys. Lett. B **662**, 245 (2008).

[234] D. Ronchen, M. Doring and U. Meissner, Eur. Phys. J. A **54**, 110 (2018).

[235] K. L. Wang, L. Y. Xiao and X. H. Zhong, Phys. Rev. C **95**, 055204 (2017).

[236] B. Hunt and D. Manley, Phys. Rev. C **99**, 055204 (2019).

[237] M. Tanabashi *et al.* [Particle Data Group], Phys. Rev. D **98**, 030001 (2018).

[238] S. Scherer, Adv. Nucl. Phys. **27**, 277 (2003).

[239] S. Scherer and M. R. Schindler, Lect. Notes Phys. **830**, 1 (2012).

[240] V. Koch, nucl-th/9512029.

[241] V. Koch, Int. J. Mod. Phys. E **6**, 203 (1997).

[242] B. Kubis, arXiv:hep-ph/0703274.

[243] N. Cabibbo, E. C. Swallow, and R. Winston, Ann. Rev. Nucl. Part. Sci. **53**, 39 (2003).

[244] H. Haberzettl, C. Bennhold, T. Mart and T. Feuster, Phys. Rev. C **58**, R40 (1998).

[245] T. Leitner, O. Buss, L. Alvarez-Ruso and U. Mosel, Phys. Rev. C **79**, 034601 (2009).

[246] R. González-Jiménez *et al.*, Phys. Rev. D **95**, 113007 (2017).

[247] W. Rarita and J. Schwinger, Phys. Rev. **60**, 61 (1941).

[248] M. Fierz and W. E. Pauli, Proceedings of the Royal Society of London Series A Mathematical and Physical Sciences **173**, 211 (1939).

[249] V. Pascalutsa and R. Timmermans, Phys. Rev. C **60**, 042201 (1999).

[250] T. Mart, J. Kristiano and S. Clymton, Phys. Rev. C **100**, 035207 (2019).

[251] T. Vrancx, L. De Cruz, J. Ryckebusch and P. Vancraeyveld, Phys. Rev. C **84**, 045201 (2011).

[252] M. Rafi Alam, L. Alvarez-Ruso, M. Sajjad Athar and M. J. Vicente Vacas, AIP Conf. Proc. **1663**, 120014 (2015).

[253] M. Sajjad Athar, S. Ahmad and S. K. Singh, Nucl. Phys. A **782**, 179 (2007).

[254] S. K. Singh, M. Vicente-Vacas and E. Oset, Phys. Lett. B **416**, 23 (1998).

[255] M. Sajjad Athar, S. Chauhan and S. K. Singh, J. Phys. G **37**, 015005 (2010).

[256] M. Rafi Alam, M. Sajjad Athar, L. Alvarez-Ruso, I. Ruiz Simo, M. J. Vicente Vacas and S. K. Singh, [arXiv:1311.2293 [hep-ph]].

[257] M. Sajjad Athar, S. Ahmad and S. K. Singh, Phys. Rev. D **75**, 093003 (2007).

[258] S. Ahmad, M. Sajjad Athar and S. K. Singh, Phys. Rev. D **74**, 073008 (2006).

[259] L. Alvarez-Ruso, E. Oset, S. K. Singh and M. Vicente-Vacas, Nucl. Phys. A **663**, 837 (2000).

[260] M. Valverde, J. Nieves, E. Hernandez, S. K. Singh and M. Vicente Vacas, Mod. Phys. Lett. A **23**, 2309 (2008).

[261] C. H. Llewellyn Smith, Phys. Rept. **3**, 261 (1972).

[262] G. L. Fogli and G. Nardulli, Nucl. Phys. B **160**, 116-150 (1979).

[263] T. Feuster and U. Mosel, Phys. Rev. C **59**, 460 (1999).

[264] M. Benmerrouche, N. C. Mukhopadhyay and J. F. Zhang, Phys. Rev. D **51**, 3237 (1995).

[265] T. Feuster and U. Mosel, Nucl. Phys. A **612**, 375 (1997).

[266] W. Suciawo, S. Clymton and T. Mart, J. Phys. Conf. Ser. **856**, 012011 (2017).

[267] C. G. Callan, Jr. and D. J. Gross, Phys. Rev. Lett. **22**, 156 (1969).

[268] A. D. Martin *et al.*, Eur. Phys. J. C **4**, 463 (1998).

[269] M. Gluck *et al.*, Eur. Phys. J. C **5**, 461 (1998).

[270] M. Gluck *et al.*, Eur. Phys. J. C **53**, 355 (2008).

[271] A. D. Martin *et al.*, Eur. Phys. J. C **63**, 189 (2009).

[272] S. Alekhin *et al.*, arXiv:1609.03327 [hep-ph].

[273] S. Chekanov *et al.* [ZEUS Collaboration], Phys. Rev. D **67**, 012007 (2003).

[274] Z. Zhang [H1 and ZEUS Collaborations], Acta Phys. Polon. Supp. **8**, 957 (2015).

[275] L. Del Debbio *et al.* [NNPDF], JHEP **03**, 039 (2007).

[276] P. M. Nadolsky *et al.*, Phys. Rev. D **78**, 013004 (2008).

[277] A. Accardi, M. E. Christy, C. E. Keppel, W. Melnitchouk, P. Monaghan, J. G. Morfín and J. F. Owens, Phys. Rev. D **81**, 034016 (2010).

[278] L. A. Harland-Lang, A. D. Martin, P. Motylinski and R. S. Thorne, Eur. Phys. J. C **75**, 204 (2015).

[279] P. Dennery, Phys. Rev. **127**, 664 (1962).

[280] N. Dombey, Phys. Rev. **127**, 653 (1962).

[281] S. L. Adler, Annals Phys. **50**, 189 (1968).

[282] R. E. Marshak, Riazuddin, and C. P. Ryan, *"Theory of Weak Interactions in Particle Physics"*, Wiley-Interscience, New York (1969).

[283] S. X. Nakamura, H. Kamano, T.-S. H. Lee and T. Sato, AIP Conf. Proc. **1663**, 070005 (2015).

[284] B. D. Serot and X. Zhang, Phys. Rev. C **86**, 015501 (2012).

[285] T. Leitner, O. Buss, U. Mosel and L. Alvarez-Ruso, Phys. Rev. C **79**, 038501 (2009).

[286] J. T. Sobczyk. and J. Zmuda, Phys. Rev. C **87**, 065503 (2013).

[287] K. M. Graczyk and J. T. Sobczyk, Phys. Rev. D **77**, 053003 (2008).

[288] Y. Nambu and G. Jona-Lasinio, Phys. Rev. **124**, 246 (1961).

[289] Y. Nambu and G. Jona-Lasinio, Phys. Rev. **122**, 345 (1961).

[290] S. Scherer and M. R. Schindler, A Primer for Chiral Perturbation Theory, Springer- Verlag, Berlin (2012).